UNIVERSITY OF NAIROBI

COLLEGE OF BIOLOGICAL AND PHYSICAL SCIENCES

DEPARTMENT OF CHEMISTRY

NATURAL PRODUCT-LOADED NANOPARTICLES FOR CANCER THERAPY: FORMULATION, CHARACTERIZATION, *IN SILICO* AND CELLULAR STUDIES

BY

ANDIMA MOSES

I80/50060/2015

A THESIS SUBMITTED IN FULFILLMENT OF THE REQUIREMENTS FOR THE AWARD OF THE DEGREE OF DOCTOR OF PHILOSOPHY IN CHEMISTRY AT THE UNIVERSITY OF NAIROBI

SEPTEMBER 2020

DECLARATION

I declare that this thesis is my original work and has not been submitted elsewhere for examination, award of a degree or publication. Where other people's work, or my own work has been used, this has properly been acknowledged and referenced in accordance with the University of Nairobi's requirements.

------------------------------------   --------------------------------------

Andima Moses   Date

I80/50060/2015

This PhD thesis has been submitted with our approval as research supervisors.

-------------------------------   ------------------------------------

Dr. Solomon Derese   Date

Department of Chemistry

University of Nairobi,

P.O box 30197-00100, Nairobi, Kenya

sderese@uonbi.ac.ke

----------------------------------   --------------------------------------

Dr. Albert J. Ndakala   Date

Department of Chemistry

University of Nairobi,

University of Nairobi,

P.O box 30197-00100, Nairobi, Kenya

andakala@uonbi.ac.ke

DEDICATION

This Ph.D. Thesis is dedicated to my parents for their sacrifices to provide for my education. I also dedicate this work to my loving and caring wife Jackline Abau and our children Bamuke Aaron Andima, Mungufeni Nathan Andima, Munguleni Hannah Andima and Letasi Peace Andima.

ACKNOWLEDGMENTS

ABSTRACT

Cancer is a dreadful disease affecting all categories of people globally. Treatments for cancer such as chemotherapy, radiation therapy, and surgical removal of tumors and / or combination therapies exist, but they present serious side effects to patients. There is significant interest in identifying well tolerated alternative therapies or re-engineering of the existing therapies. Natural products have been sought as sources of anticancer drugs. Unfortunately, therapeutic efficacies of anti-cancer compounds found in natural extracts are limited by their low bioavailability. In this study, the anticancer potential of natural products from four plant species was investigated. The use of nanoparticle drug delivery systems to enhance anticancer activity of β-sitosterol as a model natural products was also investigated. The plant species selected were: *Zanthoxylum zanthoxyloides* (Lam.) Zepern. and Timler, *Aloe tororoana* Reynolds, *Aloe schweinfurthii* var. *labworana* Reynolds, and *Taberneamontana ventricosa* Hochst. Ex. A.DC. Chromatographic separation of the plant extracts and structure elucidation using a combination of spectroscopic methods led to identification of 25 compounds. The extract of *Z. zanthoxyloides* yielded five compounds (**80-84**). Six compounds (**5**, **47**, **85**-**88**) were isolated from the extract from *A. tororoana.* Seven compounds consisting of three anthraquinone derivatives (**89-91**), one aryl derivative (**92**), one naphthaquinone (**93**) and two steroidal compounds (**5** and **47**) were isolated from *A. schweinfurthii*: Extracts from *T. ventricosa* yielded nine compounds consisting of five ibog-type indole alkaloids (**94**, **96**, **98**, **100** and **101**), one vobasinyl-type indole alkaloid (**95**) and three non-alkaloidal compounds (**97**, **99** and **47**). *In vitro* antiproliferative studies indicate that dihydrochelerythrine (**81**) inhibited proliferation of liver cancer (HCC) cells (IC$_{50}$ 8.9 μM) and breast cancer (BT549) cells, (IC$_{50}$ 21.2 μM). Similarly, sesamin (**82**) exhibited moderate inhibitory activity against BT549 cancer cells (IC50 47.6 μM). Ursolic acid (**99**) exhibited high inhibitory activity against A549 cells (IC$_{50}$: 6.6 μM). Chrysophanol (**89**) was highly active against liver cancer (HCC) cells (IC50 2.4 μM) while voacristine (**98**) exhibited moderate inhibitory activity against liver cancer (HepG2) cells (IC50 23.0 μM). *In silico* docking studies were carried out to establish the possible mechanism of action of the isolated compounds against molecular targets in the p53 pathway. The results suggest that some of the compounds possibly inhibit cancer cell

proliferation by inducing cell cycle arrest and apoptosis as evidenced by high binding affinities to cyclin-dependent kinases (CDK2 and CDK6), Bcl-2 protein and low binding affinities to caspases 3 and 8. In order to assess the effect of formulation into nanoparticles on bioavailability and efficacy, one of the isolated compounds, β-sitosterol was formulated into nanoparticles. Poly (lactide-co-glycolic acid) (PLGA) and block copolymers of poly (ethylene glycol)-block-poly (lactic acid) (PEG-PLA) were used to encapsulate β-sitosterol (β-Sit) into nanoparticles. β-Sitosterol-loaded PLGA and PEG-PLA nanoparticles (β-Sit-PLGA and β-Sit-PEG-PLA) were prepared by simple emulsion-solvent evaporation technique. The nanoparticles were characterized for particle size, polydispersity index (PDI), surface charge (ζ) and encapsulation efficiency. β-Sit-PLGA and β-Sit-PEG-PLA nanoparticles were spherical in shape with average particle sizes of 215.0±29.7 and 240.6±23.3 nm, ζ of -13.8±1.61 and -23.5±0.27 mV, respectively, and PDI < 0.2. The encapsulation efficiencies of β-Sit were 62.89±4.66 and 51.83±19.72 % in PLGA and PEG-PLA nanoparticles, respectively. Cellular internalization and antiproliferative activities of the formulated nanoparticles were studied in MCF-7 and MDA-MB-231 human breast cancer cells using flow cytometry, laser scanning confocal microscopy and MTT assays, respectively. Fluorescence activated cell sorting analysis (FACS) indicated that β-Sit-PLGA nanoparticles were internalized by both cell lines compared to β-Sit-PEG-PLA and the respective blank nanoparticles. β-Sit-PLGA nanoparticles were therefore selected to evaluate antiproliferative activity. Cell viability was inhibited by up to 80% in a concentration range of 6.64-53.08 μg/mL of β-Sit in nanoparticles compared to the untreated cells. The release of β-Sit from the nanoparticle matrix was studied *in vitro* in PBS and PBS/with 0.2% Tween20 which showed an initial burst release in 24 hours followed by a sustained release. Stability studies showed that β-Sit-PLGA nanoparticles were generally more stable in a protein rich medium (PBS/FBS) whereas β-Sit-PEG-PLA nanoparticles had a tendency to aggregate. The results of this study indicate that, compounds **81**, **82**, **89**, **98** and **99** hold potential as anticancer agents.Furthermore, encapsulation of β-Sit in PLGA nanoparticles is a promising strategy to enhance anticancer activity against breast cancer cells.

TABLE OF CONTENTS

LIST OF TABLES

LIST OF FIGURES

LIST OF APPENDICES

LIST OF PUBLICATIONS FROM THIS WORK

Journal Publications

Andima, M., Costabile, G., Isert, Ndakala, J. A., Derese, S., and Merkel, O., Evaluation of β-Sitosterol Loaded PLGA and PEG-PLA Nanoparticles for Effective Treatment of Breast Cancer: Preparation, Physicochemical Characterization, and Antitumor Activity. *Pharmaceutics*, 2018. *10*(4): p. 232. DOI:10.3390/pharmaceutics10040232

Andima M, Coghi P, Yang LJ, Kam Wai Wong V, Ngule CM, Heydenreich M, Ndakala AJ, Yenesew A, Derese S. 2020. Antiproliferative Activity of Secondary Metabolites from Zanthoxylum zanthoxyloides Lam: *In vitro* and *in silico* Studies. *Pharmacognosy Communications*. 10(1).2020,**10**(1): p. 44-51. DOI:10.5530/pc.2020.1.8

Conference presentations

Andima, M., Ndakala, A., Derese, S., (2018). Anticancer potential of secondary metabolites from Zanthoxylum *zanthoxyloides*: An *in vitro* and *in silico* investigation. PACN congress, University of Nairobi, Nairobi, Kenya. (Poster).

Andima, M., Costabile, G., Isert, L, Ndakala, J. A., Derese, S., and Merkel, O., (2019). Enhancement of Therapeutic Efficacy of Selected Natural Products Using Nanomedicine. NAPRECA-Uganda Meeting, Makerere University, Kampala. (Oral presentation).

LIST OF ABBREVIATIONS AND SYMBOLS

Å	Angstrom
ANOVA	Analysis of variance
AR	Analytical grade reagent
B94	(3S)-3-({[(5S,8R)-2-(3-carboxypropyl)-8-(2-{[(4-chlorophenyl)acetyl]amino}ethyl)-1,3-dioxo-2,3,5,8-tetrahydro-1H-[1,2,4]triazolo[1,2-a]pyridazin-5-yl]carbonyl}amino)-4-oxopentanoic acid
COSY	Correlation spectroscopy
CPTLC	Circular preparative thin layer chromatography
DAPI	4′,6-diamidino-2-phenylindole
d	doublet
dd	doublet of doublet
ddd	doublet of doublet of doublet
dG	Gibb's free energy
DNA	Deoxyribonucleic acid
DTQ	4-[3-hydroxyanilino]-6,7-dimethoxyquinazoline
FACS	Fluorescence activated cell sorting
FBS	Fetal bovine serum
FSE	3,7,3',4'-Tetrahydroxyflavone
HMBC	Heteronuclear multiple bond correlation
HPLC	High performance liquid chromatography.
HRESIMS	High resolution electrospray ionization mass spectrometry.
HSQC	Heteronuclear single quantum coherence.
IC_{50}	Concentration of 50% inhibition.
IMZ	imidazoline
J	Coupling constant.
Kcal/mol	Kilo calories per mole.
LC-ESI-MS	Liquid chromatography electrospray ionization mass spectrometry.

L1O	4-[4-methoxy-4 (phenylmethyl)piperidin-1-yl]-N-[4-[(2-methyl-1-phenylsulfanyl-propan-2-yl)amino]-3-nitro-phenyl]sulfonyl-benzamide
m	multiplet.
MHz	Mega Hertz.
MMFF94X	Merck molecular force field 94X.
MTT	[3-(4,5-dimethylthiazol-2-yl)-2,5-diphenyltetrazolium bromide]
nm	Nanometer.
NMR	Nuclear magnetic resonance.
NOESY	Nuclear overhauser and exchange spectroscopy.
PBS	Phosphate buffer saline
PEG-PLA (R25)	Polyethylene glycol-block-polylactic acid containing 25% PEG.
PEG-PLA (R45)	Polyethylene glycol-block-polylactic acid containing 45% PEG.
PDI	Polydispersity index.
PMI	[2-amino-6-(2,6-difluoro-benzoyl)-imidazo[1,2-A]pyridine-3-yl]-phenyl-methanone.
ppm	parts per million.
p21$^{WAF1/CIP1}$	Cyclin-dependent kinase inhibitor protein 21.
RNA	Ribose nucleic acid.
RXB	(1S)-2-oxo-1-phenyl-2-[(1,3,4-trioxo-1,2,3,4-tetrahydroisoquinolin-5 yl)amino]ethyl acetate
s	singlet.
SMILES	Simplified molecular input line entry system.
t	triplet.
TLC	Thin layer chromatography.
UV-Vis	Ultraviolet-visible.
WHO	World health organization.
λ_{max}	Maximum wavelength of absorption.
δ	Chemical shift
1D NMR	One dimensional nuclear magnetic resonance.

2D NMR   Two dimensional nuclear magnetic resonance.

3D   Three dimensional.

7KC   (S)-N-2-(dimethylamino)-1-phenyl-ethyl]-6,6-dimethyl-3-[(2-methylthieno[3,2-

            d]pyrimidin-4-yl)amino]-1,4-dihydropyrrolo[3,4-c]pyrazole-5-carboxamide

CHAPTER 1: INTRODUCTION

1.1 Background of the Study

Cancer is a complex disease which originates from uncontrolled cell proliferation accompanied by changes in cellular, biochemical and enzymatic parameters (Cooper and Hausmans, 2007). By the year 2018, there were 18.1 million cases of cancer with 9.6 million deaths reported (Bray *et al.*, 2018). Cancer cases are projected to rise from 18.1 million in 2018 to 29.5 million in 2040. (Bray *et al*., 2018). The most common cancers diagnosed among men and women were lung, prostate, breast, colorectal, liver, and cervical and stomach cancers. Global cancer incidences and deaths vary from one region of the world to the other; with Europe accounting for 23.4% of cases and 20.3% deaths, the Americas accounting for 21.0% of cases and 14.4% of deaths, while Asia and Africa account for 48.4% and 5.8% cases and 57.3% and 7.3% deaths, respectively in 2018 (Bray *et al.*, 2018; WHO, 2018).

Conventionally, therapeutic strategies against cancer include chemo, radiation and combination therapies and surgical removal of tumors (Chen *et al.*, 2013). All these conventional therapies are expensive to the common man and are often laden with major side effects. In many cases, recrudescence occurs due to resistance to chemo and radiation therapies and aggressive metastasis (Chen *et al.*, 2013). In cases where surgery has been used to remove cancerous tumors, only cancer follicles are removed leaving behind free cancer cells which are often the origin of relapse (He *et al.*, 2013).

Owing to the challenges posed by conventional cancer therapies, the search for alternative treatments or improvement of the current treatment options is eminent. A lot of research has been directed towards exploitation of medicinal plants whose extracts have shown good anticancer

activity. For example, *Curcuma longa* (Shi *et al.*, 2006; Yue *et al.*, 2010)*, Camellia sinensis* (Conde *et al*., 2014*)* and *Camptotheca acuminata (Zhang et al., 2007)* are some plants that have been exploited for their anticancer potential. Unfortunately, phytomedicines have low solubility in water, which decreases their bioavailability. Moreover some phytomedicines suffer from reduced absorption and increased systemic clearance which limits their clinical use in cancer therapy (Bell *et al.*, 2014; Mathur and Vyas, 2013; Thapa *et al.*, 2013).

A number of strategies have been explored to circumvent some of the fore mentioned challenges associated with natural products. Among these, nanotechnology is one of the emerging clinically valuable strategies for delivering therapeutic payloads to target cells. Use of nanoparticles (NPs) has been demonstrated in recent strategies aimed at delivering recombinant proteins, vaccines, conventional drugs and, more recently nucleotides to target cells (Ramos-Tejadaa *et al.*, 2015). The advantages that accrue from using NPs include; ability to transport and release the active therapeutic agents selectively to target cells consequently decreasing adverse effects and enhancing efficacy and specificity (Suraf, 2010). For instance the clinical application of paclitaxel (**1**), a natural anticancer drug is restricted by its poor solubility in water. However, *in vitro* studies show that its nanoformulations enhanced its therapeutic efficacy several folds in comparison with the free drug (Gu *et al.*, 2013). In a similar study, encapsulation of curcumin (**2**), a natural product from *Curcuma longa* into nanoparticles enhanced its bioavailability 9-folds in comparison with the free drug (Shaikh *et al.*, 2009).

1 **2**
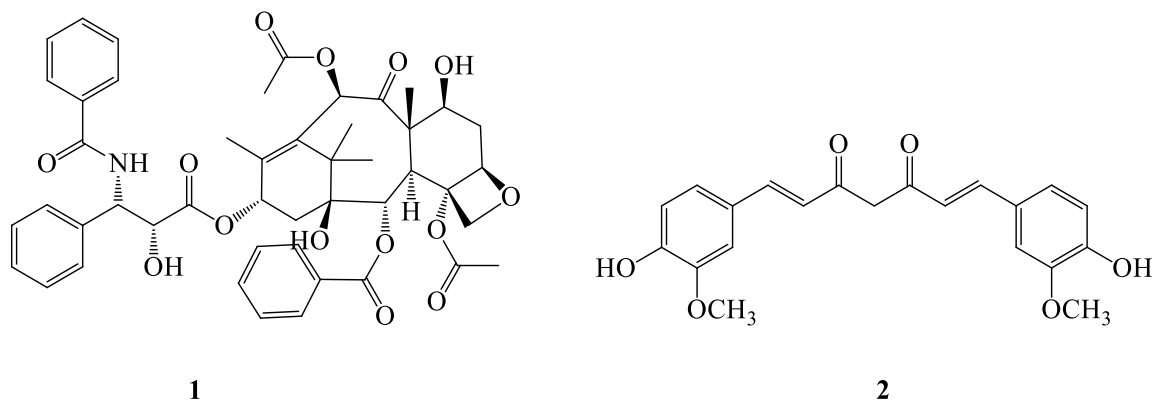
A number of anticancer drugs including paclitaxel (**1**) and curcumin (**2**) are obtained from plants. Among the current anticancer drugs, 49 % are either natural products or derivatives of natural products (Newman and Cragg, 2016). In this study therefore, the potential of natural products from selected medicinal plants as anticancer drugs was investigated. In order to enhance anticancer activity of natural products, nanoparticle formulation strategy was adopted.

Zanthoxylum zanthoxyloides (Lam.) Zepern and Timler*, Aloe tororoana* Reynolds*, Aloe schweinfurthii* var. *labworana* Reynolds*,* and *Taberneamontana ventricosa* Hochst. Ex. A.DC. were selected as sources for isolation of secondary metabolites for cancer treatment. Anticancer activities of crude extracts and some isolated secondary metabolites from the same genera of the selected plants have been reported in previous studies (Gunasekera *et al.*, 1980; Guo *et al.*, 2007; Huang *et al.*, 2013; Kassim *et al.*, 2005; Kaur *et al.*, 2011; Kuete *et al.*, 2011; Santhanam *et al.*, 2016). For instance benzophenanthridine alkaloids; fagorinine (**3**) and nitidine (**4**) isolated from the genus *Zanthoxylum* has been indicated as a DNA intercalating agent and inhibitor of DNA topoisomerase I and II enzymes (Larsen *et al.*, 1993).
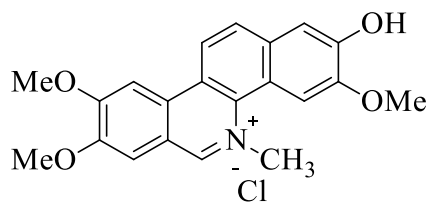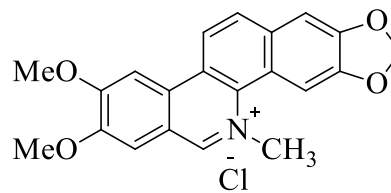
3   **4**

Although there is no phytochemical information on the two *Aloe* spp selected here, it is noteworthy that plants belonging to the genus *Aloe* contain anthraquinones, naphthoquinones and cardiac glycosides (CGs) which have been demonstrated to exhibit cytotoxicity against different cancer cell lines (Abdissa *et al.*, 2014; Lu *et al.*, 2013; Menger *et al.*, 2012; Perchellet *et al.*, 2000; Winnicka *et al.*, 2006). Meanwhile, several indole alkaloids isolated from different species of *Taberneamontana* have been reported to inhibit several cancer cells (Lim *et al.*, 2015; Zhang *et al.*, 2015). Some of the compounds from *Taberneamontana* genus have also been shown to reverse multidrug resistance in some cancer cells (Toh-Seok *et al.*, 1998).

1.2   Statement of the Problem

The current conventional anticancer therapies face several limitations including low efficacy, adverse side effects, and multidrug resistance among others. In some cases, the therapies are non-specific and often lead to relapse just after a course of treatment due to aggressive metastasis of some cancers (Chen *et al.*, 2013; da Silva *et al.*, 2012). This highlights the need to search for more anticancer therapies which are efficacious and safer. Over a long time, natural products have been the pillar of chemotherapy for different diseases including cancer. Till now, natural products continue to provide a vivacious source for drug discovery (Cragg and Newman, 2005). Despite the wide interest in natural products, they face limitations such as low solubility in aqueous media hence reducing their bioavailability and therapeutic efficacy. These limitations of natural products call for the need to exploit strategies to enhance therapeutic efficacy of some promising natural

4

products. The use of nanoparticle drug delivery systems are being explored as a means to offset some of the limitations associated with natural products (Bilia *et al.*, 2017). However, this effort has been concentrated on very few compounds leaving out several natural products which show promising anticancer activity.Thus, in this study, selected plant species were investigated for anticancer principles. Furthermore, the use of nanoparticle drug delivery systems were exploited to enhance therapeutic efficacy of β-sitosteol, a promising but neglected compound, as a model natural product.

1.3   Objectives of the Study

1.3.1   General Objective

The main objective of this study was to identify anticancer natural products from selected medicinal plants and assess their anticancer potential when formulated into nanoparticles.

1.3.2   Specific Objectives

To achieve the overall objective, the study was divided into the following specific objectives:

i.   To characterize isolated natural products from the selected plants.

ii.   To determine the *in vitro* antiproliferative activity of the isolated compounds

iii.   To establish the anticancer mechanism of action of the isolated compounds through *in silico* studies.

iv.   To characterize natural product-loaded nanoparticles (Nat-NPs) formulated from selected natural products.

v.   To establish the anticancer activity of the Nat-NPs against selected cancer cell lines.

1.4   Justification and Significance of the Study

The use of natural products to treat different diseases is as old as mankind. Some of the topical drugs in clinical use against cancer such as paclitaxel (**1**), curcumin (**2**), camptothecin (**5**), doxorubicin (**6**), and vincristine (**7**) are typical examples of natural products. Basing on the several reports of medicinal uses (Iqbal *et al.*, 2017; Shareef *et al.*, 2016), plants still hold potential as sources to search for novel secondary metabolites against cancer and other diseases.

| (5) | (6) | (7) |
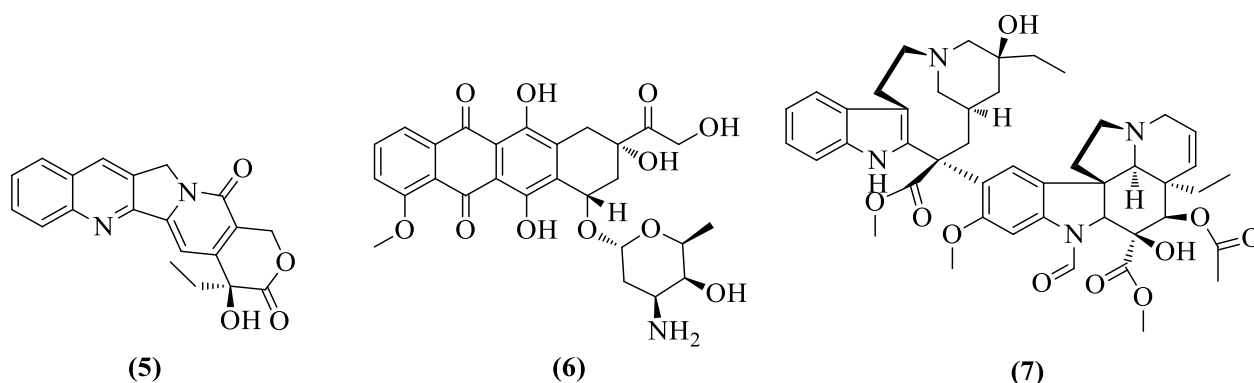
A lot of effort has been invested to augment the therapeutic potential of a good number of natural products. Incorporation of natural products into nanoparticle drug delivery systems is one of the approaches that has been utilized in several studies to enhance their therapeutic efficacy (Bharali *et al.*, 2011; Fonseca *et al.*, 2002; Yao *et al.*, 2006). These studies (Bharali *et al.*, 2011; Fonseca *et al.*, 2002; Yao *et al.*, 2006) indicate that nanoformulations of natural products enhance their anticancer activity several folds compared to the free drug. Nanoformulation of natural products confers several advantages including high bioavailability, enhanced efficacy, specificity and consequently decreased side effects and toxicity (Gunasekaran *et al.*, 2014; Saraf, 2010). Furthermore, imaging probes such as fluorescent dyes, quantum dots and so on can be incorporated into drug-loaded nanoparticles for theranostic applications (Zavaleta *et al.*, 2018). From the aforementioned studies, it is evident that incorporation of some natural products into nanoparticle drug delivery systems holds promise to enhance their therapeutic efficacy.

# CHAPTER 2: LITERATURE REVIEW

2.1 Cancer and Carcinogenesis

Cancer is a complex disease that results from uncontrolled cell proliferation accompanied by changes in cellular, biochemical and enzymatic parameters (Cooper and Hausmans, 2007). It is a three-stage process that results from the accumulation of errors in vital regulatory cellular pathways (Cooper and Hausmans, 2007; Pitot, 2002). In the first stage (initiation stage), cancer cells are generated when a single somatic cell upon exposure to one or a combination of physical or chemical agents called carcinogens causes abnormalities in the genes (Cooper and Hausmans, 2007; Pitot, 2002) . In the second stage (promotion stage), initiated cells are stimulated to grow by interacting with various factors. The abnormalities induced in the genes result in formation of an abnormal cell, which then multiplies and acquires additional changes that give it a survival advantage over the neighboring normal cells (Marks *et al.*, 2007). The third stage (progression stage) involves proliferation of altered cells to generate billions of abnormal cells that constitute a cancer. It is a complex stage in carcinogenesis accompanied by well-defined morphological, molecular and functional changes in the preneoplastic cells (Cavallaro and Christofori, 2000). Different factors such as alcohol intake, tobacco smoke, some viral infections such as human papilloma virus, exposure to certain radiations and chemicals, and others are known to cause cancers (Danaei *et al.*, 2005).

2.1.1 Types of Cancers

Cancer is considered as a collection of different diseases but all of them characteristically arise from uncontrolled growth of altered cells. Cancers can be categorized depending on their origin (Sever and Brugge, 2015). Most cancers develop body lining tissue (epithelial tissue), expressing as carcinomas in organs such as the liver, breast, lung, skin and the pancreas. Cancers that arise

from mesenchymal tissues constitute sarcomas and they occur in adipocytes, fibroblasts, myocytes and osteoblasts. Cancers that arise from nonepithelial cells such as the nervous system are classified as neuroblastomas, gliomas and medulloblastomas. Other nonepithelial tumors arising from hematopoietic tissues constitute leukemias and lymphomas. Globally, there are patent variations in the type of cancers that affect diverse populations depending on environmental variations and lifestyle (Danaei *et al.*, 2005). Cancers of the breast, prostate, colorectum, lung, bowel, stomach, ovary, thyroid, liver, leukemia, non-Hodgkin and pancreas are the most common cancers worldwide (Bray *et al.*, 2018; GLOBOCAN, 2012). Over 200 types of cancers have been diagnosed (Cancer Research UK, 2015, November), however, in the interest of this study, the most common cancers occurring globally have been mentioned here above.

2.1.2 Cancer Prevalence

Over the years, cancer cases have been rising gradually with substantial deaths each year. In 2012, the number of males and females diagnosed with various cancers were 7.4 and 6.7 million respectively, accounting for 14.1 million cancer cases estimated worldwide (Cancer Research UK, 2014; WHO, 2017). Lung, prostate, bowel, stomach and liver cancers were the most common cancers in males while breast, bowel, lung, cervical and stomach cancers were the most common cancers afflicting females (Cancer Research UK, 2014), Figure 2.1. A total of 18.1 million cases with 9.6 million deaths were reported in 2018 (Bray *et al.*, 2018; WHO, 2018). Most deaths were attributed to lung cancer though deaths due to other cancers represent a considerable statistic Figure 2.1 (Cancer Research UK, 2014; WHO, 2018). In fact cancer cases are projected to rise to 29.5 million by 2040 (Bray *et al.*, 2018; WHO, 2018). In low-income countries, the situation presents a depressing outlook. The mortality rates in these countries (low and middle-income countries) are typically higher compared to the rate of infections (American Cancer Society, 2017).

8

Four critical issues that make management of cancer difficult are; late diagnosis, aggressive metastasis, multidrug resistance (MDR), and recrudescence (Chen *et al.*, 2013). The reason for high mortality rates in low and middle-income countries is adequate screening programs which lead to late diagnosis and this making it difficult to treat. MDR to chemotherapy results in up to 90% chemotherapeutic failure (Maeda and Khatami, 2018; Mansoori *et al.*, 2017) and this aggravates the problem. The increasing cases of cancers and the very low survival rates under the current conventional therapies have prompted search for novel strategies for cancer treatment.
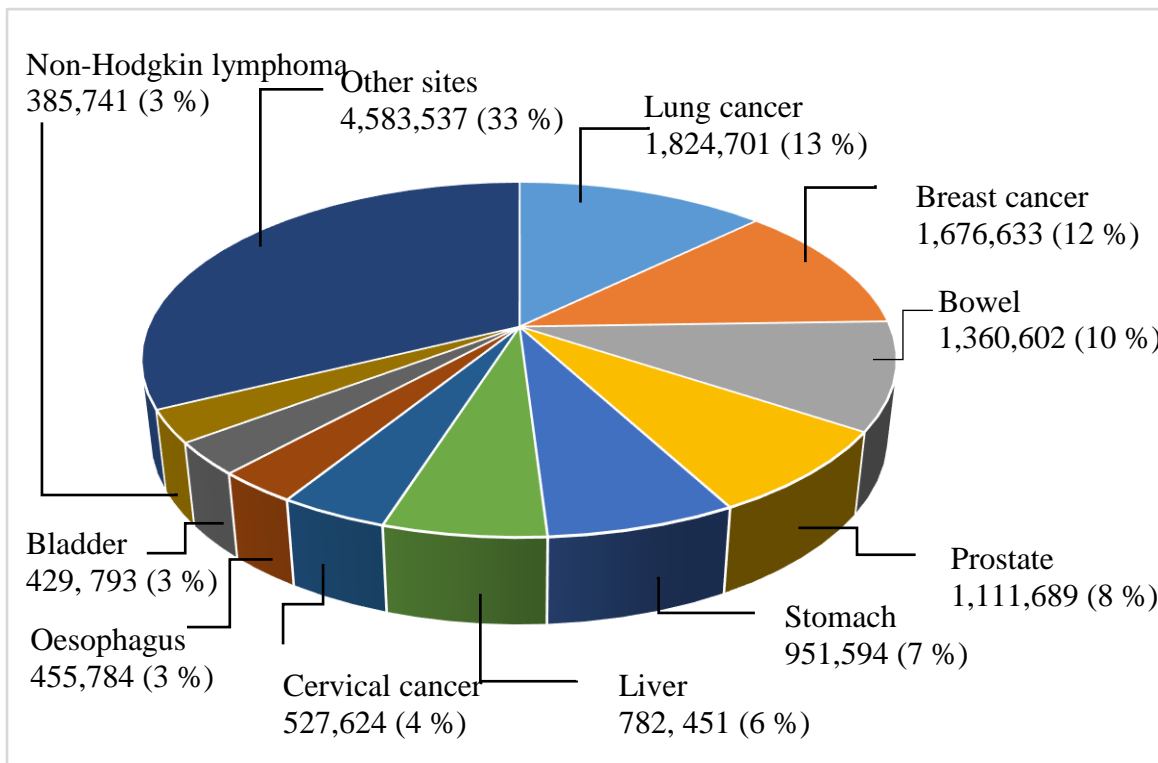
Figure 2.1: Incidences of major cancers worldwide reported in 2012. The data is shown in rank order as a number of cases and the percentage of the total number of cases (14,090149). Source: Cancer Research UK, http://www.cancerresearchuk.org/health-professional/cancer-statistics/incidence:Accessed 11/11/2015

2.2   Cancer Therapy

Treatment of different cancers takes a multidisciplinary approach consisting of surgery, chemotherapy, radiotherapy, immunotherapy, hormone therapy, stem cell transplant and precision

medicine (U.S. Department of Health and Human Services *et al.*, 2015). Surgery, radiotherapy and stem cell transplant are nonchemical means of treating cancer while chemotherapy, immunotherapy, hormone therapy, and precision medicine are chemical or biochemical means of treating cancer. The therapeutic regimen chosen depends on whether the cancer cells are localized or disseminated and the type of cancer (U.S. Department of Health and Human Services *et al.*, 2015). Whichever regimen, the intent of cancer treatment are two-fold, either curative or palliative (Neugut and Prigerson, 2017; Wolinsky *et al.*, 2012). In most cases, combination therapy, for instance, surgery with chemotherapy and/or radiation therapy is used to treat cancers (Fernandes *et al.*, 2015; U.S. Department of Health and Human Services *et al.*, 2015). Where the cancer cells are localized in a particular part of the body, they can be treated by surgical removal or using ionizing radiation followed by chemotherapy to prevent metastasis of remnant cancer cells (U.S. Department of Health and Human Services *et al.*, 2015).

Over the years, there has been significant improvement in cancer therapy translating in a better quality of life and longer survival for many cancer patients. For example, in the United States, cancer death rates declined by 20% from a peak of 215.1 in 1991 to 171.8 in 2010 per 100,000 population (Masters *et al.*, 2015) . These achievements have been as a result of vested effort and resources in cancer research. Moreover, in the past years, the US Food and Drug Administration approved a number of new anticancer drugs thus, giving more hope to patients with resistant cancers (Masters *et al.*, 2015). The new drugs are credited for their ability to target cancer cells at the molecular level. Some current therapies as described by the American Society of Clinical Oncology (ASCO) are highlighted in the proceeding subsections. While there has been tremendous progress in the reduction of cancer cases globally, cancer cases are still on the rise. This observation is substantiated by the projected increase in cancer cases from 18.1 million in 2018 to

29.5 million cases by 2040 (WHO, 2018) cancer incidences globally over the next two decades (WHO, 2017). Critical issues such as multidrug resistance to chemoprevention, high toxicity, non-specificity of chemotherapies, late diagnosis as well as the high cost of cancer treatment still hinder efficient cancer treatment (Bharali *et al.*, 2011; Blanco *et al.*, 2011; Gunasekaran *et al.*, 2014). Collectively, these factors preclude the therapeutic potential of most anticancer treatments.

2.2.1 *Chemotherapy*

Chemotherapy is a treatment option in which anticancer drugs (chemical or biochemical) are administered to arrest rapidly dividing cancer cells in the body (Florence and Salole, 1993). The purpose of chemotherapy is several folds; as a primary treatment to destroy cancer cells, to shrink a tumor before another treatment, to destroy any remaining free cancer cells after another treatment, or to relieve symptoms of advanced cancer (Balis, 1998; Cancer Treatment Centres of America, 2019). There are different types of chemotherapeutic agents as discussed in the proceeding sub-sections.

2.2.1.1 Alkylating Agents

Alkylating drugs are a diverse group of chemotherapeutic small molecules which inhibit DNA replication and transcription by forming alkyl adducts with DNA bases (Balis, 1998). Alkylation results in abnormal nucleotide sequences and miscoding of messenger RNA, thus inhibiting cancer cell proliferation (Freres *et al.*, 2017). In most cases, alkylating agents are bifunctional (having two alkylating centers) and form crosslinking DNA adducts at the N-7 position of the adjacent guanine base (Balis, 1998). There are six types of alkylating agents currently in clinical which include;

(a) Mustard gas derivatives such as chlorambucil (**8**), melphalan (**9**), cyclophosphamide (**10**), and ifosfamide (**11**). The first two, (**8**) and (**9**) directly cross-link DNA while the next two (**11**) and (**12**) require metabolic activation (Balis, 1998; Cancer Research UK, 2017).

$HO-\overset{O}{\underset{\parallel}{C}}-CH_2CH_2CH_2$—⬡—$N\begin{cases} CH_2CH_2Cl \\ CH_2CH_2Cl \end{cases}$

8

$HO-\overset{O}{\underset{\parallel}{C}}-\underset{\underset{NH_2}{|}}{C}HCH_2CH_2$—⬡—$N\begin{cases} CH_2CH_2Cl \\ CH_2CH_2Cl \end{cases}$
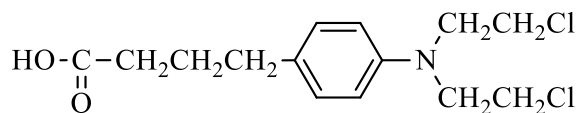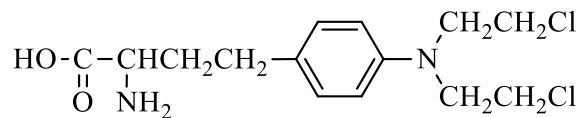
9
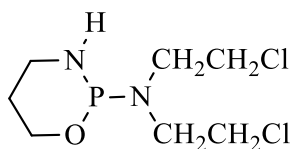
10
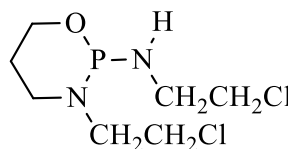
11

(b) Ethylenimines including thiotepa (**12**) and hexamethylmelamine (**13**).
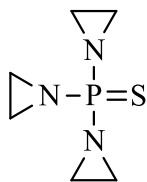
12
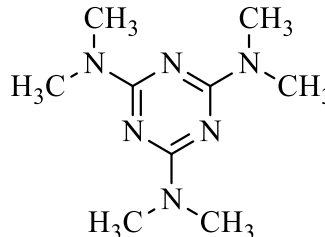
13

(c) Alkyl sulfonates: Example Busulfan (**14**).
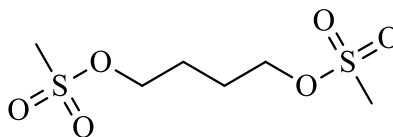
14

(d) Hydrazines and triazines which include procarbazine (**15**), dacarbazine (**16**), and temozolomide (**17**).
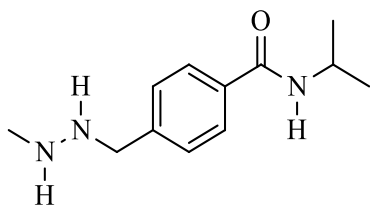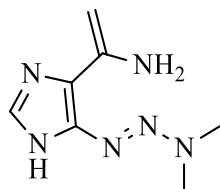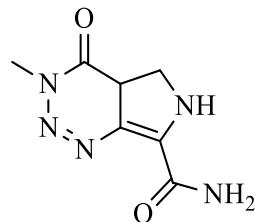
15   **16**   **17**

(e) Nitrosoureas: These are unique alkylating chemotherapeutic agents used to treat brain tumors because of their capacity to cross the blood brain barrier (BBB). Examples of nitrosoureas in clinical use include; carmustine (**18**), lomustine (**19**), and streptozocin (**20**).
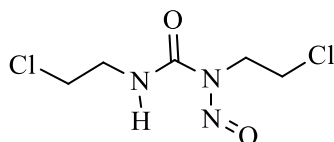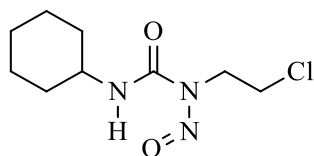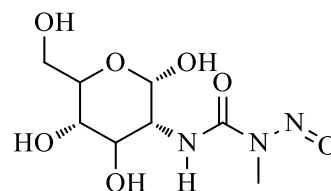
18   **18**   **20**

(f) Metal salts: Examples include carboplatin (**21**), cisplatin (**22**), and oxaliplatin (**23**).
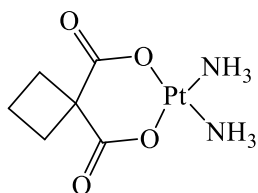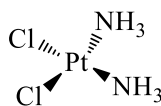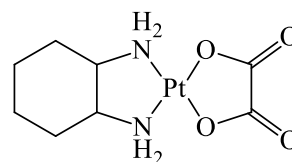
21   **22**   **23**

2.2.1.2 Topoisomerase Inhibitors

Topoisomerase inhibitors are cancer chemotherapy drugs which function by inhibiting topoisomerases (topoisomerase I and II) (Freres *et al.*, 2017). The role of topoisomerase enzymes is to catalyze the breakage and rejoining of phosphodiester bonds of the DNA chains in the normal cell cycle. When topoisomerases are inhibited by a chemotherapeutic agent, it results in inhibition

of DNA consequently leading to cell death (Cancer Research UK, 2017; Cancer Treatment Centres of America, 2019; Freres *et al.*, 2017). Chemotherapeutic agents in clinical use as topoisomerase I inhibitors include the camptothecin derivatives; irinotecan (**24**) and topotecan (**25**), while topoisomerase II inhibitors include the epipodophyllotoxin derivatives; etoposide (**26**), etoposide phosphate (**27**), and teniposide (**28**) (Cancer Research UK, 2017; Cancer Treatment Centres of America, 2019; Freres *et al.*, 2017).

24   **25**   **26**

27   **28**
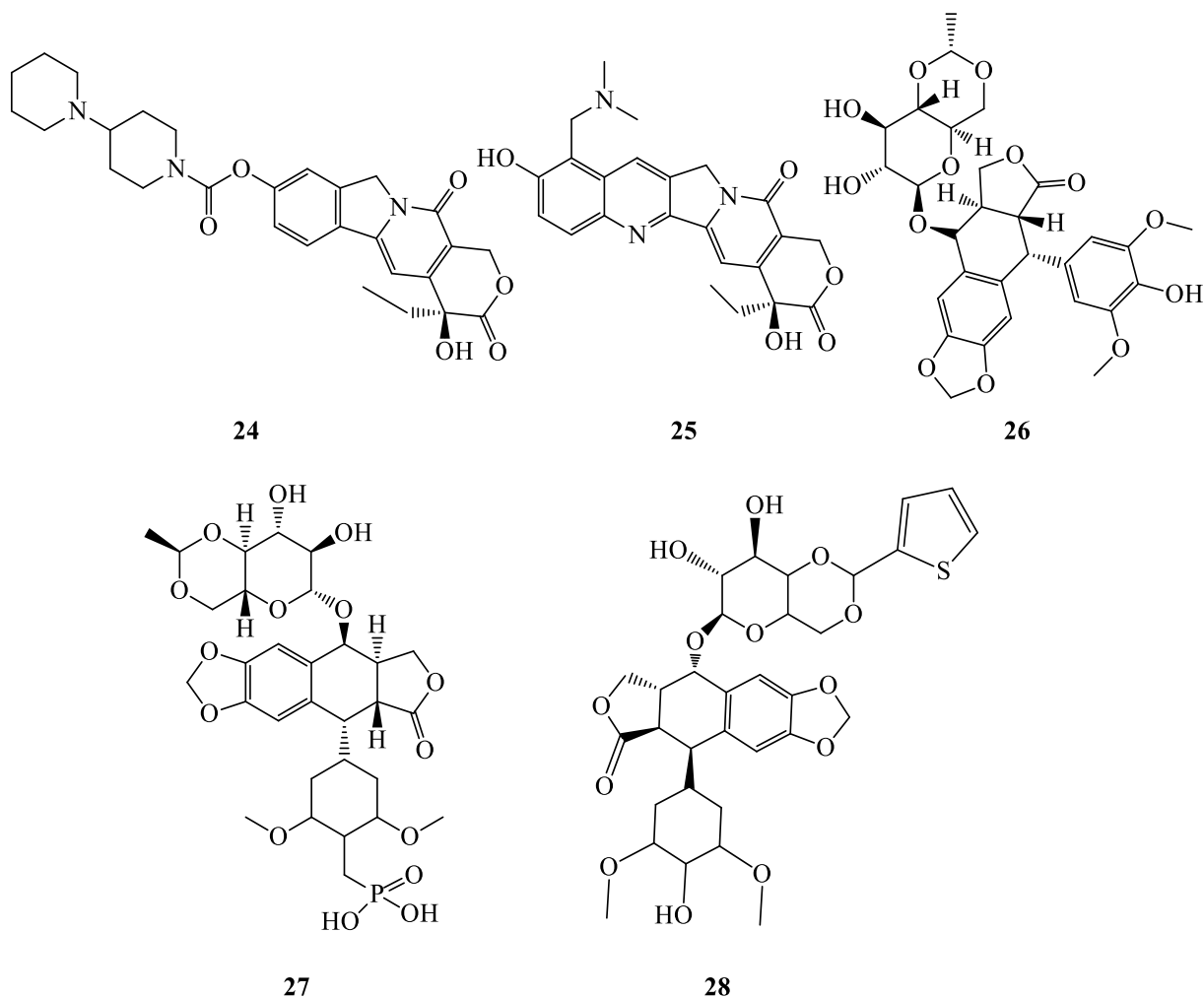
2.2.1.3 Antimetabolites

Structurally, antimetabolites are analogs of natural molecules (metabolites such as; amino acids, nucleosides, and vitamins) which are essential for normal cell growth (Freres *et al.*, 2017). They exert their anticancer activity by competitive inhibition of essential enzymes or receptors involved in cell growth and division; in so doing, they interfere with DNA synthesis (Cancer Research UK, 2017; Freres *et al.*, 2017). Most antimetabolites inhibit cell division at a specific phase of the cell cycle; in most cases at the S-phase. Among the different antimetabolites in clinical use include antifolates such as methotrexate (**29**) and pemetrexed (**30**), and pyrimidine analogs such as cytarabine (**31**), hydroxyurea (**32**), 5-fluorouracil (**33**), capecitabine (**34**), and gemcitabine (**35**).
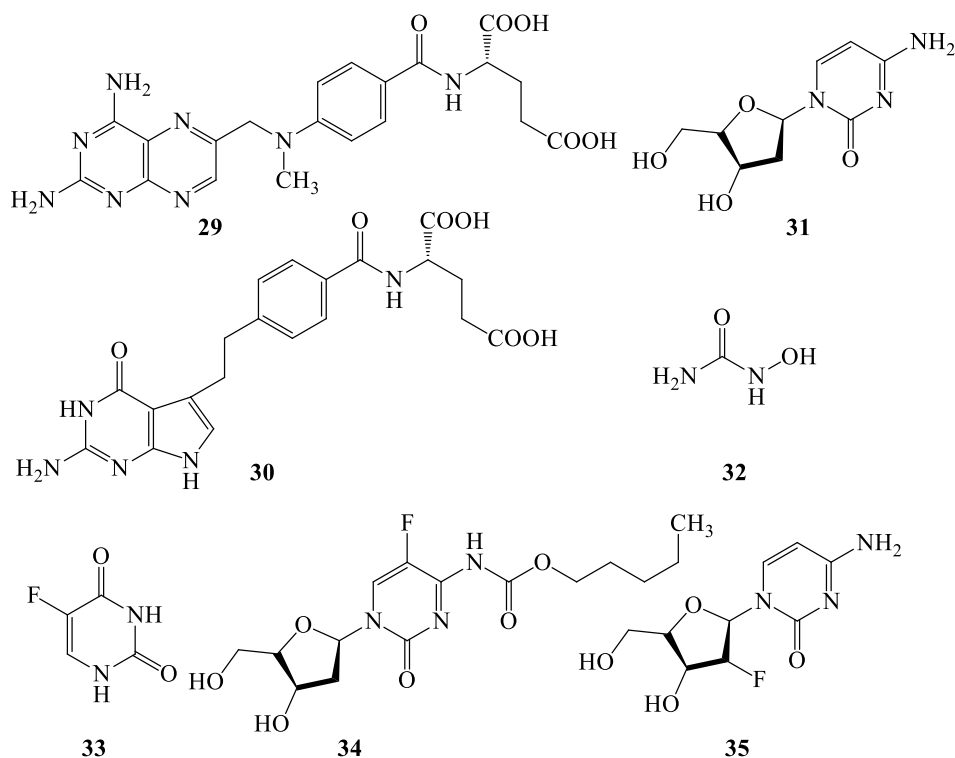
2.2.1.4 Antitumor Antibiotics

These are cell-cycle nonspecific chemotherapeutic agents derived from microorganisms. They are used to treat slow-growing cancer tumors. Their anticancer mechanism relates to the induction of

breakage of DNA strands, intercalation of DNA, and inhibition of topoisomerase II (Cancer Research UK, 2017; Freres *et al.*, 2017). Some examples of antitumor antibiotics currently being used in cancer treatment include anthracyclines for example; daunorubicin (**36**), doxorubicin (**6**), epirubicin (**37**) and idarubicin (**38**).

36   **37**

38
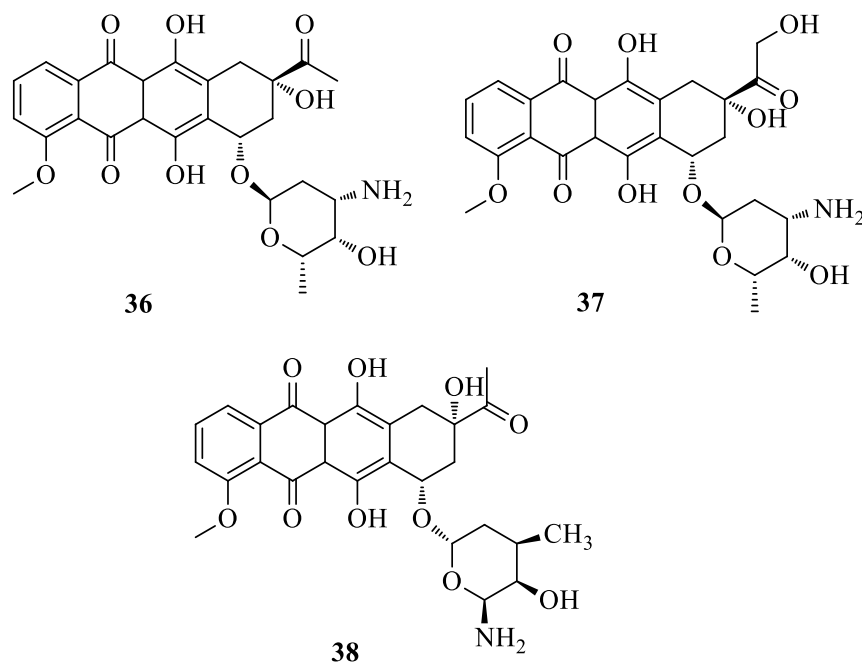
2.2.1.5 Mitotic spindle Toxic Agents

This class of chemotherapeutic agents consists of naturally derived alkaloids and their derivatives. They destroy cancer cells by binding to microtubule proteins, thus inhibiting microtubule assembly at the M-phase (Cancer Research UK, 2017; Freres *et al.*, 2017). Examples of these chemotherapeutic agents include the vinca alkaloids; vinblastine (**39**), vincristine (**7**), vindesine (**40**), and vinorelbine (**41**) and taxanes such as paclitaxel (**1**) and cabazitaxel (**42**). Taxanes in addition to binding to the microtubule proteins also promote the formation of microtubules and depolymerization leading to dysfunctional microtubules (Freres *et al.*, 2017).
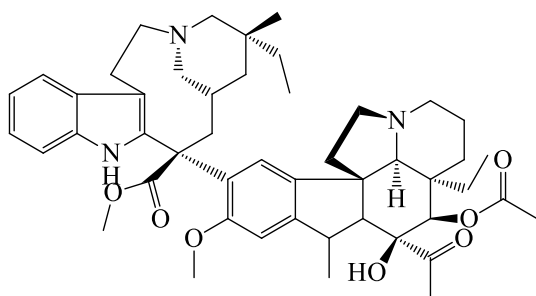
39
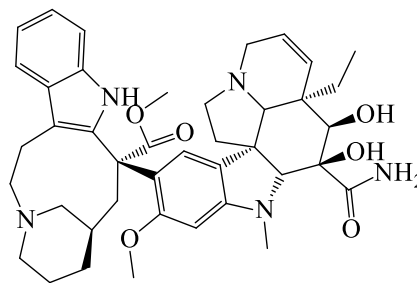
40
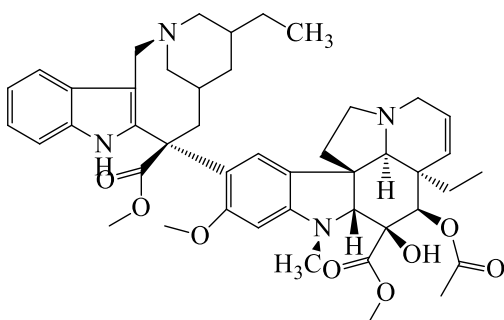
41
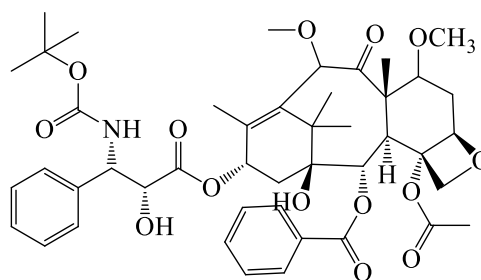
42

The types of chemotherapies discussed in the preceding sections involve use of cytotoxic chemotherapeutic agent. In most cases, these therapies are accompanied by several side effects thus, they are not well tolerated by patients (Cancer Research UK, 2017). Discovery of new signaling networks that regulate cellular activities including cell proliferation led to a paradigm shift in cancer chemotherapy with a view of minimizing side effects, off-target toxicity and increased therapeutic efficacy (Chabner and Roberts Jr, 2005). Beyond the abovementioned types of chemotherapies, other forms of chemo treatments currently in clinical use involve the use of combination therapy, targeted therapy, immunotherapy, and hormone therapy as discussed in the proceeding sections.

2.2.2 Combination Chemotherapy

Combination therapy is a treatment strategy that combines two or more drugs concurrently. This form of therapy offers enormous advantages. For instance, radiotherapy and chemotherapy

17

combination added 5 years in the survival of patients compared with radiotherapy alone (Masters *et al.*, 2015). The same authors reported that combination therapy delayed cancer cell proliferation by 10 years than the 4 years in a radiotherapy single treatment course. The main challenge they highlighted with combination therapy was that each therapy in the combination adds its own adverse effects thus calling for more research to evaluate the balance of risks and benefits for combination therapy.

2.2.3   Targeted Therapy

Targeted therapy is treatment that is directed to specific molecules in or on cancer cells or in the tumors immediate surroundings. The goal of targeted therapy is to prevent cancer cell proliferation and metastasis without causing damage to healthy cells. One way of achieving this involves modifying the surface of a cancer drug carrier vehicle to deliver the drug specifically to the tumor microenvironment. For example, cancer drug carriers can be designed to facilitate passive diffusion into the tumor microenvironment through the hypothesized principle of enhanced permeability and retention (EPR) effect (Greish, 2010). Due to rapid proliferation, tumors are characterized by fenestrated vasculature and poor lymphatic drainage system (Kobayashi *et al.*, 2013). This is believed to facilitate uptake of small size nanoparticles and their subsequent accumulation at the tumor site through EPR thus releasing the therapeutic payload at the tumor site (Tran *et al.*, 2017; Wicki *et al.*, 2015). On the other hand, most cancers overexpress certain functional biological molecules on their surfaces which act as receptors. In practice, the surface of cancer drug carriers is tuned with ligands which target the receptors expressed on the cancer cell surface. In this way, the nanoparticle can be targeted to only the cancer cells sparing the normal cells. Folate receptors ,glucose transporters, transferrin receptors have been investigated extensively in targeted drug deliver (Hilgenbrink and Low, 2005; Sudimack and Lee, 2000).

2.2.4   Immunotherapy

Immunotherapy is a form of treatment that involves administering antibodies or cell-based immunotherapies or cancer vaccines. It is intended to boost the body's natural defense. The anticancer mechanism of immunotherapies include, stopping or slowing cancer cell proliferation, preventing cancer cell metastasis, boosting the immune cells to kill abnormal cells and flagging cancer cells for destruction (Masters *et al*., 2015). Ipilimumab is a topical immunotherapy drug that was approved by FDA in 2011 for melanoma (FDA, 2011) and has been credited for its ability to reduce the recurrence risk of early-stage melanoma.

2.3   Cancer Molecular Targets and Cancer Drug Development

Carcinogenesis, which is the process of cancer development is characterized by alterations in cellular, genetic and epigenetic levels (Sever and Brugge, 2015). The process allows transformed cells to evade homeostatic controls and causes them to proliferate aberrantly. The malignant transformation of normal cells into cancer cells requires activation of multiple oncogenes and the loss of function of tumor suppressor genes (Powis, 1994). Most of the changes in genetic, epigenetic and cellular levels are mediated by a complex interplay of signaling pathways. The progression of cancer is mapped to dysregulation of the signaling transduction pathways (Powis, 1994; Sever and Brugge, 2015). Several genes involved in the various signaling pathways have been explored as novel targets for development of anticancer drugs. While there are a number of signaling pathways with myriad signaling molecules mediating various cellular processes, in this study, focus was placed on the p53 pathway.

Protein 53 (p53) is a tumor suppressor that functions to eliminate and inhibit the multiplication of abnormal cells through induction of apoptosis, cell cycle arrest and senescence (Haupt *et al.*, 1997; Sun, 2006). Normally, p53 is inactivated in cancerous cells as a means of evading apoptosis

(Hainaut and Hollstein, 1999; Harris and Levine, 2005). Studies have shown that the p53 pathway is activated in the presence of stress factors in cells such as UV radiation, free radicals or expression of activated oncogenes (Figure 2.2) (Harris and Levine, 2005; Vogelstein *et al.*, 2000). Accumulation of p53 has been shown to occur upon DNA damage thereby causing cell cycle arrest or apoptosis of the affected cells (Hainaut and Hollstein, 1999). MDM2 (murine double minute-2) protein which is an E3 ligase binds p53 and regulates the functions of p53 through a negative feedback loop (Figure 2.2) (Harris and Levine, 2005). The negative feedback mechanism operates in such a way that an increase in nuclear p53 concentration activates MDM2. MDM2 in turn blocks the p53 transactivation domain programing p53 for degradation (Harris and Levine, 2005; Haupt *et al.*, 1997; Ray-Coquard *et al.*, 2012). Inhibiting p53-MDM2 interaction would activate p53 and thus resulting in arrest of the cell-cycle and programmed cell death. The various functions of p53 are also mediated by a number of downstream targets (Figure 2.3) some of which include the p21$^{WAF1/CIP1}$ and CDKs (CDK2, CDK6); genes involved in cell cycle control and Bcl-2 family proteins involved in programmed cell death. Secondary metabolites from different plants have been shown to have a modulatory effect on the expression and function of the p53 gene as well as some of the downstream targets in the p53 pathway (Aderonke *et al.*, 2013; Yazdanpanahi *et al.*, 2014).
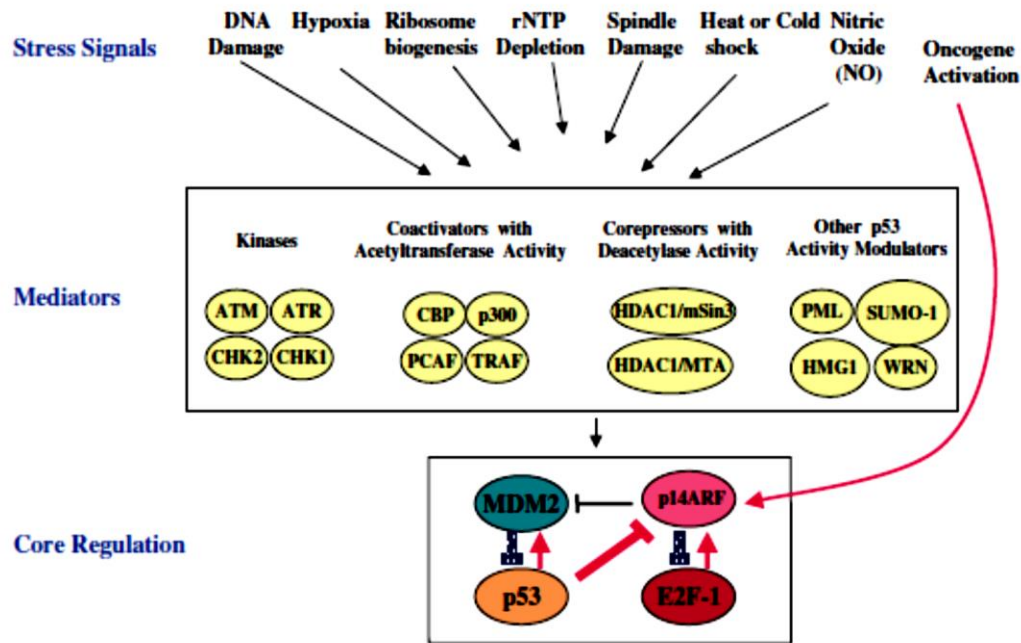
Figure 2.2: Range of stress signals that activate p53 and its regulation by MDM2. (Used with permission from (Harris and Levine, 2005))
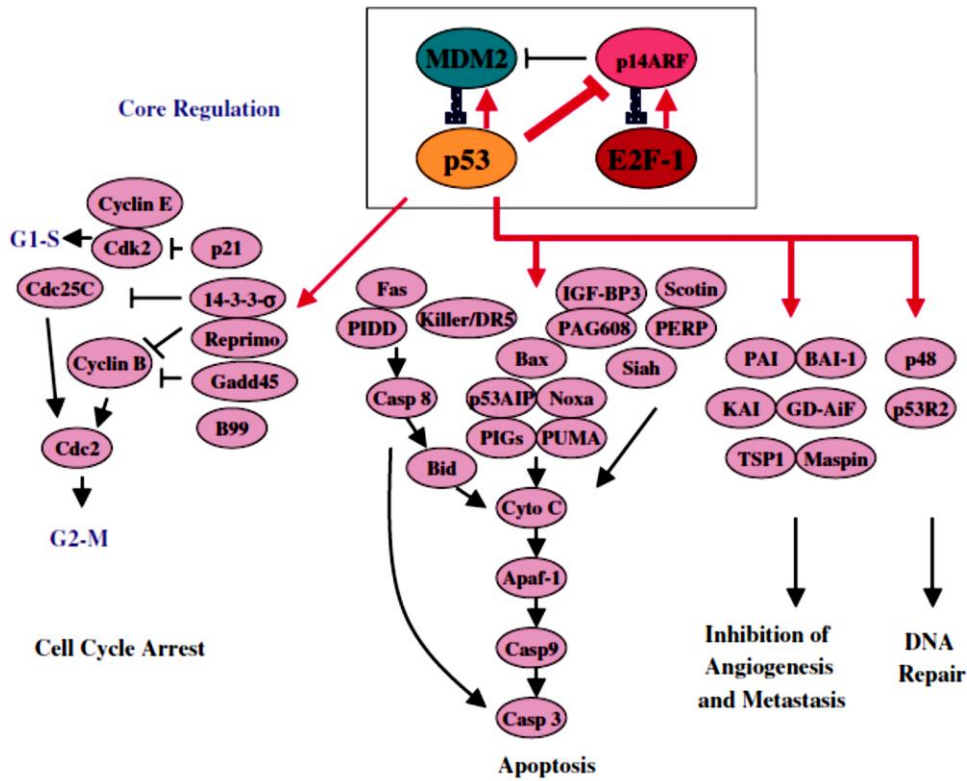
Figure 2.3: Downstream mediator molecules of the p53 transcription factor (Used with permission from (Harris and Levine, 2005))

2.4   Natural Products in Cancer Chemotherapy

A long history exists about the use of secondary metabolites derived from plants for treatment of cancer. Precisely, the systematic exploration of anti-cancer principles from plants can be traced way back in the 1950s (Cragg and Newman, 2005; Kaur *et al.*, 2011). This systematic search was accompanied by the discovery of vinca alkaloids; vinblastine (**39**) and vincristine (**7**) and the subsequent isolation of podophyllotoxins, etoposide (**26**) and teniposide (**28**) (Cragg and Newman, 2005; Mann, 2002). In 1960, the United States National Cancer Institute (NCI) initiated a far-reaching program to collect plants chiefly to isolate medicinally valuable phytochemicals (Cragg and Newman, 2005; Mann, 2002). To date, several phytochemicals with anti-cancer properties have been isolated from different plants. The following subsections describe some of the anticancer phytochemicals that have been isolated from different plants.

2.4.1   Alkaloids

Alkaloids are nitrogen containing groups of natural products distributed widely in the plant kingdom. The basic structure of most alkaloids consists of a heterocyclic ring with nitrogen as the hetero-atom. The anticancer activity of numerous alkaloids isolated from different medicinal plants have been evaluated by different research groups *in vitro* and *in vivo* (Garcez *et al.*, 2011; Sandjo *et al.*, 2014; Santhanam *et al.*, 2016; Tarus *et al.*, 2006). In fact some of the alkaloids for example camptothecin (**5**), vincristine (**7**) and vinblastine (**39**) have already been developed as chemotherapeutic drugs (Huang *et al.*, 2007). Several systematic anticancer studies have been carried out on several alkaloids reported in the reviews (Isah, 2016). Nonetheless, systematic anticancer studies are still lacking on other alkaloids such as fagorinine (**3**), nitidine (**4**) chelerythrine (**43**), lycorine (**44**); natural products isolated from *Zanthoxylum* species. Preliminary

studies have indicated the potential of these compounds as anticancer agents (Garcez *et al.*, 2011; Larsen *et al.*, 1993; Tarus *et al.*, 2006).

Alkaloids generally exert their anticancer activity by modulating multiple signaling pathways resulting in inhibition of carcinogenesis, induction of cell cycle arrest, apoptosis, autophagy, inhibition of metastasis, angiogenesis and so on (Jin-Jian *et al.*, 2012).

43   **44**
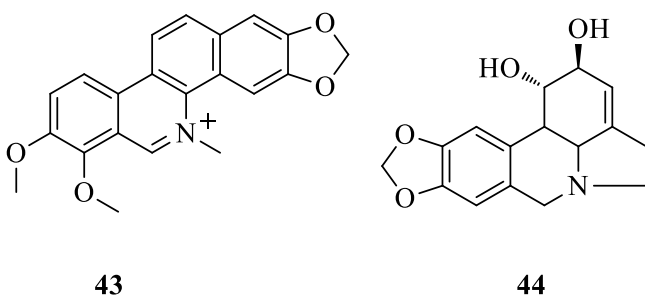
2.4.2 *Phytosterols*

Phytosterols are plant secondary metabolites with structural similarity to cholesterol. Representative examples of phytosterols that have been isolated from natural sources include β-sitosterol **(45),** campesterol (**46**), stigmasterol (**47**), β-sitosterol-3-O-glucoside (**48**), ergosterol (**49**), and β-sitostenone (**50**) (Gathumbi *et al.*, 2002). Credible evidences from different studies suggest anticancer activity of phytosterols against prostate cancer (Debat, 1974; Gathumbi *et al.*, 2002; Shenouda *et al.*, 2007), lung cancer (Mendilaharsu *et al.*, 1998), cancer of the stomach (Awad *et al.*, 2007; Awad *et al.*, 2000; Awad and Fink, 2000; Awad *et al.*, 2003; Awad *et al.*, 2001; De Stefani *et al.*, 2000), ovarian cancer and breast cancer (McCann *et al.*, 2003). Generally, different studies cited in the review by Woyengo and others (2009) suggest that phytosterols restrain cancers by the activation of caspase enzymes consequently hindering growth and inducing apoptosis.

45   **46**   **47**

48   **49**   **50**
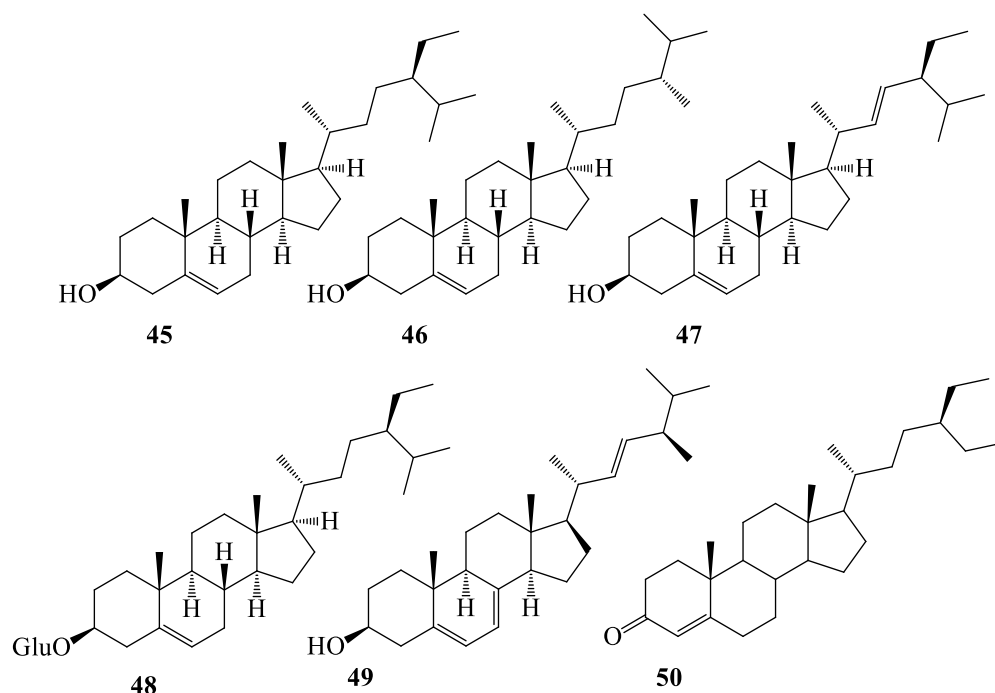
2.4.3   Cardiac Glycosides

Cardiac glycosides represent diverse group of secondary metabolites with steroid sub-unit as their structural backbone (Newman *et al.*, 2008; Prassas and Diamandis, 2008). The steroid sub-unit is doubly substituted by a lactone ring at position 17 and sugar moiety at position 3 (Newman *et al.*, 2008; Prassas and Diamandis, 2008). Depending on the lactone moiety, cardiac glycosides are classified into cardenolides **(A)** and bufadienolides **(B),** Figure 2.4. The cardenolides such as digoxin **(51)**, digitoxin **(52)**, ouabain **(53)** and oleandrin **(54)** (Table 2.1) have a five membered ring unsaturated butyrolactone, meanwhile bufadienolides such as bufalin **(55)**, has a six membered ring unsaturated pyrone (Prassas and Diamandis, 2008). The common sugar moieties found in cardiac glycosides include glucose, galactose, mannose, rhamnose and digitalose.

24
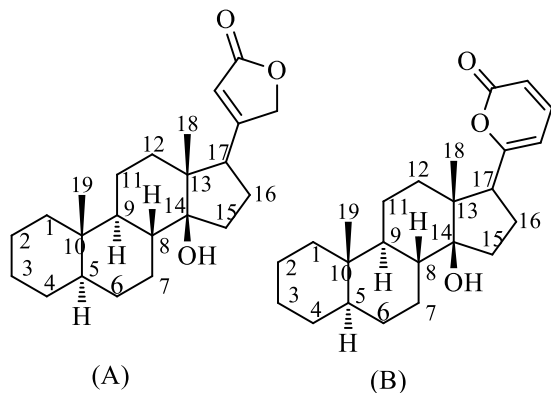
Figure 2.4: General structure of cardiac glycosides (**A**) Cardenolides and (**B**) Bufadienolides

Table 2.1: Examples of cardiac glycosides

	1	3	5	10	11	12	14	16
Cardenolides								
Digoxin (**51**)		(Dig)$_3$		CH$_3$		OH	OH	
Digotoxin (**52**)		(Dig)$_3$		CH$_3$			OH	
Ouabain (**53**)	OH	Rham	OH	OH	OH		OH	
Oleandrin (**54**)	CH$_3$	Rham	CH$_3$	CH$_3$			OH	OCOCH$_3$
Bufadienolides								
Bufalin (**55**)		OH		CH$_3$			OH	

Well known therapeutic application of cardiac glycosides is in treatment of congestive heart failure and as an anti-arrhythmic agent (Kepp *et al.*, 2012; Newman *et al.*, 2008; Prassas and Diamandis, 2008). Their application in treatment of proliferative diseases such as cancer is an emerging application in chemotherapy. Several pieces of work cited in the review by Prassas and Diamandis (Prassas and Diamandis, 2008) indicate that cardiac glycosides show *in vitro* and *in vivo* antiproliferative activity against a number of cancers such as breast cancer, prostate cancer, lung cancer, melanoma, leukemia, neuroblastoma, and renal adenocarcinoma. The anticancer mechanism of cardiac glycosides is not well stated, though several studies and reviews propose that when cardiac glycosides bind to preassembled Na$^+$/K$^+$-ATPase signalosome complex, it

activates multiple signal transduction cascades that can result in tumor death through either apoptosis, or autophagy-related mechanisms (Newman *et al.*, 2008; Prassas and Diamandis, 2008). Divergently, more recent studies (Kepp *et al.*, 2012), suggest that clinical anticancer activity of cardiac glycosides is ascribed to their influence on the immune response at multiple levels and induction of immunogenic demise of cancer cells.

2.4.4 Flavonoids

Flavonoids belong to the wide group of phytochemicals called polyphenols which are products of secondary metabolism in plants. They have a characteristic molecular structure comprising two aromatic rings (A and B rings) connected by a three-carbon heterocyclic ring (Chahar *et al*., 2011). Precisely, the basic structure of flavonoids can be described as C6-C3-C6. They can comfortably be described as a versatile storehouse of anticancer drugs. These studies (Manthey *et al*., 2001; Middleton *et al*., 2000; Surh, 2003) indicate that flavonoids offer therapeutic advantage in treatment of various cancers. Anticancer activity of flavonoids relates to inactivation of carcinogens (Le Marchand *et al*., 2000), antiproliferative activity (Chang *et al*., 1993), cell cycle arrest (Senderowicz, 1999), induction of apoptosis and inhibition of angiogenesis (Chahar *et al*., 2011). These anticancer activities are attributed to the structural characteristics and the system of glycosylation on ring C. There are a number of flavonoids which show promising anticancer activity, while others such as quercetin (**56**), breviscapine (**57**), naringenin (**58**), genistein (**59**), flavone-8-acetic acid (**60**), flavopiridol (**61**) and silybin (**62**) have undergone clinical trials (Chahar *et al*., 2011). In fact, silybin (**62**) and its bioavailable derivative IdB1016 (silipide) in combination with cisplatin (**23**) have shown very good efficacy against ovarian cancer cells (Giacomelli *et al*., 2002). While Phase II single-agent clinical trials and Phase I combination trials of flavopiridol (**61**) in combination with paclitaxel (**1**) and cisplatin (**23**) have shown promising results (Kelland,

2000).

56 **57** **58**

59 **60** **61**
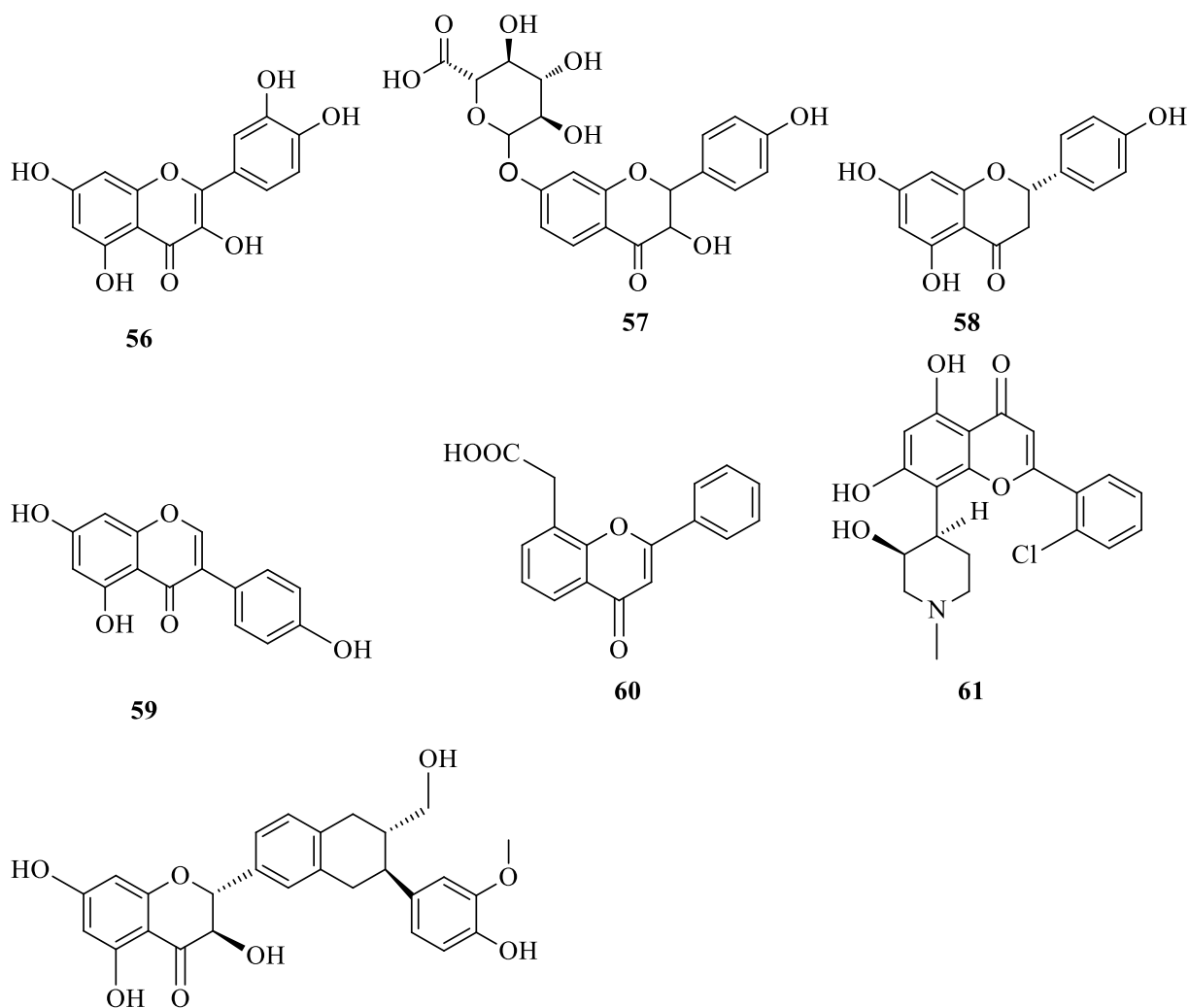
2.4.5 Terpenoids

Terpenoids are the largest and most varied class of phytochemicals among the diverse secondary metabolites produced by plants with over 36000 identified (Nassar *et al*., 2010). Generally, terpenoids are natural hydrocarbons (general formula: $(C_5H_8)n$) in addition to their oxygenated, hydrogenated and dehydrogenated derivatives. For a long period of time, terpenoids have been an important component of raw materials used in food, pharmaceutical, and chemical industries.

Nevertheless in more recent years, they have been used in the development of biofuels (Tholl, 2015). They are classified as volatile constituents of plant secondary metabolites responsible for the fragrances in several plants. They are distributed widely in the leaves, fruits, stem bark and roots of many plants.

There are several biomedical applications of terpenoids, however, in this study, their application in cancer therapy was briefly reviewed. The anticancer activity of several terpenoids has been evaluated in many studies Table 2.2.

2.4.6   *Limitations of Natural Products*

Despite the therapeutic value of plant derived compounds, several natural products face a number of limitations thus, affecting their therapeutic efficacy *in vitro* and *in vivo* (Bilia *et al.*, 2017; Gupta *et al.*, 2013; Kalepu and Nekkanti, 2015). Most natural products have low solubility in water and are poorly absorbed in the gastrointestinal tract (Bilia *et al.*, 2017). Moreover, many natural compounds are quickly metabolized, they are poorly distributed in the body and have poor targeting efficacy (Bilia *et al.*, 2017). These and other limitations affect therapeutic application of several natural products in cancer treatment.

Despite these limitations, there have been great advances in developing anticancer drug delivery systems with enhanced therapeutic activity for different natural drugs. Several techniques employed to enhance solubility and hence bioavailability of natural compounds and other poorly soluble drugs are discussed in the review (Gupta *et al.*, 2013).

Table 2.2: Examples of terpenoids with anticancer activity

Compound	Class	Source	IC$_{50}$	Cell line	Ref
β-pinene (**63**)	Monoterpene	*Xylopia parviflora*	0.155 μL/mL	HepG2	(Bakarnga-Via *et al.*, 2014)
6E,10E,14Z-(3S)-17-hydroxygeranyllinalool-17-O-β-d-glucopyranosyl-(12)-[α-L-rhamnopyranosyl-(1-6)]-β-d-glucopyranoside (**64**)	Diterpene	*Blumea lacera*	8.3 μM	MCF-7	(Akter *et al.*, 2016)
15,18-di-*O*-β-D-glucopyranosyl-13(*E*)-*ent*-labda-8(9),13(14)-diene-3β,15,18-triol (**65**)	Diterpene	*Rubus chingii*	2.32 μM	A549	(Zhong *et al.*, 2015)
Perovskiaol (**66**)	Diterpene	*Perovskia atriplicifolia*	2.35 μM 1.47 μM 0.81 μM	NB4 A549 HepG2	(Jiang *et al.*, 2016)
›hexyl)-11-hydroxy-6,12-dioxo-7,9 (11),13-obientatriene[=7-(2-oxohexyl)-taxodione (**67**)	Diterpene	*Salvia austriaca*	0.63 μM	HL-60	(Kuzma *et al.*, 2012)
Syrieteate A (**68**) Syrieteate B (**69**)	Sesquiterpene	*Ferula dissecta*	13.2 μM 19.3 μM	Cervical cancer Hela cells	
Artemisinin A (**70**)	Sesquiterpene	*Artemisia argyi*	4.0 μM	BV-2	
(2R) pterosin P (**71**) Dehydropterosin B (**72**)	Sesquiterpene	*Pteris multifida Poir*	12.07 & 4.27 μM 14.63 & 5.19 μM	PANC-1& NCI-H446 PANC-1 & NCI-H446	(Ouyang *et al.*, 2010)
Dehydrooopodin (**73**)	Sesquiterpene	*Ferula oopoda*	15 & 5 μM	MCF-7 & K562	(Kasaian *et al.*, 2014)
Hederagenin (**74**) Arjunic acid (**75**)	Triterpene	*Euscaphis japonica*	1.6 μM 2.1 μM 1.7 μM	NCI-H460 HT-29 CEM	(Zhang *et al.*, 2012)
Urmienslide B (**76**) Urmiensic acid (**77**)	Triterpene	*Salvia urmiensis*	2.8 μM 1.6 μM	MCF-7 MCF-7	(Farimani *et al.*, 2015)

63

64

65

66

67

68

69

70

71

72

73

74

75

76

77

30
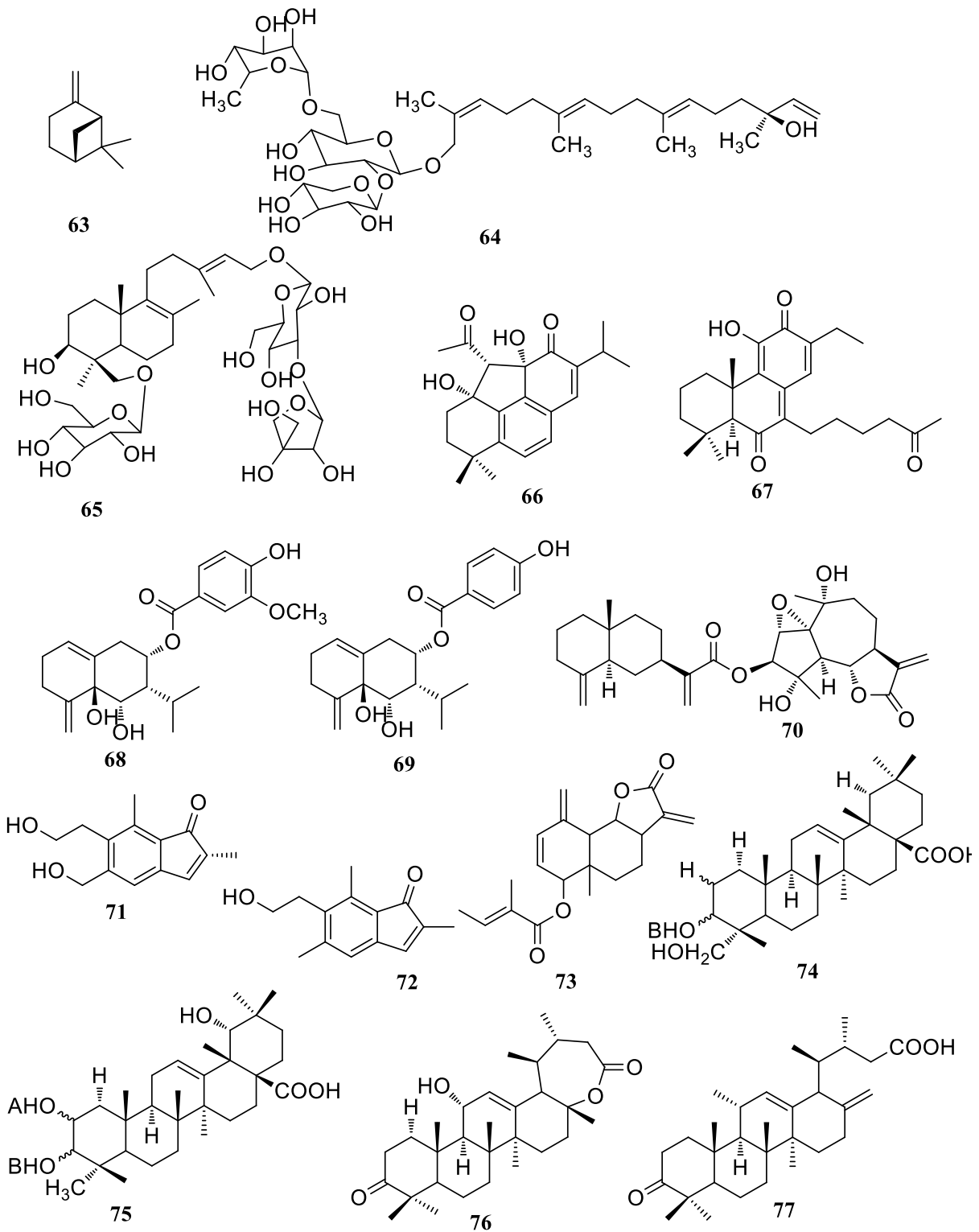
2.5   Nanotechnology in Cancer Therapy

Nanoparticles are materials whose sizes are smaller than 100 nm on at least one dimension. The development of nanoparticles can be traced back to the famous 1959 lecture of R.F Feynman (Ostiguy *et al.*, 2006). Since then, nanoparticles have been developed and applied in various fields (Ostiguy *et al.*, 2006). The wide application of nanoparticles is a function of their shapes, sizes and surface chemistry.

Nanotechnology represents an emerging technology for cancer management with robust applications in diagnosis, prevention, and therapy (Bharali *et al.*, 2011; Blanco *et al.*, 2011). The underlying theory in application of nanoparticles in cancer management is that cancer processes occur at cellular levels, ultimately requiring nanometer scale approaches for their management (Bharali *et al.*, 2011). One of the unique advantages of nanoparticles in therapy is that the therapeutic drug can be targeted to the cancer microenvironment without compromising the integrity of the incorporated drug (Bharali *et al.*, 2011; Blanco *et al.*, 2011). Furthermore, nanomedicines can be functionalized with imaging probes in the same dosage formulation for theranostic application (Conde *et al.*, 2013; Murherjee *et al.*, 2014; Zavaleta *et al.*, 2018). Common imaging probes that are combined with therapeutic agents include magnetic resonance imaging (MRI) contrast agents, fluorescent molecules (which can be organic dyes or inorganic quantum dots), and nuclear imaging agents (Zavaleta *et al.*, 2018). A number of nano technologically therapeutic formulations are under clinical trial while over ten nano carrier-based drugs have already been approved by the FDA (Table 2.3) (Bharali *et al.*, 2011; Pillai, 2014). It is envisaged that the nanotechnology market will soon reach $1 trillion with much attention on healthcare (Bharali *et al.*, 2011).

Despite the various benefitial applications of nanomaterials as highlighted in a number of studies cited in the preceeding sections, concerns over toxicity, environmental damage and organ damage caused by nanoparticles are highlighted in studies cited in these reviews (Hua and Wu, 2018; Juliano, 2012; Shubhika, 2012). However, with the increasing number of nanoparticles approved for clinical use by the regulatory bodies (Anselmo and Mitragotri, 2019), the advantages outweigh the foreseen limitations associated with nanoparticles.
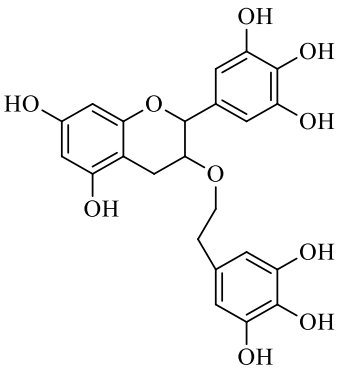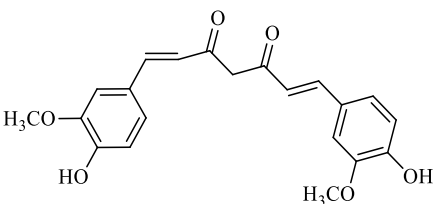
Table 2.3: Some examples of FDA approved nanomedicines used in cancer treatment.
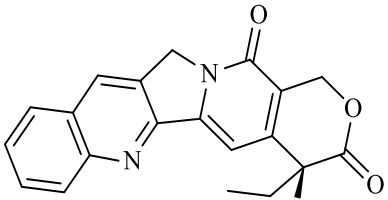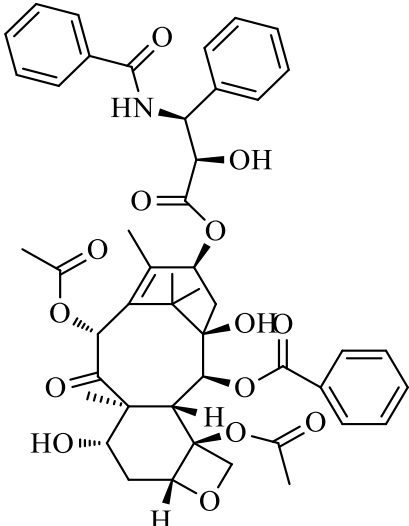
Product	Company	Active ingredient	Formulation	Indications
Doxil	Orthobiotech, Schering-Plough	Doxorubicin	PEGylated liposome	Metastatic ovarian cancer and Kaposi sarcoma in AIDS patients
DaunoXome	Nexstar pharmaceutica	Daunorubicin citrate	Liposome-encapsulated Daunorubicin	Kaposi sarcoma in AIDS patients
Emend	Merck/Elan	Aprepitant (MK 869)	Proprietary Nanocrystal® formulation	Side effects related to chemotherapy
Abraxane	Abraxis Bioscience AstraZeneca	Paclitaxel	Albumin nanoparticles	Metastatic breast cancer
Myocet	Zeneus Pharma Sopherion therapeutics	Doxorubicin	Liposome	Combinatorial therapy of breast cancer, ovarian cancer and Kaposi sarcoma.
Combidex	Advanced Magnetic Inc.	Iron oxide	Dextran10 coated iron oxide nanoparticles	Different tumor imaging.
Oncaspar	Enzon	L-asparaginase	Polymer protein conjugate.	Leukemia
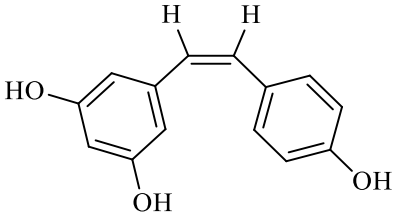
2.6   Natural Product-Loaded Nanoparticles

Herbal nanoparticle formulation represents one of the novel approaches to enhance targeted delivery of herbal medicines (Winnicka *et al.*, 2006). Different researchers have synthesized different herbal medicine-loaded nanoparticles such as polymeric nanoparticles, liposomes, proliposomes, solid lipid nanoparticles, micro-emulsion and metal nanoparticles (Ajazuddin and Saraf, 2010; Dipankar and Murugan, 2012; Mata *et al.*, 2015; Thapa *et al.*, 2013). Liposomes, micro-emulsions, lipid nanoparticles and so on represent the traditional organic nanosystems for drug delivery while metal nanoparticles represent inorganic nanoparticles (Chen *et al.*, 2013). Phytomedicine-loaded nanoparticles efficiently overcome such limitations as low water solubility, low bioavailability, low efficacy and high dose levels associated with traditional herbal drug formulations. Several nano-scale delivery systems have already been designed for systematic delivery of natural product-based drugs such as epigallocatechin-3-gallate (**78)**, resveratrol (**79**) paclitaxel (**1**) curcumin (**2**) and camptothecin (**6**) (Table 2.4). Bharali and co-workers carried out a study to validate the principle that nanotechnology increases systemic delivery and bioavailability of natural products. They observed that, encapsulated epigallocatechin-3-gallate (EGCG) retained its biological effectiveness with a ten folds dose advantage over non encapsulated EGCG (Bharali *et al*., 2011). Additionally, encapsulated EGCG was found to release therapeutic payloads in a sustained manner suggesting lower dose requirement for treatment. Similar studies have also shown that herbal medicine-loaded nanoparticles have increased bioavailability, efficacy and water solubility (Bilia *et al.*, 2017; Gu *et al.*, 2013; Gupta *et al.*, 2013; Khalil *et al.*, 2013; Maya *et al.*, 2013).

Table 2.4: Examples of natural product-loaded nanoparticles.

Structure of natural product	Chemical classification and source	Therapeutic activity	Nano-formulation	Benefit of formulation	Ref
78	Polyphenol from green tea (*Camellia sinensis*)	Chemopreventive, anticarcinogenic, Antioxidant, antiaging, antiviral	Nanocapsule	Increased efficacy, sustained drug release, enhanced bioavailability	(Bharali *et al.*, 2011)
(2)	Polyphenol isolated from the root of *Curcuma longa*	Antitumor, antioxidant, antiplatelet aggregation, anti-inflammatory	Polymeric nanoparticle	Enhanced solubility and bioavailability	(Sahu *et al.*, 2008)

Structure of natural product	Chemical classification and source	Therapeutic activity	Nano-formulation	Benefit of formulation	Ref
(3)	Cytotoxic quinolone alkaloid isolated from the back and stem of *Camptotheca acuminate*	Anticancer activity against gastric, rectum, bladder, colon, breast cancers	Camptothecin nanocapsules	Prolonged systemic circulation and high accumulation in tumors	(Bharali *et al.*, 2011)
(1)	A diterpenoid isolated from the Pacific yew tree, *Taxus brevifolia*	Anticancer activity against leukemias, and solid tumors of the breast, ovary, brain and lungs.	Polymeric nanoparticles	Biphasic release pattern, increased efficacy	(Fonseca *et al.*, 2002)

Structure of natural product	Chemical classification and source	Therapeutic activity	Nano-formulation	Benefit of formulation	Ref
 (79)	Phenolic compound in several plants	Antioxidant, cell survival, apoptotic modulator, tumor angiogenesis, anticancer activity against skin, lung, breast, prostate cancers	Chitosan nanoparticles	Increased efficacy, increased bioavailability	(Yao *et al.*, 2006)

2.7   Preparation of Drug-Loaded Nanoparticles

Broadly, the methods for preparation of nanoparticles can be divided into four groups; i.e. physical, chemical, enzymatic and biological methods (Kuppusamy *et al.*, 2014). For drug-loaded nanoparticles, the method chosen for drug formulation depends on factors such as the nature of the drug and the type of drug carrier to be used. In the interest of this study, the primary methods used to formulate drug-loaded nanoparticles from preformed polymers (drug carrier) are discussed.

2.7.1   Emulsion-Solvent Evaporation Method

This is a two-step method used to prepare drug-loaded polymeric nanoparticles. It utilizes solutions of polymers such as poly(lactic-co-glycolic acid) (PLGA), polylactic acid (PLA), poly(Ɛ-caprolactone), cellulose acetate phthalate and others alike (Pal *et al.*, 2011). In the first step of the synthesis, the polymer is dissolved in a volatile organic solvent and then mixed with an aqueous solution to form an emulsion. In the second step, the polymer solution is precipitated by evaporation of the polymeric solvent (Govender *et al.*, 1999). The nanoparticles are separated by ultracentrifugation.and purified by washing with ultrapure distilled water and then lyophilized. The emulsion-solvent evaporation method is applicable to formulate liposoluble drugs into nanoparticles. A modification to this method involves subjecting the O/W to high speed hormogenisation to break the emulsion into nanoparticles (Jaiswal *et al.*, 2004).Once nanoparticles are formed, the organic phase solvent is removed by stirring the emulsion. In this method, the size of the nanoparticles formed can be controlled by adjusting the process and formulation parameters such as the ratio of the aqueous phase to the organic phase, the homogenization rate, the duration of solvent evaporation, viscosity of organic and aqueous phases.

2.7.2   Double Emulsion and Evaporation Method

This method of nanoparticle preparation is applicable to encapsulate hydrophilic drugs (Pal *et al.*, 2011) . Here, a solution of the drug in water is mixed with an organic polymer forming an emulsion. Then the emulsion is mixed with the second aqueous phase resulting in an aqueous-organic-aqueous (W/O/W) emulsion. Through continuous stirring, or other means, the solvent is evaporated and the nanoparticles are separated by ultracentrifugation. Purification is accomplished by thoroughly washing with ultrapure distilled water.

2.7.3 Salting-Out Method

This method is modified from the emulsification/solvent diffusion method. It operates on the principle that a a solvent that is miscible with water can separate from an aqueous phase via a salting-out effect (Galindo-Rodriguez *et al.*, 2004; Reis *et al.*, 2006). The initial step involves dissolving the polymer and drug in acetone for example as a volatile solvent. This solution of the polymer in acetone is then mixed with an electrolyte such as magnesium chloride, calcium chloride, and magnesium acetate or non- electrolytes such as sucrose. These electrolytes or non-electrolyte act as salting-out agents. The emulsion is stabilized using polyvinylpyrrolidone or hydroxyethylcellulose. Sufficient quantity of water is used to dilute the emulsion consequently inducing the formation of nanospheres. Polymer solutions used in this method include PLA, poly (methacrylic) acid and so on. The advantages associated with the salting out method are; high entrapment efficiency, does not require increased temperatures and minimizes stress to protein encapsulants. However, it is exclusively applied to entrap lipophilic drugs.

2.7.4 Emulsion-Diffusion

This is a method that has been used to prepare several drug-loaded nanoparticles for example, doxorubicin encapsulated in PLGA nanoparticles, mesotetra (hydroxyphenyl) porphyrin encapsulated in PLGA (p-THPP) nanoparticles, and cyclosporine A (cy-A) encapsulated in sodium glycolate nanoparticles (El-Shabouri, 2002; Vargas *et al.*, 2004; Yoo *et al.*, 1999). Here the polymer is dissolved in solvent that is partially miscible with water to a point of saturation. The polymer solution saturated with water is then mixed with an aqueous solution containing the drug and a stabilizer. This leads to solvent diffusion to the external phase consequently forming nanospheres or nanocapsules depending on the ratio of oil to the polymer. The excess solvent is then filtered off or evaporated under vacuum. The advantages ascribed to this method include, high

drug entrapment efficiency (about 70%), homogenization is not required, high reproducibility between different batch formulations, it is easy to scale up, simplicity and low polydispersity index (Pal *et al.*, 2011). The main disadvantages associated with this method are (i) there is a large quantity of water used that has to be removed from the nanoparticle suspension and (ii) Some soluble drugs can easily leak into the saturated aqueous phase (Pal *et al.*, 2011)

2.8   Characterisation of Drug-Loaded Nanoparticles

Generally, a nanoparticle is defined by its particle size. The main characteristics used in identifying nanoparticles are the size, morphology and the surface charge. These characteristics determine the stability of nanoparticles and their distribution profile *in vivo*. A number of techniques are employed to measure the size and particle size distribution of nanoparticles . For routine analysis in solution or suspension dynamic light scattering (DLS), synonymously called photon correlation spectroscopy (PCS) is used to determine the size of nanoparticles. This technique relies on the ability of suspended submicron particles to scatter incident light. Thus the random changes in the intensity of light scattered by the particles can be analysed to get information about the size of the light scattering particles (Pecora, 2000). DLS also gives information about the distribution of the particle sizes (polydispersity index) and surface charge (zeta potential). Advanced microscopic techniques such as scanning electron microscopy (SEM), atomic force microscopy (AFM) and transmission electron microscopy (TEM) are used to determine the size and morphology of the nanoparticles. Each of the microscopic techniques vary in principle but provide generally similar information (size and morphology) about nanoparticles (Pal *et al.*, 2011). Energy dispersive x-ray spectroscopy (EDX) and X-ray diffraction (XRD) techniques are used to obtain information about the chemical composition (elemental composition) and crystallinity of nanoparticles respectively. Other techniques employed include fourier transform infrared spectroscopy (FTIR) which

provides information about the chemical composition of nanoparticle formation. Classical techniques such as UV-VIS spectroscopy, high performance liquid chromatography are used to measure the progress of nanoparticle formation, drug content encapsulated and drug release kinetics.

2.9   Molecular Docking

Molecular docking is a computational method used widely to virtually study binding interactions (binding mode and binding affinity) between a ligand and a target protein (receptor). Docking simulations are designed with the aim of identifying correct poses of ligands in the receptor binding site and to predict the affinity of the ligand to the protein. Depending on the type of ligand, docking simulations can be classified into protein–small molecule (ligand) docking, protein–nucleic acid docking and protein–protein docking (Roy *et al.*, 2015). The first step in a docking experiment is the generation of all possible conformations and orientations of the ligand docked in the binding site of the protein. The second step involves scoring the interactions using a suitable scoring function to evaluate the favourable interactions. Molecular docking has become one of the handy tools in drug discovery process for many reasons. It is relatively cheap, rapid and a large library of compounds can be screened within a short time. A detailed discussion of moleculat docking is not in the interest of this study. However, here, the basic principle, its applications, advantages and related examples are highlighted. Several molecular docking studies have been done to screen for lead compounds for drug development to treat human, animal and plant diseases as illustrated in these and more studies (Aamir *et al.*, 2018; Al-Khodairy *et al.*, 2013; Chen *et al.*, 2017).

CHAPTER 3: MATERIALS AND METHODS

3.1   Materials

3.1.1   Solvents and Reagents

General grade organic solvents namely methanol (MeOH), ethyl acetate (EtOAc), hexane, acetone, and dichloromethane (DCM) together with silica gel (0.06-0.2 mm mesh size, Merck) were supplied by Scielab suppliers, Nairobi, Kenya. The solvents were distilled before they were used for sample extraction and column chromatography. Analytical grade EtOAc, DCM and acetone along with polyvinyl alcohol (PVA) Mw ~205 kDa), stigmasterol (95%), coumarin-6, and 2-hydroxypropyl-beta-cyclodextrin (HP-β-CD) were bought from Sigma-Aldrich (St. Louis, MO, USA). Poly(D,L-lactide-co-glycolic acid) (PLGA) 50:50 (molecular weight 7 kDa) and mPEG-PLA diblock co-polymer (mPEG-PLA (R25) and mPEG-PLA (R45) were bought from Evonik Nutrition and Care GmbH (Essen, Germany). β-Sitosterol >70% was supplied by Cayman Chemicals (Ann Arbor, MI, USA), and Sulphuric acid (ACS grade) and acetic anhydride (AR) were obtained from Thermofisher Scientific (Waltham, MA, USA).

3.1.2   Plant Materials

Roots of *Z. zanthoxyloides* were sourced from Ngora in Ngora district, Eastern Uganda in the month of January, 2016. *Aloe tororoana* (whole plant) was collected from the cliffs of Tororo rock in Tororo Town, Tororo district, in Eastern Uganda in the month of January 2016. *A. schweinfurthii* (whole plant) was collected from Kachumbala, Bukedea district in Uganda in January. *Taberneamontana ventricosa* roots, stem bark and leaves were collected from central Kenya in the month of April, 2017. All the plant materials were authenticated at the Herbarium in the School of

Biological Sciences, University of Nairobi and voucher specimens (AM2016/01, AM2016/02, AM2016/03, and AM2017/04, respectively) were deposited.

3.2   Methods

3.2.1   General Methods

Column chromatography comprising of silica gel (0.06-0.2 mm mesh size) with or without impregnation with a solution of 3% oxalic acid was used to separate compounds from the different plant extracts. Pre-coated silica gel plates (60 F254, Merck) were used to perform analytical TLC. Gel filtration was done on Sephadex LH-20 column. Molecular masses were determined using high resolution electron impact mass spectrometry (HR-EI-MS) on Micromass GC-TOF Micro Mass Spectrometer (Micro mass, Wythenshawe, Waters Inc., UK). 1D and 2D nuclear magnetic resonance spectra of compounds were acquired using a Bruker Avance 500 and 600 Spectrometer with residual solvent peaks as references (^{1}H: δ 5.32 for CD_2Cl_2, 2.50 for DMSO-d_6, 3.34 for MeOD, and 7.26 for CDCl$_3$, ^{13}C NMR: 53.8 for CD_2Cl_2, 39.5 for DMSO-d_6, 49.86 for MeOD and 77.3 for CDCl$_3$). UV-Vis Spectra were measured using quartz 96-well plate on a microplate reader (FLUOstar Omega, BMG labtech, Ortenberg, Germany).or Jenways spectrophotometer using quartz cuvettes. Size, polydispersity index (PDI) and surface charge of nanoparticles were analysed using zetasizer (Nano ZS, Malvern Instruments, Malvern, UK). Scanning electron microscope (SEM) (FEI, Helios G3 UC) was used to determine nanoparticle surface morphology. A laser scanning confocal microscope (Leica SP8 inverted) equipped with LAS X software (Leica microsystems GmbH, Wetzlar, Germany) was used to take fluorescence images of cells. Cellular uptake was studied by fluorescence activated cell sorting analysis (FACS) using a flow cytometer (Attune NxT flow cytometer, Thermofisher Scientific, Waltham, MA, USA). Molecular operating

environment (MOE, Chemical computing group; Montreal Canada) was used for in silico docking simulations.

3.2.2 Extraction and Isolation of Compounds from Z. zanthoxyloides

Air dried root samples (1000 g) were pulverized and extracted with a mixture of MeOH and DCM (1:1 vol/vol, 3 x 3 L) by cold percolation over 24 hour period each. The extracts were pooled and concentrated at 60° C using a rotary evaporator at reduced pressures. The crude extract (178.39 g) was partitioned four times between MeOH (400 mL) and hexane (200 mL) to remove nonpolar oily fraction. The methanol fraction (152.42 g) was then chromatographed on a silica gel column (800 g) and eluted using a mobile phase comprising of n-hexane with increasing concentration of EtOAc. The fraction that eluted at 2% EtOAc in n-hexane yielded tridecan-2-one (**80**, 100.4 mg). The fraction that was collected at 4-6% ethyl acetate in n-hexane was purified by gel filtration on sephadex LH-20 column (mobile phase MeOH/DCM, 1:1 vol/vol) producing a benzo[c]phenanthridine alkaloid, dihydrochelerythrine (**81**, 84.4 mg) and a lignan, sesamin (**82**, 471.6 mg). The fraction that eluted at 30-40% ethyl acetate in n-hexane yielded a furoquinoline alkaloid, skimmianine (**83**, 50.2 mg). While, the fraction that eluted at 10% methanol in EtOAc was purified by gel filtration on sephadex LH-20 column giving hesperidin (**84**, 42.7 mg).

3.2.3 Extraction and Isolation of Compounds from A. tororoana

Dry pulverized whole plant sample (1900 g) was exhaustively extracted four times by soaking in a solvent mixture consisting of MeOH and DCM (1:1, vol/vol, 4x4 L) at room temperature. The solvents were evaporated using a rotary evaporator at low pressure giving a dark brown paste (150.94 g, 7.94% dry weight). A portion of the crude extract (100.0 g) was separated using column chromatography with stationary phase comprising of silica gel (800 g) impregnated with 2% oxalic acid and mobile phase comprising of n-hexane with increasing concentration of EtOAc. The

fraction which eluted at 100% n-hexane was repeatedly separated on sephadex LH-20 column yielding β-sitosterol (4**5**, 63.4 mg) and stigmasterol (**47**, 57.3 mg). The fraction which was collected at 10% ethyl acetate in n-hexane was further separated on sephadex LH-20 to afford a mixture of two anthraquinones, aloe emodin (**85**) and laccaic acid ester (**86**). The identities of two anthraquinones was confirmed using TLC against authentic reference samples and by analyzing their NMR spectral data. Compound (**87**) identified as Aloenin was isolated from the fraction eluted at 10% methanol in EtOAc. The fraction eluted with 20% EtOAc in n-hexane was further separated using preparative thin layer chromatography producing aloesaponarin II (**88**, 2.4 mg).

3.2.4   *Extraction and Isolation of Compounds from A. schweinfurthii (var. Laborwana)*

The whole plant was chopped into pieces, air dried and pulverized. The pulverized sample (1761 g) was soaked thrice in methanol/DCM mixture (1:1 vol/vol 3x4 L) for 24 hours duration each to extract compounds. The dark brown extract (338 g) was chromatographed on a silica gel column (700 g) impregnated with 2% oxalic acid. The mobile phase solvent consisted of n-hexane with increasing concentration of ethyl acetate and then EtOAC:MeOH, 1:1 vol/vol. The fraction that eluted with 0-2 % ethyl acetate in n-hexane was purified using sephadex LH-20 (solvent MeOH/DCM, 1:1 vol/vol) producing chrysophanol (**89**, 40.6 mg). The identity of compound **89** was further confirmed using TLC against an authentic sample. The fraction which eluted at 4-8 % ethyl acetate was separated on a sephadex LH-20 eluting with a mobile phase consisting of MeOH: DCM (1:1 vol/vol). This separation produced 5-allyl-3-methoxybenzene-1, 2-diol (**90**, 8.70 mg) and sub-fraction which was a mixture (8.20 mg). This sub-fraction (8.20 mg) was purified by eluting through a silica gel column (20 g) using a mobile phase comprising of EtOAc: n-hexane (1:1, vol/vol) producing chrysalodin (**91**, 3.02 mg). The fraction which eluted at mobile phase composition of 10% EtOAC in n-hexane was purified using preparative thin layer chromatography

(PTLC) producing aloesaponarin 1 (**92**, 44.9 mg). Droserone (**93**, 5.2 mg) was isolated from the fraction eluted with 8% EtOAc in *n*-hexane by gel filtration on Sephadex LH-20 (solvent MeOH: CH2Cl2, 1:1 vol/vol).

3.2.5   Extraction and Isolation of Compounds from T. ventricosa

Here, compounds were isolated separately from the root bark, stem bark and leaves. In all cases, air dried samples were milled into a powder (root bark 793.75 g, stem bark 1681 g and leaves 3889 g) and extracted exhaustively (4 x 3 L) with methanol containing 1% water. The extracts were concentrated using a rotary evaporator at 60° C under reduced pressure. The crude extracts (root bark 120.48 g, stem bark 160.32 g and leaves 936.72 g) were acidified using a solution of 0.5 M hydrochloric acid (pH 1-2) and partitioned between EtOAC thrice. The aqueous layer was treated with concentrated ammonia solution (pH 10) and further partitioned between ethyl acetate thrice. The organic layer containing mainly alkaloids (root bark 26.01 g, stem bark 27.4 2 g and leaves 27.57 g) were separated using column chromatography with stationary phase consisting of silica gel and mobile phase consisting of DCM with increasing concentration of MeOH.

3.3.4.1 Isolation of Compounds from T. ventricosa Root Bark Extract.

The fraction eluted with 100% DCM was further separated using CPTLC eluting with a mixture of n-hexane:DCM:Triethylamine (TEA) (6:3:1 vol/vol) producing 3-ketopropylcoronadine (**94**, 65.82 mg). The fraction eluted with 2% MeOH in DCM was further purified using CPTLC eluting with n-hexane:DCM:TEA (6:3:1 vol/vol) to obtain vobasine vobasine (**95**, 8.7 mg). The non-alkaloidal fraction was separated on a silica gel column using n-hexane with an increasing amount of EtOAc as the eluent. The fraction eluted at 8-10 % EtOAc in n-hexane was purified using CPTLC eluting with a mixture of n-hexane:EtOAc (3:7 vol/vol) to produce stigmasterol (**47**, 50.2 mg).

3.3.4.2 Isolation of compounds from T. ventricosa stem bark extract.

The fraction eluted with 6% MeOH in DCM after further separation using CPTLC yielded a pale-yellow pasty solid identified as ibogamine (**96**, 4.23 mg). The fraction which was eluted at 100% methanol produced white crystalline solids identified as quebrachitol (**97**, 80.4 mg) (McCance and Lawrence, 1933)

3.3.4.3 Isolation of compounds from T. ventricosa leaf extract

Initial separation of the alkaloid rich fraction using column chromatography yielded five fractions. The fraction which eluted at 1-2 % MeOH in DCM was further separated by CPTLC using acetone:Hexane solvent mixture (2:3 vol/vol) producing a colourless oily liquid identified as voacristine (**98**, 21.3 mg). The fraction which eluted at 2% MeOH in DCM gave 2 spots on TLC. Further separation using CPTLC with acetone:Hexane (2:3 vol/vol) as mobile phase yielded ursolic acid (**99**, 98.3 mg) and 10-hydroxy coronaridine (**100**, 24.4 mg). The fraction which eluted at 5% MeOH in DCM was purified using Sephadex LH-20 (mobile phase MeOH:DCM, 1:1) producing 10-hydroxy ibogamine (**101**, 30.4 mg).

3.3 Physical and Spectroscopic Data of the Isolated Compounds

The physical and spectroscopic characteristics of the compounds isolated from the different plants are outlined here under. Some of the spectra are presented in appendices 1-23.

Tridecan-2-one (**80**)

White amorphous solid, $R_f = 0.8$ (Hex: EtOAc, 8:2). UV λ_{max} (MeOH): 280 nm, Melting point 24-27 °C, ^{1}H NMR (600 MHz, CD_2Cl_2) and ^{13}C NMR (151 MHz, CD_2Cl_2) (Table 4.1). GC-MS: *m/z* = 198.3449.

Dihydrochelerythrine (81)

White crystalline solid, R_f = 0.71 (solvent: Hex:EtOAc, 4:1). Melting point 113-115 °C. LC-HRMS-ESI m/z = 348.1229, [M-H]$^+$ (calculated for $C_{21}H_{19}NO_4$, 349.1314). ^{1}H NMR (600 MHz, CD$_2$Cl$_2$): δ_H 7.71 (1H, d, J = 8.6 Hz, H-11), 7.65 (1H, s, H-4), 7.51 (1H, d, J = 8.6 Hz, H-10), 7.48 (1H, d, J = 8.5 Hz, H-12), 7.11 (1H, s, H-1), 6.96 (1H, d, J = 8.5 Hz, H-9), 6.05 (2H, s, 2H, -OCH$_2$O-), 4.26 (2H, s, 2H, H-6), 3.91 (3H, s, 8-OCH$_3$), 3.85 (3H, s, 7-OCH$_3$), 2.57 (3H, s, N-CH$_3$). ^{13}C NMR (151 MHz, CD$_2$Cl$_2$) δ_C 152.8 (C-8), 148.5 (C-2), 148.0 (C-3), 146.6 (C-7), 143.1 (C-5a), 131.2 (C-1a), 126.8 (C-10a), 126.5 (C-4a), 126.4 (C-11a), 124.6 (C-6a), 124.0 (C-12), 120.4 (C-11), 118.9 (C-10), 111.5 (C-9), 104.5 (C-1), 101.6 (-OCO-), 100.9 (C-4), 61.2 (7-OCH$_3$), 56.1 (8-OCH$_3$), 49.1 (C-6), 41.5 (N-CH$_3$).

Sesamin (82)

White crystalline solid, R_f = 0.78 (Solvent: Hex: EtOAc, 4:1). Melting point 121-122 °C. ^{1}H NMR (600 MHz, CD$_2$Cl$_2$): δ_H 6.84 (2H, d, J = 1.6 Hz, H-2′/2″), 6.80 (2H, ddd, J = 8.0, 1.7, 0.6 Hz, H-9′/9″), 6.77 (2H, d, J = 8.0 Hz, H-8′/8″) 5.94 (4H, s, H-5′/5″), 4.69 (2H, m, H-2/6), 4.20 (2H, m, H-4/8), 3.84(2H, m, H-4/8), 3.02 (2H, m, H-1/5. ^{13}C NMR (151 MHz, CD$_2$Cl$_2$): δ_C 148.3 (C-3′/3″), 147.4 (C-7′/7″), 135.9 (C-1′/1″), 119.6 (C-9′/9″), 108.3 (C-8′/8″), 106.8 (C-2′/2″), 101.6 (C-5′/5″), 86.1 (C-2/6), 72.1 (C-4/8), 54.8 (C-1/5).

Skimmianine (83)

Yellow crystals, R_f = 0.68 (solvent: Hex:EtOAc, 4:1), Melting point: 177.0-179.0 °C. LC-HRMS-ESI m/z = 260.0919, [M+H]$^+$ (calculated for $C_{14}H_{13}NO_4$, 259.0845). ^{1}H NMR (600 MHz, CD$_2$Cl$_2$) and ^{13}C NMR (151 MHz, CD$_2$Cl$_2$): (Table 4.4).

Hesperidin (84)

Pale yellow amorphous solid, UV (λ_{max} MeoH): 258 nm and 321 nm. Melting point 258-262 °C. ^{1}H NMR (600 MHz, DMSO-d$_6$): δ_H 12.01 (1H, s, 5-OH), 9.08 (1H, s, 3′-OH), 6.93 (3H, m, H-2′, H-5′, H-6'), 6.13 (2H, m, H-6, H-8), 5.49 (1H, m, H-2), 5.38 (1H, d, J = 5.1 Hz, OH), 5.17 (d, J = 5.5 Hz, OH), 5.15 (1H, J = 5.0 Hz, OH), 4.97 (1H, d, J = 7.8 Hz, Glc-1″), 4.52 (1H, br s, Rha-1‴), 3.79 (1H, m, Glc-CH$_2$), 3.77 (3H, s, 4′-OCH$_3$), 3.64 (1H, m, Rha-2‴), 3.54 (1H, m, Glc-5″), 3.43 (3H, m, Rha-3‴, Glc-CH$_2$ Rha-5), 3.28 (2H, m, H-3,), 3.23 (1H, m, Glc-3), 3.16, (2H, m, Rha-4‴, Glc-4″), 2.77 (1H, m, H-3), 1.09 (3H, d, J = 6.2 Hz, Rha-CH$_3$). ^{13}C NMR (151 MHz, DMSO-d$_6$) δ_C 197.0 (C-4), 165.1 (C-7), 163.0 (C-5), 162.4 (C-8a), 147.9 (C-4′), 146.4 (C-3′), 130.9 (C-1′), 117.9 (C-6′), 114.1 (C-2′), 112.0 (C-5′), 103.3 (C-5a), 100.6 (Glc-1), 99.4 (Rha-1), 96.3 (C-8), 95.5 (C-6), 78.3 (C-2), 76.2 (Glc-3), 75.5 (Glc-5), 72.9 (Glc-2), 72.0 (Rha-4), 70.7 (Rha-3), 70.2 (Rha-2), 69.5 (Glc-4), 68.3 (Rha-5), 66.0 (Glc-CH$_2$), 55.7 (4′-OCH$_3$), 42.0 (C-3), 17.8 (Rha-CH$_3$).

Aloenin (85)

White amorphous solid. ^{1}H NMR (600 MHz, DMSO-d$_6$) δ_H 9.83 (s, 1-OH), 6.50 (d, J = 2.1 Hz, H-3′), 6.37 (dd, J = 2.2, 0.8 Hz, H-5′), 6.25 (d, J = 2.2 Hz, H-5), 5.60 (d, J = 2.2 Hz, H-3), 4.82 (d, J = 7.7 Hz, H-1″), 3.84 (4-OMe) 3.69/3.48 (ddd, J = 11.8, 5.4, 2.2 Hz, H-6″), 3.26 (m, H-3″), 3.24 (m, H-5″), 3.12 (m, 4″), 3.11 (m, H-2″), 2.13 (s, 6′-Me), ^{13}C NMR (151 MHz, DMSO-d$_6$) δ_C 171.0 (C-4), 164.1 (C-2), 159.5 (C-4′), 157.9 (C-6), 156.6 (C-2′), 138.9 (C6′), 113.4 (C-1′), 110.8 (C5′), 104.2 (C-5), 100.8 (C3′), 100.2 (C-1‴), 87.8 (C), 77.1 (C-3″), 76.7 (C-5″), 73.2 (C-2″), 69.5 (C-4″), 60.6 (C-6″), 56.2 (4-OMe), 19.8 (6′-Me).

Aloe-emodin (86)

Yellow amorphous solid, ^{1}H NMR (600 MHz, DMSO-d$_6$) δ_H11.98 (s, 1H, 8-OH), 11.92 (s, 1H, 1-OH), 7.82 (dd, 1H, J= 8.4, 1.1 Hz, H-6), 7.73 (dd, 1H, J = 8.4, 1.1 Hz, H-5), 7.70 (d, J = 1.4 Hz, 1H, H-4), 7.39 (dd, J = 8.4, 1.1 Hz, 1H, H-7), 7.31 (d, J = 1.4 Hz, 1H, H-2), 4.64 (d, J = 4.8 Hz, 2H). ^{13}C NMR (151 MHz, DMSO-d$_6$) δ_C 191.6 (C-9), 181.4 (C-4), 161.6 (C-1), 161.3 (C-8) 153.7 (C-3), 136.5 (6), 134.1 (C-4a), 133.1 (5a), 124.3 (C-7), 120.6 (C-2), 116.5 (C-4), 115.9 (C-8a), 114.4 (C-1a), 62.0 (3-CH$_2$).

Laccaic acid D-methyl ester (87)

Yellow amorphous solid, ^{1}H NMR (600 MHz, DMSO-d$_6$) δ_H 13.08 (s, 1H, 1-OH), 7.60 (s, 1H, H-5), 7.07 (d, J = 2.4 Hz, 1H, H-4), 6.60 (d, J = 2.4 Hz, 1H, H-2), 3.92 (s, OMe), 2.62 (s, 3H, 8-Me).^{13}C NMR (151 MHz, DMSO-d6) δ_C 187.7 (C-9), 181.8 (C-10), 167.2 (7-CO), 164.4 (C-1), 164.1 (C-6), 158.2 (C-3), 140.5 (C-8), 137.3 (C-4a), 133.3 (C-5a), 129.6 (C-7), 122.5 (C-8a), 112.0 (C-5), 110.2 (C-1a), 108.3 (C-2), 107.2 (C-4), 52.4 (-OMe), 19.7 (8-Me).

Aloesaponarin II (88)

Orange amorphous solid, UV (λ_{max}, CHCl$_3$, nm): 282, 316, 386 and 412, ^{1}H NMR (600 MHz, DMSO-d$_6$) δ_H 14.72 (s, 5-OH), 7.50 (t, 7.9 Hz, H-7), 7.49 (dd, 7.9, 1.6 Hz, H-8), 7.14 (dd, J = 7.9, 1.6 Hz, H-6), 6.73 (d, J = 2.5 Hz, H-1), 6.17 (d, J = 2.4 Hz, H-3), 2.51 (overlap, 4-CH$_3$), 1.66 (s, -COM$_e$). ^{13}C NMR (151 MHz, DMSO-d$_6$) δ_C 185.7 (C-10), 184.4 (C-9), 162.2 (C-6), 161.7 (C-1), 145.5 (C-8), 133.9 (C-3), 133.4 (C-4a), 128.7 (C-7), 124.0 (C-2), 119.0 (C-5), 118.3 (C-1a), 117.3 (C-4), 111.7 (C-8a), 25.0 (Ar-CH$_3$).

Chrysophanol (89)

Orange needles, R_f 0.76 (Hex:EtOAc:AcAH 70:25:5 vol/vol/vol). ^{1}H NMR (600 MHz, CD$_2$Cl$_2$), δ_H 12.04 (s, 8-OH), 11.92 (s, 1-OH), 7.75 (dd, J = 7.6, 1.3 Hz, H-5), 7.74 (dd, J = 8.3, 7.5 Hz, H-6), 7.66 (d, J = 1.6 Hz, H-4), 7.25 (dd, J = 8.4, 1.2 Hz, H-7), 7.06 (dq, J = 1.4, 0.8 Hz, H-2), 2.47 (s, 3-CH$_3$). ^{13}C NMR (151 MHz, CD$_2$Cl2) δ_C 192.9 (C-9), 182.0 (C-10), 163.0 (C-1), 162.7 (C-8), 150.0 (C-3), 137.3 (C-6), 134.0 (5a), 133.6 (4a), 124.3 (C-7), 124.7 (C-2) 121.5 (C-4), 120.0 (C-5), 116.2 (C-, 114.0 (C-1a), 22.4 (3-CH$_3$).

Chrysalodin (90)

Red crystalline solid, ^{1}H NMR (600 MHz, DMSO-d$_6$, 25 °C) δ_H 12.26 (s, O-H-8), 12.19 (s, O-H-1), 12.02 (s, OH-8′), 11.47 (s, O-H-1′), 8.67 (d, J = 8.0 Hz, H-6′), 7.87 (d, J = 8.0 Hz, H-5′), 7.50 (t, J = 8.0 Hz, H-6), 7.39 (d, J = 1.8 Hz, H-4′), 7.06 (t, J = 1.3 Hz, H-2′), 6.93 (dd, J = 8.3, 1.1 Hz, H-7), 6.79 (m, H-2), 6.76 (dd, J = 8.0, 1.1 Hz, H-5), 6.64 (s, H-4), 2.33 (s, CH$_3$′), 2.22 (s, -CH$_3$). ^{13}C NMR (151 MHz, DMSO-d$_6$, 25 °C) δ_C 193.1 (C-9), 192.1 (C-9′), 181.5 (C-10′), 161.9 (C-1′), 161.8 (C-1), 161.5 (C-8), 158.1 (C-8′), 149.62, 148.9 (C-3), 148.4 (C-5a), 148.3 (C-4a), 142.1 (C-7′), 137.3 (C-6), 133.3 (C-6′), 133.27 (C-5a′), 132.8 (C-4a′), 124.3 (C-2′), 120.9 (C-4′), 120.88 (C-4), 119.8 (C-5), 119.4 (C-5′), 117.2 (C-2), 116.9 (C-7), 115.9 (C-8a′), 114.7 (C-8a), 114.0 (C-1a′), 112.6 (C-1a), 70.0 (C-10), 22.2 (-CH$_3$), 22.0 (-CH$_3$′).

Aloesaponarin 1 (91)

Yellow solid, ^{1}H NMR (600 MHz, DMSO-d$_6$) δ_H 12.79 (s, 1-OH), 11.73 (s, 3-OH), 7.71 (dd, J = 8.3, 7.5 Hz, H-3), 7.61 (dd, J = 7.5, 1.2 Hz, H-4), 7.60 (s, H-5), 7.32 (dd, J = 8.4, 1.2 Hz, H-2), 3.88 (s, -OMe), 2.59 (s, 8-CH$_3$). ^{13}C NMR (151 MHz, DMSO-d$_6$) δ_C 189.7 (C-9), 182.2 (C-10), 167.2 (CO), 161.4 (C-1), 158.8 (C-6), 141.0 (C-8), 136.7 (C-5a), 132.3 (C-4a), 129.6 (C-7), 124.4 (C-2), 122.5 (C-8a), 118.1 (C-4), 116.7 (C-1a), 112.0 (C-5), 52.5 (-OMe), 19.9 (8-CH$_3$).

5-allyl-3-methoxybenzene-1,2-diol (92)

Yellow amorphous solid. ^{1}H NMR (600 MHz, MeOD-d_4) δ_H 6.28 (s, H-4), 6.28 (s, H-6), 5.90 (m, H-8), 5.02 (m, H-9), 3.78 (s, 3-OMe), 3.21 (d, J = 6.82 Hz, H-7). ^{13}C NMR (151 MHz, MeOD) δ_C 149.5 (C-3), 146.4 (C-2), 139.3 (C-8), 133.3 (C-1), 132.2 (C-5), 115.4 (C-9), 110.0 (C-6), 104.8 (C-4), 56.5 (3-OMe), 41.0 (C-7).

2,5,8-Trihydroxy-3-methyl-[1,4]naphthoquinone (Droserone) (93)

Red crystals: (Solvent; DCM:MeOH, 1:1 vol/vol), ^{1}H NMR (600 MHz, CD$_2$Cl$_2$) δ_H 12.78 (s, 1H, 5-OH), 11.46 (s, 1H, 8-OH), 7.50 (brs 1H, 3-OH), 7.28 (d, J = 9.4 Hz, 1H, H-7), 7.18 (d, J = 9.4 Hz, 1H, H-6), 2.08 (s, 3H, 2-CH$_3$). ^{13}C NMR (151 MHz, CD$_2$Cl$_2$, 25 °C) δ_C 189.3 (C-1), 182.5 (C-4), 157.9 (C-3), 157.4 (C-5), 154.3 (C-8), 131.6 (C-6), 127.8 (C-7), 121.9 (C-2), 111.1 (C-4a), 110.9 (C-1a), 8.3 (2-CH$_3$).

3-ketopropylcoronaridine (94)

Pale yellow oily liquid, ^{1}H NMR (600 MHz, Chloroform-d) δ_H 7.82 (brs, N-H), 7.46 (d, J = 7.84 Hz, H-9), 7.24 (d, J = 7.84 Hz, H-12), 7.14 (ddd, J = 8.1, 7.0, 1.2 Hz, H-11), 7.08 (ddd, J = 8.1, 7.0, 1.2 Hz, H-10), 3.70 (s, -OCH$_3$), 3.58 (m, H-21), 3.33 (m, H-3), 3.28-320 (m, H-5), 3.00-3.18 (m, H-6) 2.70, 2.52 (m, H-22), 2.65 (m, H-17), 2.11 (s, H-24), 1.70 (m, H-14), 1.57, 1.23 (m, H-19), 1.43 (m, H-20), 1.28 (m, H-15), 0.89 (t, J = 7.4 Hz, 9H). ^{13}C NMR (151 MHz, CDCl$_3$) δ_C 208.7 (C-23), 175.5 (C-25), 136.5 (C-2), 135.5 (C-13), 128.7 (C-8), 122.0 (C-11), 119.2 (C-10), 118.4 (C-9), 110.3 (C-12), 110.0 (C-7) 58.2 (C-21), 55.2 (C-3), 54.8 (C-16), 52.7 (OCH$_3$) 51.4 (C-5), 46.6 (C-22), 38.4 (C-15), 37.6 (C-17), 31.0 (-COCH$_3$), 30.7 (C-14), 26.9 (C-19) 26.7 (C-20), 22.0 (C-6), 11.7 (C-18).

Vobasine (95)

Pale yellow oily liquid. UV λ_{max} (205, 233, and 299 nm). ^{1}H NMR (600 MHz, Methylene Chloride-d_2) δ_H 9.14 (brs, 1H, N-H), 7.65 (dd, J = 8.1, 1.0 Hz, 1H, H-9), 7.29 (dd, J = 8.1, 1.0 Hz, 1H, H-12), 7.26 (td, J = 8.40, 1.20 Hz, 1H, H-11), 7.07 (ddd, J = 8.0, 6.7, 1.2 Hz, 1H, H-10), 5.36 (qd, J = 6.8, 1.8 Hz, 1H, H-19), 3.84 (ddd, J = 10.7, 8.1, 3.3 Hz, 1H, H-5), 3.72, (d, J = 14.0 Hz, 1H, H-21), 3.64 (m, 1H, H-15), 3.41. 3.31 (dd, J = 14.7, 10.2 Hz, 2H, H-6), 2.86 (d, J = 14.1 Hz, 1H, H-21), 2.73 (t, J = 3.4 Hz, 1H, H-16), 2.58 (dd, J = 13.5, 7.3 Hz, 1H, H-14), 2.56 (s, OCH$_3$), 2.47 (overlap , 3H, N-CH$_3$), 1.63 (d J = 6.9 Hz, 3H, H-18). ^{13}C NMR (151 MHz, CD$_2$Cl2) δ_C 190.0 (C-3), 171.3 (C-22), 136.50 (overlap, C-13/20), 134.1 (C-2), 128.6 (C-8), 126.5 (C-11), 120.8 (C-9), 120.5 (C-7), 120.2 (C-19), 120.1 (C-10), 111.9 (C-12), 57.2 (C-5), 51.8 (C-21), 50.2 (OCH$_3$), 46.8 (C-16), 43.2 (C-14), 42.1 (N-CH$_3$), 30.5 (C-15), 20.1 (C-6), 12.1 (C-18). HR-ESI-MS m/z = 353.1873, [M+H]$^+$ Calculated C$_{21}$H$_{24}$N$_2$O$_3$, 352.1787.

Ibogamine (96)

Pale yellow oily liquid. ^{1}H NMR (600 MHz, Methylene Chloride-d_2) δ_H 7.80 (s, N-H), 7.43 (dd, J = 7.4, 1.3 Hz, H-9), 7.25 (d, 1H, H-12), 7.07 (td, J = 7.4, 1.3 Hz, H-11), 7.03 (td, J = 7.4, 1.3 Hz , H-10), 3.34 (ddd, J = 16.2, 12.9, 4.6 Hz, H-5), 3.33/2.69 (overlap 2H, H-6), 3.13 (overlap, 1H, H-5), 3.08/3.00 (m, 2H, H-3), 2.87 (s, 1H, H-21), 2.07/1.64 (m, 2H, H-17),1.85 (overlap, 1H, H-14), 1.83/1.24 (overlap, 2H, H-15), 1.68 (m, 1H, H-16), 1.58 (m, 2H, H-19), 1.47 (m, 1H, H-20), 0.91 (t, 3H, J = 7.2 Hz H-18). ^{13}C NMR (151 MHz, CD$_2$Cl2) δ_C 142.5 (C-2), 135.1 (C-13), 130.1 (C-8), 121.1 (C-11), 119.2 (C-10), 118.1 (C-9), 109.4 (C-7), 58.0 (C-21), 54.6 (C-5), 50.1 (C-3), 42.2 (C-20/16), 34.5 (C-17), 32.4 (C-15), 28.2 (C-19), 26.9 (C-14), 20.9 (C-6), 12.1 (C-18).

Quebrachitol (97)

White crystalline solid. ^{1}H NMR (600 MHz, Methanol-d_4) δ_H 4.14 (t, J = Hz, H-6), 3.93 (t, J = Hz, H-5), 3.60 (dd, J = Hz, H-4), 3.48 (m, H-3), 3.48 (m, H-2), 3.32 (s, -OCH3), 3.27 (dd, J = H-1). ^{13}C NMR (151 MHz, MeOD-d_4) δ_C 80.1 (C-1), 72.7 (C-3), 71.8 (C-2), 71.3 (C-5), 70.3 (C-4), 67.0 (C-6), 56.8 (-OCH3).

Voacristine (98)

Colourless, UV-active (254 nm) oily liquid. ^{1}H NMR (600 MHz, CDCl$_3$-d) δ_H 7.73 (s, 1H, N-H), 7.15 (d, J = 8.8 Hz, 1H, H-12), 6.91 (d, J = 2.4 Hz, 1H, H-9), 6.83 (dd, J = 8.7, 2.4 Hz, 1H, H-11), 4.18 (m, 1H, H-19), 3.88 (overlap, 1H, H-21), 3.85 (s, 3H, -OCH$_3$), 3.74 (s, 3H, -CO$_2$C$\underline{H}_3$), 3.48, 3.16 (m, 2H, H-5), 3.14, (overlap 2H, H-6), 3.02 (overlap 1H, H-3), 2.83 (d, J = 9.1 Hz, 1H, H-3), 2.60, 1.99 (m, 2H, H-17 a and b) 2.04 (m, 1H, H-14), 1.92, 1.56 (m, 2H, H-15), 1.49 (t, 1H, H-20), 1.11 (d, J = 6.3 Hz, 3H, H-18). ^{13}C NMR (151 MHz, CDCl$_3$) δ_C 174.9 (C=O), 154.3 (C-10), 136.6 (C-2), 130.6 (C-13), 128.9 (C-8), 112.3 (C-11), 111.3 (C-12), 109.6 (C-7), 100.7 (C-9), 71.3 (C-19), 59.9 (C-21), 56.0 (-OCH$_3$), 54.1 (C-16), 53.0 (-CO$_2$Me), 52.3 (C-5), 51.2 (C-3), 39.5 (C-20), 37.0 (C-17), 26.7 (C-14), 22.9 (C-15), 21.6 (C-6), 20.4 (C-18).

Ursolic acid (99)

White, UV-active (254 nm) amorphous solid. ^{1}H NMR (600 MHz, DMSO-d_6) δ_H 11.95 (s, 1H, -OH), 5.13 (t, J = 3.7 Hz, 1H, H-12), 4.31 (d, J = 5.1 Hz, 1H, 3-OH), 3.00 (dt, J = 10.3, 5.2 Hz, 1H, H-3), 2.10 (m, 1H, H-18), 2.04 – 1.71 (m, 4H), 1.64 – 1.37 (m, 9H), 1.35 – 1.20 (m, 4H), 1.04 (s, 3H, H-27), 0.93 (m, 1H, H-1), 0.91 (m, 3H, H-30), 0.89 (overlap (H-2/H-23), 0.87 (m, 3H, H-25), 0.82 (d, J = 6.4 Hz, 3H, H-29), 0.75 (s, 3H, H-26), 0.68 (s, 3H, H-24). ^{13}C NMR (151 MHz, DMSO-d_6) δ_C 178.7 (C=O), 138.6 (C-13), 125.03 (C-12), 77.3 (C-3), 55.2 (C-5), 52.8 (C-18), 47.2 (C-17), 46.8 (C-9), 41.6 (C-14), 38.9 (C-8), 38.8 (C-1), (C-7), 38.6 (C-19), 38.5 (C-20), 37.0 (C-

10), 36.4 (C-22), 32.8 (C-6/7), 30.2 (C-21), 28.7 (C-2), 28.3 (C-23), 28.0 (C-15), 27.5 (C-4), 23.7 (C-11/16), 23.3 (C-27), 21.1 (C-30), 17.0 (C-29), 16.9 (C-26), 16.1 (C-24), 15.2 (C-25).

10-hydroxycoronaridine (100)

Yellow UV-active (254 nm) oily liquid, ^{1}H NMR (600 MHz, Chloroform-d) δ_H 7.65 (s, 1H, N-H), 7.08 (d, J = 8.6 Hz, 1H, H-12), 6.88 (d, J = 2.4 Hz, 1H, H-9), 6.71 (dd, J = 8.7, 2.4 Hz, 1H, H-11), 3.71 (s, 3H, -OCH$_3$), 3.53 (m 1H, H-21), 3.36/3.19 (m, 2H, H-5), 3.09/2.90 (m, 2H, H-6), .2.90/2.80 (m, 2H, H-3), 2.57/1.88 (m, 2H, H-17), 1.73/1.12 (m, 2H, H-15), 1.56/1.43 (m, 2H, H-19), 1.26 (m, 1H, H-14), 0.89 (t, J = 7.4 Hz, 3H, H-18). ^{13}C NMR (151 MHz, CDCl3) δ_C 175.8 (C=O), 149.3 (C-10), 137.9 (C-2), 130.7 (C-13), 129.6 (C-8), 111.4 (C-11), 110.9 (C-12), 109.8 (C-7), 103.3 (C-9), 57.6 (C-21), 55.2 (C-16), 53.1 (C-5), 52.6 (-OCH$_3$), 51.4 (C-3), 39.2 (C-20), 36.5 (C-17), 32.0 (C-15), 27.3 (C-14), 26.7 (C-19), 22.2 (C-6), 11.8 (C-18).

10-hydroxyibogamine (101)

Pale yellow UV-active (245nm) oily liquid, ^{1}H NMR (600 MHz, MeOD-d$_4$) δ_H 7.00 (d, J = 8.6 Hz, H-12), 6.73 (d, J = 2.3 Hz, H-9), 6.54 (dd, J = 8.5, 2.4 Hz, 1H, H-11), 3.88/3.04 (m, 2H, H-3), 3.28/3.03 (m, 2H, H-5), 3.23/2.54 (m, 2H, H-6), 2.94 (ddd, J = 11.8, 4.3, 1.9 Hz, 1H, H-16), 2.81 (, s, 1H, H-21), 1.57 (m, 1H, H-20), 1.55/1.48 (m, 2H, H-19), 2.05/1.55 (m, 2H, H-17), 1.82/1.16 (m, 2H, H-15), 1.79 (m, 1H, H-14), 0.95 (t, J = 7.3 Hz, 3H, H-18). ^{13}C NMR (151 MHz, MeOD-d$_4$) δ_C 149.6 (C-10), 142.6 (C-2), 130.1 (C-13), 110.2 (C-12), 109.7 (C-11), 106.9 (C-7), 101.7 (C-9), 58.0 (C-21), 54.4 (C-5), 49.5 (,41.9 (C-20), 40.4 (C-16), 33.7 (C-17), 31.5 (C-15), 27.3 (C-19), 26.3 (C-14), 20.1 (C-6), 10.93 (C-18). HR-TOF-ESI-MS m/z = 296.1882, [M+H]$^+$ Calculated C$_{19}$H$_{24}$N$_2$O, 296.1889.

β-sitosterol (45)

White amorphous solid, Melting point: 136-140.0 °C, UV λmax (DCM): 280 nm. ^{1}H NMR (600 MHz, Methylene Chloride-d2) and ^{13}C NMR (151 MHz, CD_2Cl_2): (Table 4.20).

Stigmasterol (47)

White amorphous solid, melting point: 136-140.0 °C, UV λ_{max} (DCM): 280 nm ^{1}H and ^{13}C NMR data (Table 4.20).

3.4   Cytotoxicity of the Isolated Compounds

Cytotoxicity of the isolated secondary metabolites was investigated against seven cancer cell lines including; renal cancer (786-0), human breast adenocarcinoma cells (MCF-7) triple negative breast cancer cell (BT549), hepatocellular carcinoma cells(HCC), human liver cancer cell (HepG2), human epithelial type 2 laryngeal carcinoma (HeP2), human alveolar basal epithelial cells (A549) and three normal human cells namely; immortalized human bronchial epithelial cells (BEAS), immortalized human liver cells (LO2), immortalized breast cells (MCF-10a). The [3-(4,5-dimethylthiazol-2-yl)-2,5-diphenyltetrazolium bromide] (MTT) calorimetric assay described in previous studies was adapted for this purpose (Coghi *et al.*, 2018). Cells were cultured in standard media (Dulbecco's modified eagle medium (DMEM) or minimum essential medium (MEM) or Roswell Park Memorial Institute (RPMI) 1640 medium depending on the cell type, and supplemented with 10% FBS, 1% antibiotic and maintained at 37° C and 5% CO_2. Cells were plated in 96 well plates (1 x 10^{4} cells per well) and incubated for 24 hours. The cells were then dosed with the isolated compounds at varying concentrations and incubated for a further 24 hours. The cell medium was aspirated and then washed with PBS. Afterwards, MTT solution (5 mg/mL, 10 μl) was added and incubated at 37°C for four hours. The purple formazan crystals were then dissolved using a solubilization buffer (10 mM HCl in a solution of 10% of SDS,100 μl) followed

by overnight incubation or using DMSO (200 µl) and incubated for 20 minutes. Absorbance was read at 570 nm. Untreated cells were used as controls. While the anticancer drug, paclitaxel was used as a positive control. Cell viability was calculated from equation 1.

Cell viability (%) $= \frac{A_{treated}}{A_{control}} \; x \; 100$………………………………….. 1

Where *A* is absorbance. A characteristic graph of at least three independent experiments is presented in appendix 24.

3.5 *In Silico* Docking Studies

Molecular operating environment (MOE) software version 2008.10 (Chemical Computing Group, Montreal, Canada) was used to perform *in silico* docking simulations (Herrmann *et al.*, 2017). Default settings in the MOE docking simulation tool were used for docking using the London dG scoring function. Before docking simulations were performed, ligands and proteins were prepared and the docking method was validated as described here under.

3.5.1 *Ligand Preparation*

2D structures of the molecules were drawn using chembiodraw ultra software, version 12.0 (Cambridge soft) and imported into the MOE structure builder tool as SMILES string to generate 3D structures. The energy of the 3D molecules was minimized by applying the Hamiltonian MMFF94X force field. The minimized molecules were used to develop a local library for docking simulations.

3.5.2 *Protein Preparation*

The crystal structures of protein molecular targets involved in the P53 pathway; that is MDM2 (PDB ID: 1RV), P21 (PDB ID: 2X4Z), (CDK2, (PDB ID: 1DI8, 1PYE), CDK6 (PDB ID: 1XO2),

Bcl-2 (PDB ID: 2O2F), Caspase 3(PDB ID: 3DEI), and Caspase 8 (PDB ID: 3KJQ) were retrieved from the protein data bank (PDB). The receptors (proteins) were protonated using the 3D protonate tool in MOE, partial charges were added, unbound water molecules were removed and the energy of the protein was minimized by applying the empirical Hamiltonian MMFF94X force field.

3.5.3 Docking Method Validation

The docking method was first validated by self-docking the native ligand into the binding site of the protein. Here an induced fit docking mode was adopted (where both the ligand and the amino acid side chains were left flexible in order to achieve an optimal fit) (Herrmann *et al.*, 2017). Validity of the docking method was evaluated basing on the root mean square deviation (RMSD) upon superposition of the best docked pose to the experimental native ligand conformation. RMSD value < 2Å was considered acceptable. The binding affinities measured in terms of S-score in Kcal/mol were used for comparison with the binding affinities of the test ligands

3.5.4 In Silico Docking of Compound Library

The compound library of the secondary metabolites was docked into the inhibitor binding site of the target proteins. The resultant docking poses of the ligands were ranked basing on the S-score, in this case, the more negative the S-score, the stronger the binding affinity to the target protein.

3.6   Preparation, Characterization and Biological Investigation of Natural Product-Loaded Nanoparticles

Beta-sitosterol (β-Sit) was selected as a model natural product to investigate whether incorporation of natural products with moderate to low anticancer activity in nanoparticle drug delivery systems can enhance their activity. The methods for formulation, characterization and biological studies are described in the following sub-sections.

3.6.1 Method Development for Quantitative Analysis of β-Sitosterol

The concentration of β-sitosterol incorporated in nanoparticles or in solution was assayed by a modified calorimetric method utilizing Liebermann-Burchard reagent described previously (Araújo *et al.*, 2013; Kenny, 1952; Mosmann, 1983; Nath *et al.*, 1946). A standard curve was prepared as follows: β-sitosterol (80 mg) was dissolved in DCM (HPLC grade, 20 mL) assisted by vortex mixing to make a stock solution. The stock solution was serially diluted to make working standards over the concentration range of 0.0125-2.0 mg/mL with DCM. The standard solutions were reacted with conc. H_2SO_4 in acetic anhydride (Liebermann-Burchard reagent) to form a green colored product, then after 10 minutes, absorbance of the chromogenic product was measured at 622 nm using a microplate reader in a 96-well quartz plate. The time duration for the calorimetric reaction was first determined by measuring the time course for the chromogenic reaction (Appendix 25). A plot of absorbance against concentration was used to prepare a standard curve. The analytical method was partially validated for linearity, method precision, accuracy and recovery (Appendix 25). All experiments were carried out in replicate. Appropriate blank samples were assayed to correct for the absorbance of interfering substances in the sample matrices.

3.6.2 Preparation of β-Sit-loaded Nanoparticles

Simple emulsion-diffusion-solvent evaporation method (Wang *et al.*, 2016) was adapted to formulate drug-loaded nanoparticles with slight modifications. Polymers (PLGA and PEG-PLA) and drug (β-Sit) were separately dissolved in a volatile organic solvent (ethyl acetate or acetone). Then the organic solutions of polymer and β-sitosterol were mixed on vortex to ensure homogenous interaction of the two solutions. The polymer and drug solution (5 mL) was emulsified with a solution of polyvinyl alcohol (PVA, 2%, 1 mL) to form an oil-in-water emulsion. To produce nanoparticles, the oil-in water emulsion was homogenized using a probe sonicator for

2 minutes. The organic solvent was allowed to evaporate while stirring the nanoparticle solution using a magnetic stirrer for 15 hours. Nanoparticles were purified by three cycles of washing with ultra-pure water followed by 30 minutes of ultra-centrifugation at 16900 g and 4 °C. Purified nanoparticles were dispersed in filtered ultrapure water (10 mL) for further analysis. Fluorescently labelled nanoparticles were prepared similarly by adding coumarin-6 (10 µL) from a stock solution of coumarin-6 (50 µg mL^{-1}) to the organic phase along with the β-Sit.

3.6.3 *Nanoparticle Size, Surface Charge and Surface Morphology*

A dynamic light scattering instrument (Zetasizer) was used to measure the size, polydispersity index (PDI) and surface charge (ζ) of the formulated nanoparticles. In this case, nanoparticle suspension (100 µL) was diluted 10-folds with filtered ultra-pure water before measurement. All measurements were done in triplicate.

3.6.4 *Determination of Encapsulation Efficiency and Drug Loading Capacity*

To determine the drug loading capacity and encapsulation efficiency, a known volume (2 mL) of the nanoparticle suspension was centrifuged at 16,900 x g for 30 minutes. After removing the supernatant, the nanoparticle pellet was dissolved in DCM assisted by an ultrasound or vortex mixing. The absorbance of the solution was measured as described in section 3.5.1 at 622 nm. The procedure was repeated thrice. The calibration curve prepared in section 3.5.1 was used to determine the concentration of β-sitosterol encapsulated in the nanoparticles. Encapsulation efficiency (EE) and drug-loading capacity were calculated from equations 2 and 3 (Zhang *et al.*, 2016)

$$\text{Encapsulation efficiency } = \frac{Weight\ of\ \beta-sit\ (mg)\ in\ nanoparticle\ suspension}{Weight\ of\ \beta-sit\ used\ for\ formulation}\ \text{x } 100 \qquad (2)$$

$$\text{Drug-loading capacity } = \frac{Actual\ weight\ of\ \beta-sit\ (mg)\ in\ nanoparticle\ suspension}{Theoretical\ weight\ of\ \beta-sit\ +Theoretical\ weight\ of\ polymer}\ \text{x } 100 \qquad (3)$$

3.6.5. Drug Release Profile

To establish the drug release profile of β-Sit-loaded nanoparticles, a known amount of nanoparticle solution (1.5 mL) was centrifuged as before to collect nanoparticles. After the supernatant was aspirated off, the nanoparticle pellet was dispersed in PBS (1.5 mL) or PBS supplemented with 0.2% Tween20 (1.5 mL) and maintained at physiological temperature (37±0.5 ℃) in a reciprocating shaker. Due to very low solubility of β-sitosterol in aqueous medium, the release medium was amended with Tween20 to maintain sink conditions (Raval *et al.*, 2017). At known time intervals, the nanoparticles were separated from the release medium by centrifugation as before. Aliquots of the supernatant were withdrawn and added to DCM (2 mL) to extract β-sitosterol released from the nanoparticles. An equivalent volume of fresh medium was added to the drug release medium to replenish the release medium withdrawn for analysis. Absorbance of the DCM extract was measured as before at 622 nm. Amount of β-sitosterol released was calculated from the standard curve prepared previously. All experiments were replicated three times.

3.6.6. Determination of Stability of Nanoparticles

Stability of nanoparticles was evaluated on storage and in a biological milieu. For storage stability, nanoparticles were suspended in previously filtered ultrapure water and maintained on the shelf and under refrigerated conditions (4 ℃). Variation in nanoparticle size, PDI and surface morphology were used to evaluate their stability. For stability in a biological milieu, fixed volumes of the nanoparticle suspension (1 mL) were first centrifuged at 16900 xg. The nanoparticle pellets were re-suspended in PBS (0.01 M, pH 7.4) or PBS/FBS (1:1, *v/v*) and maintained at 37 ℃ for 24 hours in a laboratory shaker (Baek *et al.*, 2016; Li *et al.*, 2017). At regular time intervals, samples

were purified by washing with ultrapure water followed by ultracentrifugation. The size, PDI and surface morphology of the nanoparticles was measured as described in section 3.6.3.

3.6.7 *Cellular Uptake and In Vitro Anticancer Assay of Nat-NPs*

Cellular uptake and antiproliferative activity of the formulated β-Sit-nanoparticles were studied using MCF-7 and MDA-MB-231 breast cancer cells as described in the proceeding sections.

3.6.7.1 Cell Culture

MCF-7 cells (representing hormone dependent breast cancer cells) were maintained in recommended culture medium (EMEM supplemented with 10% FBS, 1% penicillin/streptomycin, 2 mM L-glutamine and 1% non-essential amino acids in a humidified incubator saturated with 5% Carbondioxide (CO_2) at 37 °C). MDA-MB-231cells (representing hormone independent breast cancer cells) were cultured in recommended medium (DMEM supplemented with 10% FBS and 1 % penicillin/streptomycin in a humidified incubator saturated with 5% CO_2 at 37 °C).

3.6.7.2 Measurement of Cellular Uptake by Flow Cytometry

Uptake of nanoparticles by cells was studied as follows: MCF-7 and MDA-MB-231 cells were seeded in 24 well plates (5×10^4 cells per well) and maintained in the culture medium for 24 hours. Thereafter, the cell media were innoculated with courmarin-6-labeled β-sit-PLGA and β-sit-PEG-PLA nanoparticles (100 µL). Untreated cells were used as controls. After 4 and 24 hour time durations, the cell media were aspirated, cells were detached by adding trypsin and then washed twice with cold PBS. Cellular internalization of the nanoparticles was then evaluated by FACS analysis using a flow cytometer. Coumarin-6 was excited at 488 nm and detected at fluorescence wavelength of 525 nm. Data were collected for 10,000 gated events per sample (Lee *et al.*, 2015). All experiments were replicated in triplicate.

3.6.7.3 Study of Cellular Uptake by Confocal Microscopy

Laser scanning fluorescence confocal microscopy was used to study cellular internalization of the nanoparticles by MDA-MB-231 and MCF-7 cells. The cells were plated in 8 well chamber slides ($2x10^4$ cells per well) and maintained in the culture medium at physiological temperature for 24 hours. The medium was aspirated and the cells were cleaned with sterile PBS and transfected with coumarin-6 labeled nanoparticles and maintained in the culture medium for a further 4 hours. Then Lyso Tracker^{TM} red was added to the cell medium and maintained in culture for another one hour. This was followed by a three cycles of washing with sterile PBS. The cells were then fixed with 4% paraformaldehyde (PFA) solution (200 µL) per chamber and incubated for 15 minutes. Excess PFA was removed by further washing with sterile PBS. Afterwards, the cells were then treated with 4',6-diamidino-2-phenylindole (DAPI, 1 µg/mL, 200 µL per chamber) to contrast the cells nuclei. After final cleaning with PBS, the cells were mounted on the slides using Fluorsave^{TM} for imaging using laser scanning confocal microscope. The image acquisition parameters were customized as follows: DAPI channel was excited at 405 nm and the emission wavelength at 420-520 nm, Coumarin-6 channel was excited at 488 nm and emission at 490-550 nm while Lysotracker red was excited at 552 nm and emission at 600-730 nm.

3.6.7.4 Antiproliferative Assay

The MTT calorimetric assay (Mosmann, 1983) was adapted to study inhibitory activity of the nanoparticles against MDA-MB-231 and MCF-7 breast cancer cells. Here, cell were plated in 96 well plates ($1x10^4$ cells per well) and incubated overnight to allow cells to attach. The cells were then treated with known concentrations of nanoparticles (equivalent to 53.08, 26.24, 13.12 and 6.64 µg/mL of β-sitosterol in nanoparticle solution) and maintained in the culture medium for 24 hours. The media were aspirated and then MTT solution (10 µL) was added to the cell medium

and maintained in culture for a further 4 hours. DMSO (200 µL) was added to solubilize MTT and formazan crystals. To ensure complete solubilization of MTT and formazan crystals, the cells were incubated for 10 minutes. Absorbance of the formazan solution or unreduced MTT solution was measured at 570 nm using a microplate reader. Untreated cells and cells treated with blank nanoparticles (6.64-53.08 µg/mL) were used as controls. In all cases, the experiments were carried out in triplicate.

3.7   Statistical Analysis

Results for each biological assay were averaged and reported as mean ± standard deviation. One-way or two-way ANOVA and Bonferroni post-tests were run to evaluate statistical differences between treatment groups using Graphpad Prism version 5.0 (Graphpad software, La Jolla, CA, USA 2007). Differences between treatment groups were considered significant where $P < 0.05$.

CHAPTER 4: RESULTS AND DISCUSSION

In this chapter, the isolation, characterization, *in vitro* antiproliferative activity, and *in silico* anticancer mechanism of action of the isolated secondary metabolites from the selected medicinal plants is presented. The formulation, characterization and *in vitro* anticancer activity of Nat-NP is also discussed.

4.1   Characterization of Secondary Metabolites from the Selected Plants

Compounds were isolated from four plant species namely; *Zanthoxylum zanthoxyloides, Aloe tororoana*, *Aloe schweinfurthii* and *Taberneamontana ventricosa*. The compounds were characterized using NMR (1D and 2D) and mass spectrometry.

4.1.1   Characterization of Secondary Metabolites from Zanthoxylum zanthoxyloides

The root extract of *Z. zanthoxyloides* upon chromatographic separation yielded five (5) compounds: tridecan-2-one (**80**), dihydrochelerythrine (**81**), sesamin (**82**), skimmianine (**83**), and hesperidin (**84**).

*4.1.1.1 Tridecan-2-one (**80**)*

Compound **80** was a UV-inactive (254 nm) white amorphous solid suggesting lack of conjugated system. Analysis using GC-MS shows m/z = 198.34. The ^{13}C-NMR spectrum (Table 4.1) showed thirteen (13) signals consisting of one carbonyl carbon atom resonance peak at δ_C 209.1 and the rest being characteristic methyl and methylene carbon atom resonance peaks suggesting compound **80** to be an alkyl ketone. The ^{1}H-NMR spectrum shows six (6) signals consisting of a de-shielded methylene group resonance peaks at δ_H 2.39 (t, J = 7.5 Hz, 2H,) and de-shielded methyl group resonance peak at δ_H 2.08 (s, 3H) suggesting that these groups must be bonded to the carbonyl carbon. HMBC correlations between proton resonance peaks at δ_H 2.38 and δ_H 2.08 with the

carbonyl carbon δ_C 209.1 was used to confirm these assignments. Additionally the signal at δ_H 0.88 (t, 3H) which couples with the overlapping signals at δ_H 1.27 (m) in H-H COSY indicated the terminal methyl moiety at the tail-end of the alkyl ketone. The overlapping multiplets resonating at δ_H 1.27 in the ^{1}H-NMR spectrum were indicative of methylene protons. Compound **80** was identified as tridecan-2-one previously isolated from *Z. armatum* (Bisht and Chanotiya, 2011).
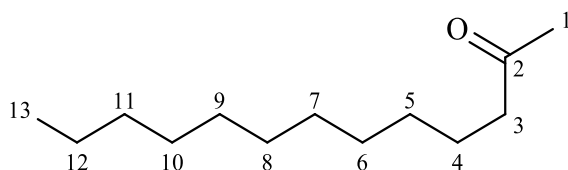
80

Table 4.1: [1]H (600 MHz), ^{13}C (151 MHz) NMR data and HMBC (^2J and ^3J) correlations of tridecan-2-one (**80**) in CD$_2$Cl$_2$

C-position	δ_C (ppm)	δ_H (m, H, J in Hz)	HMBC (^2J, ^3J)
1	30.3	2.08 (s)	C-2, 3
2	209.1		
3	44.0	2.39 (t)	C-1, 2, 4
4	24.3	1.53 (p, 2H, J =7.4 Hz,)	C-2, 3
5	29.7		
6	29.8		
7	29.9	1.27 (Overlap)	C-3, 4, 12, 10
8	30.0		
9	30.0		
10	29.6		
11	31.9	1.27 (Overlap)	
12	23.1	1.29 (Overlap)	C-12, 4-10 (overlap)
13	14.3	0.88 (t)	C-11, 10

4.1.1.2 Dihydrochelerythrine (**81**)

Compound **81** was a UV-active (254 nm) white crystal. It was soluble in DCM and produced a red precipitate with Dragendorff's reagent suggesting the compound to be an alkaloid. The HRMS-ESI showed molecular ion peak at m/z = 348.1229 [M-H]$^+$ which, along with ^{13}C NMR spectrum was used to deduce the molecular formula $C_{21}H_{19}NO_4$, giving 13 degrees of unsaturation. The ^{13}C NMR spectrum (Table 4.2); shows signals for 21 carbon resonances which consist of 10 aromatic quaternary carbons, 6 methine aromatic carbons, 3 methyl carbon atoms attached to hetero atoms, and 2 methylene carbons attached to hetero atoms. The foregoing carbon resonances is consistent with an aromatic ring system with 17 carbon atoms having four substituents (δ_C 41.5; N-CH$_3$, 56.1; -OCH$_3$, 61.2; - OCH$_3$ and 101.6; -OCH$_2$O-).

The ^{1}H NMR (Table 4.2) shows six signals between δ_H 6.90 - 7.80 ppm corresponding to six aromatic protons. The H-H COSY correlations show the presence of two sets of *ortho*-coupled aromatic protons δ_H 6.95/7.50 (1H, *d, J* = 8.5 Hz) and 7.48/7.70 (1H, *d, J* = 8.5 Hz). The remaining two aromatic protons appear as two one-proton singlets at δ_H 7.11 and δ_H 7.65. Using these data and biosynthetic considerations (Takao *et al.*, 1983), the basic skeleton of compound 67 was established to be a *N*-methylated benzo[*c*]phenanthridine alkaloid. Three possible structures (81a-b) were proposed based on these data. HMBC correlations between methylene proton resonance peaks at δ_H 4.26 (s, H-6) with carbon peaks appearing at δ_C 143.1 (C-11a), 146.6 (C-7), and 152.8 (C-8) in addition to ^2J and ^3J correlations in the HMBC spectrum of the proton signal at δ_H 6.96 (d, *J* = 8.5 Hz, H-9) with the oxygenated aromatic carbon atoms δ_C 146.6 (C-7) and 152.8 (C-8) were used to confirm the oxygenation pattern in ring D. Similarly, ^3J correlations of the singlet aromatic protons at δ_H 7.11 (H-1) and δ_H 7.65 (H-4) with oxygenated carbon atoms δ_C 148.0 (C-3) and 148.5 (C-2) respectively along with ^3J correlations of the methylenedioxy protons δ_H 4.31

with the same oxygenated aromatic carbons δ_C 148.0 (C-3) and 148.5 (C-2) was used to confirm

the substitution pattern on ring A. From these and other correlations in the HMBC spectrum (Table

4.2), the structure of this compound was confirmed to be 81a. Other alternative structures (81b and

c) were eliminated basing on HMBC correlations. Compound **81** was identified as

dihydrochelerythrine which was previously reported from *Z. davyi* (Tarus *et al.*, 2006).
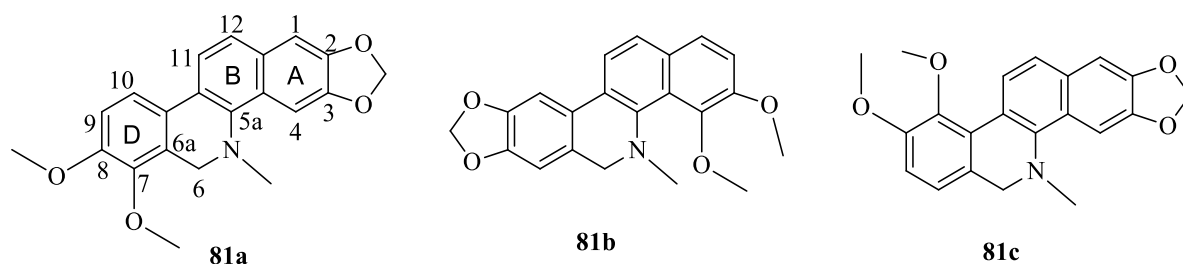

81a   81b   81c

Table 4.2: ^1H (600 MHz), ^{13}C (151 MHz) NMR data and HMBC (^2J *and* ^3J) correlations for
dihydrochelerythrine (**81**) in CD_2Cl_2

C-position	δ_C (ppm), type	δ_H (m, J(Hz))	HMBC (^2J, ^3J)
1	104.5	7.11 (s)	C-3, 4a, 12
1a	131.2		
2	148.5		
3	148.0		
4	100.9	7.65 (s, 1H)	C-1a, 2 5a
5a	143.1		
6	49.1	4.26 (s, 2H)	C-5a, 7, 8
6a	124.6		
7	146.6		
8	152.8		
9	111.5	6.96 (d, $J = 8.5$)	C-7, 8, 10a
10	118.9	7.50 (d, $J = 8.5$)	C-6a,7, 8, 10a, 11a
10a	126.5		
11a	126.4		
11	120.4	7. 71 (d, $J=8.4$)	C-1a, 5a, 10a, 11a
12	124.0	7.49 (d, $J= 8.4$)	C-1, 1a, 4a, 5a, 11,
11a,			
-OCH$_2$O-	101.6	4.26 (s)	C-2, 3
N-CH$_3$	41.5	2.57 (s)	C-5a, 6
7-OCH$_3$	61.2	3.85 (s)	146.2
8-OCH$_3$	56.1	3.91 (s)	152.3

4.1.1.3 Sesamin (**82**)

Compound **82** was isolated as a colorless crystalline solid producing a blue fluorescence in UV light (254 nm) suggesting the presence of a conjugated system. It gave a positive test with iron (iii) chloride indicative of a phenolic compound. Moreover, it gave a positive test with Dragendorff's reagent, which therefore suggested compound **82** to be either an alkaloid or a lignan since lignans too give a false positive test with Dragendorff's reagent due to conjugation (Jones and Kinghorn, 2006). The ^{13}C NMR (Table 4.3) shows signals corresponding to ten carbon atoms of which, six are characteristic aromatic carbon atom resonances, one dioxymethylene carbon atom, 2 methine carbon atoms of which, one is oxygenated and an oxygenated methylene carbon atom. The pattern of carbon resonances suggests compound **82** to be a tetrahydrofuran type of lignan with one aromatic ring.

The ^{1}H NMR (CD$_2$Cl$_2$, 600MHz) (Table 4.3) shows an ABX system of three aromatic proton resonance peaks at δ_H 6.84 (d, 2H, J = 1.69 Hz, H-2′/2″), δ_H 6.81 (dd, 2H, J = 7.97, 1.67Hz, H-5′/5″) and δ_H 6.78 (d, 2H, J = 7.97, H-6′/6″) suggesting a tri-substituted aromatic ring. The proton signal at δ_H5.94 (s, 4H) shows methylenedioxy group in the benzo-1,3-dioxole moiety. The H-H COSY correlations show mutually coupled diastereotopic protons at δ_H 3.83/4.20 (m, 4H, H-4/8) which in turn couple with the proton signal at δ_H 3.02 (m, 2H, H-1/5). Moreover in the H-H COSY spectrum, the proton signal at δ_H 3.02 also couples with the signal at δ_H 4.68 (d, 2H, H-2/6) . The coupling pattern of these protons is indicative of the tetrahydrofuran moiety. ^{3}J correlations in HMBC spectrum between proton signals at δ_H 6.81 (H-5′/5″) and δ_H 6.84 (H-2′/2″) with carbon resonance peak at δ_C 54.8 was used to establish the attachment of the tetrahydrofuran moiety to the aromatic ring. Additional HMBC correlations between δ_H 3.02, and δ_H 4.68 with aromatic carbon δ_C 135.9 further confirm the attachment of the tetrahydrofuran moiety to the aromatic ring.

68

The integral values of the protons suggest that the compound is symmetric although the ^{1}H NMR and ^{13}C NMR spectra only show signals corresponding to nine (9) protons and ten (10) carbon atoms. Compound **82** was identified as sesamin previously isolated from *Z. zanthoxyloides* and *Z. alatum* (Roxb) (Chaaib *et al.*, 2003; Mukhija *et al.*, 2014)
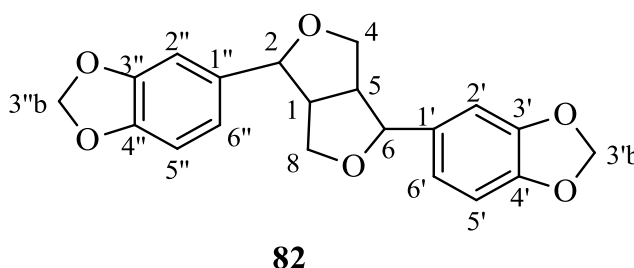

82

Table 4.3: [1]H (600 MHz), ^{13}C (151 MHz) NMR data and HMBC (^2J and ^3J) correlations for sesamin (**82**) in CD$_2$Cl$_2$

C-position	δ_C (ppm)	δ_H (m, J (Hz)	HMBC (^2J, ^3J)
1/5	54.8	3.02 (m)	C-1′, 6′
2/6	86.1	4.68 (d, 1H, $J = 4.2$)	C-1,1′ 4
4/8	72.1	4.20 (m)	C-1, 2
		3.83 (m)	C-1, 2
1′/1″	135.9		
2′/2″	106.8	6.84 (d, $J = 1.69$)	C-2, 4′, 6′
3′/3″	148.3		
3′b/3″b	101.6	5.94 (s)	C-3′, 4′
4′/4″	147.4		
5′/5″	108.3	6.78 (d , $J =7.97$)	C-3′, 1′
6′/6″	119.6	6.81 (dd, $J = 7.97. 1.67$)	C-2, 2′, 4′

4.1.1.3 Skimmianine (**83**)

Compound **83** was isolated as a pale yellow crystalline solid. It gave a red precipitate with Dragendorff's reagent indicating an alkaloid. The LC-ESI-MS gave a molecular ion peak at *m/z* = 260.0919 [M+H]$^+$ which, along with ^{1}H NMR and ^{13}C NMR data was used to deduce the molecular formula to be C$_{14}$H$_{13}$NO$_4$. The index of hydrogen deficiency was calculated to be nine (9).

The ^{1}H NMR spectrum (Table 4.4); shows seven signals consisting of three singlet peaks δ_H 4.01 (s, 3H), 4.03 (s, 3H) and, 4.48 (s, 3H) characteristic of methoxy group proton resonance peaks, and four characteristic aromatic proton resonance peaks. The H-H COSY reveals two sets of mutually coupled aromatic protons δ_H 7.25/8.02 (1H, d, J = 9.3 Hz) and δ_H 7.10/7.61 (1H, d, J = 2.8 Hz). The coupling constants indicate that the former set of protons is *ortho*-coupled while the latter is either *meta*-coupled or a set of *ortho*-coupled protons in a strained ring with an electronegative atom bonded to the same carbon atom as the vicinally coupled protons. The ^{13}C-NMR spectrum reveals fourteen carbon peaks consisting of seven quaternary aromatic carbon atoms, four aromatic methine carbon atoms and three oxygenated methyl carbon atoms. The foregoing data coupled with biosynthetic considerations is indicative of a furoquinoline alkaloid having three methoxy substituents with four possible structures 83a-d

The HMBC spectrum shows ^3J correlations between proton signals at δ_H 8.02 (H-5) and δ_H 7.10 (H-3) with carbon resonance peak at δ_C 156.1 for C-4 and ^2J and ^3J correlations between proton signals at δ_H 7.25 (H-6) and δ_H 8.02 (H-5) with the oxygenated carbon resonance peak at δ_C 152.1 (C-7). These cross-correlations in the HMBC spectrum were used to eliminate other proposed structures (83b-d) and confirmed the structure to be 83a. Compound **83** was thus identified as skimmianine previously reported in the family Rutacaea (Jackson *et al.*, 1990).
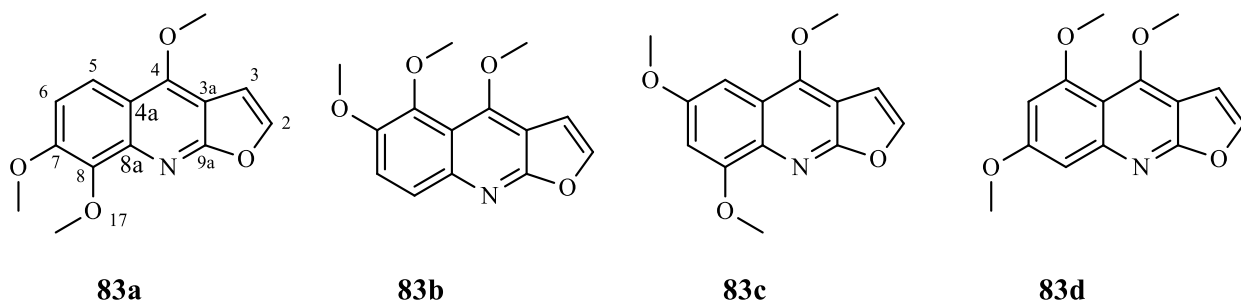

83a	**83b**	**83c**	**83d**

Table 4.4: ^{1}H (600 MHz), ^{13}C (151 MHz) NMR data and HMBC (^2J and ^3J) correlations of skimmianine (**83**) in CD_2Cl_2

C-position	δ_C (ppm)	δ_H (m, J in Hz)	HMBC (^2J, ^3J)
2	142.7	7.61 (d, $J = 2.8$)	C-9a, 3, 3a
3	104.6	7.10 (d, $J = 2.8$)	C-9a, 4, 3a
3a	101.7		
4	156.1		
4a	114.7		
5	117.8	8.02 (d, $J = 9.4$)	C-7, C6, C4
6	112.0	7.25 (d, $J = 9.4$)	C-7
7	152.1		
8	141.8		
8a	141.3		
9a	164.1		
4-OCH$_3$	58.8	4.43 (s)	C-4
7-OCH$_3$	56.5	4.01 (s)	C-7
8-OCH$_3$	61.0	4.03 (s)	C-8

4.1.1.5 Hesperidin (**84**)

Compound **84** was a pale yellow powder. The UV λ_{max} (230 and 290 nm), ^{1}H NMR (δ_H 5.49 (H-2), 3.28 and 2.77 (H-3) and ^{13}C NMR (δ_C 78.3 for C-2 and 42.0 for C-3 and 197.0 for C-4) suggested a flavanone derivative (Agrawal, 2013). The NMR spectral data (Table 4.5), $\delta_{C/}$ δ_H [(δ_C 114.1/ δ_H 6.94), (δ_C 112.0/δ_H 6.93) and (δ_C 117.9/δ_H 6.90)] indicated that the B-ring is di-substituted. The overlapping signals at δ_H 6.13 for H-6 and H-8 correspond to the *meta*-coupled protons in ring A. The high-field chemical shift of H-6 and H-8 is an indication of oxygenation at C-7 (δ_C 165.9). The configuration at C-2 was established by measuring the coupling constant between H-2, H-3a and H-3b (Jadeja *et al.*, 2017). The large coupling constant between H-3b and

H-2 ($J = 12.38$ Hz) and calculated dihedral angle $\phi = 180^\circ$ indicates that H-2 and H-3b are in axial position whereas the small coupling constant between H-2 and H-3a ($J = 3.17$ Hz) and small dihedral angle $\phi = 51.8^\circ$ between H-3a-C3-C2-H-2 suggests that H-3a must be in equatorial position (Jadeja *et al.*, 2017). This arrangement places ring B in an equatorial position. Thus the relative configuration at C-2 was designated as S* (Jadeja *et al.*, 2017). Eleven signals between δ_C 66.0-100.6 in the ^{13}C NMR spectrum indicated a diglycoside substituent whose attachment to the aglycone was established by considering the ^3J correlation of the anomeric proton (δ_H 4.97/δ_C 101.2) with C-7. The signal at δ_H 1.09 (d, 3H, $J = 6.2$ Hz)/δ_C 17.8 which correlates with carbon resonance peaks at δ_C 72.0 and δ_C 68.3 suggest that one of the sugar molecules is rhamnose, while the other sugar moiety was identified as a glucopyranoside unit based on the 1D and 2D spectral information. Compound **5** was thus identified as hesperidin. It is found abundantly in citrus fruits (Garg *et al.*, 2001) and was previously isolated from the root bark of *Z. zanthoxyloides (Queiroz et al., 2006).*

84
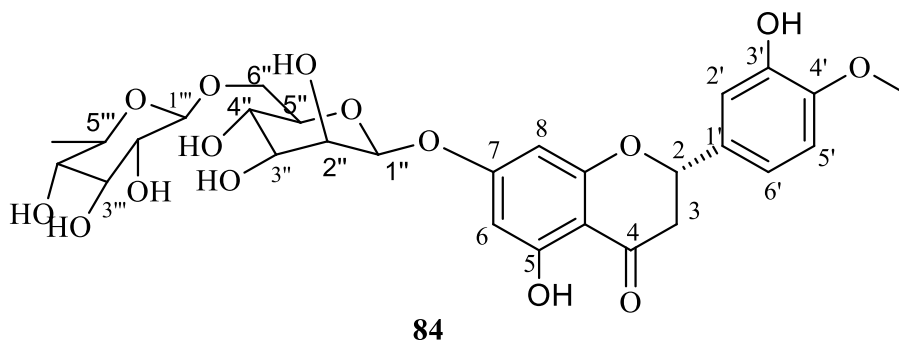
Table 4.5: ^1H (600 MHz), ^{13}C (151 MHz) NMR data and HMBC (^2J and ^3J) correlations for hesperidin (**84**) in DMSO-d$_6$

C-position	δ_C (ppm)	δ_H (m, H, J(Hz)	HMBC (^2J, ^3J)
2	78.9	5.51 (dd, 1H, J = 12.38, 3.13)	C-4, 2′, 6′
3	42.5	3.30 (dd, 1H, J = 12.38, 3.17),	C-4, 2
		2.78 (m, 1H)	
4	197.2	-	
5	163.5	-	
5a	103.9	-	
6	96.8	6.15 (Overlap)	C-7, 5a
7	165.9	-	
8	96.2	6.13 (overlap)	C-7, 5a
1′	131.4	-	
2′	114.2	6.95 (overlap)	C-1′, 3′, 4′ 6′
3′	146.9	-	
4′	148.5	-	
5′	112.1	6.94 (overlap)	C-1′, 3′, 4′,
6′	118.1	6.91 (overlap)	C-2′, 4′
5-OH		12.05 (s, 1H)	C-5, 5a, 6
3′-OH		9.07 (s, 1H)	C-4′, 2′
4′-OCH$_3$	56.2	3.78 (s, 3H)	C-148.5
Glc-6″	101.2	4.99 (t, 1H, J = 10.26, 5.19)	C-165.9
Rha-2″	101.1	4.53 (d, 1H)	C-68.8
Rha-CH$_3$	18.60	1.10 (d, 3H, J = 6.34)	C-69.0, 72.6

4.1.2 Characterization of Secondary Metabolites from Aloe tororoana

The whole plant extract of *A. tororoana* after chromatographic separation yielded six (6) compounds: aloenin (**85**), aloe-emodin (**86**), laccaic acid ester (**87**), aloesaponarin II (**88**) β-sitosterol (**5**) and stigmasterol (**47**). This is the first phytochemical investigation of the species *Aloe tororoana*.

4.1.2.1 Aloenin (**85**)

Compound **85** was isolated as white, amorphous and blue-fluorescent (254 nm) solid from whole plant extract of *A. tororoana*. It was identified as 6-substituted-4-methoxy-2-pyrone derivative from ^{13}C NMR signals at δ_C 164.1 (C-2), 171.0 (C-4), 157.9 (C-6), and 87.9 (C-3) and the *meta*-coupled proton signals at δ_H 5.61/6.26 (*d*, 1H, *J*= 2.2) in the ^{1}H NMR spectrum (Kazuo *et al.*, 1976). The highly shielded aromatic carbon signal at δ 87.8 (C-3) indicates oxygenation at C-4 of the 2-pyrone ring, thus shielding C-3 due to resonance. HMBC spectrum shows ^2J and ^3J of H-3 with C-2, 4 and 5, and of H-5 with C-3, 4, 6 and 1′ which confirms the 6-substituted-4-methoxy-2-pyrone skeleton.
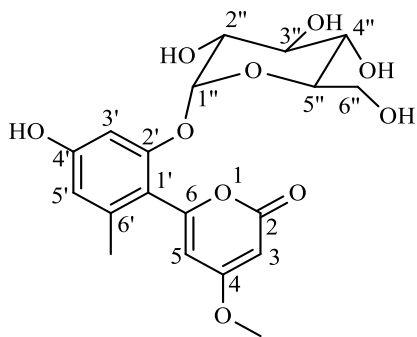
85

The ^{13}C NMR revealed 19 carbon resonance peaks (Table 4.6). The signals appearing between δ_C 77.0 to δ_C 60.6 along with proton signals correlating with them in HSQC spectrum revealed the presence of a glycoside moiety except for the anomeric carbon signal which appears at δ_C 100.7.

The HMBC spectrum shows ^3J correlation of the anomeric proton δ_H 4.82 (*d*, 1H, *J* = 7.73) to δ_C 156.5 (C-2′) which established the attachment of the glycoside moiety to the O-aglycone. Methylation of the aryl ring was confirmed by NMR signals at δ_H 2.14/δ_C 20.3 which shows correlation to C-1′, 5′ and 6′. The deshielded singlet peak at δ_H 9.89 corresponds to the hydroxyl group proton resonance and its correlation with δ_C 100.2 and δ_C 110.7 was used to confirm the assignments in the aryl moiety. Compound **85** was thus identified as aloenin, a common metabolite in the genus aloe after close examination of the HMBC correlations and in consultation with literature (Abd-Alla *et al.*, 2009; Hirata and Suga, 1978; Kazuo *et al.*, 1976)

Table 4.6: ^{1}H (600 MHz), ^{13}C (151 MHz) NMR data and HMBC (^2J and ^3J) correlations of hesperidin (**85**)

C-position	δ_C (ppm)	δ_H (m, H, *J*(Hz)	HMBC (^2J, ^3J)
2	164.1	-	
3	87.8	5.60 (d, 1H, *J* = 2.22)	C-2, 4, 5
4	171.0	-	
5	104.2	6.25 (d, 1H, J = 2.23)	C-1′, 3,4, 6,
6	157.9	-	
1′	113.4	-	
2′	156.6	-	
3′	100.2	6.50 (d, 1H, *J* = 2.16)	C-1′, 2′, 4′, 5′
4′	159.5	-	
5′	110.8	6.37 (d, 1H, *J* = 2.21)	C-4′, 1′, 3, 6′-Me
6′	138.9	-	
1″	100.8	4.82 (d, 1H, J = 7.73)	C-2′, 2″
2″	73.2	3.10, (m, 1H)	C11′, 5″
3″	77.1	3.26, (m, 1H)	C-1′, 5″,4″
4″	69.5	3.14 (m, 1H)	C-6″, 5″
5″	76.7	3.24 (m, 1H)	C-4″, 2″
6″	60.6	3.69 (m, 1H), 3.49 (m, 1H)	C-4″, 5″
4-OMe	56.2		C-4
4′-OH		9.83 (s, 1H)	C-3′, 4′, 5′
6′-Me	19.8	2.14 (*s*, 3H)	C-1′, 5′. 6′

4.1.2.3 Aloe-emodin (**86**)

Compound **86** was isolated as a yellow amorphous solid and identified as an anthraquinone derivative from UV (λ_{max} 293.71, 360.63, 415.83 and 532.92 nm), ^{13}C NMR peaks at δ_C 181.8 for C-10 and δ_C 192.1 for C-9 and ^{1}H NMR peaks at δ_H 11.93 (s, for 1-OH) and δ_H 12.00 (*s*, for 8-OH) (Table 4.7) (Danielsen *et al.*, 1992; Thomson RH, 2012)
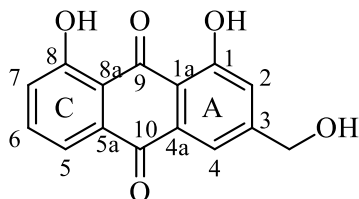
86

The ^{1}H NMR (Table 4.7) shows two downfield shifted proton resonance singlet peaks at δ_H 12.00 and δ_H 11.93 indicative of hydrogen bonded hydroxyl protons. An ABX spin system for three aromatic proton resonance peaks at δ_H 7.82 (t, J = 8.3, H-6), 7.73 (d, J = 8.3 Hz, H-5) and 7.40 (d, J = 8.3Hz, H-7) revealed a monosubstituted aromatic ring. Additionally, a pair of *meta*-coupled proton resonance peaks appear at δ_H 7.31/7.70 (d, J = 1.4Hz) indicative of protonation pattern in the di-substituted aromatic ring A of an anthraquinone derivative. HMBC spectrum shows [3]J correlation between proton resonance peaks at δ_H 7.73 and 7.07 with carbon resonance peak at δ_c 182.0 which confirms the protonation pattern in compound **86**. From biosynthetic considerations, methylation at C-3 was expected however, here, the methyl group is oxidized giving the oxymethlene group as observed in compound **86**. NMR signals at δ_H 4.65/δ_C 62.0 confirmed oxidation of the biogenetically expected methyl group. Compound **86** was identified as 1,8-dihydroxy-3-(hydroxymethyl)anthracene-9,10-dione, common name Aloe-emodin (**86**), a common secondary metabolite found in the genus aloe (Dagne *et al.*, 2000). The identity of **86** was further confirmed by comparing its TLC profile with an authentic sample.

Table 4.7: ^{1}H (600 MHz), ^{13}C (151 MHz) NMR data and HMBC (^{2}J and ^{3}J) correlations of **86**

C-position	δ_C (ppm)	δ_H (m, H, J(Hz)	HMBC (^{2}J and ^{3}J)
1	161.6	-	
1a	114.4	-	
2	120.6	7.31 (d, 2.4)	C-1a, 1, 3-$\underline{C}$H$_2$
3	153.7	-	
4	116.5	7.70 (s)	C-1a, 2, 10
4a	134.1	-	
5	118.8	7.73 (dd, 7.4, 2.4)	C-7, 8a, 10
5a	133.1	-	
6	136.5	7.82 (dd, 7.4, 2.4)	C-5a, 8
7	124.3	7.40 (dd, 7.4, 2.4)	C-5, 8a
8	161.3	-	
8a	115.9	-	
9	191.6	-	
10	181.4	-	
3-CH$_2$OH	62.0	4.65 (d, 4.75)	C-2, 3, 4
1-OH	-	11.93 (s)	C-1, 1a, 2
8-OH	-	12.00 (s)	C-8, 8a, 7

*4.1.2.4 Laccaic acid D-methyl ester (**87**)*

Compounds **87** was isolated as a red-crystalline solid and identified as an anthraquinone derivative from its UV (λ_{max} (MeOH) 293.71, 360.63, 415.83 and 532.92 nm), ^{13}C NMR: δ_C 182.4 for C-10 and 188.7 for C-9, 20.3 for 8-CH$_3$ and ^{1}H NMR: δ_H 13.01 (s, for 1-OH) and δ_H 2.60 (s, for 8-CH$_3$) (Table 4.8) (Danielsen *et al.*, 1992; Thomson RH, 2012).
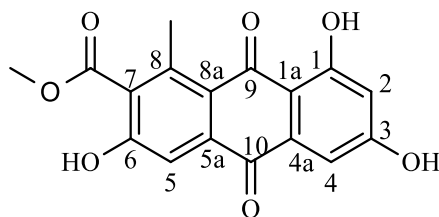
87

The ^{1}H NMR (Table 4.8) indicates a singlet peak at δ_H 7.60 which shows correlations with carbon resonance peaks at δ_C 182.4 (C-10), 158.9 (C-6), 137.0 (C-7), 130.2 (C-5a), and 123.2 (C-8a) in HMBC spectrum suggesting a trisubstituted ring. The presence of the biogenetically expected aromatic methyl proton resonance peak at δ_H 2.61/δ_C 20.3 which shows HMBC correlation with C-7 made it possible to place the methyl group in the trisubstituted ring C. In addition, a set of *meta*-coupled proton signals at δ_H 7.07/6.60 (*d*, *J* = 2.4 Hz) suggested a monosubstituted ring-A. NMR signals at δ_H 3.92/δC 52.4 and δC 167.7 (for the ester carbonyl) were used to infer the presence of the methyl ester moiety. Based on the spectral information as discussed and in consultation with other literature, this compound was identified as methyl 3,6,8-trihydroxy-1-methyl-9,10-dioxo-9,10-dihydroanthracene-2-carboxylate; trivial name laccaic acid D-methyl ester previously reported in *Aloe graminicola* (Yenesew *et al.*, 1993).

Table 4.8: ^{1}H (600 MHz), ^{13}C (151 MHz) NMR data and HMBC (^2J and ^3J) correlations for **87** in DMSO-d$_6$

C-position	δ_C (ppm)	δ_H (m, H, J(Hz))	HMBC (^2J and ^3J)
1	164.4	-	
1a	110.2	-	
2	108.3	6.60 (d, J = 2.43)	C-1a, 1, 4
3	158.2	-	
4	107.2	7.07 (d, J =2.42)	C-1a, 2, 10
4a	137.3	-	
5	112.0	7.60 (s)	C-7, 8a, 10
5a	133.3	-	
6	164.1	-	
7	129.6	-	
8	140.5	-	
8a	122.5	-	
9	187.7	-	
10	181.8	-	
1-OH	-	13.00 (s)	C-1a, 1, 2
7-C=O	167.2	-	
-OMe	52.4	3.92 (s)	
8-Me	19.7	2.61 (s)	C-7-<u>C</u>=O C-7, 8, 8a

*4.1.2.2 Aloesaponarin II (**88**)*

Compound **88** was isolated as a red crystalline solid. Like compounds **86** and **87**, compound **88** exhibited UV-Vis absorption maxima (λ_{max} (CHCl$_3$) nm: 282, 316, 386 and 412) indicative of anthraquinones (Dagne *et al.*, 2000). Characteristic NMR signals (δ_H 14.72 (brs) for 8-OH, δ_H 2.51/δ_c 25.0, δ_c 185.7 and δ_C184.4) indicate that compound **88** is an anthraquinone derivative.

CH$_3$ O OH

8 8a 9 1a 1

7 2

6 5a 10 4a 3

HO 5 4

O

88
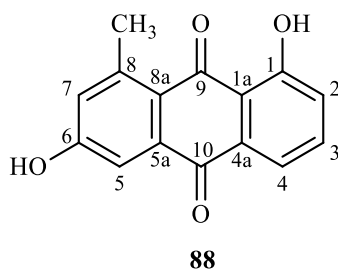
The ^{13}C NMR spectrum (Table 4.9) revealed fifteen carbon signals consisting of five (5) aromatic methine carbon atoms, seven aromatic quaternary carbons, two carbonyl carbons and a methyl group carbon similar to that of chrysophanol. The ^{1}H-NMR (Table 4.9) shows an ABX spin system corresponding to proton resonance peaks at δ_H 7.49 (dd, J = 7.9, 1.6 Hz, H-4), δ_H 7.50 (t, J = 7.9 Hz, H-3), and δ_H 7.14 (dd, J = 7.9, 1.6 Hz, H-2) and this protonation pattern indicates a monosubstituted ring A. Additionally, a pair of *meta*-coupled proton resonance peaks appear at δ 6.16/6.72 (*d*, J = 2.4 Hz). $^3J_{C,H}$ correlations between H-5/H-4 and C-10 along with H-H COSY correlations were used to confirm the protonation pattern. A biosynthetically expected methyl substituent is evident at δ_H 2.51/δc 25.0 whose placement is consistent with HMBC correlation between δ_H 2.51 and δ_C 128.7 for C-2 and also correlation between proton signal at δ_H 6.16 9 (H-2) with carbon resonance peak at δ_C 25.0. This compound was identified as 3,8-dihydroxy-1-methylanthracene-9,10-dione, trivially called aloesaponarin II. It has already been reported in other *Aloe* species (Abdissa *et al.*, 2017; Dagne *et al.*, 1994)

Table 4.9: [1]H (600 MHz), ^{13}C (151 MHz) NMR data and HMBC (^2J and ^3J) correlations for aloesaponarin II (**88**) in DMSO-d_6

C-position	δ_C (ppm)	δ_H (m, J(Hz))	HMBC (^2J, ^3J)
1	162.0		
1a	118.3		
2	124.0	7.14 (dd, 7.9, 1.6)	C-4
3	133.9	7.50 (t, J = 7.9)	C-1, 4a,
4	117.3	7.49 (dd, J = 7.9, 1.6)	C-1a, 2, 10
4a	133.4		
5	119.0	6.72 (d, J = 2.4)	C-5a, 7, 10
5a	133.0		
6	162.1		
7	128.7	6.16 (d, J =2.4)	C-5, 8a, 8-$\underline{C}H_3$
8	145.5		
8a	111.7		
9	184.4	-	
10	185.7	-	
1-OH		14.72 (brs)	C-1a, 1, 2
8-CH$_3$	25.0	2.51 (s)	C-7, 8, 8a

4.1.2.4 Miscellaneous compounds from A. tororoana

Beta-sitosterol (**5**) and stigmasterol (**47**) are additional compounds that were isolated from *A. tororoana*. Their structures were confirmed by comparing their NMR data (1D and 2D) with previously published literature (Jaju *et al.*, 2010; Suttiarporn *et al.*, 2015) and comparing their TLC profiles with authentic samples. The main difference between compound **5** and **47** is that in stigmasterol, there is an additional double bond at C-22.

4.1.3 Characterization of Secondary Metabolites from Aloe schweinfurthii var. laborwana

Seven compounds were isolated from *A. schweinfurthii* using column chromatography: Chrysophanol (**89**), chrysalodin (**90**), aloesaponarin 1 (**91**), 5-allyl-3-methoxybenzene (**92**) and droserone (**93**), β-sitosterol (**5**) and stigmasterol (**47**). The compounds were characterized basing on their physicochemical properties and spectroscopic data as described below.

4.1.3.1 Chrysophanol (**89**)

Compound **89** was isolated as a red solid. It gave a yellow fluorescent spot on TLC which turns red when exposed to ammonia vapor suggesting the presence of hydrogen bonded hydroxyl group in a quinone (Negera, 2014). UV (λ_{max}, MeOH: 213, 287, 323, 396) and ^{1}H NMR signals at δ_H 12.04 (for 8-OH), 11.93 (for 1-OH) and 2.44 (for 3-CH$_3$), ^{13}C NMR signals at δ_C 192.9 (for C-9), 182.0 (for C-10) and 22.4 (for 3-CH$_3$) established the basic structure of compound **89** to be an anthraquinone (Danielsen *et al.*, 1992; Thomson RH, 2012)

89
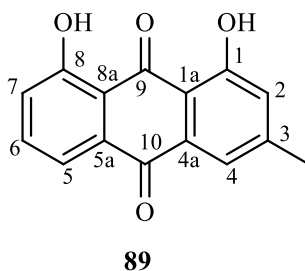
The ^{13}C NMR spectrum (Table 4.10) revealed fifteen carbon signals consisting of five (5) aromatic methine carbon atoms, seven (7) aromatic quaternary carbons, two carbonyl carbons and a methyl group carbon similar to aloesaponarin II (**88**). In the ^{1}H NMR spectrum (Table 4.10), three mutually coupled protons exhibiting an ABX spin system are visible at δ_H: 7.75 (dd, J = 8.4, 1.14 Hz, H-5), 7.74 (t, J = 8.4 Hz, H-6) and 7.25 (dd, J = 8.4, 1.38 Hz, H-7). Additionally a set of *meta*-coupled proton resonances appear at δ_H 7.66 (d, J = 1.40 Hz, H-4) and δ_H 7.06 (d, J = 1.40 Hz, H-

2). Proton resonance due to biogenetically expected methyl group appears at δ_H 2.47 (s, 3H). Two down field shifted proton signals at δ_H 12.04 and δ_H 11.92 indicated hydrogen bonded hydroxyl groups. The placement of the hydroxyl groups was established by their correlations (^3J and ^2J) to C-7, C-8a, C-2 and C-1a respectively in the HMBC spectrum. Correlation of proton signals at δ_H 7.75 (H-5) and δ_H 7.66 (H-4) with carbon δ_C 182.0 (C-10) made it possible to completely propose the structure of this compound and thus identified as chrysophanol. This compound was further confirmed by comparing its TLC profile with an authentic sample. Compound **89** is a common metabolite found in the family Asphodelaceae and other higher plants (Dagne *et al.*, 2000).

Table 4.10: ^{1}H (600 MHz), ^{13}C (151 MHz) NMR data and HMBC (^2J and ^3J) correlations for chrysophanol (**89)** in DMSO-d$_6$)

C-position	δ_C (ppm)	δ_H (m, H, J(Hz)	HMBC (^2J, ^3J)
1	163.0	-	
2	124.7	7.06 (d, J = 1.40)	C-4, 1a
3	150.0	-	
4	121.5	7.66 (d, J = 1.23)	C-2, 1a
4a	133.6	-	
5a	134.0	-	
5	120.0	7.75 (dd, J = 7.45, 1.14)	C-7, 10, 8a
6	137.3	7.74 (t, J = 8.19, 7.76)	C-8, 5a
7	124.5	7.25 (dd, J = 8.39, 1.2)	C-5, 8a
8	162.7	-	
8a	116.2	-	
9	192.9	-	
10	182.0	-	
1a	114.0		
1-OH		11.92 (s)	C-1, 1a, 2
8-OH		12.04 (s)	C-8, 8a, 7
3-CH$_3$	22.4	2.47 (s)	C-2, 3, 4

4.1.3.2 Chrysalodin (**90**)

Compound **90** was isolated as a UV-active (254 nm) red crystalline solid. It produced a yellow spot on TLC which turned red on exposure to ammonia vapor suggesting it could be an anthraquinone derivative. Characteristic NMR signals δ_H (12.25 (s, 1H), 12.18 (s, 1H), 12.01 (s, 1H), 11.47 (*s*, 1H), 2.23 (*s*, 3H)) and δ_C (192.6, 191.7, and 181.0) (Table 4.11) revealed an anthraquinone derivative (Danielsen *et al.*, 1992; Thomson RH, 2012). In addition, nine aromatic proton resonance peaks appear at $\delta_{H:}$ 8.66, 7.86, 7.50, 7.38, 7.06, 6.93, 6.78, 6.75 and 6.63 ppm suggesting the molecule to be a dimeric anthraquinone. This suggestion was further reinforced by the presence of three carbonyl carbon resonance peaks at δ_C 192.6, 191.7 and 181.0 in the ^{13}C NMR spectrum.

90
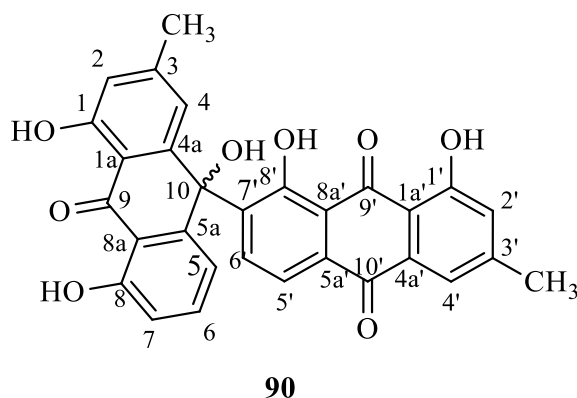
The ^1H NMR spectrum of one half of the molecule revealed an ABX spin system for three mutually coupled aromatic proton resonance peaks at δ_H 7.49 (*t*, *J* = 8.20 Hz, H-6), 6.93 (*dd*, *J* = 8.20, 0.91 Hz, H-7) and 6.78 (dd, *J* = 8.20, 0.98 Hz, H-5). Additionally, *meta*-coupled proton signals appear at $\delta_{H:}$ 6.75 (d, 1H, H-2) and 6.63 (d, 1H, *J* = 1.21 Hz, H-4) interspaced by a biogenetically expected methyl group whose signal appears at δ_H 2.22 in the ^1H NMR spectrum. Correlations between signals at δ_H 12.25 with δ_C 116.4 (C-7) and between proton signal at δ_H 12.18 with δ_C 116.7 (C-2) in HMBC spectrum were used to verify the structural assignments in this half of compound **90**.

The foregoing NMR data is consistent with the structure of chrysophanol anthrone leaving C-10 as the point of attachment to the next monomer.

In the next monomer, a set of *ortho*-coupled aromatic proton signals appear at δ_H: 8.66 (d, 1H, $J =$ 7.9 Hz, H-6′) and 7.86 (d, 1H, $J =$ 7.9Hz, H-5′). An additional pair of *meta*-coupled aromatic proton resonances interspaced by a methyl group appear at δ_H 7.38 (d, 1H, $J =$ 1.49 Hz, H-4′) and 7.06 (d, 1H, H-2′). The correlation of protons H-5′ and H-4′ with the carbonyl carbon at δ_C 181.0 in addition to two hydrogen bonded hydroxyl groups in this monomer leaves only C-7′ for attachment to the other monomer. Moreover, proton H-6′ shows correlation to C-10 in the other monomer which confirms that C-7′ and C-10 are the points of attachment of the two monomers. This compound was identified as 10-(chrysophanol-7'-yl)-10-hydroxychrysophanol-9-anthrone (trivial name: chrysalodin) which was previously isolated from the roots of *Kniphofia foliosa* Hoechst (Asphodelaceae) and *Kniphofia ensifolia* (Dai *et al.*, 2014; Wube *et al.*, 2005).

Table 4.11: ^1H (600 MHz), ^{13}C (151 MHz) NMR data and HMBC (^2J and ^3J) correlations for chrysalodin **(90)** in DMSO-d_6)

C-position	δ_C (ppm)	δ_H (ppm, J in Hz)	HMBC ^2J and ^3J
1	161.3	-	-
1a	112.2	-	-
2	116.7	6.75 (dd, J = 8.0, 1.1)	C-4, 1a, 3-CH$_3$
3	148.4	-	-
4	120.4	6.63 (s)	C-2, 10, 1a
4a	147.7	-	
5	119.4	6.78 (dd, J = 8.0, 1.1)	C-10, 8a, 7
5a	147.8	-	-
6	136.9	7.49 (t, J = 8.0)	C-8, 5a
7	116.4	6.93 (dd, J = 8.3, 1.1)	C-8a, 5
8	161.0	-	-
8a	114.2	-	-
9	192.6	-	-
10	69.5	-	-
1-OH		12.18 (s)	C-1, 1a, 2
8-OH		12.25 (s)	C-8, 8a, 7
-CH$_3$	21.7	2.33 (s)	C-2,3,4
1'	161.4	-	-
1a'	113.6	-	-
2'	123.9	-	-
3'	149.2	-	-
4'	120.4	7.06, (d, 1.8)	
4a'	132.3	-	-
5'	118.9	7.38 (d, 1.8)	C-10', 2', 1a', 3'-CH$_3$
5a'	133.8	-	-
6'	133.9	7.86 (d, 8.0)	C-10', 7', 6' 8a', 5a'
7'	141.7	-	-
8'	157.7	8.66 (d, 8.0)	C-8', 2', 10', 4a'
8a'	115.5	-	-
9'	191.7	-	-
10'	181.0	-	-
1'-OH		11.47 (s)	C-1', 2', 1a'
8'-OH		12.01 (s)	C-8', 7', 8a'
-CH$_3$'	21.5	2.22 (s)	C-3', 2', 4'

4.1.3.3 Aloe saponarin 1(**91**)

Compound **91** was isolated as red crystalline solid, the TLC spot gave a yellow fluorescent spot in UV light (254 nm) and turned red on exposure to ammonia vapor indicating the presence of an anthraquinone derivative. Characteristic NMR signals (Table 4.12): ^{1}H NMR δ_H (12.78 for 1-OH and 2.59 for 8-CH$_3$) and ^{13}C NMR δ_C (181.8 for C-10 and 189.7 for C-9) are indicative of an anthraquinone derivative.
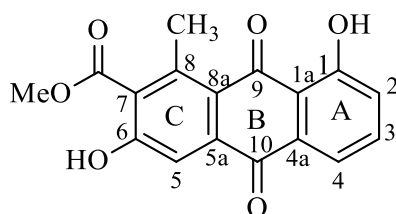
91

The ^{13}C NMR spectrum (Table 4.12) revealed seventeen carbon signals consisting of four aromatic methine carbon atoms, eight aromatic quaternary carbons, three carbonyl carbons, and two methyl group carbon atoms. The ^{1}H NMR shows three mutually coupled protons with an ABX spin system at, δ_H 7.60 (dd, J = 8.4, 1.2 Hz, H-5), 7.71 (t, J = 8.4 Hz, H-7), and 7.31 (dd, J = 8.4, 1.2 Hz, H-6). Additionally a singlet proton resonance peak at δ_H 7.59 (s, H-4) suggested a trisubstituted aryl ring. The placement of the protons H-5 and H-4 is consistent with their ^3J correlations with C-10 in HMBC spectrum. A biogenetically expected methyl moiety resonates at δ_H 2.59 and a methoxy group at δ_H 3.88. The correlation of the methoxy moiety with carbon resonance at δ_H 167.2 in HMBC spectrum suggested an ester group. The compound was identified as 3,8-dihydroxy-1-methyl-9,10-dioxo-dihydro-anthracene-2-carboxylic acid methyl ester, common name aloe saponarin I previously isolated from *Aloe saponaria* (Dagne *et al*., 2000).

Table 4.12: ^{1}H (600 MHz), ^{13}C (151 MHz) NMR data and HMBC (^2J and ^3J) correlations of aloesaponarin I (**91**) in DMSO-d$_6$)

C-position	δ$_C$ (ppm)	δ$_H$ (m, J(Hz)	HMBC (^2J, ^3J)
1	161.4	-	
1a	116.7		
2	124.4	7.31 (dd, J = 8.33, 1.14)	C-4, 1a
3	136.1	7.71 (t, J = 8.26, 7.82)	C-1, 4a
4	118.1	7.60 (dd, J = 7.44, 1.11)	C-2, 10, 1a
4a	132.3	-	
5a	136.7	-	
5	112.0	7.59 (s)	C-7, 10, 8a
6	158.8		
7	129.6		
8	141.0	-	
8a	122.5	-	
9	189.2	-	
10	181.8	-	
8-CH$_3$	19.9	2.59 (s)	C-8, 8a, 7
1-OH		12.78 (s)	C-1, 1a, 2
7-<u>C</u>O	167.2	-	
O<u>Me</u>	52.5	3.88 (s)	C-7-<u>C</u>=O

*4.1.3.4 5-allyl-3-methoxybenzene-1,2-diol (**92**)*

Compound **92** was isolated as blue-fluorescent (UV: 254 nm) yellow solid. The compound was identified as an aryl derivative based on the following NMR data (Table 4.13): ^{13}C/^{1}H NMR along with HSQC spectrum revealed 10 signals consisting of four quaternary aromatic carbon atoms at δ$_C$ 132.2 (C-5), 133.3 (C-1), 146.4 (C-2) and 149.5 (C-3), two aromatic methine carbons at δ$_C$ 104.8/δ$_H$ 6.28 (overlap, 1H) and δ$_C$ 110.0/ δ$_H$ 6.28 (overlap, 1H), two olefinic carbon atoms at δ$_C$

115.4/δ_H 5.00 (m, 2H) and δ_C 139.3/δ_H 5.90, (m, 1H), one methylene group at δ_C 41.0/δ_H 3.21(d, J = 6.82) and a methoxy group δ_C 56.5/ δ_H 3.78 (s).
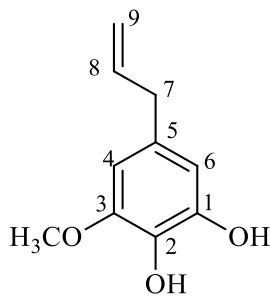
92

The H-H COSY spectrum shows coupling correlations between olefenic protons at δ_H 5.90, 5.00 and the methylene proton at δ_H 3.21 which therefore established the presence of the allyl moiety; $CH_2=CH-CH_2-$. ^3J correlations of the aromatic protons H-4 and H-6 with carbon signal at δ_C 41.0 (C-7) allowed placement of the propenyl substituent at C-5. Furthermore, ^2J and ^3J correlations of H-4 and H-6 with the oxygenated carbon signals δ_C:133.3, (C-1), 146.4 (C-2) and 149.5 (C-3) were used to establish the oxygenation pattern of the aryl ring. Compound **92** was thus identified as 5-allyl-3-methoxybenzene, previously isolated from *Bulbin capitate (*Bezabih *et al.,* 1997*), although this is the first isolation from the species *A. schweinfurthii*.

Table 4.13: ^{1}H (600 MHz), ^{13}C (151 MHz) NMR data and HMBC (^2J and ^3J) correlations of **92** in DMSO-d$_6$

C-position	δ_C (ppm)	δ_H (m, H, J (Hz))	HMBC (^2J, ^3J)
1	133.3	-	-
2	146.4	-	-
3	149.5	-	-
4	104.8	6.28 (1H, Overlap)	C-2, 3, 5, 6, 7
5	132.2	-	-
6	110.0	6.28 (1H, Overlap)	C-1, 2, 4, 5, 7
7	41.0	3.21 (d, 2H, J = 6.82)	C-4, 5, 6, 8, 9
8	139.3	5.90(m, 1H)	C-5, 7
9	115.4	5.02 (m, 2H)	C-7
3-OMe	56.5	3.78 (s, 3H)	C-3

4.1.3.5 Droserone (2,5,8-trihydroxy-3-methylnaphthalene-1,4-dione) (**93**)

This compound was isolated as red crystals. Unlike the anthraquinones discussed so far, it was identified as a naphthoquinone derivative based on the following NMR spectroscopic features. ^{13}C NMR (Table 4.14) revealed signals at δ_C: 182.5 (for C-1) and 189.3 (for C-4) indicative of carbonyl carbons of the quinone moiety in addition to six signals corresponding to six (6) aromatic carbon atoms and a biogenetically expected up-field methyl carbon signal at δ_C 8.3 (Thomson RH, 2012). The ^{1}H NMR shows two deshielded proton signals (δ_H 11.46 and 12.79) corresponding to the two hydrogen bonded hydroxyl groups. Additionally, the ^{1}H NMR reveals signals due to *ortho*-coupled protons at δ_H 7.18/7.28 (*d*, 1H, J = 9.8 Hz, H-6/H-7). The assignment of these proton signals was confirmed by ^3J correlations of δ_H 11.46 with δ_C 127.8 (C-7) and δ_H 12.79 with δ_C 131.6 (C-6) and ^2J correlations of δ_H 7.18 with δ_C 157.4 (C-5) and δ_H 7.28 with δ_C 154.3 (C-8) in HMBC spectrum. Compound **93** was identified as 2,5,8-Trihydroxy-3-methyl-[1,4] naphthoquinone, known by several other names as 3,8-Dihydroxyplumbagin, 5-Hydroxydroserone, 8-Hydroxydroserone and

hydroxydroserone. It was previously isolated from the roots of *Aloe deweii* (Abdissa *et al.*, 2014) and *in vitro* cultures of *Drosera gigantean (Budzianowski, 2000).*
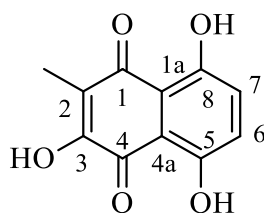
93

Table 4.14: ^{1}H (600 MHz), ^{13}C (151 MHz) NRM data and HMBC (^2J and ^3J) correlations of 2,5,8-trihydroxy-3-methylnaphthalene-1,4-dione (**93**) in DMSO-d$_6$

C-position	δ_C (ppm)	δ_H (m, H, *J*(Hz))	HMBC (^2J, ^3J)
1	189.3		
1a	110.6		
2	121.9		
3	157.9		
4	182.5		
4a	111.1		
5	157.4		
6	131.6	7.18 (d, 9.8)	C-5
7	127.8	7.28 (d, 9.8)	C-8
8	154.3		
2-CH$_3$	8.30	2.08 (s)	C-1, 2, 3
3-OH		7.50 (s)	
5-OH		12.79 (s)	C-5, 6, 4a
8-OH		11.46 (s)	C-3, 7, 1a

4.1.4 Characterization of Secondary Metabolites from Taberneamontana ventricosa

Extracts from *T. ventricosa* upon chromatographic separation yielded nine compounds consisting of five (5) iboga type indole alkaloids; ibogamine (**96**), 10-hydroxyibogamine (**101**), 10-hydroxycoronaridine (**100**), voacristine (**98**), 3-Ketopropylcoronaridine (**94**), and one vobasinyl indole alkaloid; vobasine (**95**), ursolic acid (**99**), a polyol; quebrachitol (**97**) and stigmasterol (**47**). The structures of these compounds were elucidated by analysis of their physicochemical properties and spectral data as discussed below.

4.1.4.1 Iboga type monoterpene indole alkaloids (**94, 96, 98, 100 and 101**)

Compound **96,** a pale yellow oily liquid produced a red spot on TLC when sprayed with Dragendorff's reagent suggesting an alkaloid. The UV spectrum (λ_{max}: 205, 233, and 299 nm), along with the NMR data (Table 4.15) suggested **96** to be an indole alkaloid. (Lim *et al.*, 2015; Zhang *et al.*, 2015). The ^{1}H NMR spectrum revealed broad singlet at δ_H 7.84 ppm characteristic of the indole N-H proton (Paterna *et al.*, 2016) in addition to four signals corresponding to four aromatic proton resonance signals at δ_H:7.46 (d, H-9,), 7.24 (d, H-12), 7.14 (td, H-11) and 7.08 (td, H-10). This shows that the indole A-ring is unsubstituted. Analysis of the ^{13}C NMR data (Table 4.15) along with HSQC (Appendix 13.4) revealed signals corresponding to four quaternary carbons at δ_C 109.4 (C-7), 130.1 (C-8), 135.1 (C-13) and 142.5 (C-2), four aromatic methine carbon at δ_C: 110.3 (C-12), 118.1 (C-9), 119.2 (C-10), and 121.1 (C-11), four aliphatic methine carbons at δ_C: 26.9 (C-14), 42.2 (C-16), 42.2 (C-20) and 58.0 (C-21), six methylene carbons in the secologanin moiety of the molecule and one methyl carbon signal at δ_C 12.1. The connectivity of the indole moiety to the secologanin moiety was established through HMBC correlations where, the two diastereotopic proton resonance peaks at δ_H 3.33 and 2.69 (H-6) show ^3J and ^2J correlations with δ_C 142.5 (C-2) and δ_C 109.4 (C-7) respectively. Similarly, H-6 correlates with C-5. Other

structural features were confirmed by analysis of HMBC spectrum (Appendix 13.5). Compound **96** was identified as ibogamine.

Compounds **94, 98, 100 and 101** (Figure 4.1) showed similar physicochemical properties to **96.** In all cases, the UV-spectrum (λ_{max}208, 227 and 289 nm) revealed a characteristic absorption pattern of an indole chromophore. Comparison of ^{1}H and ^{13}C NMR spectroscopic data revealed th*et al*l the compounds shared similar spectroscopic information except for the difference in the connectivity of functional groups. Unlike **96**, the ^{1}H NMR spectrum of **101** revealed features of a mono-substituted indole A-ring proton resonance peaks at δ_H 7.00 (d, $J = 8.0$ Hz, H-12), 6.73 (d, $J = 2.4$ Hz, H-9) and 6.54 (dd, $J = 8.0, 2.4$ Hz, H-11). The position of the substituent was determined by analyzing HMBC spectrum (Appendix 14.5) which revealed ^2J and ^3J correlations of proton resonance signals at δ_H 7.07 (H-11), 7.46 (H-9) and 7.25 (H-12) with δC 151.0 (C-10). The signals of H-9 and H-11 are up-field shifted, which provided evidence of oxygenation at C-10. The connectivity in the secologanin moiety of **101** is similar to that of **96**. Compound **101** was thus identified as 10-hydroxyibogamine. The principle difference between compound **101** and **100** is the presence of additional signal in the ^{1}H NMR spectrum at δ_H 3.71 and in the ^{13}C NMR spectrum at δ_C 175.7 and 52.6 which reveal a methyl ester moiety. The position of the methyl ester moiety in **100** was established from the HMBC spectrum (Appendix 15.5) which revealed ^3J correlation of proton signals at δ_H 2.57 (H-17) and δ_H 2.80 (H-21) with δ_C 175.7, thus, allowing placement of the methyl ester moiety at C-16. Compound **100** was identified as 10-hydroxycoronaridine. Compound **98** shows similar spectral data to compound **100**. However, in **98,** the NMR data (Table 4.15 and 4.16) showed additional signals at δ_H 3.88 (s**,** 3H)/δ_C 52.8 suggesting a methoxy substituent in **98.** The position of the methoxy substituent was established at C-10 from HMBC spectrum (Appendix 16.5) which revealed correlations of H-9, H-11, H-12,

and methoxy proton signal at δ_H 3.88 with carbon signal at δ_C 154.3 (C-10). In **98** C-19 is deshielded (δ_C 71.3) suggesting oxygenation at C-19. Compound **98** was identified as voacristine.

In compound **94**, the ^{1}H NMR spectrum revealed signals corresponding to four aromatic protons at δ_H 7.46 (d, 8.0 Hz, H-9), 7.08 (td, 8.0, 1.1 Hz, H-10, 7.14 (td, 8.0, 1.1 Hz, H-11) and 7.24 (d, 8.0 Hz, H-12) suggesting an un-substituted indole A-ring similar to **96.** The NMR data also revealed signals at δ_H 3.70/δ_C 52.7 and δ_C 175.6 indicating a methyl ester moiety similar to compounds **96** and **100.** The difference between **94** and the rest of the iboga type alkaloids discussed is the presence of additional signals in the NMR data (Table 4.15 and 4.16) at δ_H 2.70/2.52 (overlap), 2.11 (s) and δ_C 46.6, 31.0, 208.7 and δ_C 208.7 was. Analysis of the HMBC spectrum (Appendix 17.5) revealed correlation of δ_H 2.70, 2.52 and 2.11 with δ_C 208.7, indicating the presence of a propyl ketone group. The placement of the propyl ketone group was established from H-H COSY (Appendix 17.3) and HMBC spectra, where, H-H COSY revealed that δ_H 3.33 (H-3) coupled with δ_H 2.52 and HMBC revealed ^3J correlation of δ_H 3.33 (H-3) with δ_C 208.7. Compound **94** was thus identified as 3-ketopropylcoronaridine. 10-Hydroxycoronaridine (**100**) in addition to seven other alkaloids were previously isolated from *T. ventricosa* (Schripsema *et al.*, 1986). On the other hand, compounds **94, 96, 98,** and **101** were previously isolated from suspension culture of *T. elegans* (Van der Heijden *et al.*, 1989), nevertheless, this is their first isolation from *T. ventricosa.*
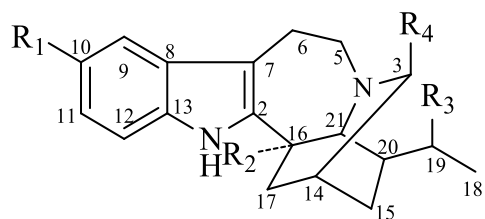
Compound	R1	R2	R3	R4
94	H	CO2Me	H	CH2COMe
96	H	H	H	H
98	OCH3	CO2Me	OH	H
100	OH	CO2Me	H	H
101	OH	H	H	H

Figure 4.1: Structures of iboga-type indole alkaloids from *T. ventricosa*

Table 4.15: ^{1}H NMR (600 MHz) data for compounds **94, 96, 98, 100** and **101** (δ in ppm and J in Hz)

Position	Compound 94	Compound 96	Compound 98	Compound 100	compound 101
3	3.33 (m)	3.00 (m)	3.02 (overlap)	2.90 (overlap)	3.04 (overlap)
		3.08 (m)	2.83 (d, 9.1)	2.80 (d, 8.8)	2.88 (dd, 11.8, 4.3)
5	3.28 (m)	3.34 (overlap)	3.48 (m)	3.36 (m,)	3.28 (m)
	3.21 (m)	3.13 (overlap)	3.16 (m)	3.19 (m)	3.03 (overlap)
6	3.20 (m)	3.33 (0verlap)	3.14 (overlap)	3.09 (m)	3.23 (overlap)
	3.01 (m)	2.69 (d, 15.6)	-	2.90 (m)	2.54 (overlap)
9	7.46 (d, 8.0)	7.43 (dd, 7.4, 1.3)	6.91 (d, 2.4)	6.88 (d, 2.4)	6.73 (d, 2.4)
10	7.08 (td, 8.0, 1.1)	7.03 (td, 7.4, 1.3)	-	-	-
11	7.14 (td, 8.1, 1.2	7.07 (td, 7.4, 1.3)	6.83 (dd, 8.7, 2.4)	6.71 (dd, 8.7, 2.4)	6.54 (dd, 8.0, 2.3)
12	7.24 (d, 8.0)	7.25 (d, 7.4)	7.15 (d, 8.8)	7.08 (d, 8.6)	7.00 (d, 8.0)
14	1.70 (m,)	1.85 (overlap)	2.04 (m)	1.26 (m)	1.79 (m)
15	1.28 (m,)	1.83 (overlap)	1.92 (m)	1.73 (m)	1.82 (m)
	-	1.24 (m)	1.56 (m)	1.12 (m)	1.16 (m)
16	-	1.68 (m)	-	-	2.94 (ddd, 11.8,4.3,1.9)
17	2.65 (m)	2.07 (m)	2.60 (m)	2.57 (dt, 15.0, 3.1)	2.05 (m)
	2.00 (m)	1.64 (m)	1.99 (m)	1.88 (overlap)	1.55 (m)
18	0.90 (t, 7.41)	0.91 (t, 7.2)	1.11 (d,J = 6.3)	0.89 (t, 7.4)	0.94 (t, 7.3)
19	1.59 (m)	1.58 (m	4.18 (m)	1.56 (m)	1.55 (m)
	1.25 (m)	1.47 (m)	-	1.43 (m)	1.48 (m)
20	1.44 (m)	2.87(s)	1.49 (m)	1.31 (m)	1.57 (m)
21	3.59 (overlap)	-	3.88 (overlap)	3.53 (s)	2.81 (s)
3-C$\underline{H_2}$COCH$_3$	2.71 (m)	-	-	-	-
	2.53 (m)	-	-	-	
3-CH$_2$COC$\underline{H_3}$	2.11 (s)	-	-	-	
N-H	7.82 (br. s)	7.70	7.73 (br. s)	7.65 (br. s)	
10-OCH$_3$	-	-	3.86 (s)	-	
16-CO$_2$Me	3.70 (s,)		3.74 (s)	3.71 (s)	

Table 4.16: ^{13}C NMR (151 MHz) data for compounds **94, 96, 98, 100 and 101** (δ in ppm)

C-position	Compound 94	Compound 96	Compound 98	Compound 100	Compound 101
2	136.5	142.5	136.6	137.8	143.9
3	55.2	50.1	51.2	51.4	50.9
5	51.4	54.6	52.3	53.4	55.7
6	22.0	20.9	21.6	22.1	21.4
7	110.0	109.4	109.6	109.8	108.2
8	128.7	130.1	128.9	129.6	131.4
9	118.4	118.1	100.7	103.2	103.0
10	119.2	119.2	154.3	149.3	151.0
11	122.0	121.1	112.3	111.4	111.0
12	110.3	110.3	111.3	110.9	111.6
13	135.5	135.1	130.6	130.6	130.1
14	30.7	26.9	26.7	27.3	27.7
15	38.4	32.4	22.9	32.0	32.9
16	54.8	42.2	54.1	55.1	41.8
17	37.6	34.5	37.0	36.5	35.0
18	11.7	12.1	11.4	11.6	12.3
19	26.9	28.2	71.3	26.7	28.6
20	26.7	42.2	39.5	39.1	43.2
21	58.2	58.0	59.9	57.6	59.4
3-CH$_2$	46.6		-	-	
3CH$_2$CO	208.7		-	-	
OCH$_3$	31.0		52.8	-	
16-CO	175.5		174.9	175.7	
-OCH$_3$	52.7		56.0	52.6	

4.1.4.2 Vobasinyl type indole alkaloids

Compound **95** was isolated as a pale yellow oily liquid with physicochemical properties similar to iboga type indole alkaloids. Positive HR-ESI-MS [M+H]$^+$ at m/z 353.1873 coupled with ^{13}C NMR spectrum was used to establish the molecular formula as $C_{21}H_{24}N_2O_3$ (Calculated for 352.4269). The base peak in the HRESIMS corresponds to the adduct ion [M+H+K]$^+$. UV spectrum (λ_{max} 205, 233, and 299 nm) was used to infer the presence of an indole ring. In the ^{1}H NMR data (Table

96

4.17), four signals at δ_H: 7.65 (d, 8.1), 7.26 (td, 8.1, 1.14), 7.07 (td, 8.1, 1.14), 7.29 (td, 8.1, 0.94) in addition to a broad singlet at δ_H 9.14 ppm pointed to an un-substituted indole ring. Analysis of the ^1H and ^{13}C NMR spectra along with 2D spectra (H, H-Cosy, HSQC, and HMBC) suggested this compound to be vobasinyl indole alkaloid. Thus, in addition to the established indole moiety, the ^1H NMR spectrum shows one methyl ester side group placed at C-16, one ethylene side group placed at δ_C 136.5 (C-20) and an *N*-methyl group. ^2J and ^3J bond correlations were used to establish the positions of the side chains (Table 4.17). Compound **95** was identified as vobasine previously isolated from *T. dichotoma* (Perera *et al*., 1983).

95
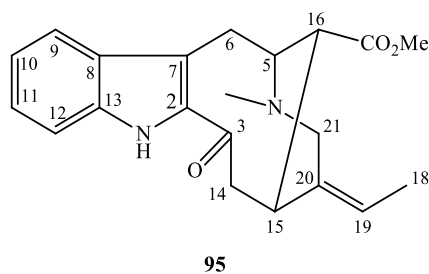
Table 4.17: Table 19: ^{1}H (600 MHz), ^{13}C NMR (151 MHz) data and HMBC correlations (^2J and ^3J) for vobasine (**95**)

C-position	δC	δH (m, J in Hz)	HMBC
2	134.1	-	
3	190.0	-	
5	57.2	3.84 (m)	21, 16, 15, 23
6	20.1	3.41 (m)	2, 8, 7, 5, 16
		3.32 (m)	2, 8, 7, 5, 16
7	120.6	-	
8	128.6	-	
9	120.9	7.65 (d, 8.11)	13, 11, 7
10	120.1	7.07 (overlap)	8, 12
11	126.5	7.26 (td, 6.8, 1.14)	13, 9
12	111.9	7.29 (td, 8.15, 0.94)	8, 10
13	136.4	-	
14	43.2	3.22 (m)	3, 2, 15, 16
		2.57 (m)	
15	30.5	3.65 (m)	20, 19, 5, 16, 14
16	46.8	2.73 (t, 3.45)	20, 5, 14, 15, 6
18	10.9	1.63 (d, 6.9)	
19	120.2	5.36 (qd, 6.8, 1.8)	
20	136.5		
21	51.8	3.72 (dt, 14.2, 2.3)	20, 19. 23, 16
		2.87 (d, 14.0)	
N-CH$_3$	46.1	2.49 (overlap)	
C=O	171.3		
N-H		9.14 (br. s)	
16- CO$_2$Me	50.	2.56 (s)	

4.1.4.3 Miscellaneous compounds from T. ventricosa

Ursolic acid (**99**)

Compound **99** was isolated as of white amorphous powder from the leave extract at 2% methanol in DCM. It stained purple with 5% H_2SO_4 in methanol suggesting it to be in the terpene class of compounds. The ^{1}HNMR (Table 4.18) gave characteristic peaks corresponding to two methyl proton doublets at δ 0.82 (H-29) and $δ_H$ 0.91(H-30) respectively. Additionally five methyl proton singlets resonating at $δ_H$ 0.68, 0.75, 0.87, 0.9 and 1.04 ppm respectively. Further characteristic

peaks corresponding to vinyl proton H-12 (δ_H 5.13, t, J = 3.24 Hz) and a doublet methine group resonating at δ_H 2.11 (H-18) established the skeletal structure as that of Ursane-12-ene (Mazumder *et al.*, 2013; Sashida *et al.*, 1992). Other characteristic peaks easily assignable to the structure were the hydroxyl group proton resonance at δ_H 4.34. A downfield shifted broad singlet at δ_H11.97 corresponding to hydroxyl proton of the carboxylic acid group. The positions of the additional protons were established by analysis of H-H COSY and HMBC spectra.

The ^{13}C NMR (Table 4.18) revealed peaks corresponding to 30 carbon atoms suggesting compound **99** to be a triterpene. The ^{13}C NMR spectrum consists of one carbonyl carbon resonance peak at δ_C178.8 (C-30) corresponding to the carboxylic acid group, six quaternary carbons with one being the olefinic quaternary carbon at δ_C 39.0 (C-4), 37.0 (C-10), 38.9 (C-12), 42.1 (C-14), 138.7 (C-13), and 47.5 (C-17), seven methine carbon atoms with one being the olefinic methine carbon at δ_C 77.3 (C-3), 55.2 (C-5), 47.3 (C-9), 125.0 (C-12) 52.8 (C-18), 38.8 (C-19), and 38.7 (C-20), nine methylene carbon atoms at δ_C 38.8 (C-1), 28.7 (C-2), 33.2 (C-7), 27.5 (C-6), 23.3 (C-11), 24.3 (C-16), 28.0 (C-15), 30.6 (C-21), and 36.8 (C-22) and seven methyl carbon atoms at δ_C 28.3 (C-23), 23.3 (C-27), 21.1 (C-30), 17.0 (C-29), 16.9 (C-26), 16.1 (C-24), and 15.2 (C-25). Compound **99** was identified as ursolic acid in further consultation with previously published data (Mazumder *et al.*, 2013; Sashida *et al.*, 1992).
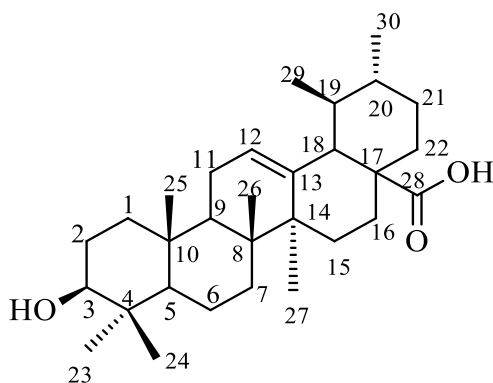
99

Table 4.18: ^1H (600 MHz), ^{13}C NMR (151 MHz) NMR data and HMBC correlations (^2J and ^3J) for ursolic acid (**99**) in DMSO-d$_6$.

C-position	δ_C (ppm)	δ_H (m, H, J(Hz)	HMBC (^2J, ^3J)
1	38.8	0.93 (m)	
2'	28.7	0.89 (m)	
3	77.3	3.02 (t)	C-2, 24
4	27.5	-	
5	55.2	0.62 (overlap)	
6	32.8	1.48/1.27 (m)	
7	32.7	1.44/1.27 (m, 2H)	
8	38.9	-	
9	46.8	1.45 (m)	
10	37.0	-	
11	23.7	1.54 (overlap)	C-9, 11, 14, 18
12	125.0	5.14 (t)	
13	138.7	-	
14	41.6	-	
15	28.0	1.36/1.08 (overlap)	
16	23.7	1.92/1.52 (m)	
17	47.0	-	
18	52.8	2.10 (d, 1H)	C-29, 28, 17, 16, 13, 12,
19	38.6	1.52 (overlap)	
20	38.5	1.52 (overlap)	
21	30.2	1.43/1.28 (m)	
22	36.4	1.55 (overlap)	
23	28.3	0.89 (s)	C-24, 5, 4, 3,
24	16.1	0.68 (s)	C-23, 5, 4, 3
25	15.2	0.87 (s)	C-9, 5, 1
26	16.9	0.75 (s, 3H)	C-14, 9, 7
27	23.3	1.04 (s, 3H)	C-15, 14, 13, 8
28	178.3	-	
29	17.0	0.82 (d, 3H)	C-20, 18
30	21.1	0.91 (overlap)	C-19

Quebrachitol (**97**)

Compound **97**, identified as a naturally occurring polyol was isolated alongside stigmasterol (**47**) from the stem bark of *T. ventricosa*. The ^{1}H NMR data (Table 4.19) showed seven sets of signals in the aliphatic region. ^{13}C NMR spectrum showed th*et al*l protons are bonded to oxygenated aliphatic carbon atoms. Analysis of H-H COSY spectrum indicated that H-1 (δ_H 3.48/δ_C 71.8) coupled with H-6 (δ_H 3.27/δ_C 80.1). H-6 coupled with H-5 (δ_H 4.14/δ_C 67.0) and H-4 (δ_H 3.93/δ_C 71.3). On the other hand, H-5 coupled with H-4 (δ_H 3.93/ δ_C 71.3) whereas H-4 coupled with H-3 (δ_H 3.60/δ_C 70.3) which in turn coupled with H-2 (δ_H 3.48/δ_C 72.7). The coupling pattern suggested that compound **97** was a cyclic hexane derivative.
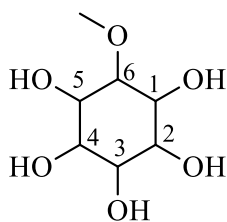
97

The presence of the signal at δ_H 3.32 (s, 3H)/δ_C 56.8 was indicative of a methoxy group whose assignment was guided by HMBC correlations of δ_H 3.27 (H-6) with δ_C 56.8 (-OMe) and correlation of δ_H 3.32 (-OMe) with δ_C 80.1 (C-6). H-6 further correlates with C-1 and C-5. Compound **97** was identified as quebrachitol (syn: ononitol, *D*-pinitol) (IUPAC name 6-methoxycyclohexane-1,2,3,4,5-pentaol). Quebrachitol was first reported to have been isolated from the bark of *Aspidosperma quebracho* in 1887 (McCance and Lawrence, 1933). It has been isolated from other plant species but here, it is reported in *T. ventricosa* for the first time.

Table 4.19: ^{1}H (600 MHz), ^{13}C (151 MHz) NMR data and HMBC correlations (^2J and ^3J) for compound **97** in MeOD

C-position	δ_C (ppm)	δ_H (m, H, J in Hz)	HMBC (^2J, ^3J)
1	71.8	3.48	C-6, 2
2	72.7	3.48	C-6, 4, 1
3	70.3	3.60	C-2
4	71.3	3.93	C-6, 5, 2, 1
5	67.0	4.14	C-6, 4
6	80.1	3.27	C-5, 1, OCH$_3$,
OCH$_3$	56.8	3.32 (s)	C-6

β-sitosterol (**45**) and *stigmasterol* (**47**)

Compounds (4**5**) and (**47**) were isolated as white amorphous solids. The ^{13}C NMR spectra for both compounds showed twenty nine peaks characteristic of a steroid skeleton, The main difference between compounds 4**5** and **47** is that the ^{13}C NMR spectrum of 4**5** shows two peaks at δ_C 140.8 and 121.8 corresponding to two olefinic carbons (C-5 and C-6) while the ^{13}C NMR spectrum of **47** shows the presence of peaks at δ_C 141.3, 121.8, 138.8 and 129.6 corresponding to four olefinic carbons (C-5, C-6, C-22 and C-23). Analysis of HSQC spectrum of 4**5** indicated one downfield shifted proton signal characteristic of an olefinic proton at δ_H 5.39 which correlates with δ_C 121.8. On the other hand, the HSQC spectrum of **47** revealed the presence of cross peaks corresponding to δ_C 121.8/δ_H 5.34, δ_C 138.8/δ_H 5.16 and δ_C 129.6/δ_H 5.03 which is consistent with the presence of two double bonds in **47**. Further examination of the HSQC spectrum of 4**5** shows the presence of nine methines, eleven methylenes, six methyl and three quaternary carbon atoms. Meanwhile, the HSQC spectrum of **47** shows the presence of eleven methines, 9 methylenes, six methyl and three quaternary carbon atoms. The NMR data, ^{13}C/^{1}H, (Table 4.20) of both compounds revealed the

presence of oxygenated sp^3 carbon and hydrogen at around δ_C 71.5 /δ_H 3.45. From the foregoing data along with consultation with literature (Chaturvedula and Prakash, 2012; Jaju *et al.*, 2010), compound 4**5** was identified to be β-sitosterol while **47** was identified to be stigmasterol respectively.

Table 4.20: ^{1}H (600 MHz) and ^{13}C NMR (151 MHz)data for β-sitosterol (4**5**) and stigmasterol (**47**) in CD$_2$Cl$_2$

	β-sitosterol (4**5**)		Stigmasterol (**47**)	
Position	δ_C (ppm)	δ_H (m, *J* in Hz)	δ_C	δH (m, J in Hz)
1	37.1	1.84/1.07 (m, 2H)	36.8	1.84/1.06 (m, 2H)
2	29.5	1.76/1.27 (m, 2H)	28.6	1.83/1.27 (m, 2H)
3	71.5	3.45 (m)	72.0	3.45 (m, 1H)
4	42.0	2.24 (m)	40.1	2.00/1.65 (m, 2H)
5	140.8	-	141.3	-
6	121.8	5.39(dt, 5.27,1.64)	121.8	5.34 (t, 1H)
7	31.7	1.99/1.53 (m, 2H)	32.3	1.97/1.50 (m, 2H)
8	31.5	1.80 (m)	32.1	1.79 (m)
9	50.0	0.94 (m)	50.6	0.93 (m)
10	36.3	-	36.8	-
11	20.9	1.49 (m)	23.4	1.25 (m)
12	39.6	2.03/1.18 (m)	40.1	2.01/1.17 (m, 2H)
13	42.1	-	42.7	-
14	56.6	1.00 (m)	57.2	1.00 (m)
15	25.8	1.18 (m)	26.4	1.18 (m)
16	24.1	1.58/1.08 (m, 2H)	28.6	1.84/1.27 (m, 2H)
17	55.9	1.12 (m)	56.4	1.12 (m)
18	11.4	0.69 (s, 3H)	11.9	0.69 (s, 3H)
19	18.4	0.93 (s, 3H)	19.6	1.01 (s, 3H)
20	35.9	1.37 (m)	42.7	2.23 (m, 1H)
21	18.6	0.82 (d, 3H)	21.2	1.02 (d, 3H)
22	33.7	1.35/1.03 (m, 2H)	138.8	5.16 (dd, 1H)
23	28.0	1.85/1.28 (m, 2H)	129.6	5.03 (dd, 1H)
24	45.7	0.95 (m)	51.6	1.53 (m)
25	29.0	1.68 (m)	29.5	1.67 (m)
26	19.0	1.00 (d, 3H)	19.6	1.01 (d, 3H)
27	19.3	0.84 (d, 3H)	19.9	0.85 (d, 3H)
28	22.8	1.25/1.28 (m, 2H)	24.6	1.57/1.07 (m, 2H)
29	11.5	0.85 (t, 3H)	11.9	0.68 (overlap)

4.2 Biological Activity of Isolated Compounds

Cytotoxicity of the isolated compounds was evaluated against seven cancer cell lines and three normal cells *in vitro*. The probable anticancer mechanism of action of the compounds was studied using *in silico* docking methods against molecular targets involved in the p53 pathway.

4.2.1 *In vitro Cytotoxicity of the Isolated Compounds*

The results of cytotoxicity investigations of the isolated compounds against selected cell lines are presented in Table 4.21. With reference to the proposed limits of cytotoxicity of pure secondary metabolites in the literature (Kuete and Efferth, 2015), several of the compounds that were tested were largely inactive against the tested cancer cells. β-sitosterol (**5**) was moderately active against breast cancer cells, BT549 (IC$_{50}$ 22.2 μM) but it was inactive against other cell lines tested. Dihydrochelerythrine (**81**) inhibited viability of liver cancer (HCC) cells (IC$_{50}$ 21.2 μM) and breast cancer (BT549) cells, (IC$_{50}$ 8.9 μM) but it was inactive against RCC-897-0, MCF-7 cancer cells and immortalized mammary cells. Sesamin (**82**) exhibited moderate inhibitory activity against BT549 cancer cells (IC$_{50}$ 47.6 μM). Hesperidin (**84**) exhibited low inhibitory activity against A549 and HeP2 cells (IC$_{50}$ 64.8 and 67.6 μM respectively) but it was significantly toxic to immortalized lung cells (BEAS, IC$_{50}$ 7.1 μM) and normal liver cell LO2 (IC$_{50}$ 30.6 μM). Ursolic acid (**99**) exhibited strong inhibitory activity against A549 cells (IC$_{50}$ 6.6 μM). Chrysophanol (**89**) was highly active against liver cancer (HCC) cells (IC$_{50}$ 2.4 μM) while voacristine (**98**) exhibited moderate inhibitory activity against liver cancer (HepG2) cells with IC$_{50}$ 23.0 μM. It is worth noting that cancer cell inhibitory activities of sesamin (**82**) against lung carcinoma (A549) and pancreatic carcinoma (MIA-PaCa) cells with IC$_{50}$ values of 37.46 and 34.04 μg/mL have been previously reported (Deng *et al.*, 2013). Similarly, skimmianine (**83**) is reported to inhibit proliferation of acute lymphoblastic leukemia cancer cell lines (Jurkat), HEP-2, KG-1a and RAJI.

Whereas, previous studies described in the review by Garg *et al* (2001) indicated that hesperidin (**84**) is considered generally safe, significant toxicity was observed against normal lung and liver cells in this study. There are limited reports on the toxicity of hesperidin (**84**) against normal cells. For instance, only slight side effects were reported in placebo experiments cited in the same review (Garg *et al.*, 2001). It has been shown to exert cytotoxic activity against human melanoma (HT-144) and breast cancer (MCF-7) cells with IC_{50} of 11 µM. The high toxicity of hesperidin (**84**) against normal lung (BEAS) and liver (LO2) cells indicates that hesperidin could be harmful to some tissues.

Table 4.21: In vitro cancer cell antiproliferative activity of some of the isolated compounds against a panel of cancer cell lines.

IC$_{50}$ in µM										
Compound	RCC-896-0	MCF10a	MCF-7	BT594	HCC	HeP2	HepG2	LO2	BEAS	A549
Tridecan-2-one (80)	>100	>100	>100	>100	3.84	43.9	-	-	-	-
Dihydrochelerythrine (81)	>100	>100	>100	21.1	8.9	64.0	-	-	-	-
Sesamin (82)	>100	>100	19.0	47.6	>100	>100	-	-	-	-
Skimmianine (83)	>100	>100	>100	>100		-	-	-	-	-
Hesperidin (84)	-	-	-	-	>100	67.6	>100	30.6	7.1	64.8
β-sitosterol (5)	>100	>100	>100	22.2	>100	-	-	-	-	-
Aloenin (85)	-	-	-	-	-	-	>100	>100	>100	>100
Chrysophanol (89)	-	-	-	-	2.4	>100	>100	>100	>100	>100
3-ketopropylcoronaridine (94)	-	-	-	-	-	-	>100	>100	>100	>100
Vobasine (95)	-	-	-	-	-	-	>100	>100	>100	>100
Ibogamine (96)	-	-	-	-	-	-	>100	>100	>100	>100
Voacristine (98)	-	-	-	-	-	-	23.0	>100	>100	>100
Ursolic acid (99)	-	-	-	-	-	-	>100	-	-	6.61
Quebrachitol (97)	-	-	-	-	-	-	>100	>100	>100	>100
Paclitaxel	-	-	-	-	-	-	0.19	< 0.1	< 0.1	0.003

- *Not determined. Results represent the mean of three measurements.*

IC$_{50}$: concentrations inhibiting parasite or cell growth by 50%.

4.2.2 *In Silico Evaluation of the Anticancer Mechanism*

Previous *in vitro* studies indicate that some of the compounds isolated from the genera of plants reported in this thesis inhibit cancer cell proliferation through various mechanisms including induction of apoptosis and cell cycle arrest (Li *et al.*, 2016; Satria *et al.*, 2019). With regard to the results of *in vitro* cytotoxicity reported thus far, the probable anticancer mechanism of action of the isolated compounds was investigated against protein targets in the p53 pathway. The extent of protein-ligand interactions were evaluated by considering the binding affinities, hydrogen bond and π-π interactions relative to those of the native ligands.

4.2.2.1 Validation of the Docking Method

The co-crystallized ligand was docked into the active site of the native protein to first validate the docking method. The binding affinities of the re-docked ligands are presented in Table 4.22. The low RMSD values (<2 Å) of the docked and experimental conformations of the co-crystallized ligands indicated similarity in binding orientations of the co-crystallized ligand (Al-Khodairy *et al.*, 2013). **Figure 4.2** shows the most stable conformations of the re-docked native ligands (red) superposed on their native conformations (grey) in the binding sites of the respective proteins.

Table 4.22: Docking method validation showing RMSD of the re-docked ligands

Target	PDB ID	Ligand	RMSD	S-Score Kcal/mol
MDM2	1RV1	IMZ	0.60	-27.25
CDK2	1DI8	DTQ	0.50	-19.80
CDK2	1PYE	PM1	0.02	-16.76
CDK6	1XO2	FSE	0.48	-12.34
P21	2X4Z	7KC	0.78	-30.64
Bcl2	2O2F	L1O	2.88	-25.15
Caspase 3	3DEI	RXB	0.75	-19.34
Caspase 8	3KJQ	B94	1.89	-17.60
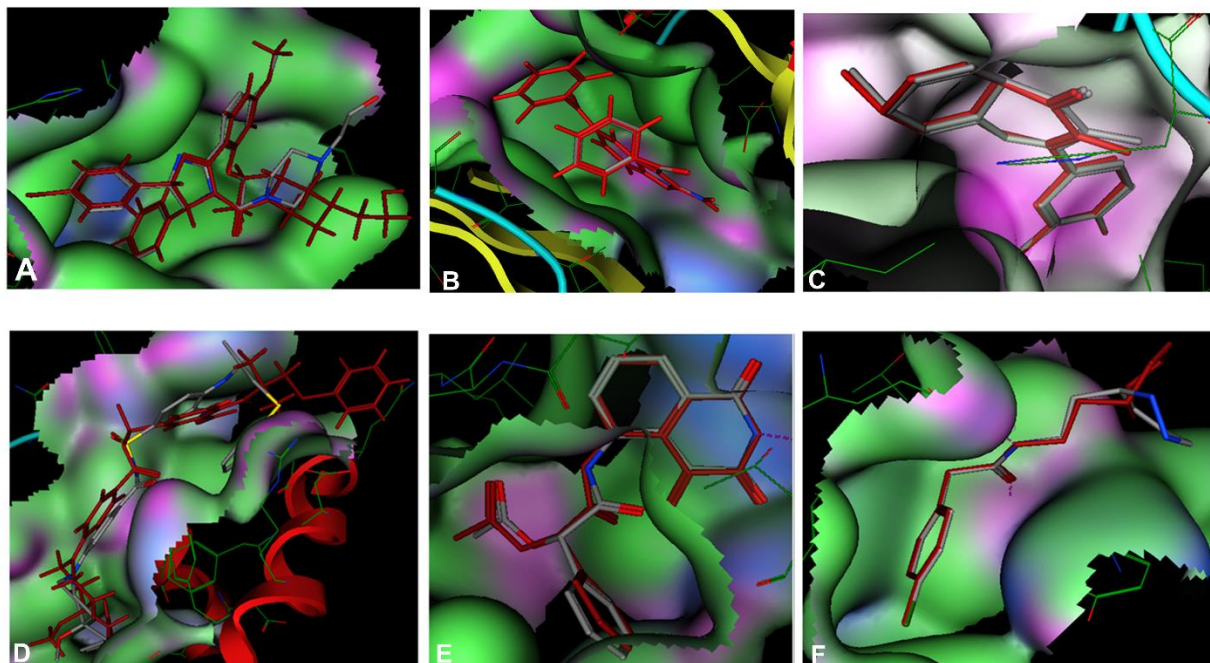
Figure 4.2: Docking method validation by superposition of co-crystallized ligand (grey/blue) with the pose of the re-docked native ligand (red) in the active site of the target proteins. **A**: MDM2, **B**: CDK2, **C**: CDK6, **D**: Bcl-2, **E**: Caspase 3, **F**: Caspase 8

4.2.2.2 In Silico Docking of Compound Library

Protein 53 (p53) is a tumor suppressor that functions to eliminate and inhibit the multiplication of abnormal cells through induction of apoptosis, cell cycle arrest and senescence (Haupt *et al.*, 1997; Sun, 2006). The function of p53 is regulated by MDM2 (murine double minute-2) protein through a negative feedback mechanism. Blocking p53-MDM2 interaction activates p53 pathway consequently leading to apoptosis or cell cycle arrest. The docking results show th*et al*l the docked compounds feebly bind to MDM2 with the best S-score -20.06 kcal/mol, (compound **84**) as compared to the known inhibitor imidazoline (S-score -26.74 kcal/mol). Hesperidin (**84**) shows one hydrogen bond interaction through amino acid residue Lys 94. Furthermore, common amino acid residues are involved in hydrophobic interaction of MDM2 with the docked compounds and

imidazole (Figure 4.3). These results suggest that **84** could inhibit the p53-MDM2 interaction thereby activating the P53 pathway consequently inducing apoptosis.
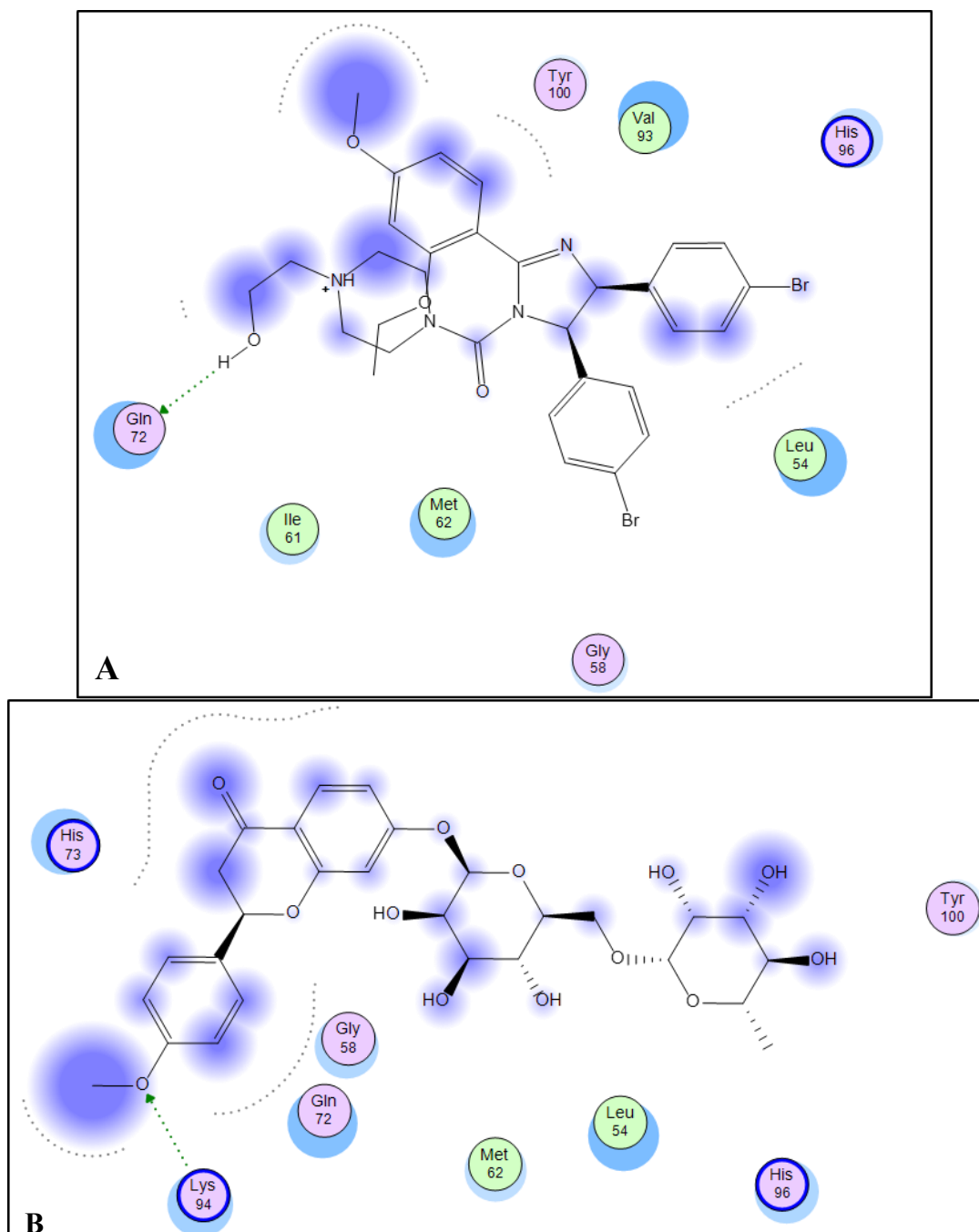
Figure 4.3: Protein-ligand interactions in the binding site of MDM2; **A**: interactions of the native ligand (Binding energy: -26.74 Kcal/mol) showing one hydrogen bond interaction with Gln 72, **B**: interactions of hesperidin (**84**), Binding energy -20.12 Kcal/mol showing one hydrogen bond interaction with Lys 94.

p21$^{WAF1/CIP1}$ one of the downstream targets of p53. It functions by inhibiting cyclin dependent kinases thus, causing cell-cycle arrest. p21$^{WAF1/CIP1}$ is therefore a suitable target for anticancer drug development since, inhibiting p21$^{WAF1/CIP1}$ induces cell cycle arrest. The docked compounds showed weak interaction with the active site of p21$^{WAF1/CIP1}$ (S-score = -22.17 Kcal/mol, for hesperidin (**84**) compared to the co-crystallized ligand (S-score = -30.64 Kcal/mol).Amino acid residues Ile 326 and Asp 458 are involved in hydrogen bond interaction with **84**. However, similar amino acid residues are involved in hydrophobic interactions with the docked compounds (Figure 4.4).

Cyclin-dependent kinases (CDK2 and CDK6) are enzymes which play essential roles in cell cycle control, programmed cell death, transcription and neuronal functions (Shapiro, 2006). They are activated when bound to associated regulatory cyclins (Graña and Reddy, 1995; Shapiro, 2006). Thus, inhibiting the interaction of cyclins (CDK2 and CDK2) with their cognate regulatory cyclins would render the CDKs inactive consequently causing cell cycle arrest. The results of our docking experiments indicate that several of the docked compounds exhibited stronger binding interaction in the active site of CDK2 than the native ligand (binding energy -16.76 kcal/mol) (Table 4.23). As shown in Figure 4.5, hesperidin, **84** (the best docked ligand) exhibited similar binding interactions to the native ligand showing extensive hydrogen bonding network with similar amino acid residues in the active site of CDK2. This suggests that some of the compounds have the potential to induce cell cycle arrest. Similarly, eight of the docked compounds exhibited stronger binding affinity to the active site of CDK6 (binding energies > -12.34 kcal/mol) compared to the co-crystallized inhibitor (binding energy -12.34 kcal/mol) (Table 4.23, Figure 4.6). Chrysalodin was the best docked ligand (Table 4.23). From these results, it can be inferred that the possible

anticancer mechanism of action of some of the compounds tested is by causing arrest of the cell cycle.
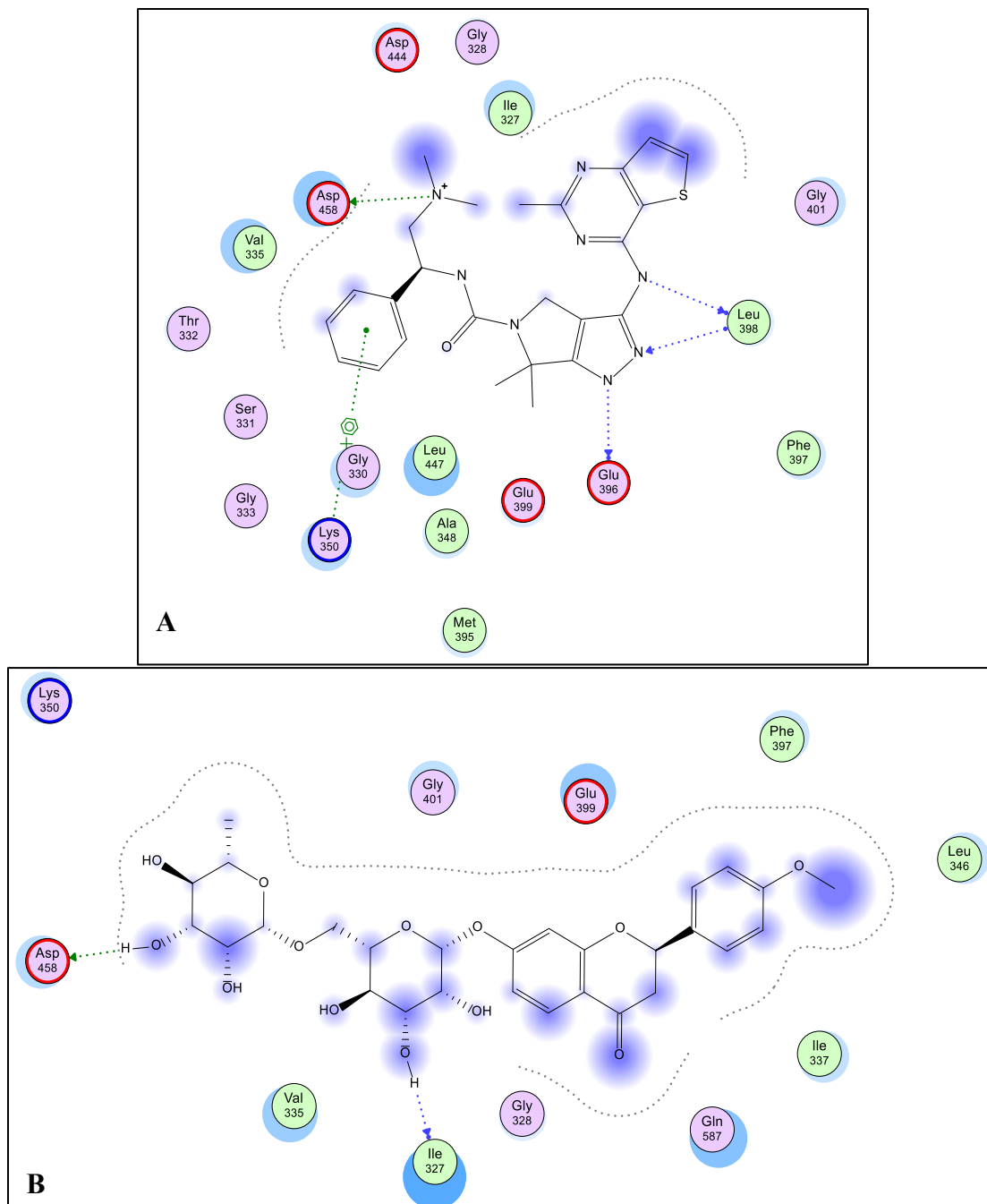
Figure 4.4: Protein-ligand interactions in the binding site of p21WAF1/CIP1; **A**: interactions of the co-crystallized ligand (Binding energy: -30.64 Kcal/mol) showing extensive hydrogen bonding interactions, **B**: interactions of hesperidin (**84**), Binding energy -21.31 Kcal/mol) showing two hydrogen bond interactions with amino acids Ile327 and Asp458

Table 4.23: Binding affinities of the best-docked compounds to the active site of CDK2 and CDK6 as compared to the co-crystallized ligands

CDK2		CDK6	
Compound	S-score; Kcal/mol	Compound	S-score. Kcal/mol
Hesperidin (**84**)	-27.56	Chrysalodin (**90**)	-32.08
Aloenin (**85**)	-25.30	Hesperidin (**84**)	-23.90
Dihydrochelerythrine (**81**)	-22.64	Aloe-emodin (**86**)	-23.50
Chrysalodin (**90**)	-21.45	Aloesaponarin 1 (**91**)	-20.32
Laccaic acid ester (**86**)	-19.60	Tridecan-2-one (**80**)	-18.23
Sesamin (**82**)	-19.12	Droserone (**93**)	-18.10
Aloe-emodin (**86**)	-18.94	Dihydrochelerythrine(**81**)	-17.78
Skimmianine (**83**)	-16.76	Sesamin (**82**)	-15.55
PMI	-16.76	FSE	-12.34

The BCL-2 family of proteins are vital regulators of apoptosis. However most cancer cells evade apoptosis by overexpressing anti-apoptotic Bcl-2 proteins which antagonise the action of the pro-apoptotic proteins such as BAX and BAK (Frenzel *et al.*, 2009). Thus inhibiting Bcl-2 proteins would allow pro-apoptotic proteins to mediate apoptosis. Out of all the docked compounds, hesperidin (**84**) exhibited stronger binding affinity to the active site of Bcl-2 (binding energy -25.88 kcal/mol) compared to the co-crystallized inhibitor (binding energy -25.15 kcal/mol). This result highlights the ability of hesperidin (**84**) to inhibit Bcl-2 thus allowing the pro-apoptotic proteins such as BAX and BAK to oligomerize in the mitochondrial membrane accordingly facilitating release of caspases. The protein-ligand interactions indicate that similar amino acid residues involved in hydrophobic interactions with the docked ligands (Figure 4.7).

All the docked compounds exhibited low binding interaction with the effector caspases 3 and 8 (Table 4.24) as compared to the co-crystallized inhibitor (S-score 19.34 Kcal/mol for caspase 3

and 17.60 Kcal/mol for caspase 8**).** This implies that treatment with the test compounds would activate caspases 3 and 8 thus inducing programmed cell.
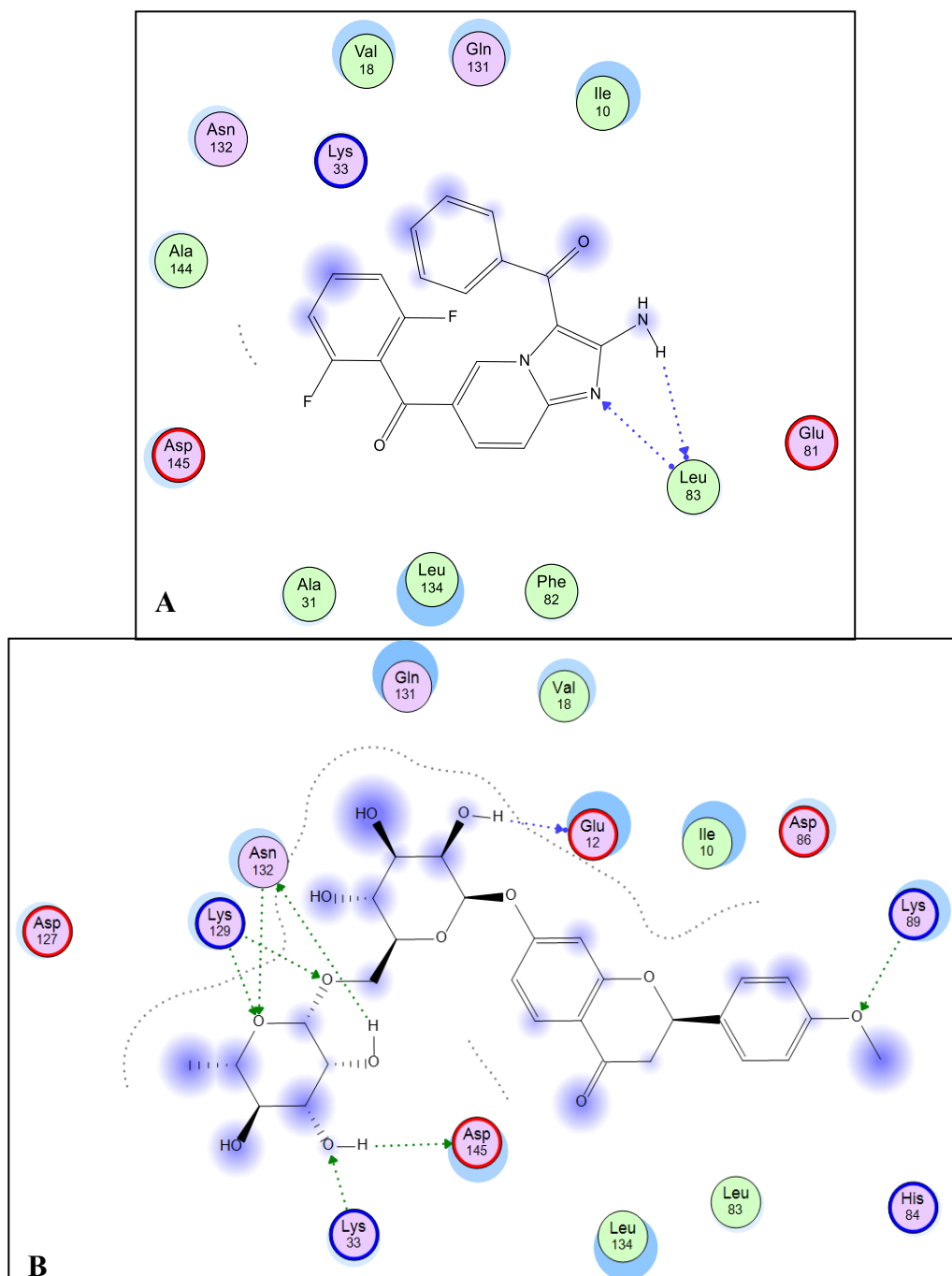
Figure 4.5: Protein-ligand interactions in the binding site of CDK2; **A**: interactions of the co-crystallized ligand (S-score: -19.82 Kcal/mol), **B**: interactions of the best docked ligand (hesperidin, **84**, S-score: -27.56 Kcal/mol) showing extensive hydrogen bonding network with several amino acid residues in the binding site.
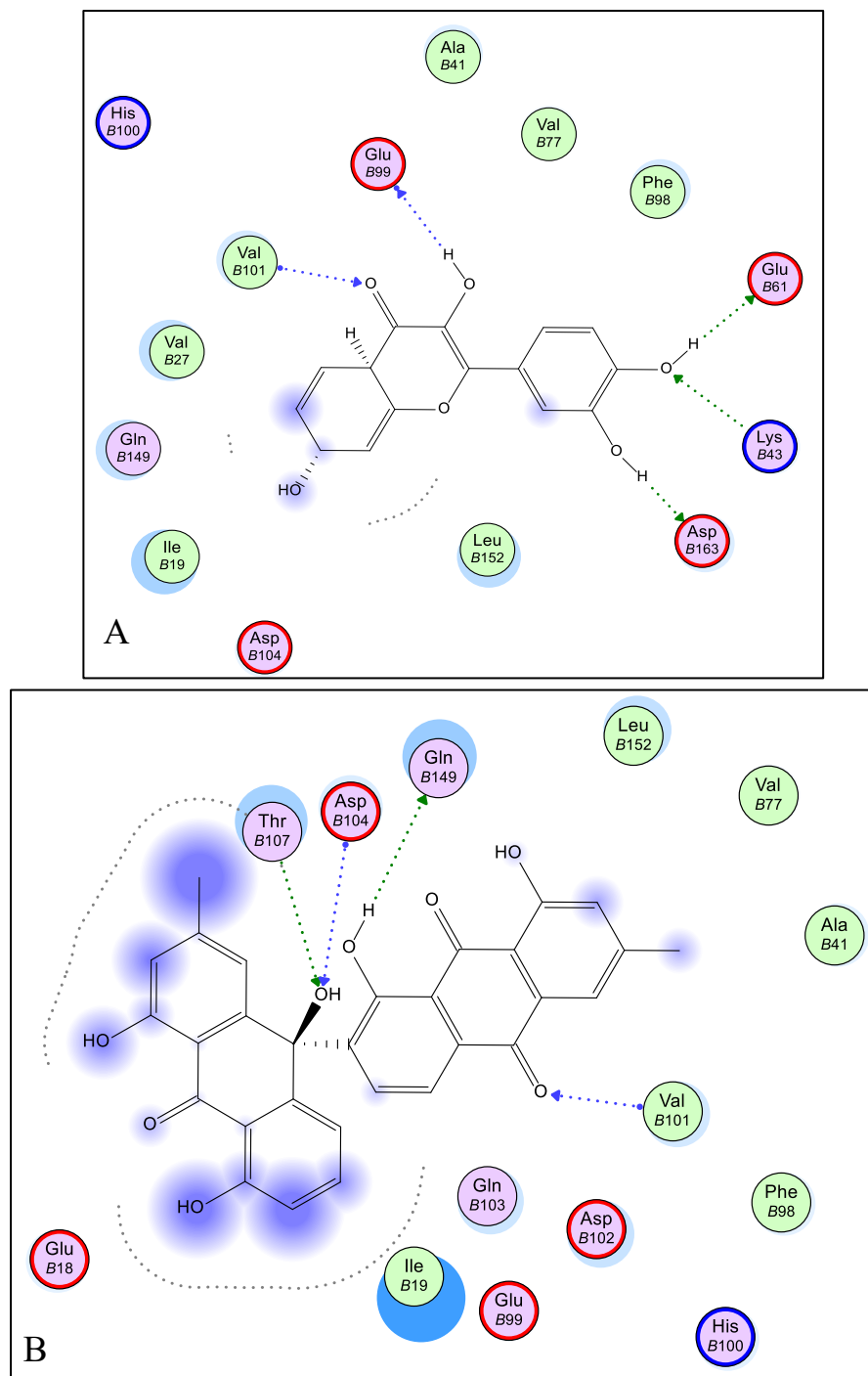
Figure 4.6: Protein-ligand interactions in the binding site of CDK6; **A**: interactions of the co-crystallized ligand (S-score: -12.34 Kcal/mol), Bottom: interactions of the best docked ligand (Chrysalodin (**90**), S-score: -32.08 Kcal/mol) showing extensive hydrogen bonding network with several amino acid residues in the binding site.
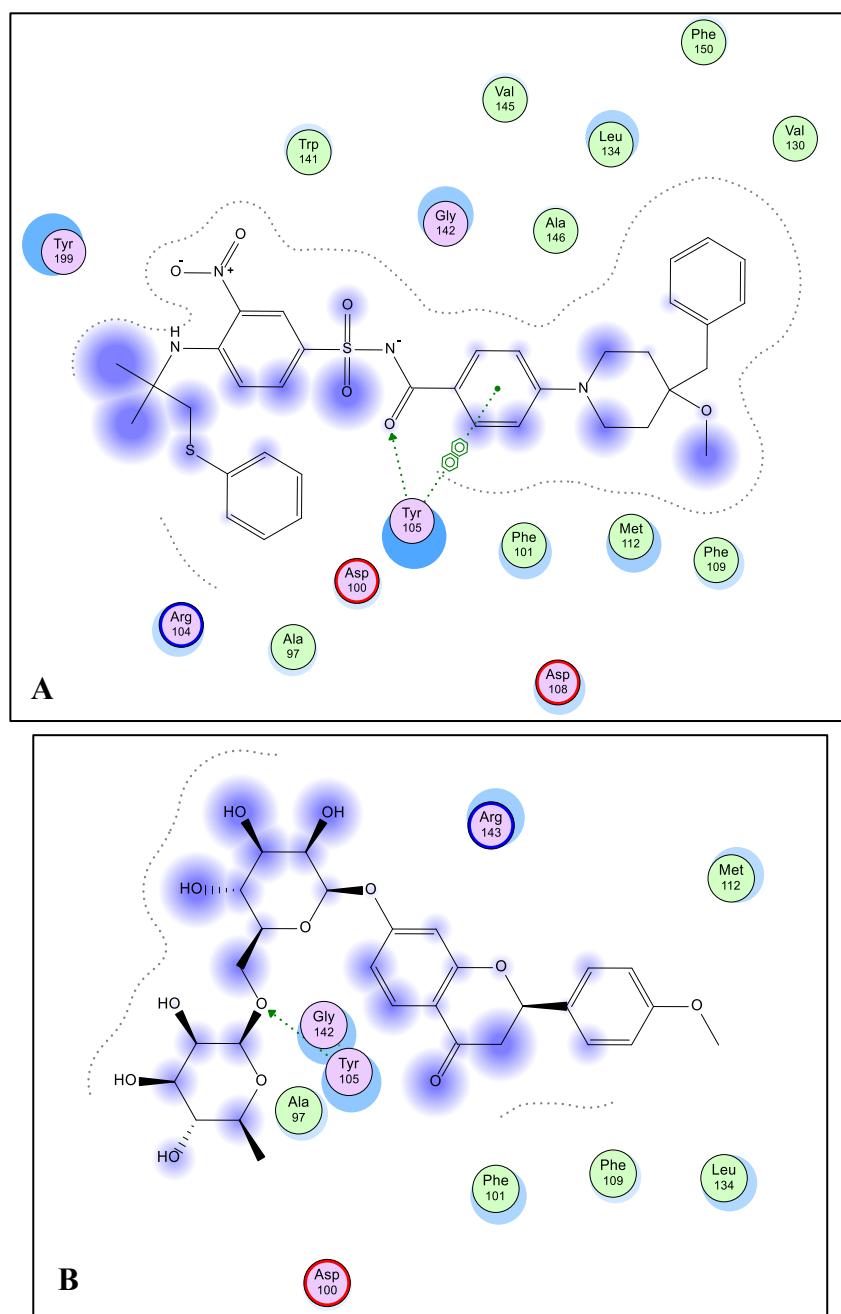
Figure 4.7: Protein -ligand interactions in the binding site of the anti-apoptotic protein Bcl-2. **A**: interactions of the co-crystallized ligand, **B**: interactions of the best docked ligand (hesperidin, **84**).

Table 4.24: Binding affinities of the top three best-docked compounds in the active site of caspase 3 and Caspase 8 in comparison with the co-crystallized inhibitor

Caspase 3		Caspase 8	
Compound	*S-score, Kcal/ mol*	*Compound*	*S-Score, Kcal/ mol*
Hesperidin (**84**)	-18.12	Hesperidin (**84**)	-16.30
Laccaic acid ester (**87**)	-16.30	Sessamin (**82**)	-15.36
Aloenin (**85**)	-15.48	Skimmianine (**83**)	-14.29
RXB	-19.34	B94	-17.60

RXB and B94 are the co-crytallized inhibitors. (see list of abbreviations for full name)

4.3 Formulation, Characterization and Cellular Studies of Natural Product-Loaded Nanoparticles

β-Sitosterol (β-Sit) was selected as a model natural product to evaluate anticancer potential of secondary metabolites when incorporated into nanoparticle drug delivery systems. It was selected as a model because previous studies indicate that it offers various health benefits such as inhibition of proliferation of several cancer cell lines. For instance, it inhibits viability of breast cancer (MCF-7 and MDB-MB-231) cells (Awad *et al.*, 2000; Awad *et al.*, 2003), colon cancer (Jayaprakasha *et al.*, 2007; Raicht *et al.*, 1980), leukemia (Park *et al.*, 2007), and prostate cancer cells (von Holtz *et al.*, 1998). Moreover, it exhibits low cytotoxicity against normal cells. In this section, the preparation, characterization and biological evaluation of β-sitosterol-loaded nanoparticles is discussed.

4.3.1   *Optimization of Parameters for Nanoparticle Formulation*

The size of nanoparticles is an important parameter which influences stability, cellular uptake, biodistribution, and drug release profiles thus, affecting the bioavailability and pharmacokinetics of the loaded drug (Li *et al.*, 2017). To identify the optimal conditions for formulation of nanoparticles, different factors (such as nature of the solvent, homogenization force, amount of polymer, amount of feeding drug and aqueous to organic phase ratio) which affect physicochemical properties of nanoparticles (such as size, particle size distribution, encapsulation efficiency) were investigated. Stigmasterol, a compound with closely related structure as β-sitosterol was used for optimization of formulation parameters since it was readily available and cheap. The experimental approach involved changing the formulation and process parameters one at a time concurrently with changing homogenization amplitude but maintaining other parameters constant, first for blank nanoparticles and then stigmasterol loaded nanoparticles.

4.3.1.1 Effect of the nature of organic phase solvent

Figure 4.8 illustrates the variation of size of the blank PLGA and PEG-PLA nanoparticles with the different organic phase solvents.

117
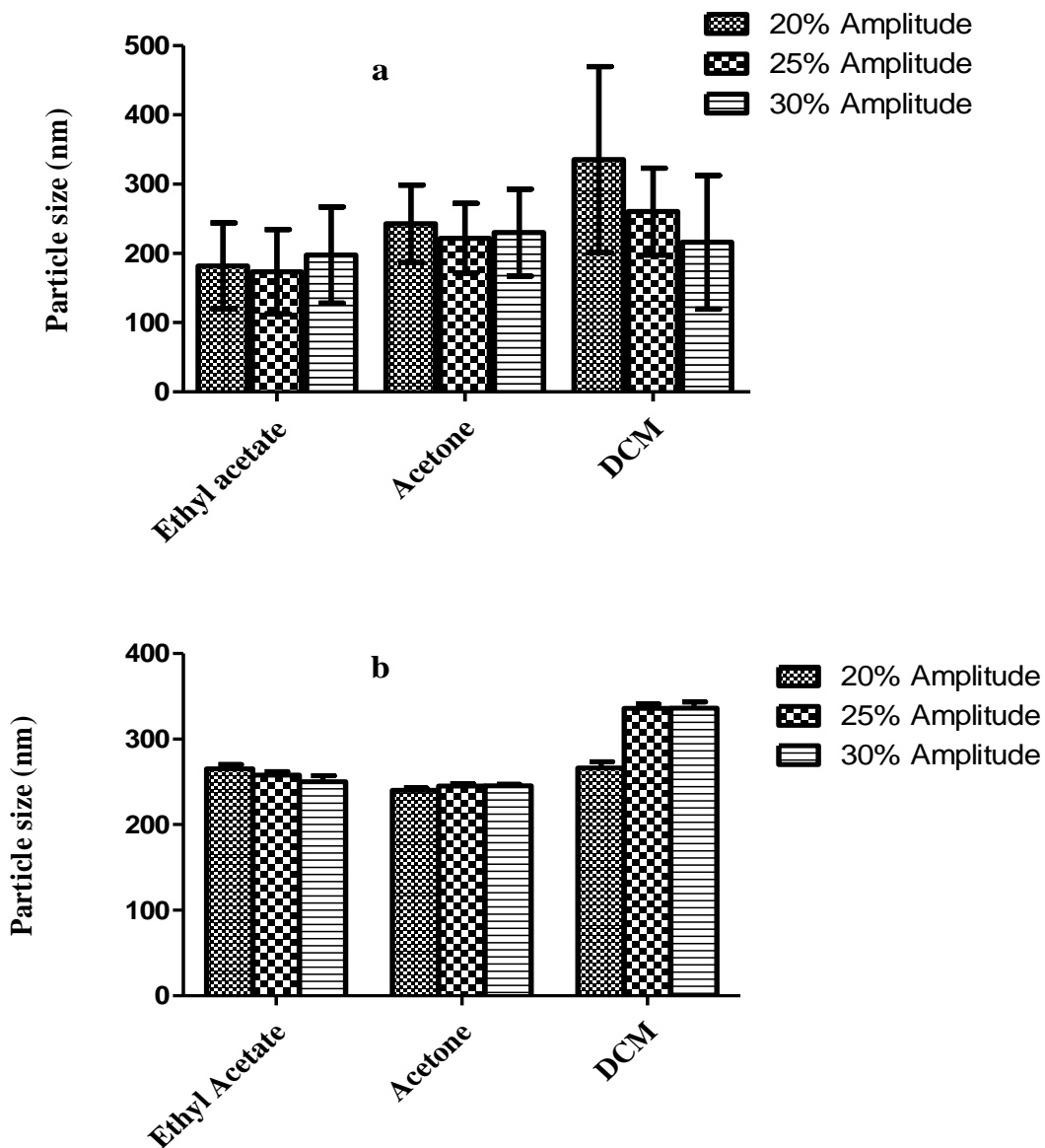
Figure 4.8: Variation of the size of blank PLGA (a) and PEG-PLA (b) nanoparticles with the organic phase solvent

Among the three solvents investigated for optimization of size, EtOAC provided the smallest sized particles in comparison with acetone and DCM for PLGA-based nanoparticles (Figure 4.8a). This is attributed to the fact that ethyl acetate is partially miscible with water hence the interfacial tension between ethyl acetate-water interface is low which prevents coalescence of emulsion

droplets resulting in smaller sized nanoparticles (McCall and Sirianni, 2013). Meanwhile DCM is highly immiscible with water resulting in very high interfacial tension between the water-DCM interface and this increases the tendency of emulsion droplets to coalesce leading to big sized particles. Song and co-workers (Song *et al.*, 2006) observed that water immiscible solvents such as DCM cause nanoparticle aggregation, giving big particle sizes when measured with dynamic light scattering instruments. On the other hand, acetone is highly miscible with water and does not permit formation of stable emulsion droplets of PLGA. Rather when the organic phase containing the polymer is emulsified, it causes the polymer (PLGA) to precipitate into submicron particles resulting in slightly big size particles (Song *et al.*, 2006). However, for PEG-PLA-based nanoparticles, acetone was the preferred solvent (Figure 4.8 b). It is worth noting that the water-soluble PEG-PLA acts as a surfactant. Thus, when a solution of PEG-PLA in acetone (a water miscible solvent) is emulsified with an aqueous solution of PVA, it further stabilizes the emulsion droplets leading to rather smaller size particles (Muranaka *et al.*, 2010). In most cases, varying the homogenization power of the sonicator herein referred to as sonication amplitude from 20–30% did not significantly affect the size of nanoparticles in the different solvents.

4.3.1.2 Effect of Duration of Solvent Evaporation

A study on the effect of duration of solvent evaporation on the size of nanoparticles (Figure 4.9) shows that when the organic solvent is evaporated over a longer time duration (15 hours), smaller sized particles were formed compared to a shorter duration (4 hours) of solvent evaporation.
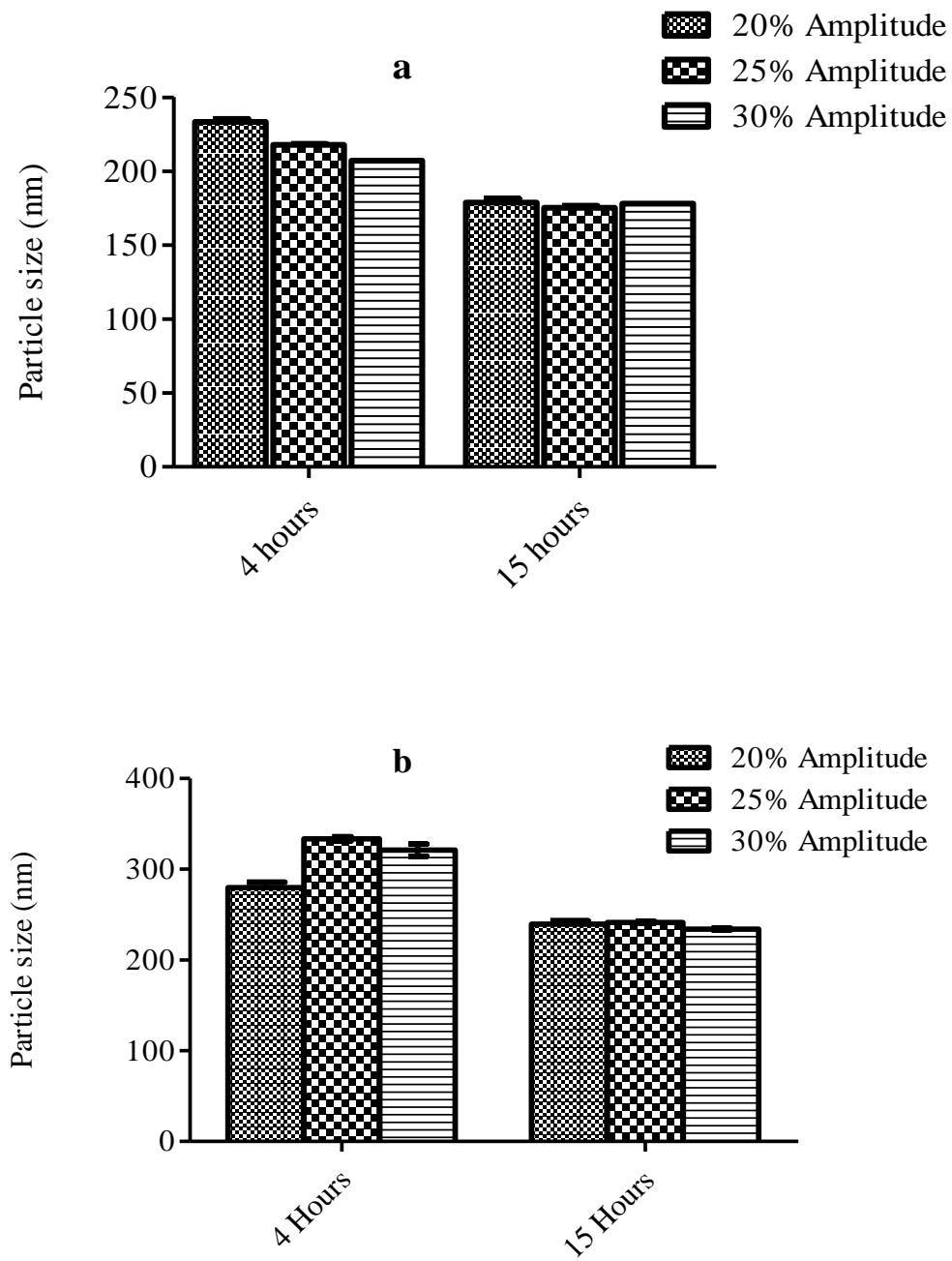
Figure 4.9: Effect of duration of solvent evaporation on the size of (a) PLGA and (b) PEG-PLA

nanoparticles

A previous study (Sharma *et al.*, 2016) indicates that when all the organic solvent is not completely removed, bigger sized nanoparticles are produced compared to when the solvent is completely evaporated over a longer time duration. During solvent evaporation, the nanodroplets solidify to form nanoparticles. Some solvent residue remains in the nanoparticle core when duration of solvent evaporation is short resulting in bigger sized particles (Sharma *et al.*, 2016). A longer duration of solvent evaporation ensures that most of organic phase solvent diffuses out of the nanoparticles resulting in smaller sized particles.

4.3.1.3 Effect of polymer concentration on the size of nanoparticles

The effect of varying the concentration of the polymer on the mean particle size of nanoparticles was studied by increasing polymer concentration from 5-20 mg/ml. The results (Figure 4.10) indicate that there was no significant variation in the size of nanoparticles when polymer concentration was increased from 5-20 mg/ml, $P > 0.05$.
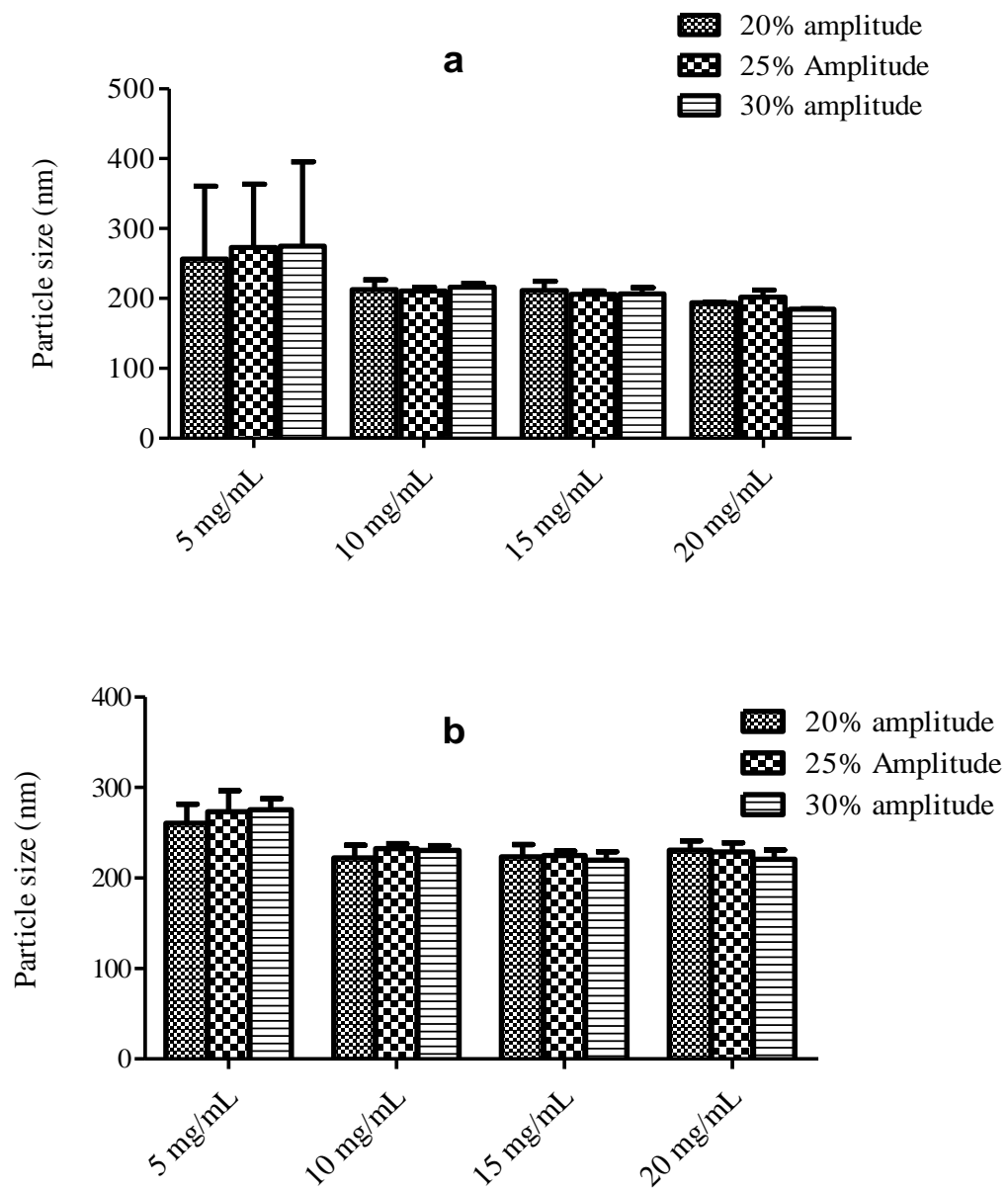
Figure 4.10: Effect of polymer concentration on the size of (a) PLGA and (b) PEG-PLA nanoparticles.

In previous studies, it was observed that the mean size of nanoparticles increased with increasing polymer concentration at a constant volume of the dispersion medium (Abdelkader *et al.*, 2018; Sharma *et al.*, 2016). We suspect that at a phase ratio of 5:1 v/v (aqueous phase to organic phase) used in this study, the volume of the dispersion medium was large enough and this did not affect the viscosity of the dispersion medium even with increasing concentration of the polymer. Thus, there was no significant variation in the size of nanoparticles. From the foregoing results for blank nanoparticles, polymer concentration of 20 mg/mL, sonication power amplitude of 30% and 15 hours of solvent evaporation were considered for further optimization studies for drug-loaded nanoparticles.

4.3.1.4 Effect of drug concentration on the size of nanoparticles

An investigation of the effect of drug concentration on the size of nanoparticles (Figure 4.11) indicates that the size of nanoparticles increased gradually as the feeding drug concentration in the organic phase was increased from 1 to 8 mg/mL.
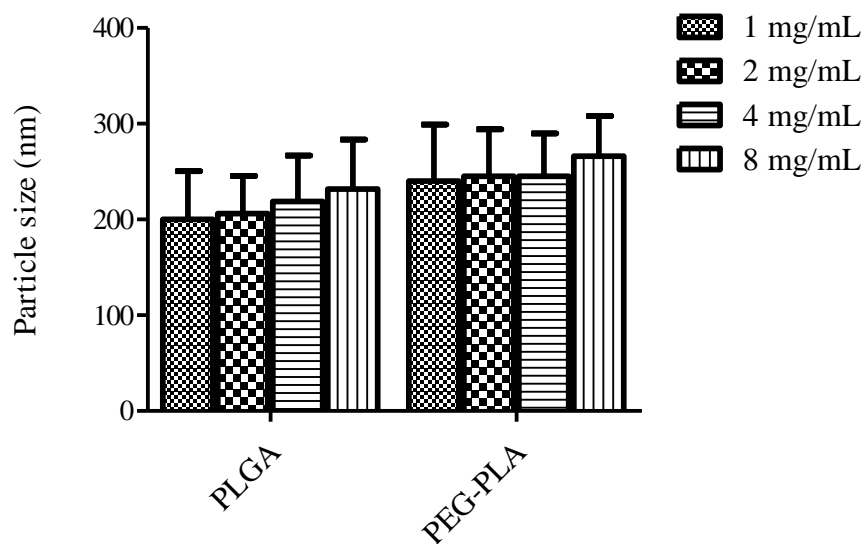
Figure 4.11: variation of mean particle size with feeding drug concentration.

In similar studies, the size of curcumin and budesonide-loaded nanoparticles increased drastically when the concentration of curcumin and budesonide was increased in the organic phase (Cella *et al.*, 2017; Krishnamachari *et al.*, 2007). Keeping other factors constant, a definite amount of a given drug is encapsulated into nanoparticles at a constant polymer to drug feeding ratio. Increasing the concentration of a given drug in the organic phase simply increases the viscosity of the nanoparticle matrix which increases resistance to droplets leading to bigger sized particles (Sharma *et al.*, 2016).

Based on these results, concentrations of 1, 2 and 4 mg/mL of the feeding drug were chosen to determine drug encapsulation efficiency (EE) of the nanoparticles. For this purpose, two methods of preparing the organic phase were investigated for preparation of stigmasterol-loaded nanoparticles. In one method (**A**), the drug powder was added to an organic solution of the polymer (PLGA and PEG-PLA) and stirred for 30 minutes to completely dissolve the drug. In the alternative method (**B**), the polymer and feeding drug (stigmasterol) were separately solubilized in the organic solvent and then the two solutions were mixed on vortex mixer or using a magnetic stirrer to ensure a homogenous mixture. Method **B** exhibited higher encapsulation efficiency than method (**A**) (Table 28).

Table 4.25: Physicochemical parameters and drug loading efficiency of stigmasterol-loaded PLGA and PEG-PLA nanoparticles.

Polymer type	Feeding drug concentration (mg/mL)	Particle size (nm)	PDI	Zeta potential (mV)	Encapsulation efficiency (%)	
					Method A	Method B
PLGA	1	200.1±87.20	0.134±0.01	-8.61±5.04	34.05±0.44	83.17±1.17
	2	206.0±68.70	0.111±0.02	-8.17±6.27	51.95±8.70	77.38±3.68
	4	218.7±83.40	0.114±0.02	-8.98±4.72	72.21±3.83	95.95±0.01
PEG-PLA (R25)	1	240.3±102.2	0.182±0.01	-24.6±4.48	64.84±1.46	81.91±2.94
	2	245.3±84.85	0.09±0.01	-19.6±6.48	51.74±0.07	83.99±
	4	245.0±77.63	0.075±0.01	-23.7±9.48	57.90±0.024	82.07±4.95

As depicted in Table 4.25, drug encapsulation efficiency was higher using method **B** than using method **A** of preparing the organic phase. It was inferred that interaction between polymer solution and drug solution were stronger than interaction between polymer solution and the powdered drug leading to higher drug encapsulation efficiency in method **B** than in method **A**.

From the foregoing optimization studies, it is apparent that the mean size of PLGA-based nanoparticles was 218.5 ± 36.7 nm while the mean size of PEG-PLA based nanoparticles was 240.23±23.3 nm. The nanoparticles exhibited monomodal size distribution (PDI < 0.02) with negative zeta potential (ζ = −12.15 ± 3.82 mV, range −7.97 to −24.6 mV). These optimum parameters were subsequently adopted to formulate β-Sit-Loaded nanoparticles.

4.3.2 *Formulation of β-Sit-loaded nanoparticles*

Based on the optimization studies with blank and stigmasterol-loaded nanoparticles, the following process and formulation parameters were adopted for the formulation of β-Sit-loaded nanoparticles: 20 mg/mL of PLGA and PEG-PLA, 2% of PVA, 2 and 4 mg/mL of β-sitosterol in the organic phase, 5:1 *v/v* aqueous to organic phase ratio and 30% sonication power amplitude and

15 hours of organic solvent evaporation. EtOAc and DCM were used for PLGA-based formulations (consequently labeled as β-Sit-PLGA-EtOAc and β-Sit-PLGA-DCM, respectively). While acetone was used in the production of β-Sit-PEG-PLA nanoparticles (hereafter called β-Sit-PEG-PLA (R25) and β-Sit-PEG-PLA (R45) to designate the type of polymer, respectively). Fluorescent nanoparticles were prepared under the same conditions by incorporating coumarin-6 in the organic phase. The purpose of labeling the nanoparticles with coumarin-6 (a fluorescent dye) was to study the biofate of the nanoparticles in a biological system.

4.3.2.1 Characterization of β-Sit-loaded nanoparticles

The size of nanoparticles, polydispersity index and zeta potential of β-Sit-loaded nanoparticles and fluorescently labeled β-Sit-loaded nanoparticles as measured using DLS are presented in Table 4.26.

Table 4.26: Particle size (Z-average), polydispersity index (PDI), and zeta potential (ζ) of (a) β-Sit-PLGA and β-Sit-PEG-PLA nanoparticles, and (b) coumarin-6-labeled nanoparticles. Results represent mean ± SD (n = 3).

	(a)					
	Concentration of β-sitosterol Used in the formulation					
Formulation	**2 mg/mL**			**4 mg/mL**		
	Z-average (nm)	**PDI**	**ζ (mV)**	**Z-average (nm)**	**PDI**	**ζ (mV)**
β-Sit-PLGA-EtOAc	215.1 ± 29.7	0.10 ± 0.003	−13.9 ± 1.61	231.2 ± 0.60	0.126 ± 0.02	−16.1 ± 7.09
β-Sit-PLGA-DCM	311.1 ± 94.4	0.242 ± 0.03	−14.0 ± 6.01	261.6 ± 4.74[a]	0.113 ± 0.03[a]	−16.5 ± 0.21 [a]
β-Sit-PEG-PLA (R45)	240.6 ± 23.3	0.18 ± 0.05	−23.5 ± 0.27	276.7 ± 1.01	0.197 ± 0.01	−21.5 ± 6.56
β-Sit-PEG-PLA (R25)	239.5 ± 7.9	0.17 ± 0.05	−24.5 ± 0.99	279.4 ± 0.85	0.112 ± 0.04	−21.2 ± 7.01
	(b)					
Formulation	**Physicochemical Properties of Coumarin 6-labeled Nanoparticles**					
	Z-average (nm)		**PDI**		**ζ (mV)**	
β-Sit-PLGA-EtOAc	228 ± 0.45		0.10 ± 0.01		−16.8 ± 0.33	
β-Sit-PEG-PLA (R45)	245 ± 0.66		0.09 ± 0.02		−19.6 ± 0.22	

[a] Result presented as mean ± SD (n = 2).

It can be observed from Table 4.26 that the size of nanoparticles increased as the concentration of β-sitosterol was changed from 2 to 4 mg/mL. Similar to the results of the optimization experiments, when ethyl acetate was used as the organic phase, the nanoparticles (β-Sit-PLGA-EtOAc) exhibited smaller size, spherical shape and monomodal distribution (PDI < 0.2). When DCM was used to make the organic phase, the particles (β-Sit-PLGA-DCM) were bigger in size. Just as in the optimization studies, acetone provided the best size of β-Sit-PEG-PLA nanoparticles. However the sizes of PEG-PLA nanoparticles were generally larger compared to PLGA-based nanoparticles. It was observed that PLGA-based nanoparticles (β-Sit-PLGA-EtOAc and β-Sit-PLGA-DCM) exhibited slightly less negative zeta potential (ca -14 mV) than PEG-PLA-based nanoparticles (ca -24 mV). Slightly higher negative surface charge of PEGylated nanoparticles is attributed to the fact that PEGylation increases the degree of hydration of the nanoparticles, consequently leading to hydrolysis (Rafiei and Haddadi, 2017). Coumarin-6-labeled nanoparticles exhibited similar physicochemical properties to those of non-fluorescent nanoparticles.

4.3.2.2 Surface morphology

The surface morphology of β-Sit-loaded nanoparticle was analyzed using scanning electron microscope (Figure 4.12). It confirmed the formation of nanoparticles with a uniform, spherical shape and a smooth surface. The SEM images also confirmed the big size of PLGA nanoparticles fabricated with DCM as the organic phase solvent.
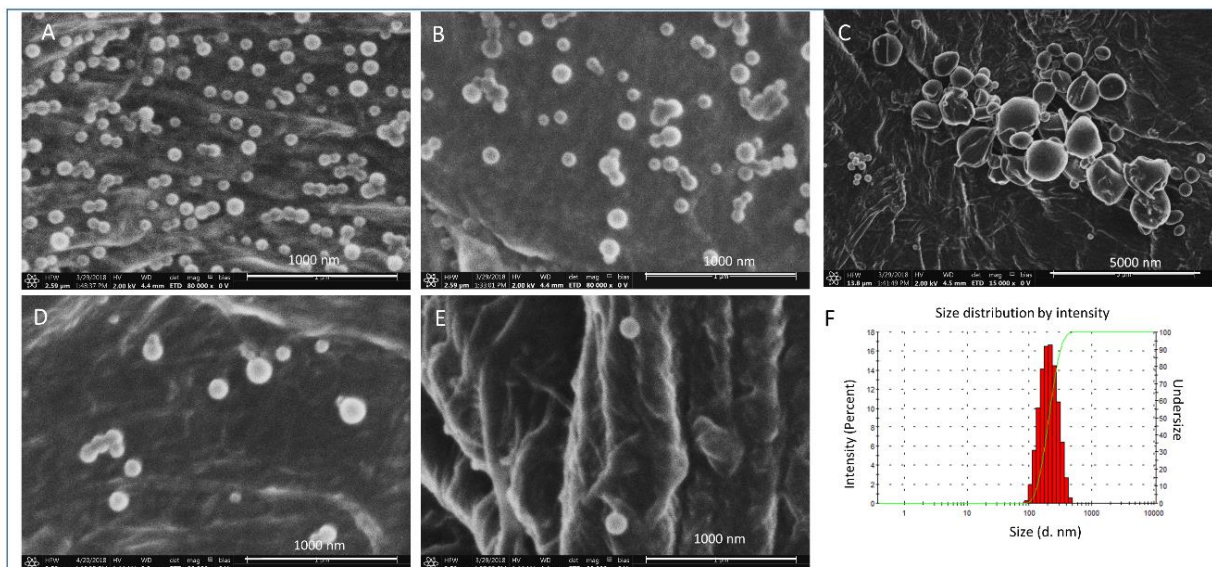
Figure 4.12*: Panels A-E show SEM images of nanoparticles: (A) Blank PLGA nanoparticles; (B) β-Sit-PLGA-EtOAc; (C) β-Sit-PLGA-DCM; (D) Blank PEG-PLA; and (E) β-Sit-PEG-PLA. (**F**) is a representative size distribution as measured using DLS.

4.3.3 Drug Encapsulation Efficiency and Drug-Loading Capacity

The drug Encapsulation Efficiency (EE) and Drug-Loading Capacity (DL) of β-Sit-PLGA and β-Sit-PEG-PLA were studied to determine the optimum amount of drug that can be loaded into the nanoparticles. The results are summarized in Table 4.27.

Table 4.27: Variation of encapsulation efficiency (EE) and drug-loading capacity (DL) of β-Sit-PLGA and β-Sit-PEG-PLA nanoparticles. Results are presented as mean ± SD (n = 3).

| Formulation | Feeding Concentration of β-sitosterol for Nanoparticle Preparation. | | | | | |
| | 2 mg/mL | | | 4 mg/mL | | |
	EE (%)	EDL %	ADL (%)	EE (%)	EDL %	ADL (%)
β-Sit-PLGA-EtOAc	62.89 ± 4.66	4.76	3.00 ± 0.22	48.41 ± 23.82	9.09	4.4 ± 2.17
β-Sit-PLGA-DCM	85.13 ± 6.35	4.76	4.05 ± 0.30	88.48 ± 0.01 [a]	9.09	8.04 ± 0.01 [a]
β-Sit-PEG-PLA (R45)	51.83 ± 19.72	4.76	2.47 ± 0.94	71.02 ± 22.48	9.09	6.46 ± 2.04
β-Sit-PEG-PLA (R25)	34.84 ± 1.71	4.76	1.67 ± 0.08	66.85 ± 8.13	9.09	6.08 ± 0.74

EE = encapsulation efficiency, EDL = expected drug loading, ADL = actual drug loading. [a] Result represents mean ± SD (n = 2). Weight of polymer used for formulation was 40 mg/ml.

Generally, the nanoparticles exhibited acceptable high drug encapsulation efficiency. For PLGA-based nanoparticles, β-sit-PLGA-DCM nanoparticles exhibited higher drug loading efficiency than β-sit-PLGA-EtOAc nanoparticles. This was expected because the bigger size of β-sit-PLGA-DCM nanoparticles facilitates encapsulation of a higher concentration of the drug than the smaller sized β-sit-PLGA-EtOAc nanoparticles. For PEG-PLA-based nanoparticles, β-Sit-PEG-PLA (R45) generally exhibited higher encapsulation efficiency than β-Sit-PEG-PLA (R25). The difference could be attributed to higher content of PEG in β-Sit-PEG-PLA (R45) which forms a bigger surface corona that possibly encapsulates more of the drug than β-Sit-PEG-PLA (R25) nanoparticles. The actual drug loading capacity was generally higher at 4 mg/mL of the feeding drug than at 2 mg/mL concentration level. Thus concentration of 4 mg/mL of the feeding drug was considered ideal for preparation of nanoparticles.

4.3.4 In Vitro Drug Release Profile

The release of β-sitosterol from the nanoparticles matrix was investigated in two different media, PBS and PBS/Tween20. The cumulative release of β-sitosterol from the nanoparticles is presented in Figure 4.13.
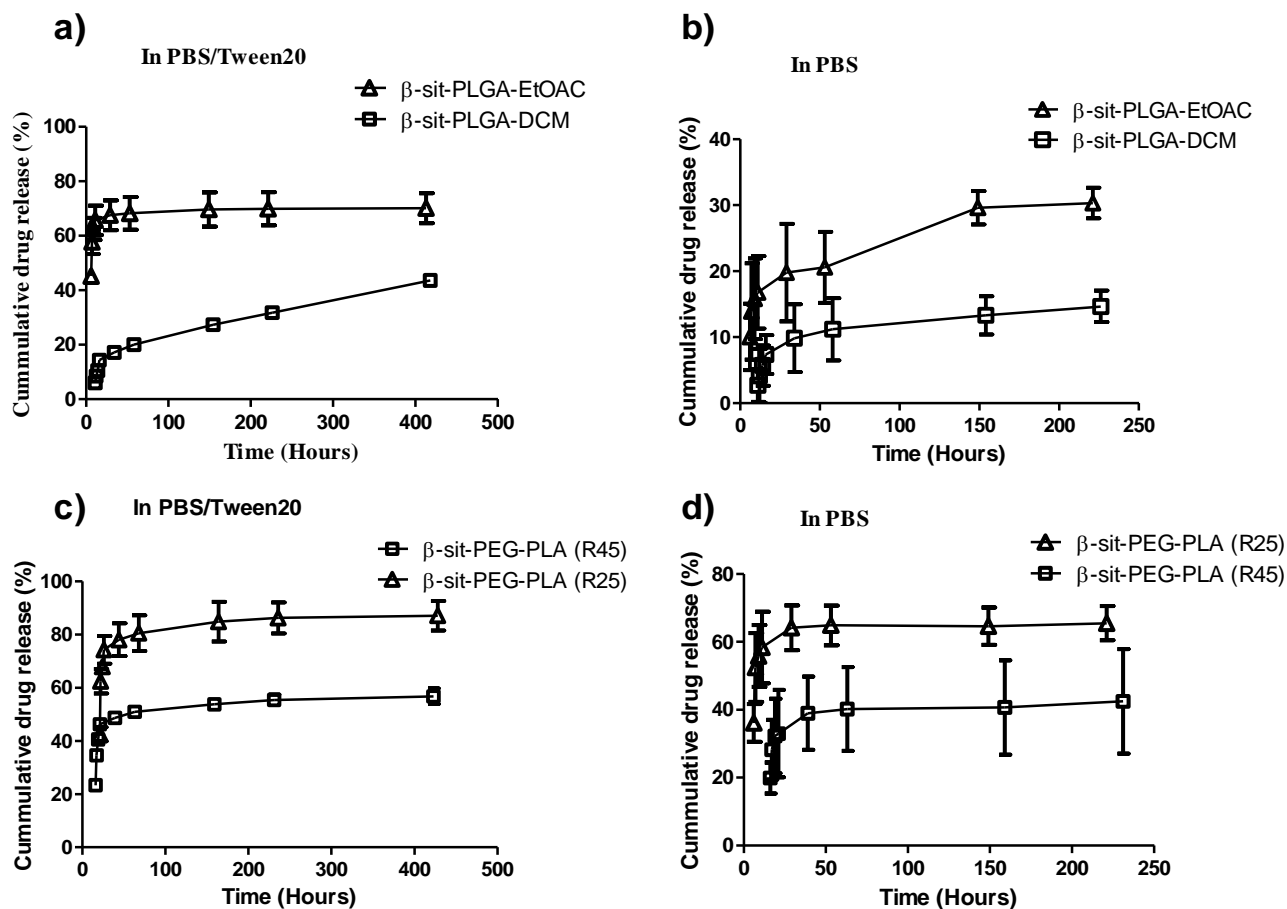
Figure 4.13: *In vitro* cumulative release profile of β-sitosterol from β-Sit-PLGA and β-Sit-PEG-PLA nanoparticles. (n = 3).

The release of β-sitosterol from PLGA-based nanoparticles in PBS/Tween 20 was initially very fast for a period of 24 hours and thereafter, the drug release was sustained (Figure 4.13 a).The cumulative release accounts for $70.10 \pm 5.50\%$ of β-sitosterol released from β-Sit-PLGA-EtOAC in a period of 408 hours. β-Sit-PLGA-DCM nanoparticles exhibited a slow and controlled release of β-sitosterol in PBS/Tween20 representing $43.61\pm3.23\%$ of β-sitosterol released in a period of 408 hours. This is attributed to the big size of these particles which increases the diffusional path length for drug molecules as the nanoparticle size increases (Chen *et al.*, 2016). On the other hand, PLGA-based nanoparticles exhibited a slow and gradual release profile in PBS representing only

130

30.32 and 14.66% of β-sitosterol released from β-Sit-PLGA-EtOAC and β-Sit-PLGA-DCM respectively over a period of 216 hours (Figure 4.13 b). The rather slow and gradual release in PBS is attributed to very low solubility of β-sitosterol in PBS. Low solubility implies that the release medium gets saturated so quickly before it is replenished and hence the drug is released slowly. It is apparent that the release of β-sitosterol from PEG-PLA-based nanoparticles in PBS/Tween20 and PBS media are similar, characterized by and initial burst release for a period of 24 hours and thereafter, the drug release was sustained (Figure 4.13 c and d). The percent cumulative release represents 87.11 and 56.83% of β-sitosterol released in PBS/Tween20 and 65.53 and 43.00% of β-sitosterol released in PBS from β-Sit-PEG-PLA (R45) and β-Sit-PEG-PLA (R25) respectively. Essentially, the initial rapid release profile is attributed to drug molecules encapsulated in the outer layers of nanoparticles and those that are weakly bound on the nanoparticle surface (Danhier *et al.*, 2009; Rafiei and Haddadi, 2017). The slow and sustained drug release kinetics exhibited after the initial burst is due to the gradual diffusion and dissolution of drug molecules encapsulated in the nanoparticle core. The slow erosion of the polymer shell causes the encapsulated drug to be released in a slow and controlled manner (Danhier *et al.*, 2009). The slow and sustained drug release profile is essential for extended treatment with one doze administration.

4.3.5 *Nanoparticle Stability*

Drug-loaded nanoparticles are prone to aggregation on storage and in biological media thus making them unsuitable for therapy (Su *et al.*, 2017) . In this study, the variation of nanoparticle size and PDI were measured on storage and under physiological conditions in a biological model system as an indicator of their stability.

4.3.5.1 Effect of Storage Conditions on Stability

The stabilities of the nanoparticles in terms of size and PDI were studied when stored on the shelve at room temperature and under refrigerated conditions (4 °C) for a period of 30 days, Figure 4.14.

Generally, the nanoparticles were stable at room temperature up to 30 days as evidenced by uniform particle size and unimodal distribution (PDI < 0.2) (Figure 4.14 a and c). Only β-Sit-PLGA-DCM nanoparticle formulation showed signs of aggregation when stored on the shelf at room temperature. When stored under refrigerated conditions (4 °C), β-Sit-PLGA-EtOAc and β-Sit-PEG-PLA (R45) nanoparticles were stable with uniform particle size and unimodal PDI except for β-sit-PLGA-DCM and β-Sit-PEG-PLA (R25) nanoparticles which showed signs of aggregation after the third day of storage (Figure 4.14 b and d). Based on these results, β-Sit-PLGA-DCM and β-sit-PEG-PLA (R25) nano-formulations were not further investigated.
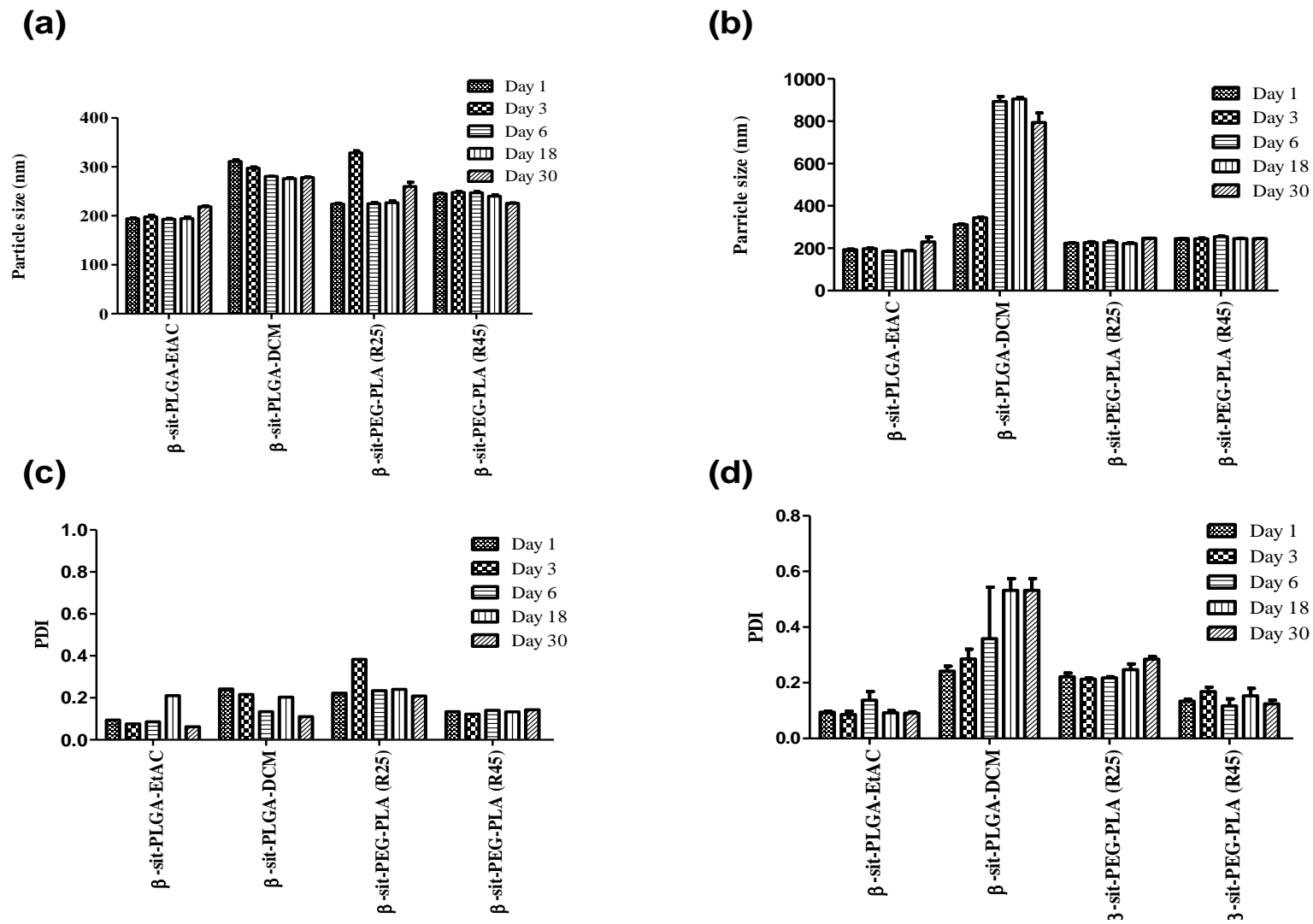
Figure 4.14: Variation of nanoparticle size and PDI as a measure of stability on storage at room temperature (a and c) and under refrigerated conditions (4 °C) (b and d), (n = 3).

4.3.5.2 Stability under Physiological Conditions

The stabilities of the nanoparticles, β-Sit-PLGA-EtOAc and β-Sit-PEG-PLA (R45), in terms of particle size and PDI were evaluated under physiological conditions (in PBS and PBS/FBS at 37 °C) for a period of 24 hours, Figure 4.15
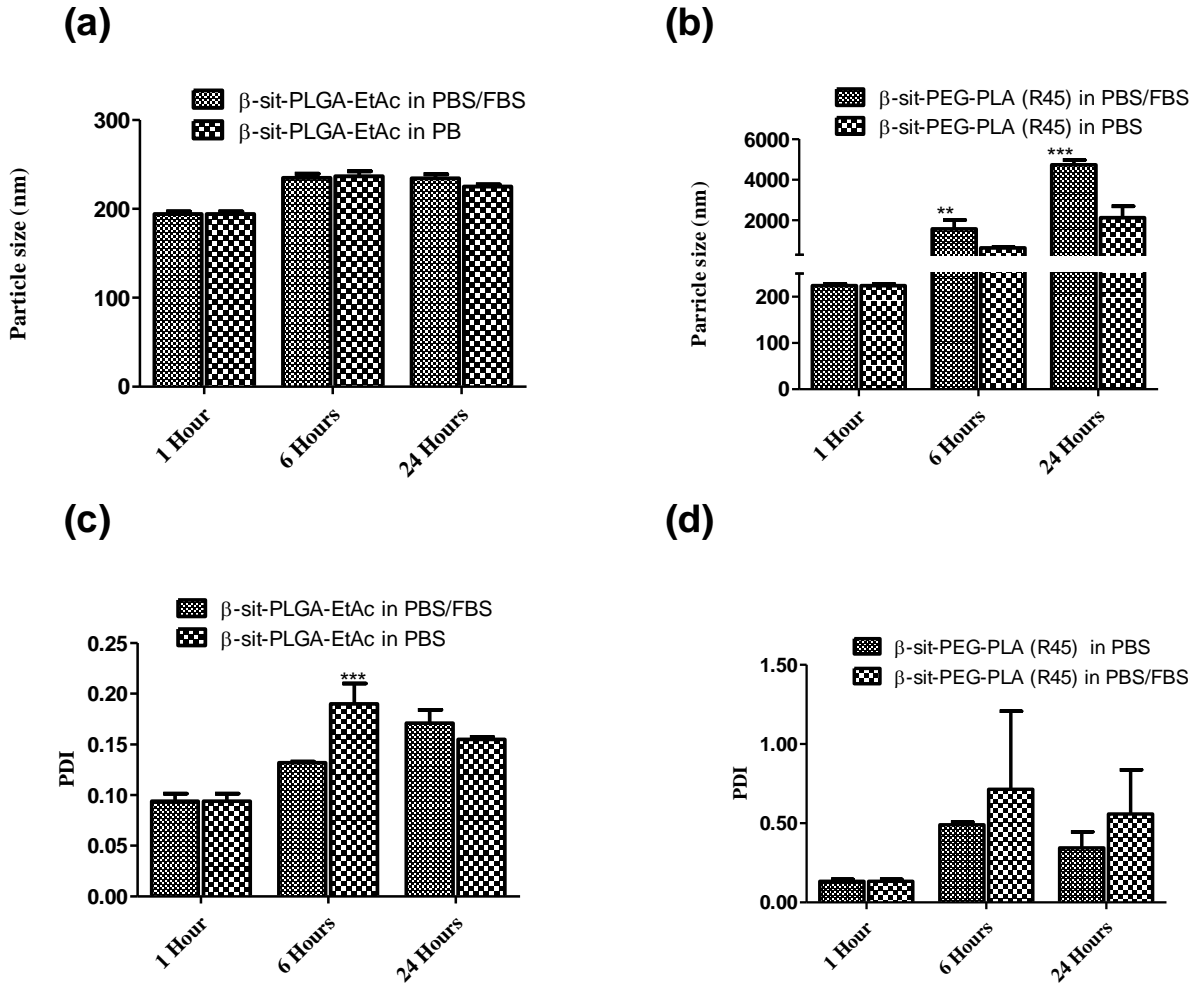
Figure 4.15: Stability of nanoparticle suspension when suspended in PBS and PBS/ FBS (50:50 v/v) at 37 °C as characterized by variation in particle size (**a** and **b)** and PDI (**c** and **d)**. (n = 3). (*** P < 0.001, ** P < 0.01).

Under physiological conditions, it was also observed that β-Sit-PLGA-EtOAc nanoparticles were stable as represented by uniform particle size and unimodal particle distribution (PDI < 0.2)

(Figure 4.15 a and c). However, β-Sit-PEG-PLA (R45) nanoparticles aggregated under physiological conditions (Figure 4.15 b and d). The aggregation tendency of β-sit-PEG-PLA nanoparticles was attributed to their very high negative surface charge which upon contact with positively charged components in FBS caused particle aggregation (Rafiei and Haddadi, 2017). The stealth property expected with PEGylation was not achieved due to inadequate covering of the nanoparticles by the PEG chain, thus explaining the aggregation in the protein rich medium (PBS/FBS) (Rafiei and Haddadi, 2017). The stability of the nanoparticles was further confirmed by scanning electron microscopy which showed that β-Sit-PLGA-EtOAc nanoparticles maintained a spherical shape with smooth surface after storage (Appendix 27).

4.3.6   Cellular Uptake of Nanoparticles

One of the objectives of nanoparticle drug formulation is to deliver the therapeutic payload selectively to the disease site in order to minimize off-target toxicity (Cho *et al*., 2008). To achieve this, the nano-encapsulated drug has to be delivered intracellularly across the cell membrane. However, the cell membrane is a complex biological barrier that could affect the bio-fate of nanoparticles (Ross *et al*., 2015). Based on this premise, an investigation of cellular uptake of nanoparticles was undertaken to determine effectiveness of cellular internalization of the formulated nanoparticles using flow cytometry analysis and laser scanning fluorescence microscopy.

4.3.6.1 Cellular Uptake by Flow Cytometry Analysis

Flow cytometry was used to study cellular uptake of nanoparticles by two breast cancer cell lines (MDA-MB-231 and MCF-7). Since β-sitosterol is non-fluorescent, coumarin-6, a fluorescent dye was encapsulated along with β-sitosterol into the nanoparticles for fluorescence-activated cell sorting (FACS) analysis. FACS analysis was done after 4 and 24 hours of incubation, Figure 20.

The FACS analysis study for MDA-MB-231 cells at 4 and 24 hours indicated that β-Sit-PLGA-C-6 was maximally internalized within four hours of incubation as compared to the control (Figure 4.16 a and b). The proportion of fluorescent cells measured at 4 hours was approximately similar to that measured after 24 hours (Figure 4.16 c). Whereas, MCF-7 cells exhibited a time-dependent profile of cellular uptake of β-Sit-PLGA-C6 nanoparticles with maximum fluorescence intensity observed after 24 hours of incubation (Figure 4.16 d, e and f). However, β-Sit-PEG-PLA-C-6 nanoparticles were feebly internalized by both cell lines. Uptake of nanoparticles by cancer cells depends on several factors including the size, shape, charge, and surface modification of the nanoparticles (Salatin and Khosroushahi, 2017). . In addition, extrinsic factors, such as the nature of the culture medium in which the nanoparticles are suspended affect the bio-fate of nanoparticles. As observed earlier, β-Sit-PLGA-based nanoparticles were smaller in size compared to β-Sit-PEG-PLA nanoparticles. This could have led to the efficient uptake of β-Sit-PLGA nanoparticles nanoparticle than β-Sit-PEG-PLA nanoparticles. Besides this, the results of stability evaluation revealed that β-Sit-PLGA particles were generally stable under physiological conditions, a factor that could have facilitated their uptake by the cells. Shan and co-workers observed that PEGylated PLA nanoparticles were poorly internalized by mononuclear phagocytes than non-PEGylated PLA nanoparticles (Shan *et al.*, 2009). From these results, it was concluded that due to the big size and high surface charge exhibited by PEGylated PLA nanoparticles (β-Sit-PEG-PLA), the culture medium probably caused the nanoparticles to aggregate thus, preventing their uptake by the cells.
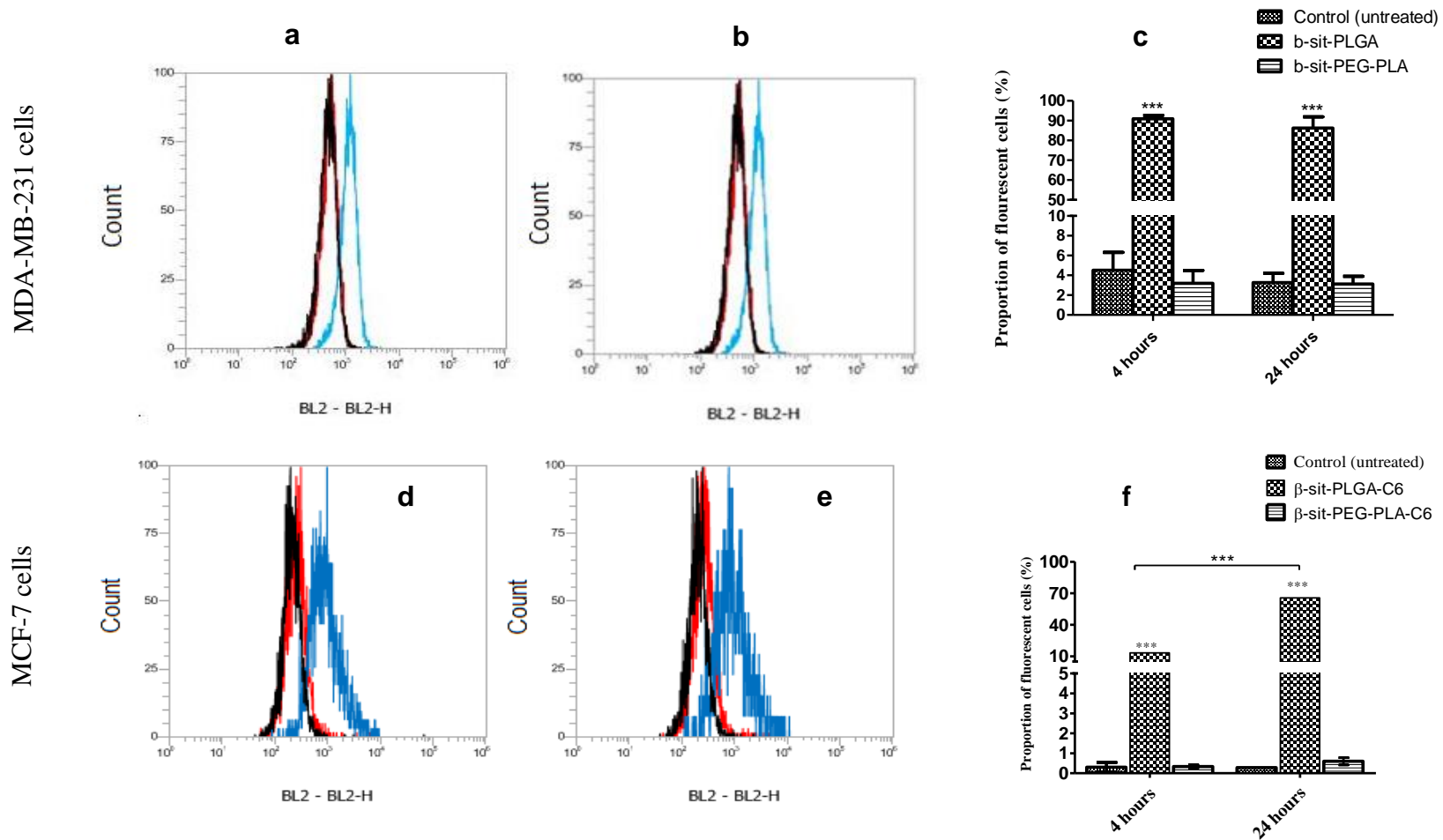
Figure 4.16: Flow cytometry side scattering intensity histograms of MDA-MB-231 and MCF-7 cells when treated with β-PLGA-C6 and β-PEG-PLA-C6 nanoparticles for 4 hours (**a** and **d**) and 24 hours (**b** and **e**): black (Control cells), red (β-PEG-PLA-C6 treated cells) and blue (β-PLGA-C6 treated cells). Proportion of fluorescent cells determined by FACS analysis at 4 and 24 hours (**c** and **f**). Untreated cells were used as controls, (n = 3). (*** $P < 0.001$)

4.3.6.2 Investigation of Cellular Uptake by Confocal Microscopy

Cellular uptake of the nanoparticles was further studied using laser scanning confocal microscopy to validate the results of FACS analysis. The images were captured after cells were incubated with coumarin-6 labeled nanoparticles. Figure 4.17 shows the fluorescence images of cells taken by a confocal microscope.

The blue fluorescence in the DAPI channel indicates the cell nuclei, the red fluorescence in the lysotracker channel indicate the lysosomes. The yellowish green fluorescence in the coumarin and merged image channels confirm cellular uptake of coumarin-6 labelled β-Sit-PLGA nanoparticles by both cell lines. This result is in conformity with those of FACS analysis. Similar to the FACS analysis, the absence of yellowish green fluorescence in the coumarin-6 and merged image channels further confirm that PEG-PLA based nanoformulations were not internalized by the test cells.
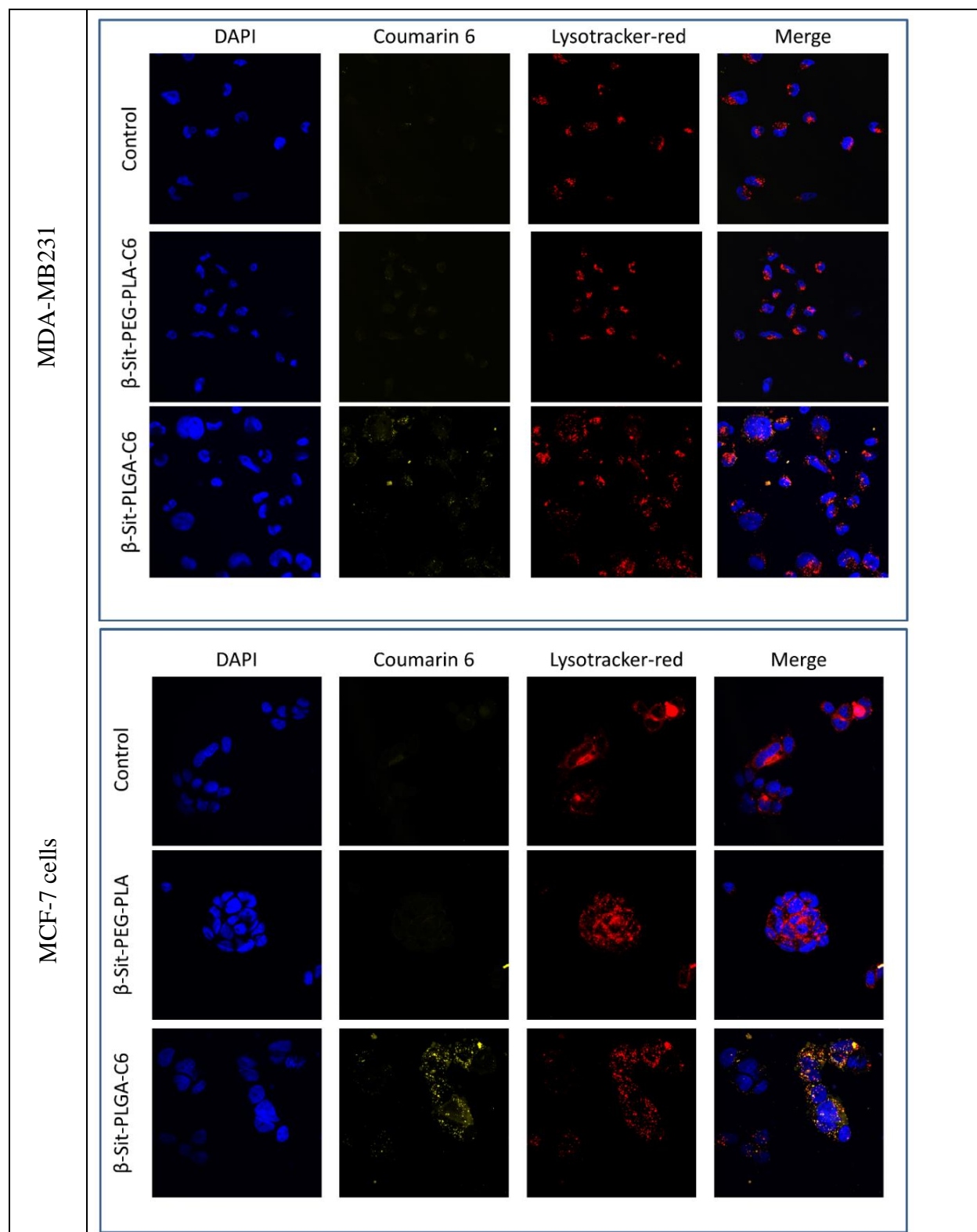
Figure 4.17: Fluorescence images of MDAMB-231 (a) and MCF-7 (b) cells taken 4 hours after cells were incubated with coumarin-6-labeled β-Sit-PLGA and β-Sit-PEG-PLA nanoparticles.

4.3.7 *In Vitro Antiproliferative Activity of β-Sitosterol Loaded Nanoparticles*

The antiproliferative activity (cell viability) of β-Sit-loaded PLGA nanoparticles against breast cancer cell lines was assessed based on the MTT assay (Denizot and Lang, 1986; Mosmann, 1983). Here, cell viability was calculated from Equation 1 and the graph showing variation of cell viability with the different treatments is presented in Figure 22. Since the results of FACS analysis and confocal microscopy showed that β-Sit-PEG-PLA nanoparticles were not internalized by the cells, they were not assessed for cell viability.

From Figure 4.18, it can be seen that treatment with β-Sit-PLGA nanoparticles decreased cell viability of both cell lines by up to 80% at 26.5–53.08 µg/mL concentration levels. There was no significant difference in antiproliferative activity between cells treated at 6.64 - 13.27 µg/mL concentration levels and free β-sitosterol (13.27 µg/mL) in HP-β-CD carrier. Blank nanoparticles at equivalent concentration as the treatment groups (6.64–53.08 µg/mL) did not show any significant inherent cytotoxicity against the test cells. It has been demonstrated in previous studies that β-sitosterol inhibited the viability of MDA-MB-231 cells by 66% and 80% after 3 and 5 days of treatment, respectively (Awad *et al.*, 2000). The present study demonstrates that nanoformulated β-sitosterol inhibited the viability of MDA-MB-231 and MCF-7 cells by up to 80% within 24 hours of treatment. It can be inferred here therefore that nanoparticle formulation offers therapeutic advantage by delivering the therapeutic agent (in this case β-sitosterol) at the site of action thus enhancing activity. β-sitosterol is practically insoluble at higher concentration levels, thus limiting its activity (Awad *et al.*, 2007). It was concluded that formulation of β-sitosterol into nanoparticles increased its solubility and this perhaps enhanced its bioavailability thus, enhancing its antiproliferative activity against breast cancer cells.
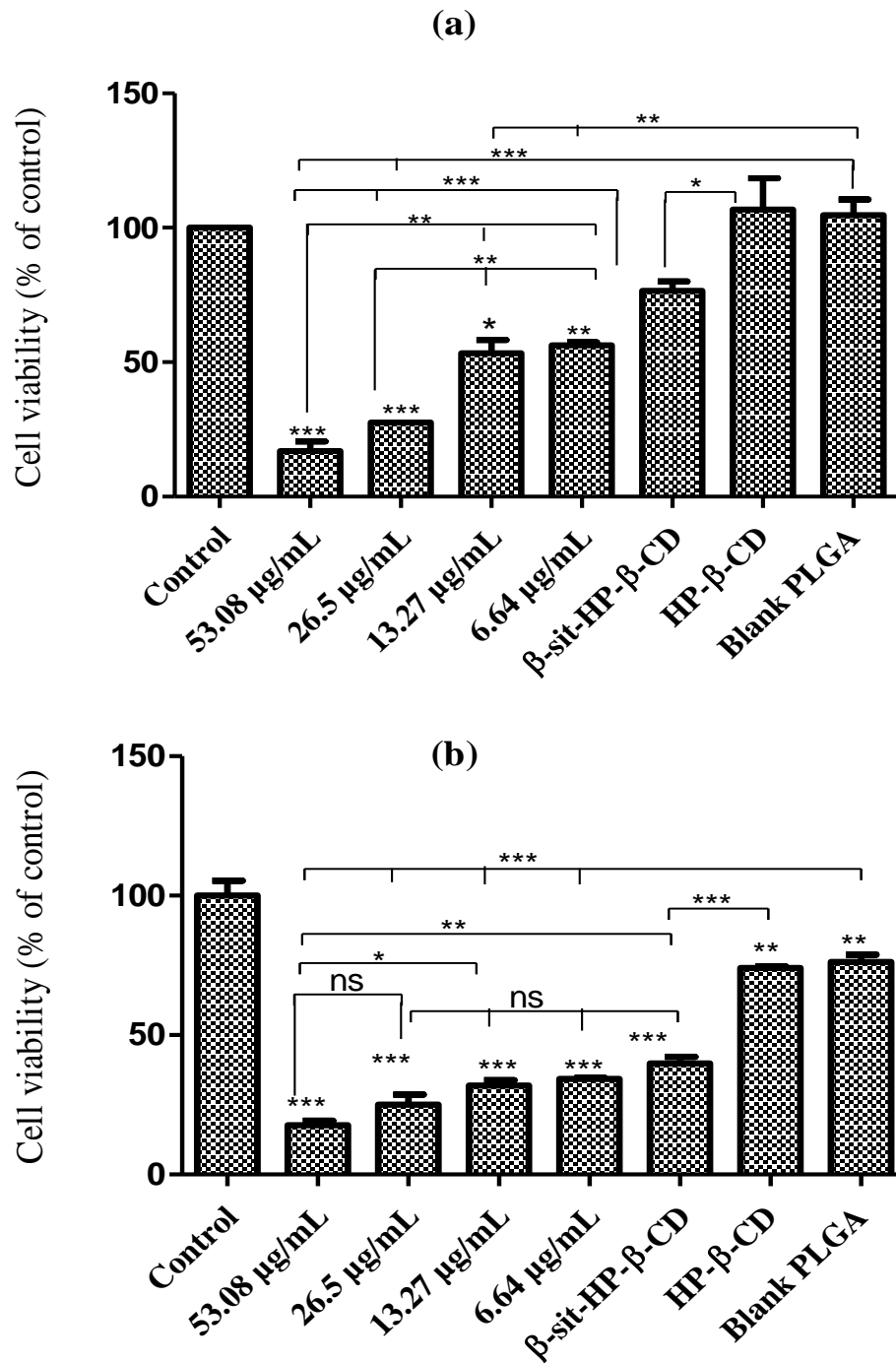
Figure 4.18: *In vitro* antiproliferative activity of B-Sit-PLGA nanoparticles against MDA-MB-231 (a) and MCF-7 cells (b). (n = 3 *** P < 0.001, ** P < 0.01, * P < 0.05, ns: no statistical difference)

CHAPTER 5: CONCLUSIONS AND RECOMMENDATIONS

The conclusions and recommendations drawn from this study are captured below.

5.1   Conclusions

1. Altogether, twenty five compounds were characterized from the four plant species investigated.

    a) For the first time, six (6) compounds were isolated from *Aloe tororoana* and identified as aloenin (**85**), aloe-emodin (**86**), laccaic acid D-methyl ester (**87**), aloesaponarin II (**88**) β-sitosterol (4**5**) and stigmasterol (**47**). All these compounds have been reported before in the family Asphodelaceae.

    b) First phytochemical investigation of *A. schweinfurthii* yielded seven known compounds identified as chrysophanol (**89**), chrysalodin (**90**), aloesaponarin 1 (**91**), 5-allyl-3-methoxybenzene (**92**) and droserone (**93**), β-sitosterol (4**5**) and stigmasterol (**47**).

    c) Nine compounds were isolated from extracts of *T. ventricosa;* consisting of five iboga type indole alkaloids; ibogamine (**96**), 10-hydroxyibogamine (**101**), 10-hydroxycoronaridine (**100**), voacristine (**98**) 3-Ketopropylcoronaridine (**94**), and one vobasinyl indole alkaloid; vobasine (**95**), ursolic acid (**99**), a polyol; quebrachitol (**97**) and stigmasterol (**47**). Except 10-hydroxycoronaridine (**100**), all the compounds were isolated from *T. ventricosa* for the first time nevertheless, they have been reported in other plants in the family Apocynaceae.

2. The compounds showed selective cytotoxicity against the tested cancer cell lines and normal cells. Dihydrochelerythrine (**81**), sesamin (**82**), chrysophanol (**89**) and ursolic acid

(**99**) were the most active compounds against liver (HCC), breast (BT549) or lung (HeP2) and (A549) cancer cell lines respectively. While Hesperidin (**84**) showed low inhibitory activity against cancer cells, it was significantly toxic to normal liver LO2 cells and lung (BEAS) cells.

3. *In silico* docking studies suggested that some of the compounds exert inhibit cancer cell proliferation by inducing cell cycle arrest and apoptosis.

4. The β-sitosterol-loaded nanoparticles were characterized by small particle size (ca. 215 nm), unimodal size distribution (PDI <0.2) and negative zeta potential (ca. -13 mV). Generally, PLGA-based nanoparticles exhibited desirable physicochemical parameters (size, PDI and zeta potential) than PEG-PLA-based nanoparticles. In all cases, the nanoparticles exhibited biphasic drug release profile characterized by an initial burst release and afterwards the drug release was sustained. PLGA-based nanoparticles were stable on storage at room temperature and under physiological conditions in a biological model system.

5. Cellular studies showed that β-sitosterol-loaded PLGA nanoparticles were easily internalized by the breast cancer cell lines (MCF-7 and MDA-MB-231).

6. Encapsulation of β-Sitosterol into nanoparticles enhanced its anticancer activity with up to 80% reduction in cell viability.

Taken together, this study demonstrates that some of the compounds isolated from the selected plants hold promise as potential anticancer agents. Furthermore, encapsulation of some natural products into nanoparticles is a viable strategy to augment their therapeutic efficacy against cancer.

5.2   Recommendations

This study recommends the following for further investigation:

1. Further phytochemical investigation of *A. tororoana* and *T. montana* should be done since some of the fractions from their extracts were complex mixtures that could not be easily separated with the available chromatographic methods at my disposal.

2. *In vitro* anticancer mechanism of action of the compounds that exhibit high cytotoxicity should be studied to fully understand their molecular mechanisms of action.

3. Given the high *in vitro* toxicity of hesperidin (**84**) to normal cells (LO2 and BEAS) further toxicity investigations are warranted to better understand its level of toxicity before *in vivo* tests can be done.

4. Some of the compounds which exhibited moderate anticancer activity could be incorporated into nanoparticles to investigate whether this can further enhance their anticancer activity.

5. Further studies are required to investigate whether co-delivery of β-sitosterol with another anticancer agent using nanoparticles can further enhance their therapeutic efficacy through synergism.

REFEFENCES

Aamir, M., Singh, V. K., Dubey, M. K., Meena, M., Kashyap, S. P., Katari, S. K., Upadhyay, R. S., Umamaheswari, A. and Singh, S. (2018) In silico Prediction, Characterization, Molecular Docking, and Dynamic Studies on Fungal SDRs as Novel Targets for Searching Potential Fungicides Against Fusarium Wilt in Tomato. *Frontiers in Pharmacology* **9**, 1-28.

Abd-Alla, H. I., Shaaban, M., Shaaban, K. A., Abu-Gabal, N. S., Shalaby, N. M. and Laatsch, H. (2009) New bioactive compounds from Aloe hijazensis. *Natural Product Research* **23**, 1035-1049.

Abdelkader, D. H., El-Gizawy, S. A., Faheem, A. M., McCarron, P. A. and Osman, M. A. (2018) Effect of process variables on formulation, in-vitro characterisation and subcutaneous delivery of insulin PLGA nanoparticles: An optimisation study. *Journal of Drug Delivery Science and Technology* **43**, 160-171.

Abdissa, D., Geleta, G., Bacha, K. and Abdissa, N. (2017) Phytochemical investigation of Aloe pulcherrima roots and evaluation for its antibacterial and antiplasmodial activities. *PloS One* **12**, 1-10.

Abdissa, N., Induli, M., Fitzpatrick, P., Alao, J. P., Sunnerhagen, P., Landberg, G., Yenesew, A. and Erdelyi, M. (2014) Cytotoxic quinones from the roots of Aloe dawei. *Molecules* **19**, 3264-3273.

Aderonke, S. T., Babatunde, J. A., Adesola, O. T., Okereke, O. U., Innocent, C., Elisha, M. O., Abolaji, O. L. and Abiola, M. O. (2013) Evaluation of retinoblastoma (Rb) and protein-53

145

(p53) gene expression levels in breast cancer cell lines (MCF-7) induced with some selected cytotoxic plants. *J. Pharmacognosy Phytother* **5**, 120-126.

Ajazuddin and Saraf, S. (2010) Applications of novel drug delivery system for herbal formulations. *Fitoterapia* **81**, 680-689.

Akter, R., Uddin, S. J., Tiralongo, J., Grice, I. D. and Tiralongo, E. (2016) A new cytotoxic diterpenoid glycoside from the leaves of Blumea lacera and its effects on apoptosis and cell cycle. *Natural Product Research* **30**, 2688-2693.

Al-Khodairy, F. M., Khan, M. K. A., Kunhi, M., Pulicat, M. S., Akhtar, S. and Arif, J. M. (2013) In Silico prediction of mechanism of Erysolin-induced apoptosis in human breast cancer cell lines. *American Journal of Bioinformatics Research* **3**, 62-71.

Anselmo, A. C. and Mitragotri, S. (2019) Nanoparticles in the clinic: An update. *Bioengineering and Translational Medicine* **4**, 1-16.

Araújo, L. B., Silva, S. L., Galvão, M. A., Ferreira, M. R., Araújo, E. L., Randau, K. P. and Soares, L. A. (2013) Total phytosterol content in drug materials and extracts from roots of Acanthospermum hispidum by UV-VIS spectrophotometry. *Revista Brasileira de Farmacognosia* **23**, 736-742.

Awad, A., Chinnam, M., Fink, C. and Bradford, P. (2007) β-Sitosterol activates Fas signaling in human breast cancer cells. *Phytomedicine* **14**, 747-754.

Awad, A. B., Downie, C. A. and Fink, C. S. (2000) Inhibition of growth and stimulation of apoptosis by ß-sitosterol treatment of MDA-MB-231 human breast cancer cells in culture. *International Journal of Molecular Medicine* **5**, 541-545.

Awad, A. B. and Fink, C. S. (2000) Phytosterols as Anticancer Dietary Components: Evidence and Mechanism of Action. *The Journal of.Nutrition* **130**, 2127-2130.

Awad, A. B., Roy, R. and Fink, C. S. (2003) β-Sitosterol, a plant sterol induces apoptosis and activates key caspases in MDA-MB-231 human breast cancer cells. *Oncology Reports* **10**, 497-500.

Awad, A. B., Williams, H. and Fink, C. S. (2001) Phytosterols reduce in vitro metastatic ability of MDA-MB-231 human breast cancer cells. *Nutrition and Cancer* **40**, 157-164.

Baek, J.-S., Kim, B.-S., Puri, A., Kumar, K. and Cho, C.-W. (2016) Stability of paclitaxel-loaded solid lipid nanoparticles in the presence of 2-hydoxypropyl-β-cyclodextrin. *Archives of pharmacal research* **39**, 785-793.

Bakarnga-Via, I., Hzounda, J. B., Fokou, P. V., Tchokouaha, L. R., Gary-Bobo, M., Gallud, A., Garcia, M., Walbadet, L., Secka, Y., Dongmo, P. M., Boyom, F. F. and Menut, C. (2014) Composition and cytotoxic activity of essential oils from Xylopia aethiopica (Dunal) A. Rich, Xylopia parviflora (A. Rich) Benth.) and Monodora myristica (Gaertn) growing in Chad and Cameroon. *BMC Complementary and Alternative Medicine* **14**, 125.

Balis, F. M. (1998) The Goal of Cancer Treatment. *Oncologist* **3**, V.

Bell, I. R., Sarter, B., Koithan, M., Banerji, P., Banerji, P., Jain, S. and Ives, J. (2014) Integrative nanomedicine: treating cancer with nanoscale natural products. *Global Advances in Health and Medicine* **3**, 36-53.

Bezabih, M., Motlhagodi, S. and Abegaz, B. M. (1997) Isofuranonaphthoquinones and phenolic and knipholone derivatives from the roots of Bulbine capitata. *Phytochemistry* **46**, 1063-1067.

Bharali, D. J., Siddiqui, I. A., Adhami, V. M., Chamcheu, J. C., Aldahmash, A. M., Mukhtar, H. and Mousa, S. A. (2011) Nanoparticle delivery of natural products in the prevention and treatment of cancers: current status and future prospects. *Cancers* **3**, 4024-4045.

Bilia, A. R., Piazzini, V., Guccione, C., Risaliti, L., Asprea, M., Capecchi, G. and Bergonzi, M. C. (2017) Improving on Nature: The Role of Nanomedicine in the Development of Clinical Natural Drugs. *Planta Medica* **83**, 366-381.

Bisht, D. and Chanotiya, C. S. (2011) 2-Undecanone rich leaf essential oil from Zanthoxylum armatum. *Natural Product Communications* **6**, 111-114.

Blanco, E., Hsiao, A., Mann, A. P., Landry, M. G., Meric‑Bernstam, F. and Ferrari, M. (2011) Nanomedicine in cancer therapy: innovative trends and prospects. *Cancer Science* **102**, 1247-1252.

Bray, F., Ferlay, J., Soerjomataram, I., Siegel, R. L., Torre, L. A. and Jemal, A. (2018) Global cancer statistics 2018: GLOBOCAN estimates of incidence and mortality worldwide for 36 cancers in 185 countries. *CA: A Cancer Journal for Clinicians* **68**, 394-424.

Budzianowski, J. (2000) Naphthoquinone glucosides of *Drosera gigantea* from in vitro cultures. *Planta Medica* **66**, 667-669.

Cavallaro, U. and Christofori, G. (2000) Molecular mechanisms of tumor angiogenesis and tumor progression. *Journal of Neuro-Oncology* **50**, 63-70.

Cella, C., Gerges, I., Milani, P., Lenardi, C. and Argentiere, S. (2017) Calcium Stearate as an Effective Alternative to Poly (vinyl alcohol) in Poly-Lactic-co-Glycolic Acid Nanoparticles Synthesis. *Biomacromolecules* **18**, 452-460.

Chaaib, F., Queiroz, E. F., Ndjoko, K., Diallo, D. and Hostettmann, K. (2003) Antifungal and antioxidant compounds from the root bark of *Fagara zanthoxyloides*. *Planta Medica* **69**, 316-320.

Chabner, B. A. and Roberts Jr, T. G. (2005) Chemotherapy and the war on cancer. *Nature Reviews Cancer* **5**, 65.

Chahar, M. K., Sharma, N., Dobhal, M. P. and Joshi, Y. C. (2011) Flavonoids: A versatile source of anticancer drugs. *Pharmacognosy Reviews* **5**, 1-12.

Chang, W. S., Lee, Y. J., Lu, F. J. and Chiang, H. C. (1993) Inhibitory effects of flavonoids on xanthine oxidase. *Anticancer Research* **13**, 2165-2170.

Chaturvedula, V. S. P. and Prakash, I. (2012) Isolation of Stigmasterol and β-Sitosterol from the dichloromethane extract of Rubus suavissimus. *International Current Pharmaceutical Journal* **1**, 239-242.

Chen, K., Huang, Y.-h. and Chen, J.-l. (2013) Understanding and targeting cancer stem cells: therapeutic implications and challenges. *Acta Pharmacologica Sinica* **34**, 732.

Chen, S., Li, X., Yuan, W., Zou, Y., Guo, Z., Chai, Y. and Lu, W. (2017) Rapid identification of dual p53-MDM2/MDMX interaction inhibitors through virtual screening and hit-based substructure search. *RSC Advances* **7**, 9989-9997.

Chen, W., Palazzo, A., Hennink, W. E. and Kok, R. J. (2016) Effect of particle size on drug loading and release kinetics of gefitinib-loaded PLGA microspheres. *Molecular Pharmaceutics* **14**, 459-467.

Chen, Y., Chen, H. and Shi, J. (2013) Inorganic nanoparticle-based drug codelivery nanosystems to overcome the multidrug resistance of cancer cells. *Molecular Pharmaceutics* **11**, 2495-2510.

Cho, K., Wang, X., Nie, S. and Shin, D. M. (2008) Therapeutic nanoparticles for drug delivery in cancer. *Clinical Cancer Research* **14**, 1310-1316.

Coghi, P., Yaremenko, I. A., Prommana, P., Radulov, P. S., Syroeshkin, M. A., Wu, Y. J., Gao, J. Y., Gordillo, F. M., Mok, S. and Wong, V. K. W. (2018) Novel Peroxides as Promising Anticancer Agents with Unexpected Depressed Antimalarial Activity. *ChemMedChem* **13**, 902-908.

Conde, J., Rosa, J. and Baptista, P. (2013) Gold-Nanobeacons as a theranostic system for the detection and inhibition of specific genes. *Protocolexchange* **088**, 1-46.

Conde, V. R., Alves, M. G., Oliveira, P. F. and Silva, B. M. (2014) Tea (Camellia Sinensis (L.)): a Putative Anticancer Agent in Bladder Carcinoma? *Anti-Cancer Agents in Medicinal Chemistry* **15**, 26-36.

Cragg, G. M. and Newman, D. J. (2005) Plants as a source of anti-cancer agents. *Journal of Ethnopharmacology* **100**, 72-79.

da Silva, S. D., Hier, M., Mlynarek, A., Kowalski, L. P. and Alaoui-Jamali, M. A. (2012) Recurrent oral cancer: current and emerging therapeutic approaches. *Frontiers in Pharmacology* **3**, 149-149.

Dagne, E., Bisrat, D., Viljoen, A. and Van Wyk, B. (2000) Chemistry of Aloe species. *Current Organic Chemistry* **4**, 1055-1078.

Dagne, E., Yenesew, A., Asmellash, S., Demissew, S. and Mavi, S. (1994) Anthraquinones, pre-anthraquinones and isoeleutherol in the roots of Aloe species. *Phytochemistry* **35**, 401-406.

Dai, Y., Harinantenaina, L., Bowman, J. D., Da Fonseca, I. O., Brodie, P. J., Goetz, M., Cassera, M. B. and Kingston, D. G. (2014) Isolation of antiplasmodial anthraquinones from Kniphofia ensifolia, and synthesis and structure–activity relationships of related compounds. *Bioorganic & Medicinal Chemistry* **22**, 269-276.

Danaei, G., Vander Hoorn, S., Lopez, A. D., Murray, C. J. L. and Ezzati, M. (2005) Causes of cancer in the world: comparative risk assessment of nine behavioural and environmental risk factors. *The Lancet* **366**, 1784-1793.

Danhier, F., Lecouturier, N., Vroman, B., Jérôme, C., Marchand-Brynaert, J., Feron, O. and Préat, V. (2009) Paclitaxel-loaded PEGylated PLGA-based nanoparticles: In vitro and in vivo evaluation. *Journal of Controlled Release* **133**, 11-17.

Danielsen, K., Aksnes, D. W. and Francis, G. W. (1992) NMR study of some anthraquinones from rhubarb. *Magnetic Resonance in Chemistry* **30**, 359-360.

De Stefani, E., Boffetta, P., Ronco, A. L., Brennan, P., Deneo-Pellegrini, H., Carzoglio, J. C. and Mendilaharsu, M. (2000) Plant sterols and risk of stomach cancer: a case-control study in Uruguay. *Nutrition and Cancer* **37**, 140-144.

Deng, P., Wang, C., Chen, L., Wang, C., Du, Y., Yan, X., Chen, M., Yang, G. and He, G. (2013) Sesamin induces cell cycle arrest and apoptosis through the inhibition of signal transducer and activator of transcription 3 signalling in human hepatocellular carcinoma cell line HepG2. *Biological and Pharmaceutical Bulletin* **36**, 1540-1548.

Denizot, F. and Lang, R. (1986) Rapid colorimetric assay for cell growth and survival: modifications to the tetrazolium dye procedure giving improved sensitivity and reliability. *Journal of Immunological Methods* **89**, 271-277.

Dipankar, C. and Murugan, S. (2012) The green synthesis, characterization and evaluation of the biological activities of silver nanoparticles synthesized from Iresine herbstii leaf aqueous extracts. *Colloids and Surfaces B: Biointerfaces* **98**, 112-119.

El-Shabouri, M. (2002) Positively charged nanoparticles for improving the oral bioavailability of cyclosporin-A. *International Journal of Pharmaceutics* **249**, 101-108.

Farimani, M. M., Bahadori, M. B., Koulaei, S. A., Salehi, P., Ebrahimi, S. N., Khavasi, H. R. and Hamburger, M. (2015) New ursane triterpenoids from Salvia urmiensis Bunge: Absolute configuration and anti-proliferative activity. *Fitoterapia* **106**, 1-6.

Fernandes, E., Ferreira, J. A., Andreia, P., Luís, L., Barroso, S., Sarmento, B. and Santos, L. L. (2015) New trends in guided nanotherapies for digestive cancers: A systematic review. *Journal of Controlled Release* **209**, 288-307.

Fonseca, C., Simões, S. and Gaspar, R. (2002) Paclitaxel-loaded PLGA nanoparticles: preparation, physicochemical characterization and in vitro anti-tumoral activity. *Journal of Controlled Release* **83**, 273-286.

Frenzel, A., Grespi, F., Chmelewskij, W. and Villunger, A. (2009) Bcl2 family proteins in carcinogenesis and the treatment of cancer. *Apoptosis* **14**, 584-596.

Galindo-Rodriguez, S., Allemann, E., Fessi, H. and Doelker, E. (2004) Physicochemical parameters associated with nanoparticle formation in the salting-out, emulsification-diffusion, and nanoprecipitation methods. *Pharmaceutical Research* **21**, 1428-1439.

Garcez, F. R., da Silva AG, F., Garcez, W. S., Linck, G., de Fatima Matos, F. C., Santos, E. C. S. and Queiroz, L. M. (2011) Cytotoxic aporphine alkaloids from Ocotea acutifolia. *Planta Medica* **77**, 383-387.

Garg, A., Garg, S., Zaneveld, L. and Singla, A. (2001) Chemistry and pharmacology of the citrus bioflavonoid hesperidin. *Phytotherapy Research* **15**, 655-669.

Gathumbi, P., Mwangi, J., Mugera, G. and Njiro, S. (2002) Toxicity of chloroform extract of Prunus africana stem bark in rats: Gross and histological lesions. *Phytotherapy Research* **16**, 244-247.

Giacomelli, S., Gallo, D., Apollonio, P., Ferlini, C., Distefano, M., Morazzoni, P., Riva, A., Bombardelli, E., Mancuso, S. and Scambia, G. (2002) Silybin and its bioavailable phospholipid complex (IdB 1016) potentiate in vitro and in vivo the activity of cisplatin. *Life Sciences* **70**, 1447-1459.

Govender, T., Stolnik, S., Garnett, M. C., Illum, L. and Davis, S. S. (1999) PLGA nanoparticles prepared by nanoprecipitation: drug loading and release studies of a water soluble drug. *Journal of Controlled Release* **57**, 171-185.

Greish, K. (2010) Enhanced permeability and retention (EPR) effect for anticancer nanomedicine drug targeting. *Methods in Molecular Biology* **624**, 25-37.

Gu, Q., Xing, J. Z., Huang, M., Zhang, X. and Chen, J. (2013) Nanoformulation of paclitaxel to enhance cancer therapy. *Journal of Biomaterials Applications* **28**, 298-307.

Gunasekaran, T., Haile, T., Nigusse, T. and Dhanaraju, M. D. (2014) Nanotechnology: an effective tool for enhancing bioavailability and bioactivity of phytomedicine. *Asian Pacific Journal of Tropical Biomedicine* **4, Supplement 1**, S1-S7.

Gunasekera, S. P., Cordell, G. and Farnsworth, N. R. (1980) Anticancer indole alkaloids of *Ervatamia heyneana*. *Phytochemistry* **19**, 1213-1218.

Guo, J.-m., Xiao, B.-x., Liu, Q., Zhang, S., Liu, D.-h. and Gong, Z.-h. (2007) Anticancer effect of aloe-emodin on cervical cancer cells involves G2/M arrest and induction of differentiation. *Acta Pharmacologica Sinica* **28**, 1991-1995.

Gupta, S., Kesarla, R. and Omri, A. (2013) Formulation Strategies to Improve the Bioavailability of Poorly Absorbed Drugs with Special Emphasis on Self-Emulsifying Systems. *ISRN Pharmaceutics* **2013**, 16.

Hainaut, P. and Hollstein, M. (1999) p53 and human cancer: the first ten thousand mutations. *Advances in Cancer Research* **77**, 81-137.

Harris, S. L. and Levine, A. J. (2005) The p53 pathway: positive and negative feedback loops. *Oncogene* **24**, 2899.

Haupt, Y., Maya, R., Kazaz, A. and Oren, M. (1997) Mdm2 promotes the rapid degradation of p53. *Nature* **387**, 296.

He, Y., Du, Z., Lv, H., Jia, Q., Tang, Z., Zheng, X., Zhang, K. and Zhao, F. (2013) Green synthesis of silver nanoparticles by Chrysanthemum morifolium Ramat. extract and their application in clinical ultrasound gel. *International journal of nanomedicine* **8**, 1809.

Herrmann, F., Sivakumar, N., Jose, J., Costi, M., Pozzi, C. and Schmidt, T. (2017) In silico identification and in vitro evaluation of natural inhibitors of *Leishmania major* pteridine reductase I. *Molecules* **22**, 2166.

Hilgenbrink, A. R. and Low, P. S. (2005) Folate receptor-mediated drug targeting: from therapeutics to diagnostics. *Journal of Pharmaceutical Sciences* **94**, 2135-2146.

Hirata, T. and Suga, T. (1978) Structure of aloenin, a new biologically-active bitter glucoside from *Aloe arborescens* var. *natalensis*. *Bulletin of the Chemical Society of Japan* **51**, 842-849.

Hua, S. and Wu, S. Y. (2018) Editorial: Advances and Challenges in Nanomedicine. *Frontiers in Pharmacology* **9**, 1397-1397.

Huang, M., Gao, H. and Chen, Y. (2007) Chimmitecan, a novel 9-substituted camptothecin, with improved anticancer pharmacologic profiles *in vitro* and *in vivo*. *Clinical Cancer Research* **13**, 1298-1307.

Huang, P.-H., Huang, C.-Y., Chen, M.-C., Lee, Y.-T., Yue, C.-H., Wang, H.-Y. and Lin, H. (2013) Emodin and Aloe-Emodin Suppress Breast Cancer Cell Proliferation through ERα Inhibition. *Evidence-based Complementary and Alternative Medicine : eCAM* **2013**, 376123.

Iqbal, J., Abbasi, B. A., Mahmood, T., Kanwal, S., Ali, B., Shah, S. A. and Khalil, A. T. (2017) Plant-derived anticancer agents: A green anticancer approach. *Asian Pacific Journal of Tropical Biomedicine* **7**, 1129-1150.

Isah, T. (2016) Anticancer Alkaloids from Trees: Development into Drugs. *Pharmacognosy Reviews* **10**, 90-99.

Jackson, G. E., Campbell, W. E. and Davidowitz, B. (1990) Two Dimensional NMR Study of 8-Methoxyflindersine, Skimmianine and Monocrotaline. *Spectroscopy Letters* **23**, 971-982.

Jadeja, Y. S., Kapadiya, K. M., Jebaliya, H. J., Shah, A. K. and Khunt, R. C. (2017) Dihedral angle study in Hesperidin using NMR Spectroscopy. *Magnetic Resonance in Chemistry* **55**, 589-594.

Jaiswal, J., Gupta, S. K. and Kreuter, J. (2004) Preparation of biodegradable cyclosporine nanoparticles by high-pressure emulsification-solvent evaporation process. *Journal of Controlled Release* **96**, 169-178.

Jaju, S. B., Indurwade, N. H., Sakarkar, D. M., Fuloria, N. K., Ali, M. D. and Basu, S. P. (2010) Isolation of β-sitosterol diglucosyl caprate from *Alpinia galanga*. *Pharmacognosy Research* **2**, 264-266.

Jayaprakasha, G. K., Mandadi, K. K., Poulose, S. M., Jadegoud, Y., Nagana Gowda, G. A. and Patil, B. S. (2007) Inhibition of colon cancer cell growth and antioxidant activity of bioactive compounds from *Poncirus trifoliata* (L.) Raf. *Bioorganic & Medicinal Chemistry* **15**, 4923-4932.

Jiang, Z. Y., Zhu, L. Y., Zhou, J., Hu, Q. F., Yang, G. Y., Huang, X. Z., Liu, W. X., Gao, L., Li, G. P. and Xia, F. T. (2016) A Novel C22 Terpenoid from the Cultured *Perovskia atriplicifolia*. *Helvetica Chimica Acta* **99**, 452-456.

Jin-Jian, L., Bao, J.-L., Chen, X.-P., Huang, M. and Wang, Y.-T. (2012) Alkaloids isolated from natural herbs as the anticancer agents. *Evidence-Based Complementary and Alternative Medicine* **2012**.

Juliano, R. (2012) The future of nanomedicine: promises and limitations. *Science and Public Policy* **39**, 99-104.

Kalepu, S. and Nekkanti, V. (2015) Insoluble drug delivery strategies: review of recent advances and business prospects. *Acta pharmaceutica Sinica. B* **5**, 442-453.

Kasaian, J., Iranshahy, M., Masullo, M., Piacente, S., Ebrahimi, F. and Iranshahi, M. (2014) Sesquiterpene lactones from Ferula oopoda and their cytotoxic properties. *Journal of Asian Natural Products Research* **16**, 248-253.

Kassim, O. O., Loyevsky, M., Elliott, B., Geall, A., Amonoo, H. and Gordeuk, V. R. (2005) Effects of root extracts of Fagara zanthoxyloides on the in vitro growth and stage distribution of Plasmodium falciparum. *Antimicrobial Agents and Chemotherapy* **49**, 264-268.

Kaur, R., Kapoor, K. and Kaur, H. (2011) Plants as a source of anticancer agents. *J Nat Prod Plant Resour* **1**, 119-124.

Kazuo, T., Toshifumi Hirata, Osamu Koshitani and Takayuki Suga. (1976) Carbon-13 Nmr spectral studies of Aloenin and its derivatives. Carbon-13 signal assignment problem of 4-methoxy-2-pyrones. *Tetrahedron Letters* **16**, 1311-1314.

Kelland, L. R. (2000) Flavopiridol, the first cyclin-dependent kinase inhibitor to enter the clinic: current status. *Expert Opin Investig Drugs* **9**, 2903-2911.

Kenny, A. P. (1952) The determination of cholesterol by the Liebermann-Burchard reaction. *Biochemical Journal* **52**, 611.

Kepp, O., Menger, L., Vacchelli, E., Adjemian, S., Martins, I., Ma, Y., Sukkurwala, A. Q., Michaud, M., Galluzzi, L., Zitvogel, L. and Kroemer, G. (2012) Anticancer activity of cardiac glycosides: At the frontier between cell-autonomous and immunological effects. *Oncoimmunology* **1**, 1640-1642.

Khalil, N. M., do Nascimento, T. C., Casa, D. M., Dalmolin, L. F., de Mattos, A. C. and Hoss, I. (2013) Pharmacokinetics of curcumin-loaded PLGA and PLGA-PEG blend nanoparticles after oral administration in rats. *Colloid Surface B* **101**, 353-360.

Kobayashi, H., Watanabe, R. and Choyke, P. L. (2013) Improving conventional enhanced permeability and retention (EPR) effects; what is the appropriate target? *Theranostics* **4**, 81-89.

Krishnamachari, Y., Madan, P. and Lin, S. (2007) Development of pH-and time-dependent oral microparticles to optimize budesonide delivery to ileum and colon. *International journal of pharmaceutics* **338**, 238-247.

Kuete, V. and Efferth, T. (2015) African flora has the potential to fight multidrug resistance of cancer. *BioMed Research International* **2015**, 1-24.

Kuete, V., Krusche, B., Youns, M., Voukeng, I., Fankam, A. G., Tankeo, S., Lacmata, S. and Efferth, T. (2011) Cytotoxicity of some Cameroonian spices and selected medicinal plant extracts. *Journal of Ethnopharmacology* **134**, 803-812.

Kuppusamy, P., Yusoff, M. M., Maniam, G. P. and Govindan, N. (2014) Biosynthesis of metallic nanoparticles using plant derivatives and their new avenues in pharmacological applications–An updated report. *Saudi Pharmaceutical Journal* **24**, 473-484.

Kuzma, L., Wysokinska, H., Rozalski, M., Krajewska, U. and Kisiel, W. (2012) An unusual taxodione derivative from hairy roots of Salvia austriaca. *Fitoterapia* **83**, 770-773.

Larsen, A. K., Grondard, L., Couprie, J., Desoize, B., Comoe, L., Jardillier, J. C. and Riou, J. F. (1993) The antileukemic alkaloid fagaronine is an inhibitor of DNA topoisomerases I and II. *Biochemical Pharmacology* **46**, 1403-1412.

Le Marchand, L., Murphy, S. P., Hankin, J. H., Wilkens, L. R. and Kolonel, L. N. (2000) Intake of flavonoids and lung cancer. *Journal of the National Cancer Institute* **92**, 154-160.

Lee, S. S., Lee, Y. B. and Oh, I. J. (2015) Cellular uptake of poly (DL-lactide-co-glycolide) nanoparticles: effects of drugs and surface characteristics of Nanoparticles. *Journal of Pharmaceutical Investigation* **45**, 659-667.

Li, K., Zhou, R., Jia, W. W., Li, Z., Li, J., Zhang, P. and Xiao, T. (2016) Zanthoxylum bungeanum essential oil induces apoptosis of HaCaT human keratinocytes. *Journal of Ethnopharmacology* **186**, 351-361.

Li, T.-P., Wong, W.-P., Chen, L.-C., Su, C.-Y., Chen, L.-G., Liu, D.-Z., Ho, H.-O. and Sheu, M.-T. (2017) Physical and Pharmacokinetic Characterizations of trans-Resveratrol (t-Rev) Encapsulated with Self-Assembling Lecithin-based Mixed Polymeric Micelles (sa LMPMs). *Scientific Reports* **7**, 10674.

Lim, K.-H., Raja, V. J., Bradshaw, T. D., Lim, S.-H., Low, Y.-Y. and Kam, T.-S. (2015) Ibogan, tacaman, and cytotoxic bisindole alkaloids from Tabernaemontana. Cononusine, an iboga alkaloid with unusual incorporation of a pyrrolidone moiety. *Journal of Natural Products* **78**, 1129-1138.

Lu, J. J., Bao, J. L., Wu, G. S., Xu, W. S., Huang, M. Q., Chen, X. P. and Wang, Y. T. (2013) Quinones derived from plant secondary metabolites as anti-cancer agents. *Anti-Cancer Agents in Medicinal Chemistry* **13**, 456-463.

Maeda, H. and Khatami, M. (2018) Analyses of repeated failures in cancer therapy for solid tumors: poor tumor-selective drug delivery, low therapeutic efficacy and unsustainable costs. *Clinical and translational medicine* **7**, 11-11.

Mann, J. (2002) Natural products in cancer chemotherapy: past, present and future. *Nature Reviews Cancer* **2**, 143.

Mansoori, B., Mohammadi, A., Davudian, S., Shirjang, S. and Baradaran, B. (2017) The Different Mechanisms of Cancer Drug Resistance: A Brief Review. *Advanced pharmaceutical bulletin* **7**, 339-348.

Manthey, J. A., Grohmann, K. and Guthrie, N. (2001) Biological properties of citrus flavonoids pertaining to cancer and inflammation. *Current Medicinal Chemistry* **8**, 135-153.

Masters, G. A., Krilov, L., Bailey, H. H., Brose, M. S., Burstein, H., Diller, L. R., Dizon, D. S., Fine, H. A., Kalemkerian, G. P., Moasser, M., Neuss, M. N., O'Day, S. J., Odenike, O., Ryan, C. J., Schilsky, R. L., Schwartz, G. K., Venook, A. P., Wong, S. L. and Patel, J. D. (2015) Clinical Cancer Advances 2015: Annual Report on Progress Against Cancer From the American Society of Clinical Oncology. *Journal of Clinical Oncology* **33**, 786-809.

Mata, R., Nakkala, J. R. and Sadras, S. R. (2015) Biogenic silver nanoparticles from Abutilon indicum: Their antioxidant, antibacterial and cytotoxic effects in vitro. *Colloids and Surfaces B: Biointerfaces* **128**, 276-286.

Mathur, M. and Vyas, G. (2013) Role of nanoparticles for production of smart herbal drug− An overview. *Indian Journal of Natural Products and Resources* **4**, 329-338.

Mazumder, K., Tanaka, K. and Fukase, K. (2013) Cytotoxic activity of ursolic acid derivatives obtained by isolation and oxidative derivatization. *Molecules* **18**, 8929-8944.

McCall, R. L. and Sirianni, R. W. (2013) PLGA Nanoparticles Formed by Single- or Double-emulsion with Vitamin E-TPGS. *JoVE*, 1-8.

McCance, R. A. and Lawrence, R. D. (1933) An investigation of quebrachitol as a sweetening agent for diabetics. *Biochemical Journal* **27**, 986-989.

McCann, S. E., Freudenheim, J. L., Marshall, J. R. and Graham, S. (2003) Risk of human ovarian cancer is related to dietary intake of selected nutrients, phytochemicals and food groups. *The Journal of nutrition* **133**, 1937-1942.

Mendilaharsu, M., De Stefani, E., Deneo-Pellegrini, H., Carzoglio, J. and Ronco, A. (1998) Phytosterols and risk of lung cancer: a case-control study in Uruguay. *Lung Cancer* **21**, 37-45.

Menger, L., Vacchelli, E., Adjemian, S., Martins, I., Ma, Y., Shen, S., Yamazaki, T., Sukkurwala, A. Q., Michaud, M., Mignot, G., Schlemmer, F., Sulpice, E., Locher, C., Gidrol, X., Ghiringhelli, F., Modjtahedi, N., Galluzzi, L., André, F., Zitvogel, L., Kepp, O. and Kroemer, G. (2012) Cardiac Glycosides Exert Anticancer Effects by Inducing Immunogenic Cell Death. *Science Translational Medicine* **4**, 1-9.

Middleton, E., Jr., Kandaswami, C. and Theoharides, T. C. (2000) The effects of plant flavonoids on mammalian cells: implications for inflammation, heart disease, and cancer. *Pharmacological Reviews* **52**, 673-751.

Mosmann, T. (1983) Rapid colorimetric assay for cellular growth and survival: Application to proliferation and cytotoxicity assays. *Journal of Immunological Methods* **65**, 55-63.

Mukhija, M., Dhar, K. L. and Kalia, A. N. (2014) Bioactive Lignans from Zanthoxylum alatum Roxb. stem bark with cytotoxic potential. *Journal of Ethnopharmacology* **152**, 106-112.

Muranaka, M., Hirota, K. and Ono, T. (2010) PEG–PLA nanoparticles prepared by emulsion solvent diffusion using oil-soluble and water-soluble PEG–PLA. *Materials Letters* **64**, 969-971.

161

Murherjee, S., Chowdhury, D., Kotcherlakota, R., Patra, S., Vinothkumar, B., Bhadra, P. M., Sreedhar, B. and Chitta, R. P. (2014) Potential theranostics application of bio-synthesized silver nanoparticles (4-in-1 system). *Theranostics* **4**, 316-333.

Nath, M. C., Chakravorty, M. K. and Chowdhury, S. R. (1946) Liebermann-Burchard Reaction for Steroids. *Nature* **157**, 103.

Neugut, A. I. and Prigerson, H. G. (2017) Curative, Life-Extending, and Palliative Chemotherapy: New Outcomes Need New Names. *The oncologist* **22**, 883-885.

Newman, D. J. and Cragg, G. M. (2016) Natural Products as Sources of New Drugs from 1981 to 2014. *Journal of Natural Products* **79**, 629-661.

Newman, R. A., Yang, P., Pawlus, A. D. and Block, K. I. (2008) Cardiac glycosides as novel cancer therapeutic agents. *Molecular Interventions* **8**, 36.

Ouyang, D.-W., Ni, X., Xu, H.-Y., Chen, J., Yang, P.-M. and Kong, D.-Y. (2010) Pterosins from Pteris multifida. *Planta Medica* **76**, 1896-1900.

Pal, S. L., Jana, U., Manna, P., Mohanta, G. and Manavalan, R. (2011) Nanoparticle: an overview of preparation and characterization. *Journal of Applied Pharmaceutical Science* **1**, 228-234.

Park, C., Moon, D. O., Rhu, C. H., Choi, B. T., Lee, W. H., Kim, G. Y. and Choi, Y. H. (2007) Beta-sitosterol induces anti-proliferation and apoptosis in human leukemic U937 cells through activation of caspase-3 and induction of Bax/Bcl-2 ratio. *Biological & Pharmaceutical Bulletin* **30**, 1317-1323.

Paterna, A., Gomes, S. E., Borralho, P. M., Mulhovo, S., Rodrigues, C. M. and Ferreira, M.-J. U. (2016) Vobasinyl–Iboga Alkaloids from *Tabernaemontana elegans*: Cell Cycle Arrest and

Apoptosis-Inducing Activity in HCT116 Colon Cancer Cells. *Journal of Natural Products* **79**, 2624-2634.

Pecora, R. (2000) Dynamic Light Scattering Measurement of Nanometer Particles in Liquids. *Journal of Nanoparticle Research* **2**, 123-131.

Perchellet, E. M., Magill, M. J., Huang, X., Dalke, D. M., Hua, D. H. and Perchellet, J. P. (2000) 1,4-Anthraquinone: an anticancer drug that blocks nucleoside transport, inhibits macromolecule synthesis, induces DNA fragmentation, and decreases the growth and viability of L1210 leukemic cells in the same nanomolar range as daunorubicin in vitro. *Anti-Cancer Drugs* **11**, 339-352.

Perera, P., Samuelsson, G., van Beek, T. A. and Verpoorte, R. (1983) Tertiary indole alkaloids from leaves of Tabernaemontana dichotoma. *Planta Medica* **47**, 148-150.

Pillai, G. (2014) Nanomedicines for cancer therapy: an update of FDA approved and those under various stages of development. *SOJ Pharm Pharm Sci* **1**, 13.

Powis, G. (1994) Signalling pathways as target for anticancer drug development. *Pharmacology & Therapeutics* **62**, 57-95.

Prassas, I. and Diamandis, E. P. (2008) Novel therapeutic applications of cardiac glycosides. *Nature Reviews: Drug Discovery* **7**, 926-935.

Queiroz, E. F., Hay, A. E., Chaaib, F., van Diemen, D., Diallo, D. and Hostettmann, K. (2006) New and bioactive aromatic compounds from *Zanthoxylum zanthoxyloides*. *Planta Medica* **72**, 746-750.

Rafiei, P. and Haddadi, A. (2017) Docetaxel-loaded PLGA and PLGA-PEG nanoparticles for intravenous application: pharmacokinetics and biodistribution profile. *International journal of nanomedicine* **12**, 935.

Raicht, R. F., Cohen, B. I., Fazzini, E. P., Sarwal, A. N. and Takahashi, M. (1980) Protective Effect of Plant Sterols against Chemically Induced Colon Tumors in Rats. *Cancer Research* **40**, 403-405.

Ramos-Tejadaa, M. d. M., Viotab, J. L., Rudzkac, K. and Delgado, V. A. (2015) Preparation of multi-functionalized Fe3O4/Au nanoparticles formedical purposes. *Colloids and Surfaces B: Biointerfaces* **128** 1–7.

Raval, A., Bahadur, P. and Raval, A. (2017) Effect of nonionic surfactants in release media on accelerated in-vitro release profile of sirolimus eluting stents with biodegradable polymeric coating. *Journal of Pharmaceutical Analysis* **8**, 45-54.

Ray-Coquard, I., Blay, J.-Y., Italiano, A., Le Cesne, A., Penel, N., Zhi, J., Heil, F., Rueger, R., Graves, B. and Ding, M. (2012) Effect of the MDM2 antagonist RG7112 on the P53 pathway in patients with MDM2-amplified, well-differentiated or dedifferentiated liposarcoma: an exploratory proof-of-mechanism study. *The lancet oncology* **13**, 1133-1140.

Reis, C. P., Neufeld, R. J., Ribeiro, A. J. and Veiga, F. (2006) Nanoencapsulation I. Methods for preparation of drug-loaded polymeric nanoparticles. *Nanomedicine: Nanotechnology, Biology and Medicine* **2**, 8-21.

Ross, K. A., Brenza, T. M., Binnebose, A. M., Phanse, Y., Kanthasamy, A. G., Gendelman, H. E., Salem, A. K., Bartholomay, L. C., Bellaire, B. H. and Narasimhan, B. (2015) Nano-enabled

delivery of diverse payloads across complex biological barriers. *Journal of Controlled Release* **219**, 548-559.

Sahu, A., Bora, U., Kasoju, N. and Goswami, P. (2008) Synthesis of novel biodegradable and self-assembling methoxy poly(ethylene glycol)–palmitate nanocarrier for curcumin delivery to cancer cells. *Acta Biomaterialia* **4**, 1752-1761.

Salatin, S. and Khosroushahi, A. Y. (2017) Overviews on the cellular uptake mechanism of polysaccharide colloidal nanoparticles. *Journal of Cellular and Molecular Medicine* **21**, 1668-1686.

Sandjo, L. P., Kuete, V., Tchangna, R. S., Efferth, T. and Ngadjui, B. T. (2014) Cytotoxic Benzophenanthridine and Furoquinoline Alkaloids from *Zanthoxylum buesgenii* (Rutaceae). *Chemistry Central Journal* **8**, 1-5.

Santhanam, R. K., Ahmad, S., Abas, F., Safinar Ismail, I., Rukayadi, Y., Tayyab Akhtar, M. and Shaari, K. (2016) Bioactive Constituents of *Zanthoxylum rhetsa* Bark and Its Cytotoxic Potential against B16-F10 Melanoma Cancer and Normal Human Dermal Fibroblast (HDF) Cell Lines. *Molecules* **21**, 652.

Saraf, S. A. (2010) Applications of novel drug delivery system for herbal formulations. *Fitoterapia* **81**, 680-689.

Sashida, Y., Ogawa, K., Mori, N. and Yamanouchi, T. (1992) Triterpenoids from the fruit galls of Actinidia polygama. *Phytochemistry* **31**, 2801-2804.

Satria, D., Silalahi, J., Haro, G., Ilyas, S. and Hasibuan, P. A. Z. (2019) Cell Cycle Inhibition of Ethylacetate Fraction of *Zanthoxylum Acanthopodium* DC. Fruit against T47D Cells. *Open access Macedonian journal of medical sciences* **7**, 726-729.

Schripsema, J., Hermans-Lokkerbol, A., Van der Heijden, R., Verpoorte, R., Svendsen, A. B. and Van Beek, T. (1986) Alkaloids of *Tabernaemontana ventricosa*. *Journal of Natural Products* **49**, 733-735.

Senderowicz, A. M. (1999) Flavopiridol: the first cyclin-dependent kinase inhibitor in human clinical trials. *Investigational New Drugs* **17**, 313-320.

Sever, R. and Brugge, J. S. (2015) Signal transduction in cancer. *Cold Spring Harbor Perspectives in Medicine* **5**, 1-21.

Shah M. U, Patel S. M, Patel P. H, Hingorani L and Jadhav R. B. (2010) Development and Validation of a Simple Isocratic HPLC Method for Simultaneous Estimation of Phytosterols in Cissus quadrangularis. *Indian Journal of Pharmaceutical Sciences* **72**, 753-758.

Shaikh, J., Ankola, D., Beniwal, V., Singh, D. and Kumar, M. R. (2009) Nanoparticle encapsulation improves oral bioavailability of curcumin by at least 9-fold when compared to curcumin administered with piperine as absorption enhancer. *European Journal of Pharmaceutical Sciences* **37**, 223-230.

Shan, X., Yuan, Y., Liu, C., Xu, F. and Sheng, Y. (2009) Comparison of the PLA-mPEG and mPEG-PLA-mPEG copolymers nanoparticles on the plasma protein adsorption and in vivo biodistribution. *Soft Matter* **5**, 2875.

Shareef, M., Ashraf, M. A. and Sarfraz, M. (2016) Natural cures for breast cancer treatment. *Saudi pharmaceutical journal* **24**, 233-240.

Sharma, N., Madan, P. and Lin, S. (2016) Effect of process and formulation variables on the preparation of parenteral paclitaxel-loaded biodegradable polymeric nanoparticles: A co-surfactant study. *Asian journal of pharmaceutical sciences* **11**, 404-416.

Shenouda, N. S., Sakla, M. S., Newton, L. G., Besch-Williford, C., Greenberg, N. M., MacDonald, R. S. and Lubahn, D. B. (2007) Phytosterol *Pygeum africanum* regulates prostate cancer in vitro and in vivo. *Endocrine* **31**, 72-81.

Shi, M., Cai, Q., Yao, L., Mao, Y., Ming, Y. and Ouyang, G. (2006) Antiproliferation and apoptosis induced by curcumin in human ovarian cancer cells. *Cell Biology International* **30**, 221-226.

Shubhika, K. (2012) Nanotechnology and medicine-The upside and the downside. *Int. J. Drug Dev. Res* **5**, 1-10.

Song, K. C., Lee, H. S., Choung, I. Y., Cho, K. I., Ahn, Y. and Choi, E. J. (2006) The effect of type of organic phase solvents on the particle size of poly (d, l-lactide-co-glycolide) nanoparticles. *Colloids and Surfaces A: Physicochemical and Engineering Aspects* **276**, 162-167.

Su, Y., Hu, J., Huang, Z., Huang, Y., Peng, B., Xie, N. and Liu, H. (2017) Paclitaxel-loaded star-shaped copolymer nanoparticles for enhanced malignant melanoma chemotherapy against multidrug resistance. *Drug Design, Development and Therapy* **11** 659–668.

Sudimack, J. and Lee, R. J. (2000) Targeted drug delivery via the folate receptor. *Advanced Drug Delivery Reviews* **41**, 147-162.

Sun, Y. (2006) p53 and its downstream proteins as molecular targets of cancer. *Molecular Carcinogenesis* **45**, 409-415.

Suraf, S. A. (2010) Applications of novel drug delivery system for herbal formulations. *Fitoterapia* **81** 680-689.

Surh, Y. J. (2003) Cancer chemoprevention with dietary phytochemicals. *Nature Reviews: Cancer* **3**, 768-780.

Suttiarporn, P., Chumpolsri, W., Mahatheeranont, S., Luangkamin, S., Teepsawang, S. and Leardkamolkarn, V. (2015) Structures of phytosterols and triterpenoids with potential anti-cancer activity in bran of black non-glutinous rice. *Nutrients* **7**, 1672-1687.

Takao, N., Kamigauchi, M. and Okada, M. (1983) Biosynthesis of Benzo [clphenanthridine Alkaloids Sanguinarine, Chelirubine and Macarpine. *HELVETICA CHEMICA ACTA* **66**, 473-484.

Tarus, P. K., P.H. Coombes, Crouch, N. R. and Mulholland, D. A. (2006) Benzo[c]phenanthridine alkaloids from stem bark of the Forest Knobwood, *Zanthoxylum davyi* (Rutaceae). *South African Journal of Botany* **72**, 555–558.

Thapa, R. K., Khan, G. M., Parajuli-Baral, K. and Thapa, P. (2013) Herbal Medicine Incorporated Nanoparticles: Advancements in Herbal Treatment. *Asian Journal of Biomedical and Pharmaceutical sciences* **3**, 7-14

Toh-Seok, K., Kooi-Mow Sim, Takashi Koyano, Mitsuhide Toyoshima, Masahiko Hayashi and Komiyama, K. (1998) Conodiparines A-D, new bisindoles from Taberneamontana. Reversal of vincristine-resistance with cultured cells. *Bioorganic & Medicinal Chemistry Letters* **8** 1693-1696.

Tran, S., DeGiovanni, P.-J., Piel, B. and Rai, P. (2017) Cancer nanomedicine: a review of recent success in drug delivery. *Clinical and translational medicine* **6**, 44.

Van der Heijden, R., Louwe, C., Verhey, E., Harkes, P. and Verpoorte, R. (1989) Characterization of a suspension culture of Tabernaemontana elegans on growth, nutrient uptake, and accumulation of indole alkaloids. *Planta Medica* **55**, 158-162.

Vargas, A., Pegaz, B., Debefve, E., Konan-Kouakou, Y., Lange, N., Ballini, J.-P., van den Bergh, H., Gurny, R. and Delie, F. (2004) Improved photodynamic activity of porphyrin loaded into nanoparticles: an in vivo evaluation using chick embryos. *International Journal of Pharmaceutics* **286**, 131-145.

Vogelstein, B., Lane, D. and Levine, A. J. (2000) Surfing the p53 network. *Nature* **408**, 307-310.

von Holtz, R. L., Fink, C. S. and Awad, A. B. (1998) β - sitosterol activates the sphingomyelin cycle and induces apoptosis in LNCaP human prostate cancer cells. *Nutrition and Cancer* **32**, 8-12.

Wang, Y., Li, P., Truong-Dinh Tran, T., Zhang, J. and Kong, L. (2016) Manufacturing techniques and surface engineering of polymer based nanoparticles for targeted drug delivery to cancer. *Nanomaterials* **6**, 26.

Wicki, A., Witzigmann, D., Balasubramanian, V. and Huwyler, J. (2015) Nanomedicine in cancer therapy: challenges, opportunities, and clinical applications. *Journal of Controlled Release* **200**, 138-157.

Winnicka, K., Bielawski, K. and Bielawska, A. (2006) Cardiac glycosides in cancer research and cancer therapy. *Acta Pol Pharm* **63**, 109-115.

Wolinsky, J. B., Colson, Y. L. and Grinstaff, M. W. (2012) Local drug delivery strategies for cancer treatment: gels, nanoparticles, polymeric films, rods, and wafers. *Journal of controlled release : official journal of the Controlled Release Society* **159**, 14-26.

Wube, A. A., Bucar, F., Asres, K., Gibbons, S., Rattray, L. and Croft, S. L. (2005) Antimalarial compounds from Kniphofia foliosa roots. *Phytotherapy Research* **19**, 472-476.

Yao, Q., Hou, S. X., He, W. L., Feng, J. L., Wang, X. C., Fei, H. X. and Chen, Z. H. (2006) Study on the preparation of resveratrol chitosan nanoparticles with free amino groups on the surface. *Zhongguo Zhong Yao Za Zhi. Zhongguo Zhongyao Zazhi. China Journal of Chinese Materia Medica* **31**, 205-208.

Yazdanpanahi, N., Behbahani, M. and Yektaeian, A. (2014) Effect of boswellia thurifera gum methanol extract on cytotoxicity and p53 gene expression in human breast cancer cell line. *Iranian journal of pharmaceutical research* **13**, 719-724.

Yenesew, A., Ogur, J. and Duddeckt, H. (1993) (R)-Prechrysophanol from *Aloe graminicola*. *Phytochemistry* **34**, 1442-1444.

Yoo, H. S., Oh, J. E., Lee, K. H. and Park, T. G. (1999) Biodegradable nanoparticles containing doxorubicin-PLGA conjugate for sustained release. *Pharmaceutical Research* **16**, 1114-1118.

Yue, G. G. L., Chan, B. C. L., Hon, P.-M., Lee, M. Y. H., Fung, K.-P., Leung, P.-C. and Lau, C. B. S. (2010) Evaluation of in vitro anti-proliferative and immunomodulatory activities of compounds isolated from Curcuma longa. *Food and chemical toxicology* **48**, 2011-2020.

Zavaleta, C., Ho, D. and Chung, E. J. (2018) Theranostic Nanoparticles for Tracking and Monitoring Disease State. *SLAS Technol* **23**, 281-293.

Zhang, H.-y., Firempong, C. K., Wang, Y.-w., Xu, W.-q., Wang, M.-m., Cao, X., Zhu, Y., Tong, S.-s., Yu, J.-n. and Xu, X.-m. (2016) Ergosterol-loaded poly(lactide-co-glycolide)

nanoparticles with enhanced in vitro antitumor activity and oral bioavailability. *Acta Pharmacologica Sinica* **37**, 834-844.

Zhang, J., Yu, Y., Liu, D. and Liu, Z. (2007) Extraction and composition of three naturally occurring anti-cancer alkaloids in *Camptotheca acuminata* seed and leaf extracts. *Phytomedicine* **14**, 50-56.

Zhang, L. J., Cheng, J. J., Liao, C. C., Cheng, H. L., Huang, H. T., Kuo, L. M. and Kuo, Y. H. (2012) Triterpene acids from Euscaphis japonica and assessment of their cytotoxic and anti-NO activities. *Planta Medica* **78**, 1584-1590.

Zhang, Y., Guo, L., Yang, G., Guo, F., Di, Y., Li, S., Chen, D. and Hao, X. (2015) New vobasinyl-ibogan type bisindole alkaloids from *Tabernaemontana corymbosa*. *Fitoterapia* **100**, 150-155.

Zhong, R., Guo, Q., Zhou, G., Fu, H. and Wan, K. (2015) Three new labdane-type diterpene glycosides from fruits of *Rubus chingii* and their cytotoxic activities against five humor cell lines. *Fitoterapia* **102**, 23-26.

Uncategorized References

Agrawal, P. K. (2013). *Carbon-13 NMR of flavonoids* (P. K. Agrawal Ed. Vol. 39): Elsevier. New York, USA, 1-573

American Cancer Society. (2017). Cancer facts & figures 2017. Atlanta.

Cancer Research UK. (2014). Worldwide cancer incidence statistics. Retrieved Nov. 11, 2015 http://www.cancerresearchuk.org/health-professional/cancer-statistics/incidence

Cancer Research UK. (2015, November). What is cancer. Retrieved 29/11/2015 http://www.cancerresearchuk.org/about-cancer/what-is-cancer

Cancer Research UK. (2017, 27/06/2017). Cancer drugs. Retrieved May 31, 2019

Cancer Treatment Centres of America. (2019). Chemotherapy. Retrieved 31/5/2019, from https://www.cancercenter.com/treatment-options/chemotherapy

Cooper, G. M. and Hausmans, R. E. (2007). *The Cell: A molecular approach* (4th ed.): Sinauer Associates, Inc. . Sunderland, (MA), 670-695

Debat, J. (1974). US Patent No. 339,205, March 8, 1973.international classification.

FDA. (2011). Ipilumumab. Retrieved 29/6/2016, from U.S. Department of Health and Human Services:

http://www.fda.gov/AboutFDA/CentersOffices/OfficeofMedicalProductsandTobacco/CDER/ucm248478.htm

Florence, A. T. and Salole, E. G. (1993). *Pharmaceutical aspects of cancer chemotherapy*: Butterworth-Heinemann. Oxford, UK, 1-132

Freres, P., Jerusalem, G. and Moonen, M. (2017). Categories of Anticancer Treatments. In P. Lancellotti, J. L. Zamorano Gómez & M. Galderisi (Eds.), *Anti-Cancer Treatments and Cardiotoxicity* (pp. 7-11). Boston: Academic Press, 7-11

GLOBOCAN. (2012). Cancer incidence and mortality worldwide. Retrieved November 23, 2015, from http://globocan.iarc.fr/Pages/fact_sheets_cancer.aspx

Jones, W. P. and Kinghorn, A. D. (2006). Extraction of plant secondary metabolites *Natural products isolation* (pp. 323-351): Springer, New York, USA, 323-351

Marks, F., Fürstenberger, G. and Müller-Decker, K. (2007). Tumor promotion as a target of cancer prevention *Cancer Prevention* (pp. 37-47): Springer, New York, USA, 37-47

Maya, S., Sabitha, M., Nair, S. and Jayakumar, R. (2013). Phytomedicine-Loaded Polymeric Nanomedicines: Potential Cancer Therapeutics. In P. K. Dutta & J. Dutta (Eds.), *Multifaceted Development and Application of Biopolymers for Biology, Biomedicine and Nanotechnology* (Vol. 254, pp. 203-239): Springer Berlin Heidelberg, 203-239

Negera, A. A. (2014). *Phytochemical investigation of four asphodelaceae plants for antiplasmodial principles.* (Ph.D), University of Nairobi.

Ostiguy, C., Lapointe, G., Ménard, L., Cloutier, Y., Trottier, M., Boutin, M., Antoun, M. and Normand, C. (2006). Nanoparticles Actual Knowledge about Occupational Health and Safety Risks and Prevention Measures (pp. 1-100). Montréal (Québec), 1-100

Pitot, H. C. (2002). *Fundamentals of oncology* (4th ed.): Marcel Dekker,Inc. New York. 1-20

Roy, K., Kar, S. and Das, R. N. (2015). Chapter 11 - SAR and QSAR in Drug Discovery and Chemical Design—Some Examples. In K. Roy, S. Kar & R. N. Das (Eds.), *Understanding the Basics of QSAR for Applications in Pharmaceutical Sciences and Risk Assessment* (pp. 427-453). Boston: Academic Press, 427-453

Thomson RH. (2012). *Naturally occurring quinones IV; Recent advances*: Blackie Academic & Professional. London SE18HN, UK, 309-453

U.S. Department of Health and Human Services, National Institute of Health and Institute, N. C. (2015). Cancer treatment. Retrieved November 23, 2015 http://www.cancer.gov/about-cancer/treatment

WHO. (2017). World Cancer day.

WHO. (2018). Latest global cancer data: Cancer burden rises to 18.1 million new cases and 9.6 million cancer deaths in 2018 [Press release]. Retrieved from https://www.who.int/cancer/PRGlobocanFinal.pdf

APPENDICES

Appendix 1: 1D and 2D NMR spectra of tridecan-2-one (**80**)
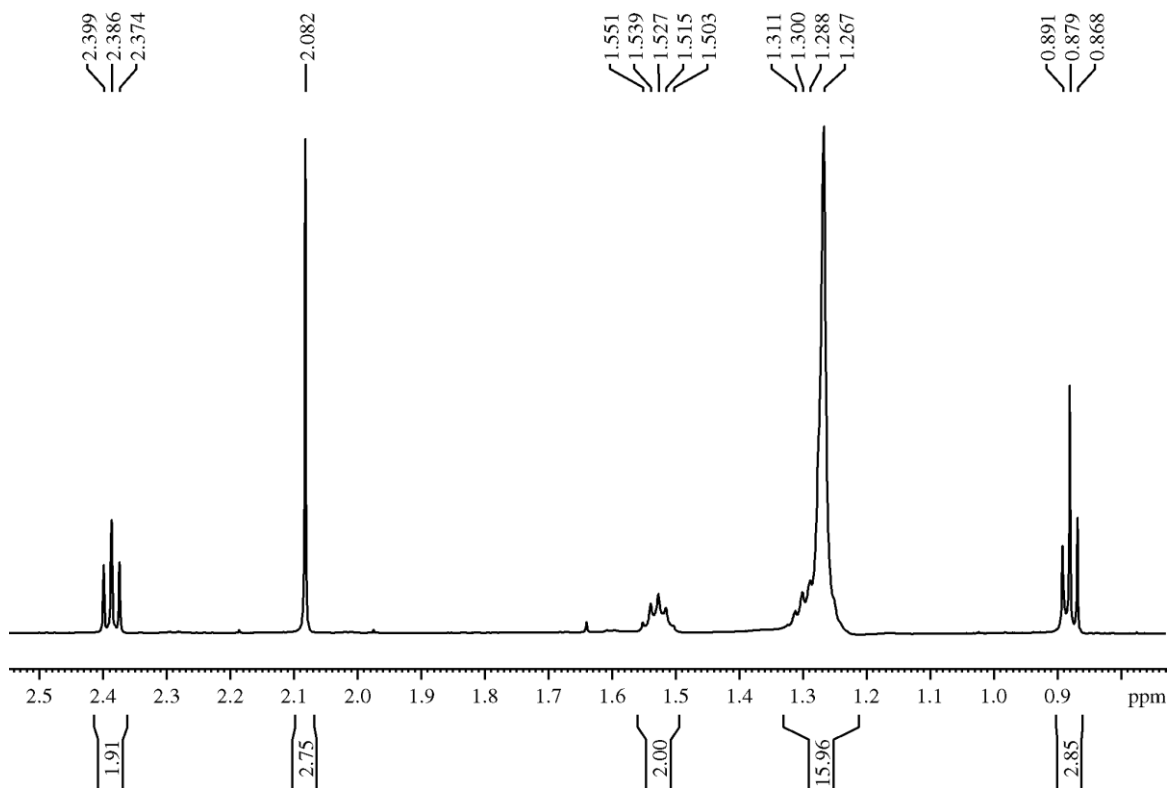
Appendix 1.1: ^{1}H NMR spectrum of tridecan-2-one (**80**) at 600 MHz in CD_2Cl_2
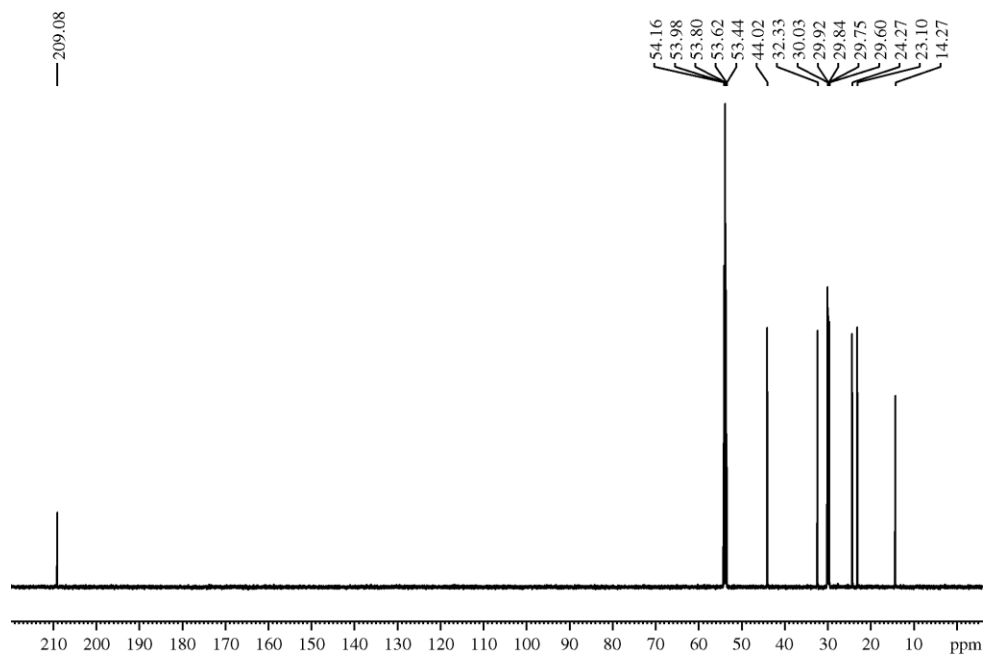
Appendix 1.2: ^{13}C NMR spectrum of tridecan-2-one (**80**) at 151 MHz in CD_2Cl_2
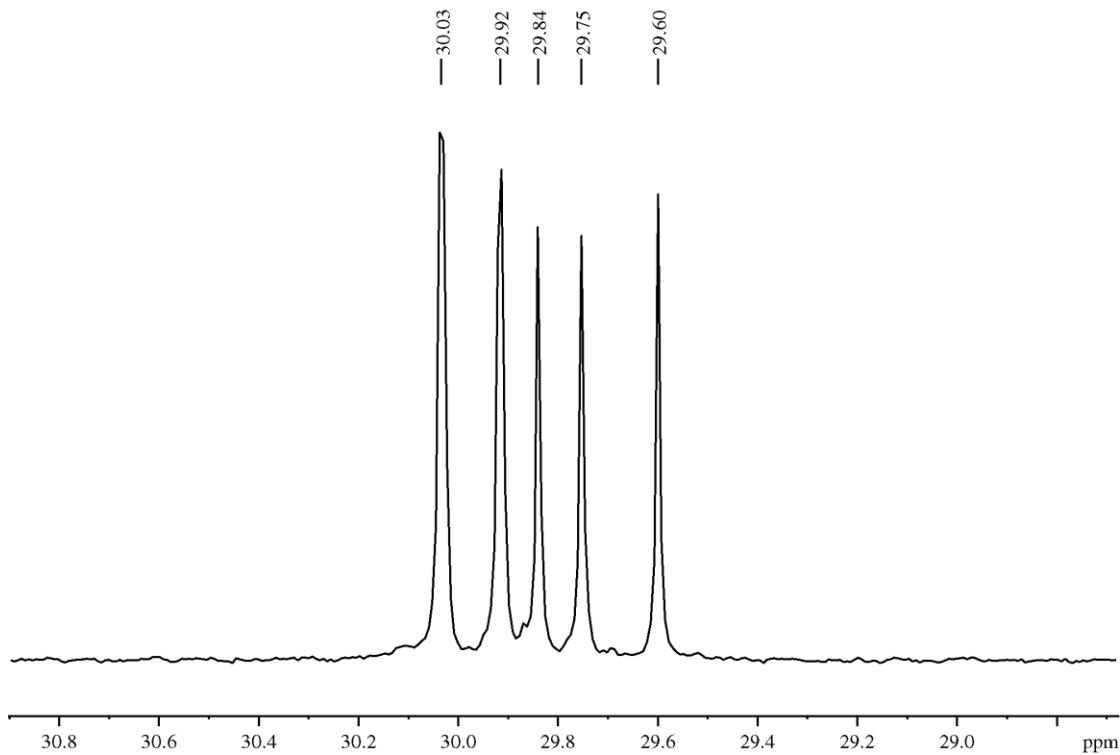
Appendix 1.3: Expansion of ^{13}C NMR spectrum of tridecan-2-one (**80**) at 151 MHz in CD_2Cl_2
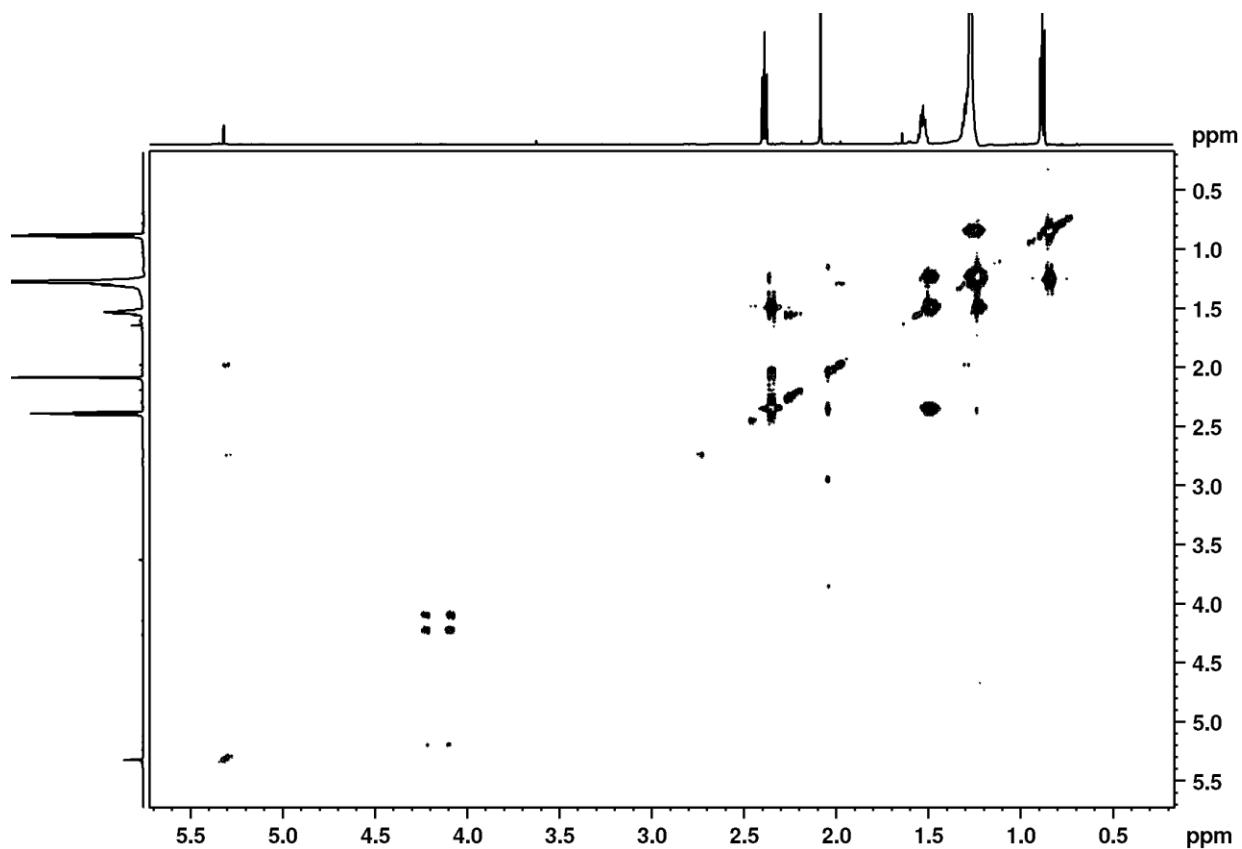
Appendix 1.4: H-H COSY spectrum of tridecan-2-one (**80**) at 600 MHz in CD$_2$Cl$_2$.
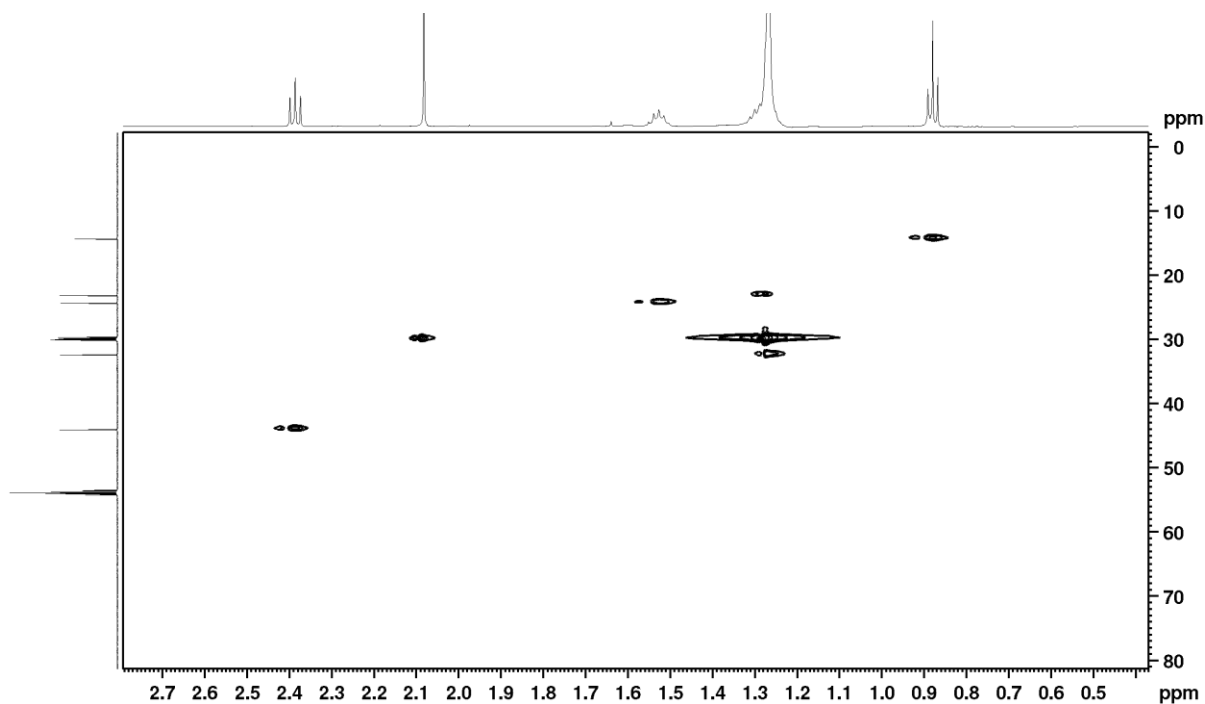
Appendix 1.5: HSQC spectrum of tridecan-2-one (**80**) at 600 MHz in CD$_2$Cl$_2$
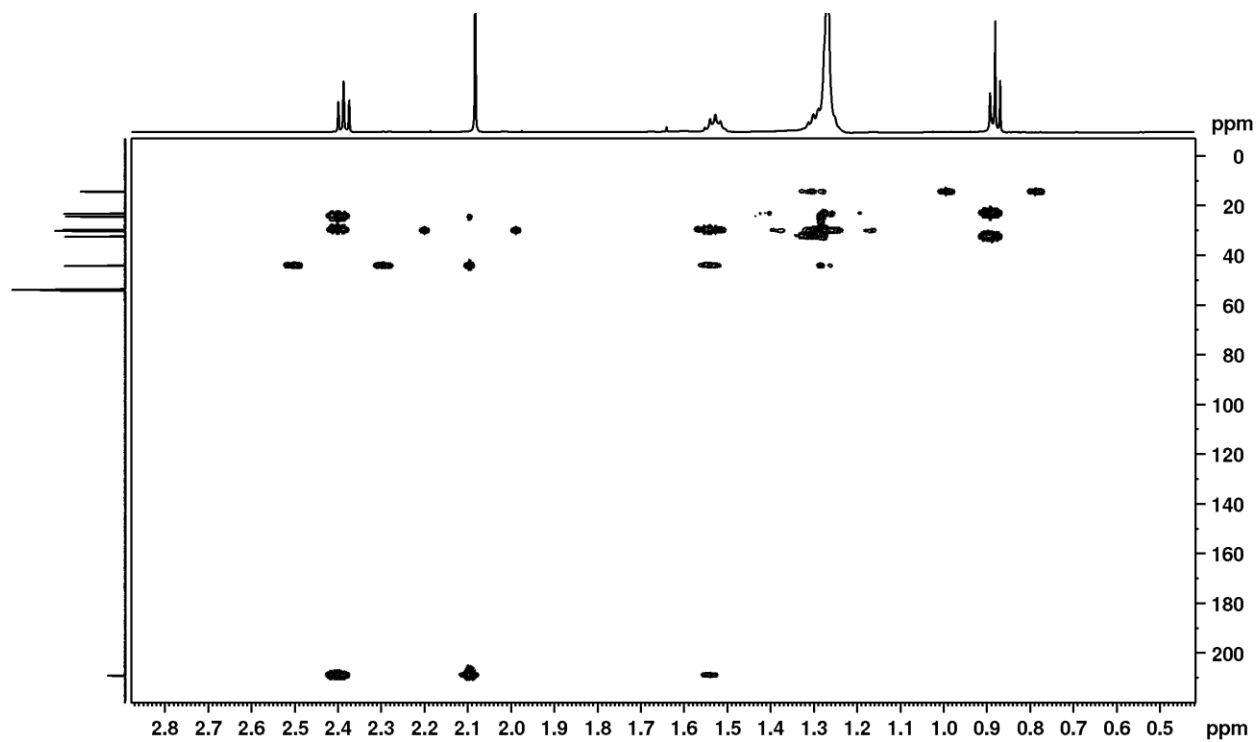
Appendix 1.6: HMBC spectrum of tridecan-2-one (**80)** at 600 MHz in CD_2Cl_2
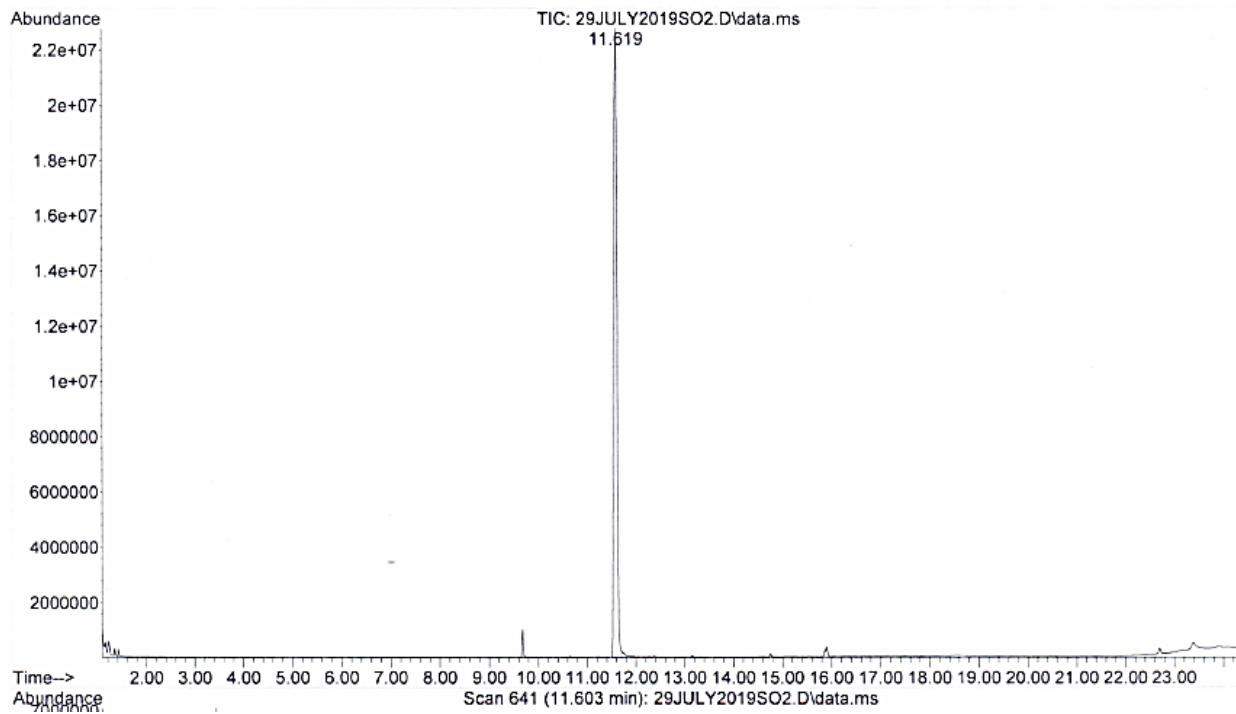
Appendix 1.7: GC-MS chromatogram of tridecan-2-one (**80)**

Hit 1 : 2-Tridecanone
C13H26O; MF: 945; RMF: 945; Prob 81.3%; CAS: 593-08-8; Lib: mainlib; ID: 24733.

(mainlib) 2-Tridecanone
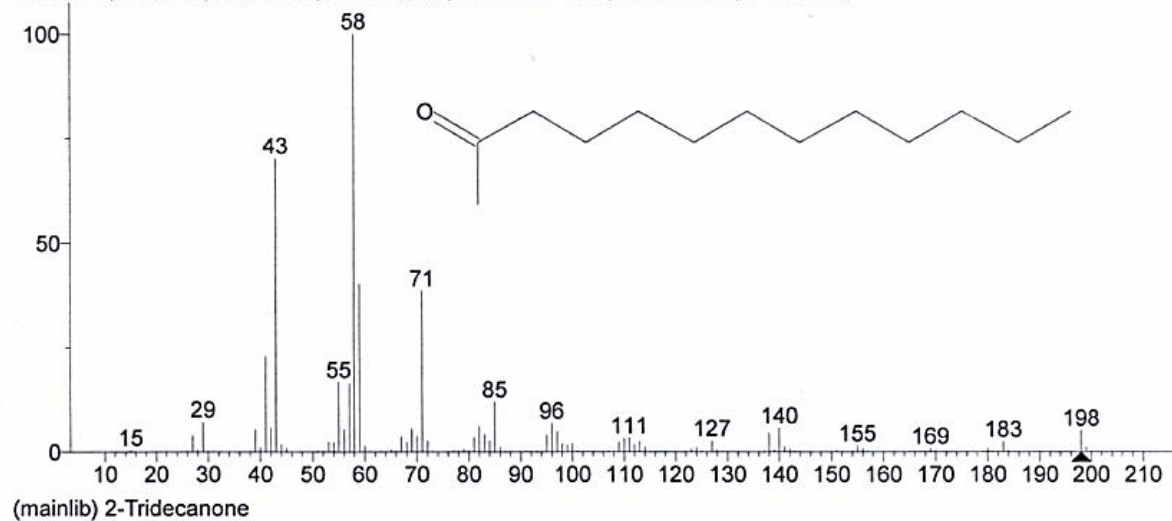
Appendix 1.8: GC-MS spectrum of tridecan-2-one (**80**)

Appendix 2: 1D and 2D Spectra of dihydrochelerythrine (**81**)
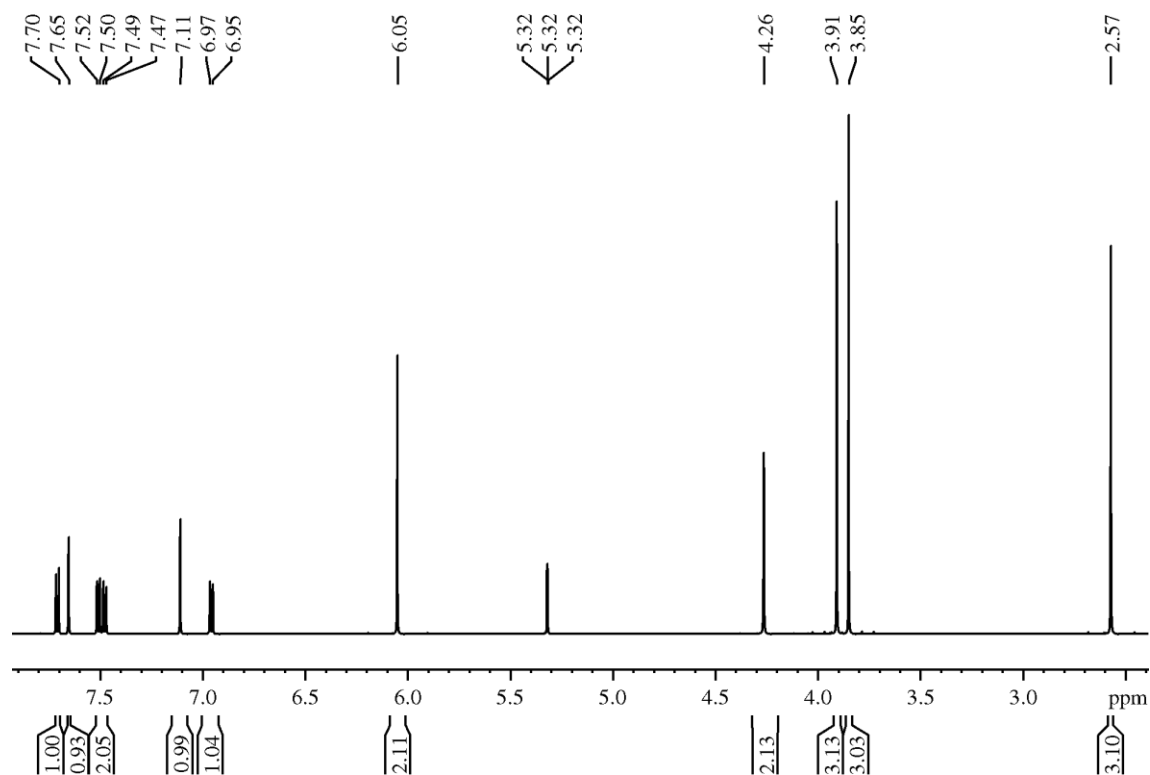
Appendix 2.1:^{1}H NMR spectrum of dihydrochelerythrine (**81**) at 600 MHz in CD_2Cl_2

179
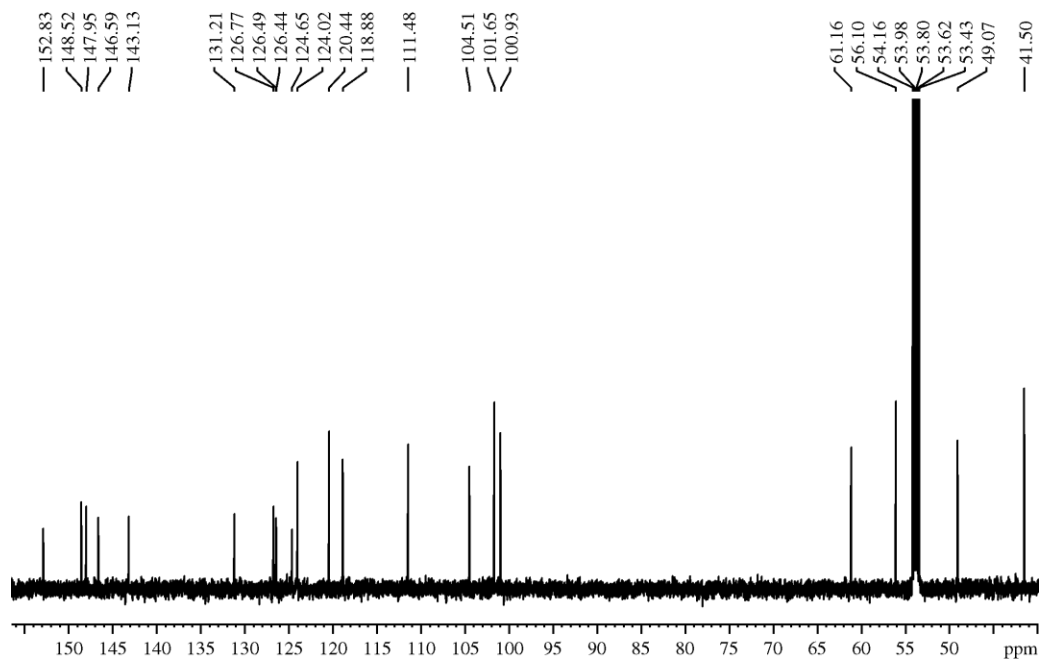
Appendix 2.2: ^{13}C NMR spectrum of dihydrochelerythrine (**81**) at 151 MHz in CD$_2$Cl$_2$
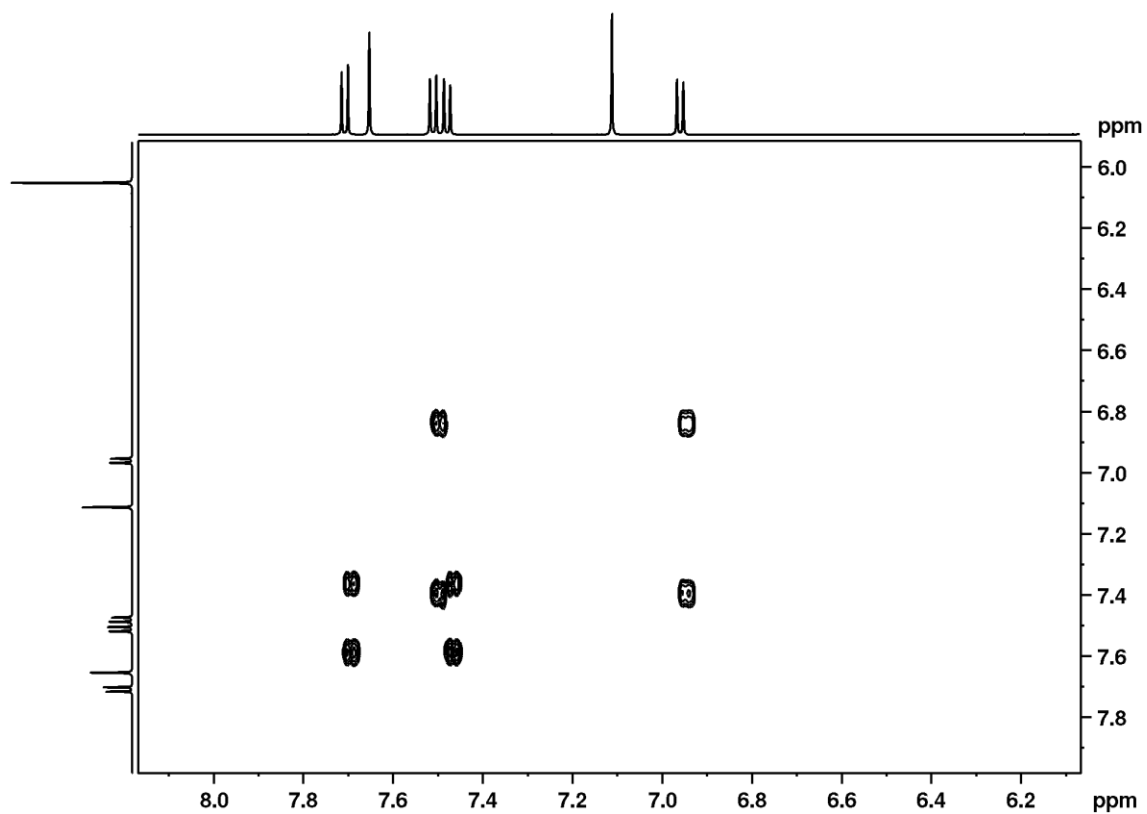
Appendix 2.3: Expansion of H-H COSY spectrum of ihydrochelerythrine (**81**) at 600 MHz in CD$_2$Cl$_2$
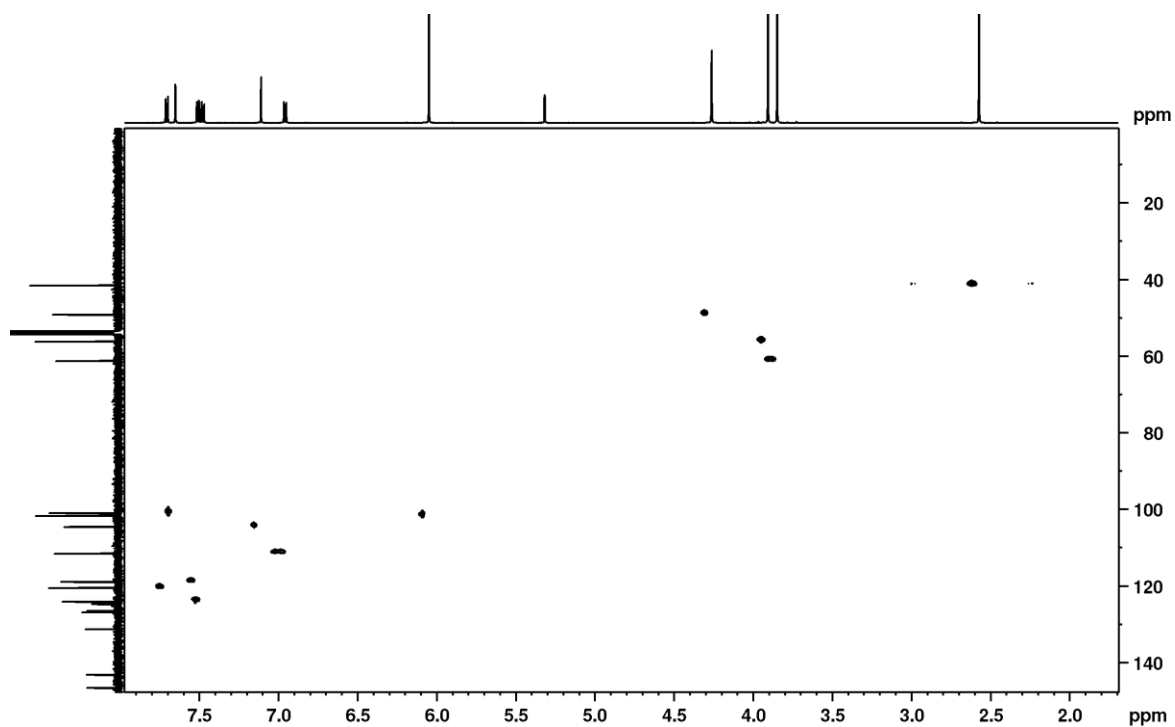
Appendix 2.4: HSQC spectrum of dihydrochelerythrine (**81**) at 600 MHz in CD_2Cl_2
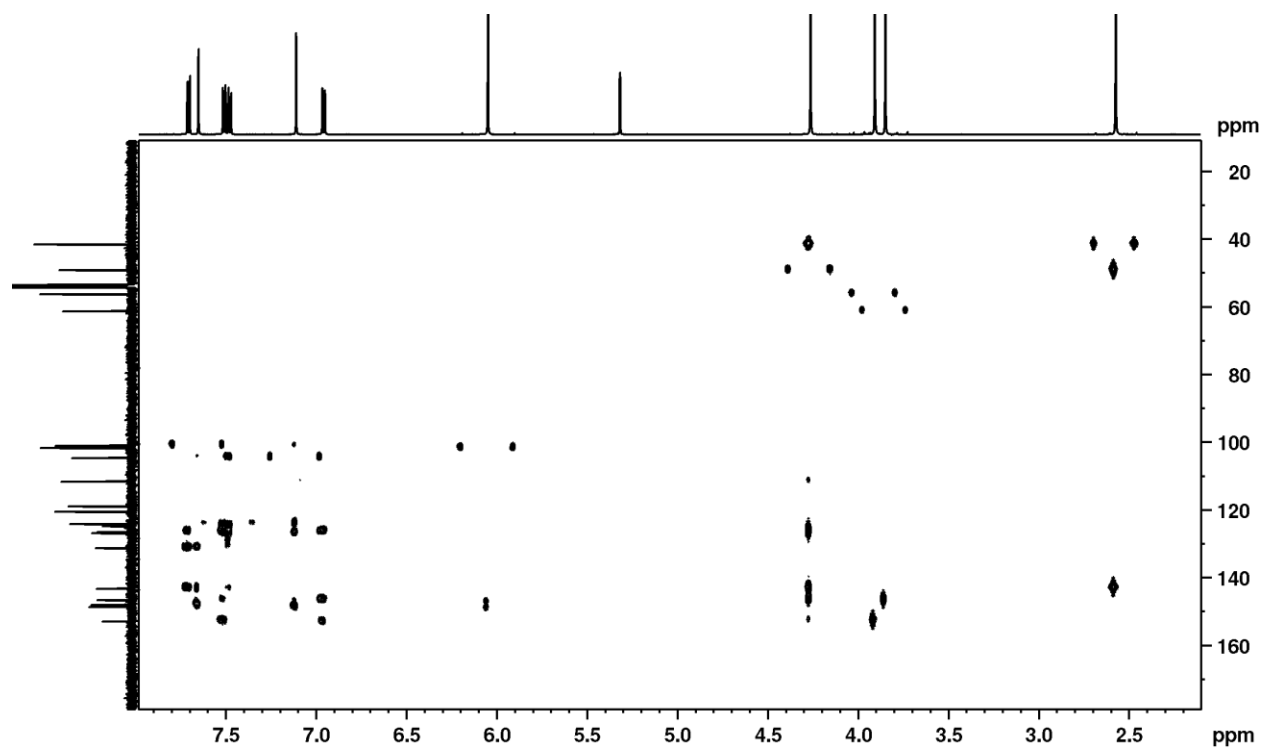
Appendix 2.5: HMBC spectrum of dihydrochelerythrine (**81**) at 600 MHz in CD_2Cl_2

181
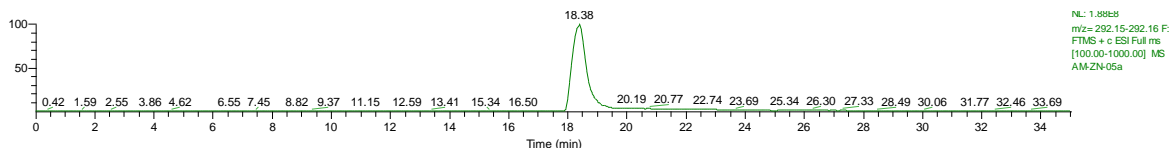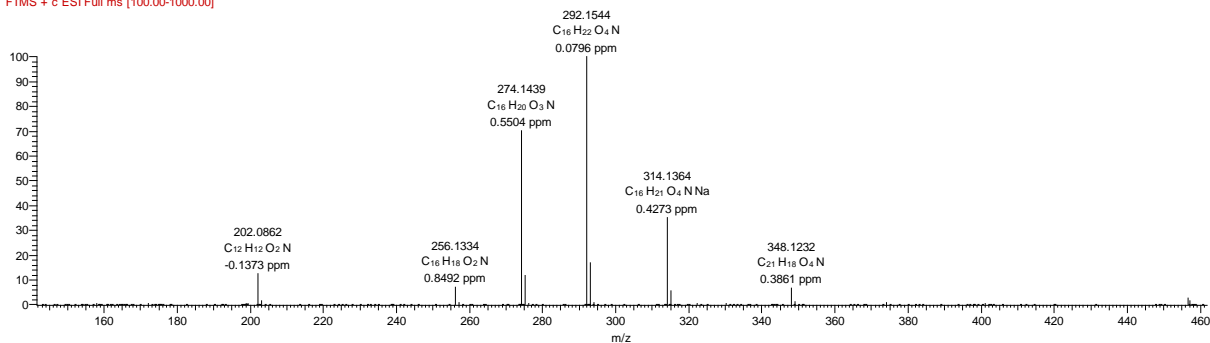
Appendix 2.6: LC-HRMS of dihydrochelerythrine (**81**).

Appendix 3: 1D and 2D NMR spectra of sesamin (**82**)
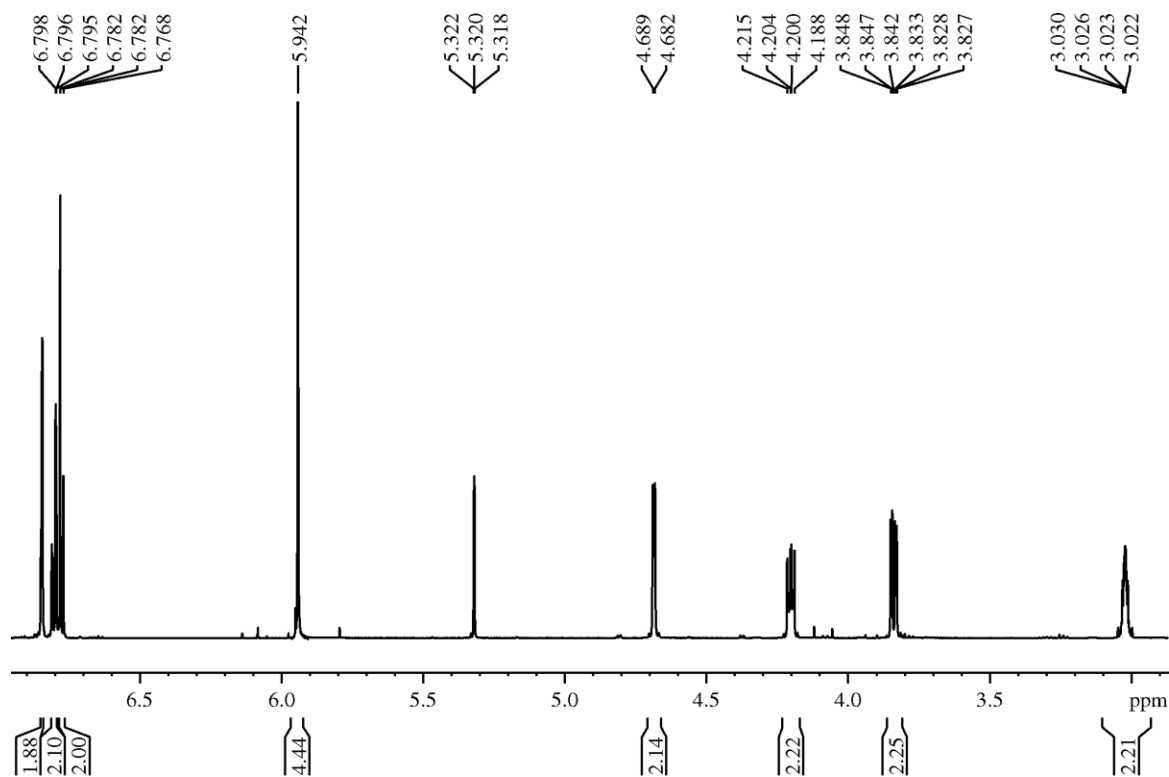
Appendix 3.1: ^{1}H NMR spectrum of sesamin (**82**) at 600 MHz in CD_2Cl_2.
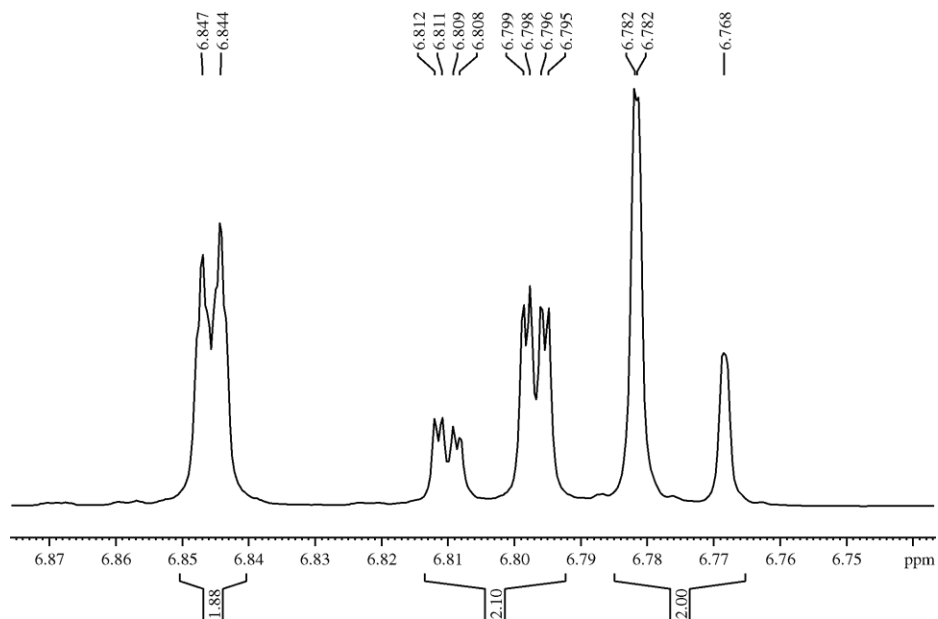
Appendix 3.2: Expansion of ^1H NMR spectrum of sesamin (**82**) at 600 MHz in CD_2Cl_2
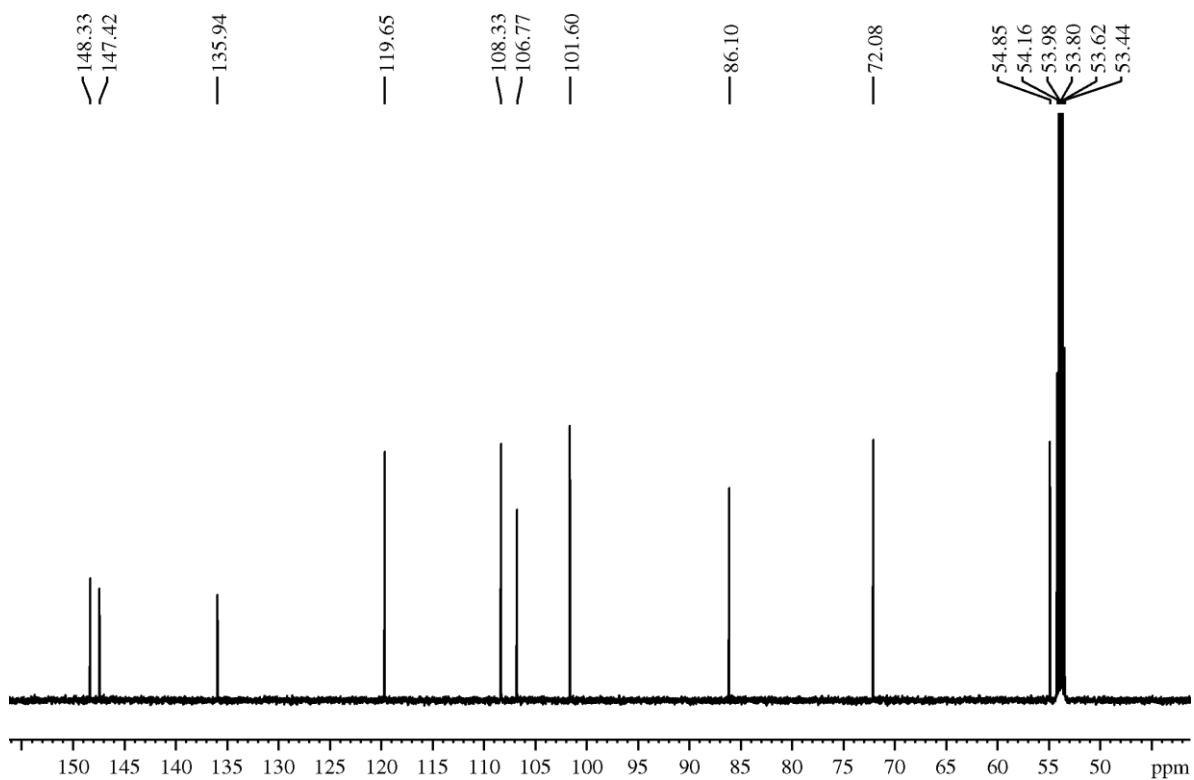
Appendix 3.3: ^{13}C NMR spectrum of sesamin (**82**) at 151 MHz in CD_2Cl_2
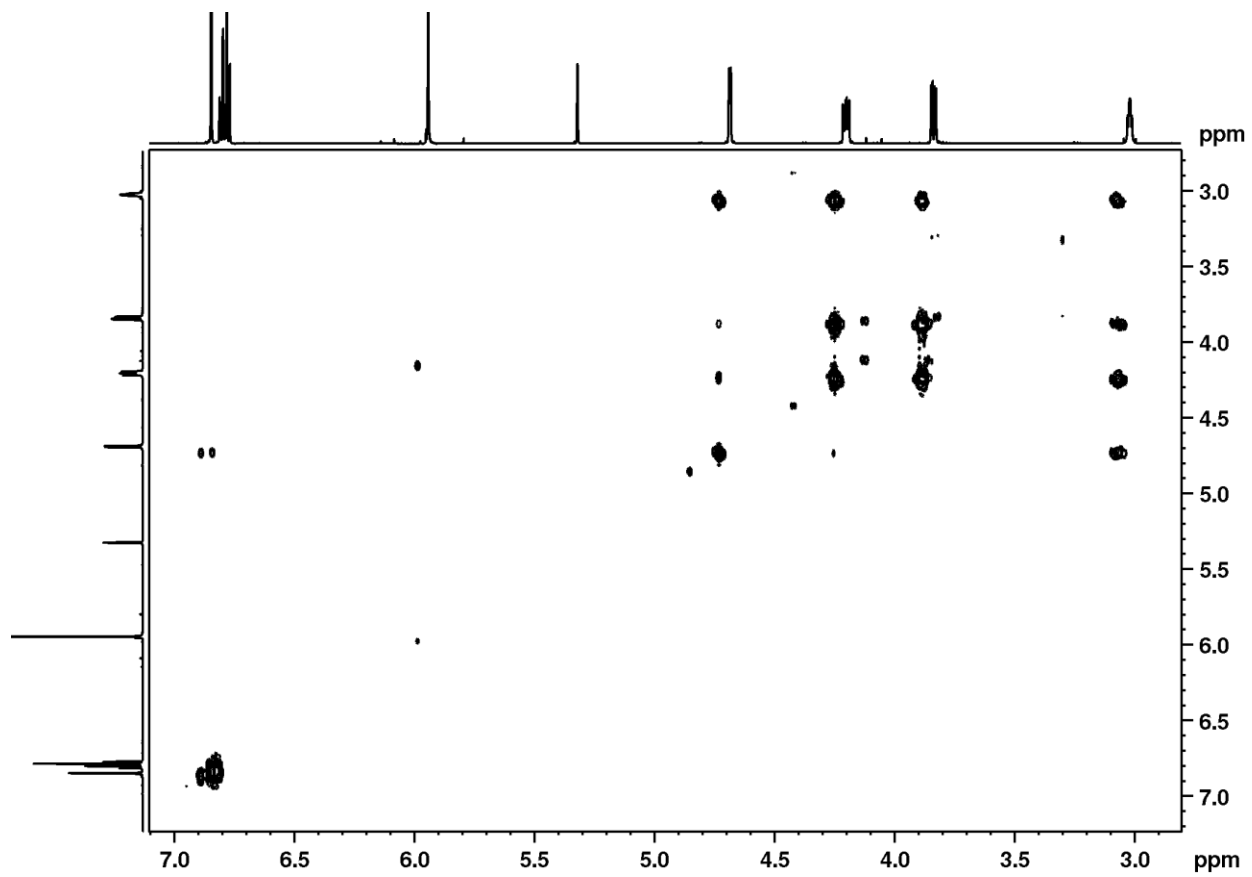
Appendix 3.4: H-H COSY spectrum of sesamin (**82**) at 600 MHz in CD$_2$Cl$_2$
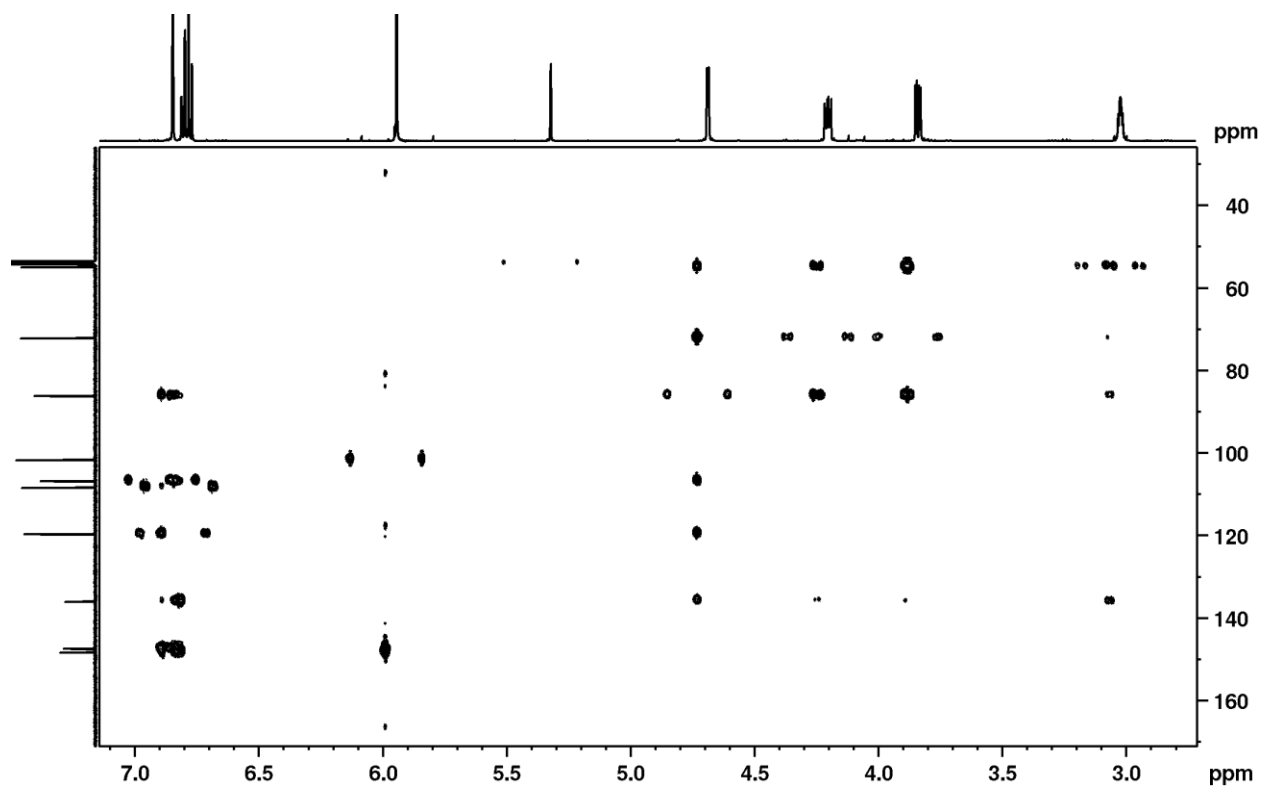
Appendix 3.5*: HMBC spectrum of sesamin (**82**) at 600 MHz in CD$_2$Cl$_2$

Appendix 4: 1D and 2D NMR spectra of skimmianine (**83**).
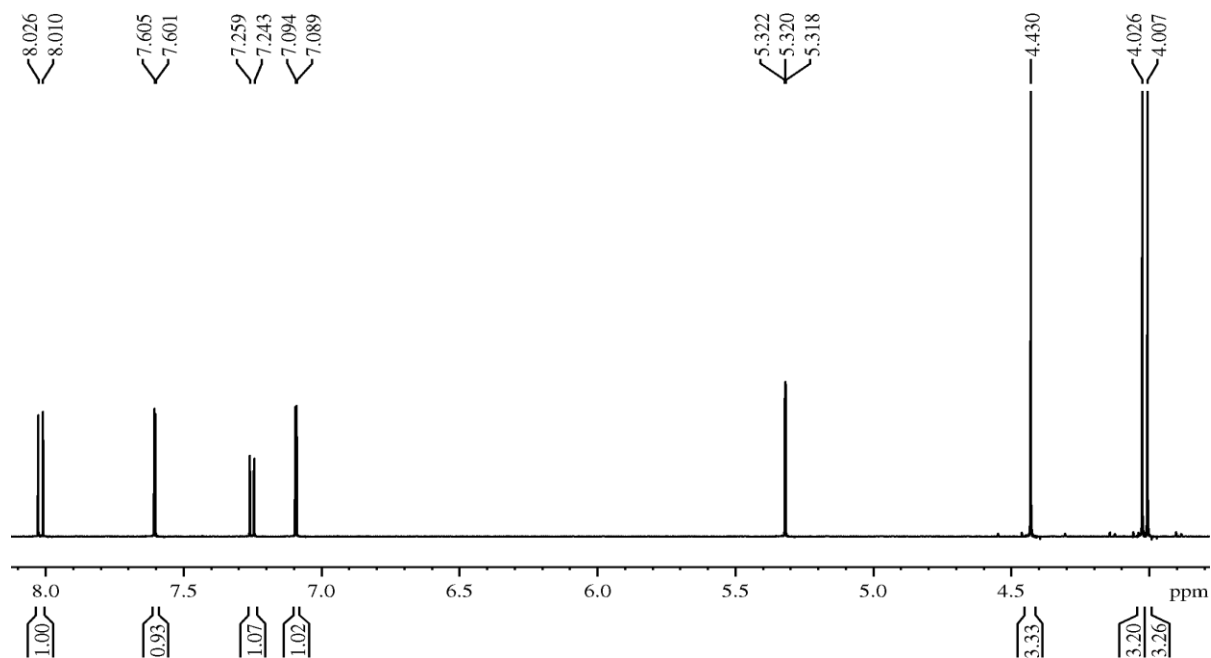
Appendix 4.1: ^{1}H NMR spectrum of skimmianine (**83**) at 600 MHz in CD_2Cl_2
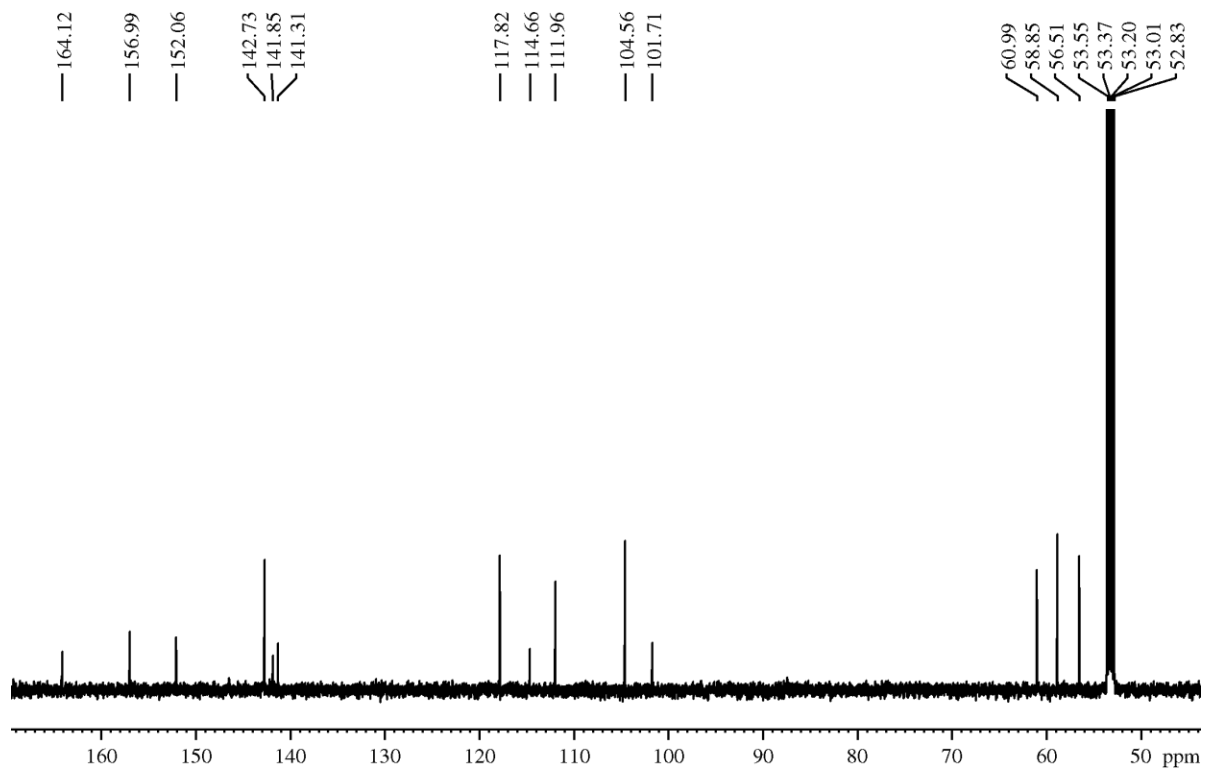
Appendix 4.2: ^{13}C NMR spectrum of skimmianine (**83**) at 151 MHz in CD$_2$Cl$_2$.
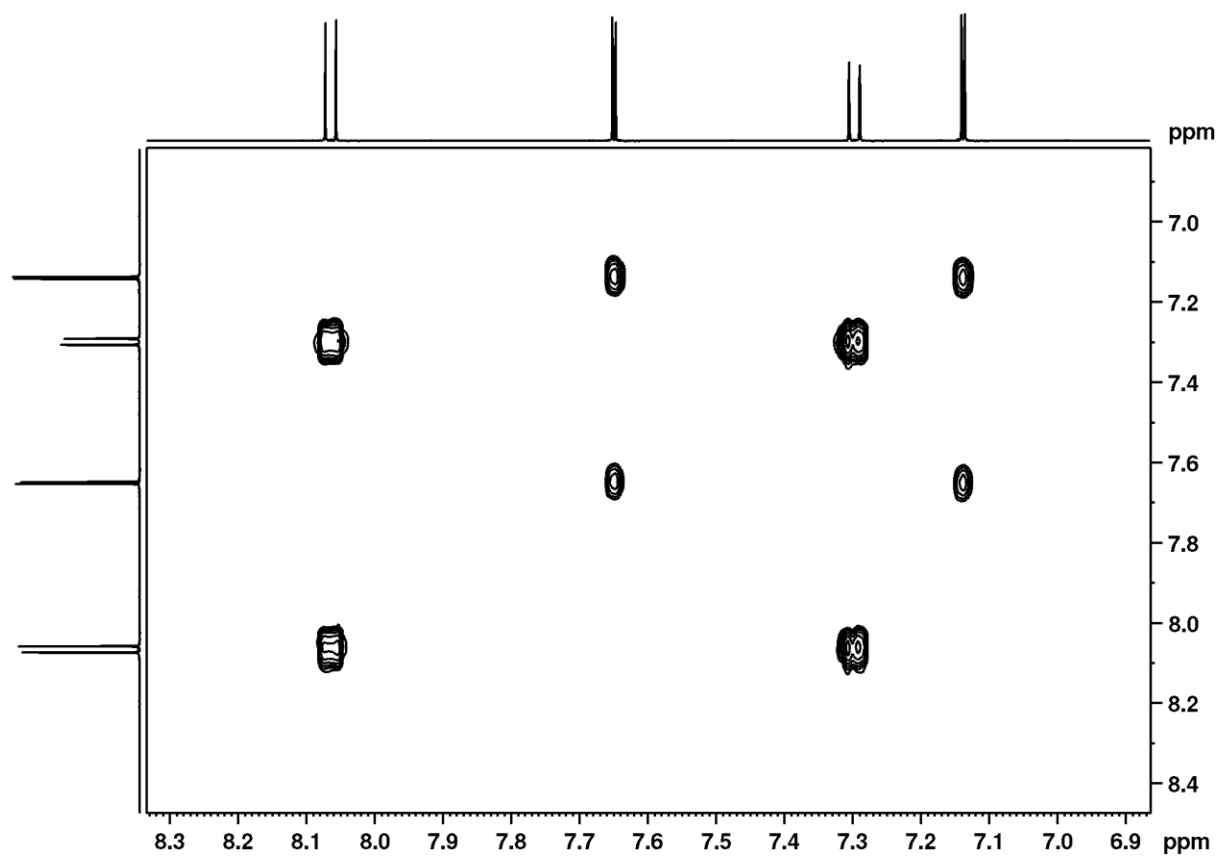
Appendix 4.3: Expansion of H-H COSY spectrum of skimmianine (**83**) at 600 MHz in CD$_2$Cl$_2$.
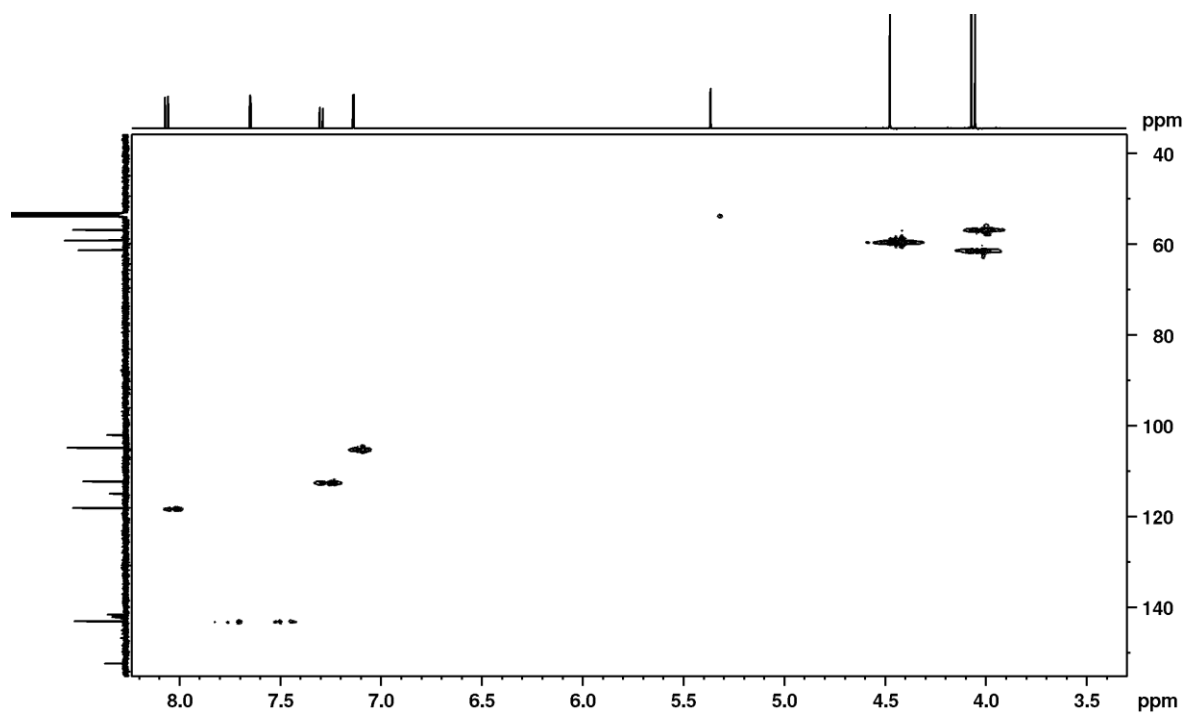
Appendix 4.4: HSQC spectrum of skimmianine (**83**) at 600 MHz in CD$_2$Cl$_2$.
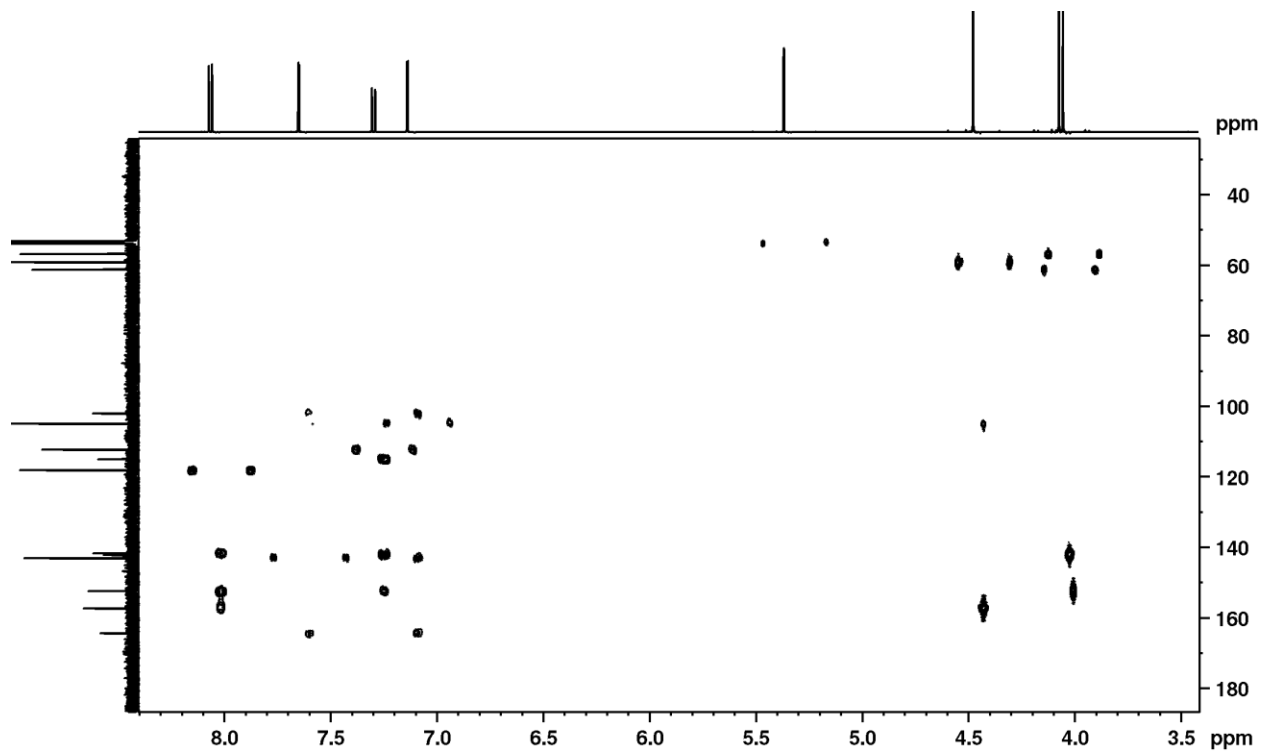
Appendix 4.5: HMBC spectrum of skimmianine (**83**) at 600 MHz in CD₂Cl₂.
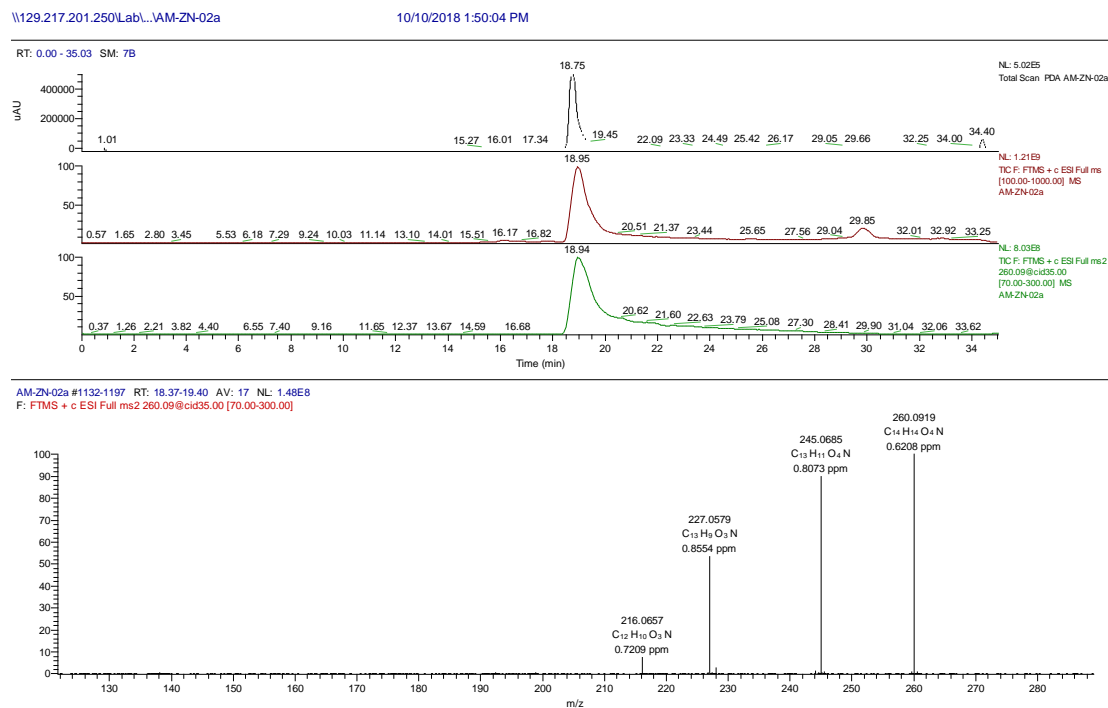
Appendix 4.6: LC-HRMS of skimmianine (**83**).

Appendix 5: 1D and 2D NMR spectra of hesperidin (**84**).
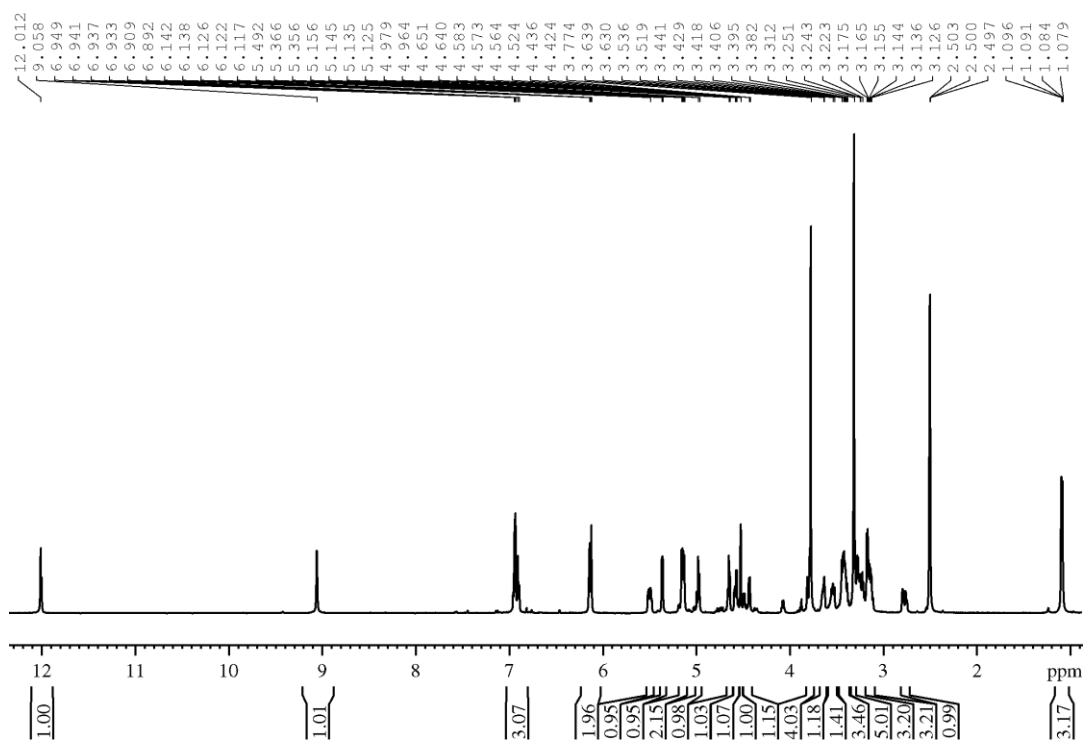
Appendix 5.1: ^{1}H NMR spectrum of Hesperidin (**84**) at 600 MHz in DMSO-d$_6$.
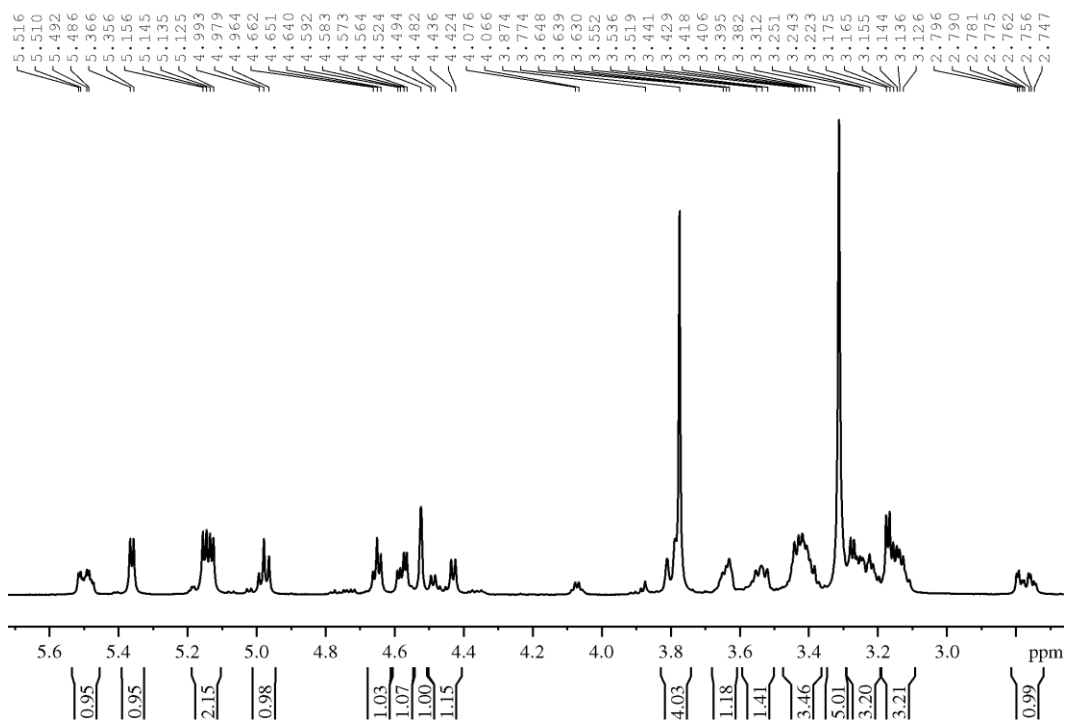
Appendix 5.2: Expansion of ^{1}H NMR spectrum of Hesperidin (**84**) at 600 MHz in DMSO-d$_6$.

190
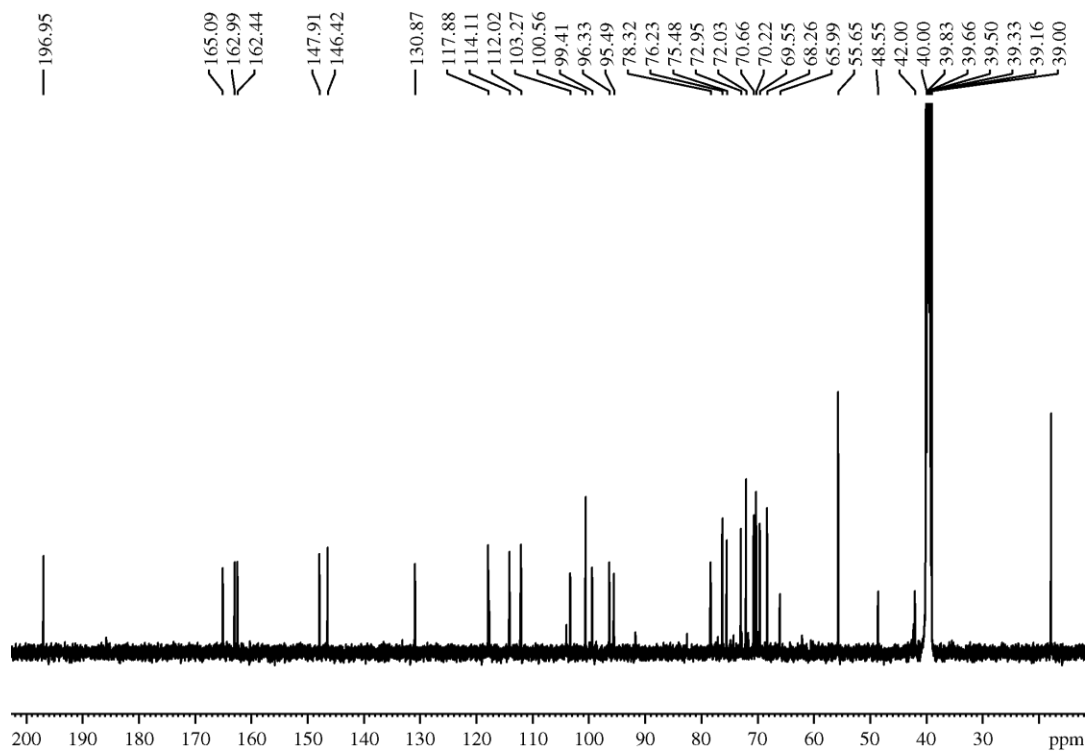
Appendix 5.3: ^{13}C NMR spectrum of Hesperidin (**84**) at 151 MHz in DMSO-d$_6$.
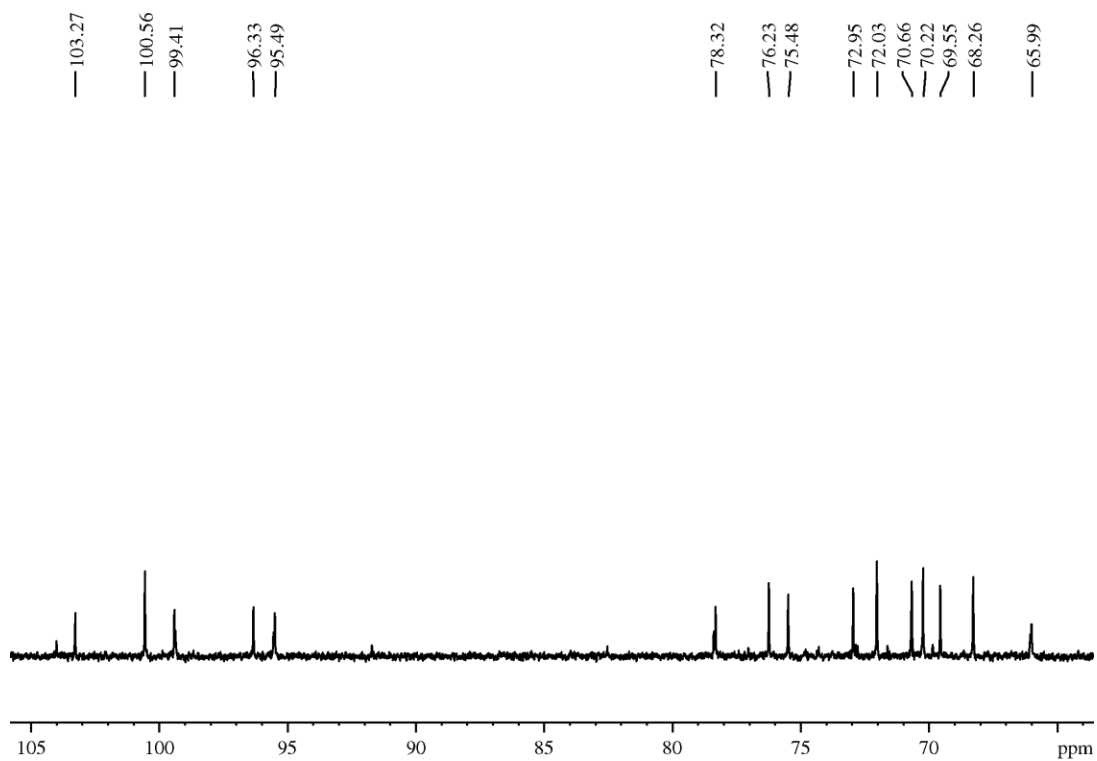
Appendix 5.4: Expansion of ^{13}C NMR spectrum of Hesperidin (**84**) at 151 MHz in DMSO-d$_6$.

Appendix 6: 1D and 2D NMR spectrum of aloenin (**85**).
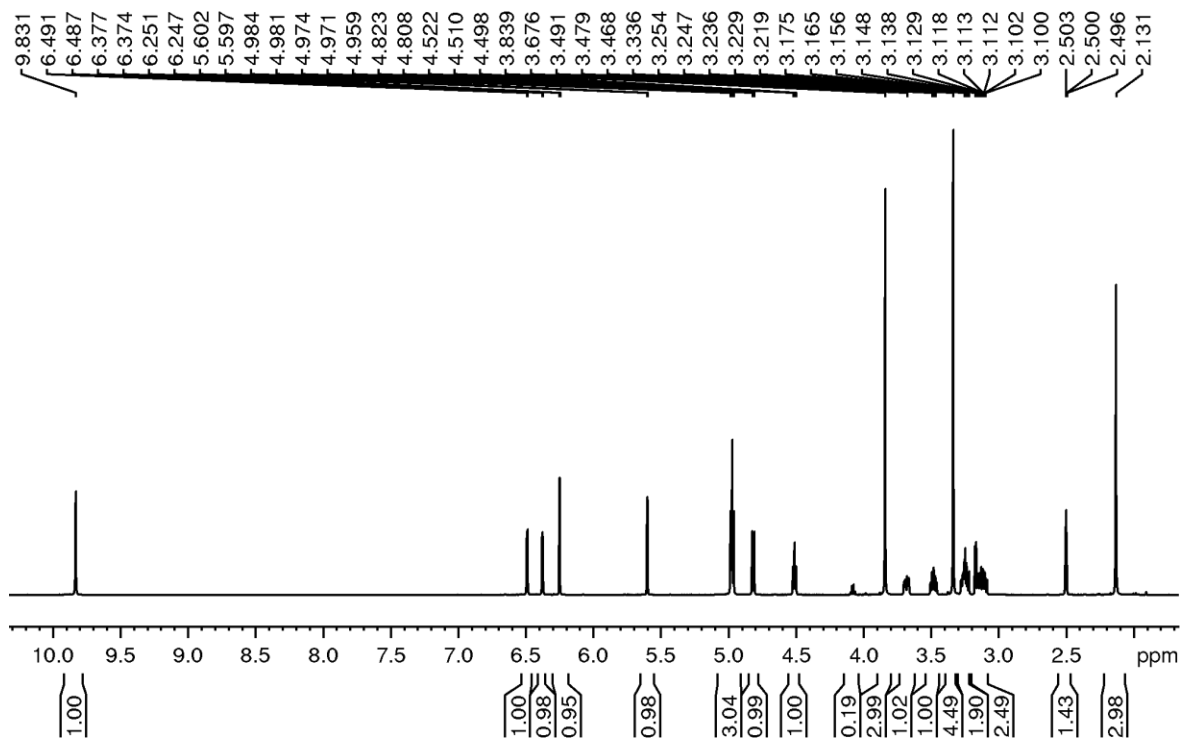
Appendix 6.1: ^{1}H NMR spectrum of aloenin (**85**) at 600 MHz in DMSO-d$_6$.
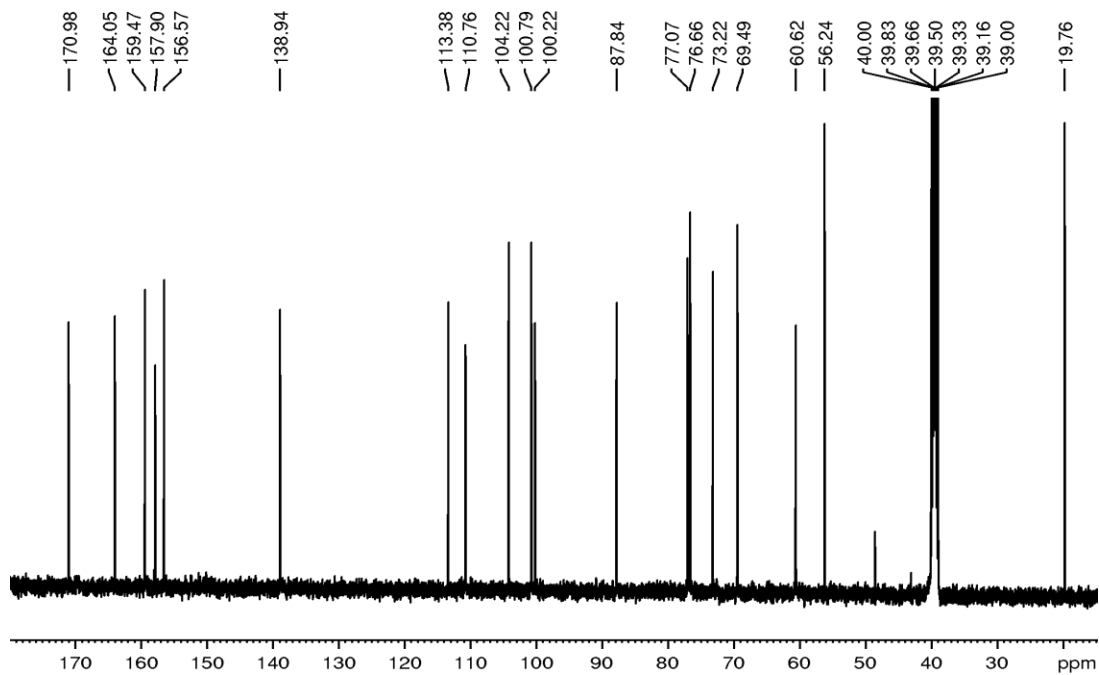
Appendix 6.2: ^{13}C NMR spectrum of aloenin (**85**) at 151 MHz in DMSO-d$_6$.
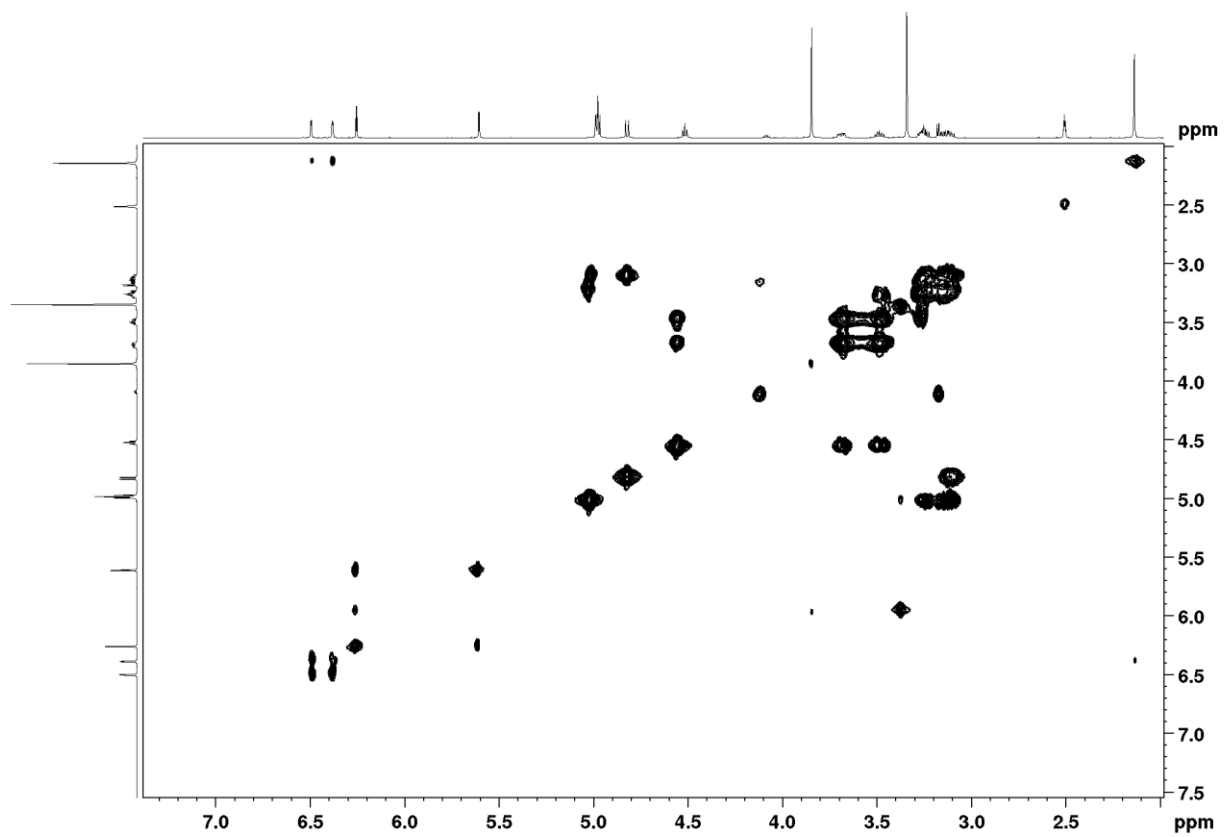
Appendix 6.3: H-H COSY NMR spectrum of aloenin (**85**) at 600 MHz in DMSO-d$_6$.
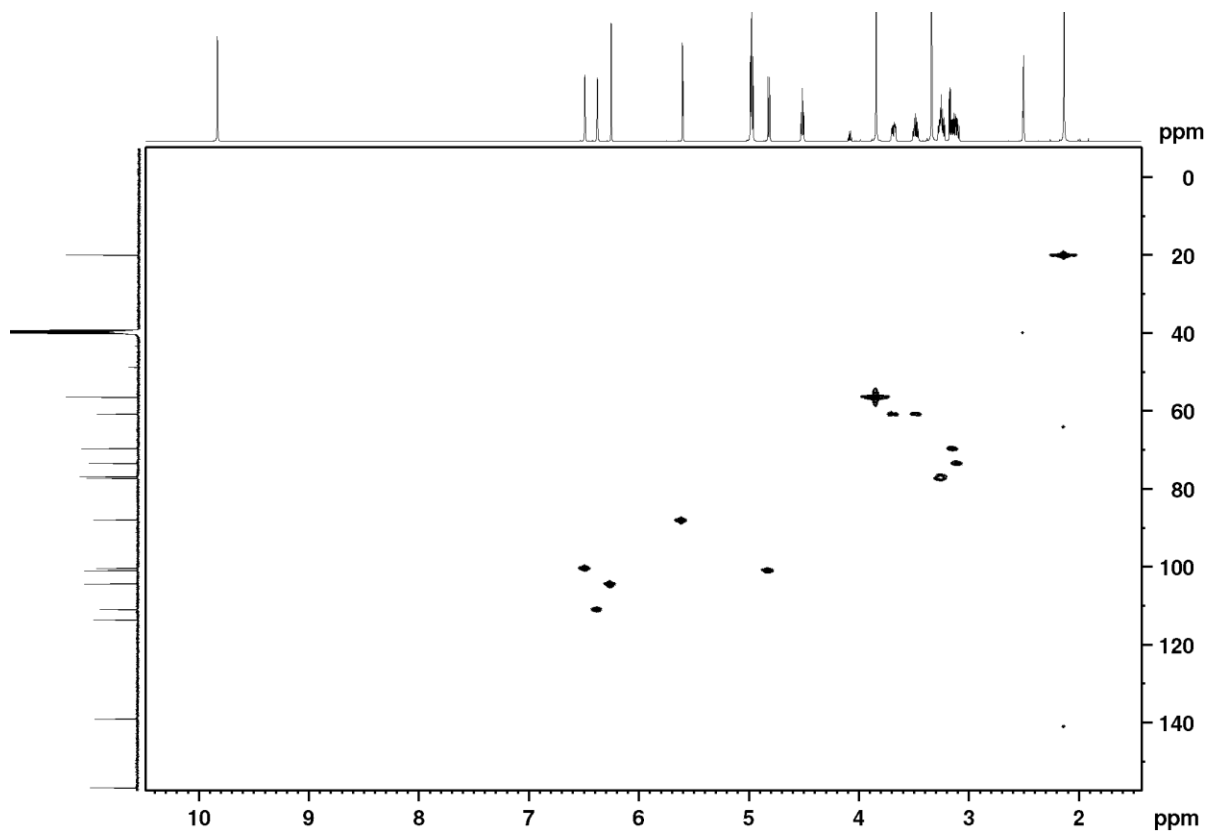
Appendix 6.4: HSQC NMR spectrum of aloenin (**85**) at 600 MHz in DMSO-d₆.
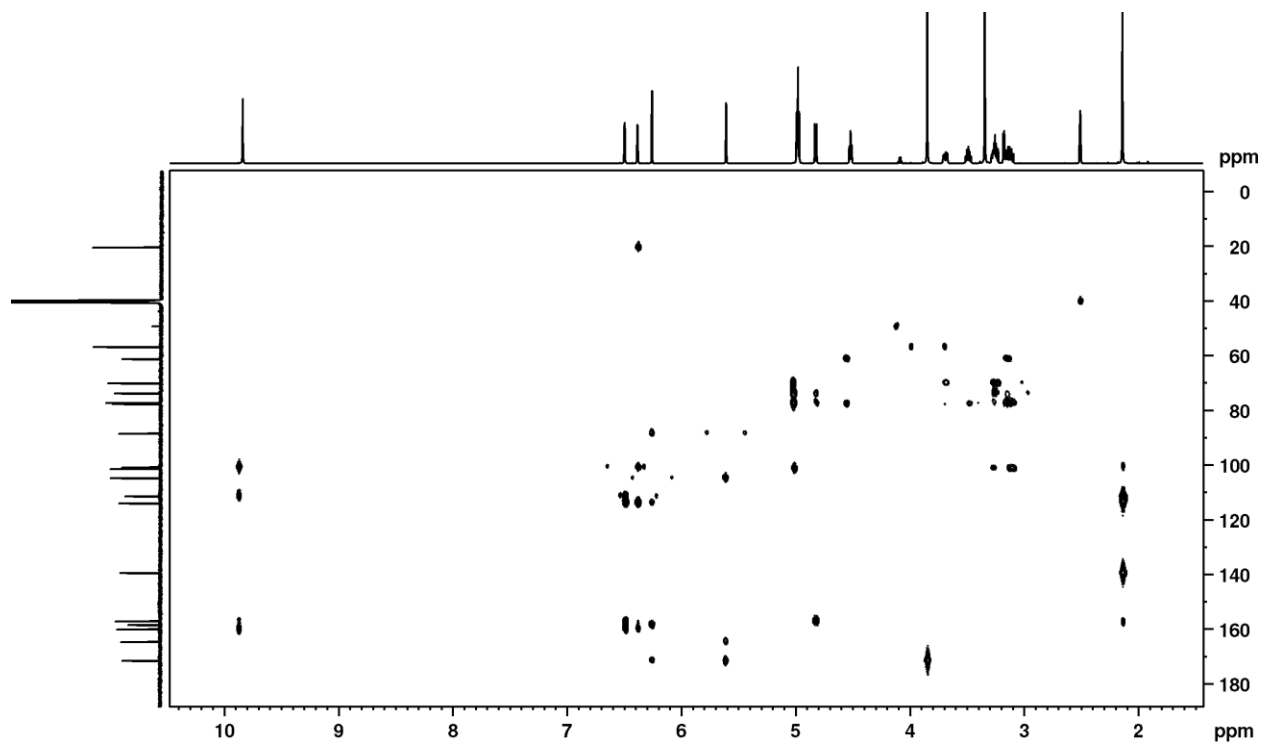
Appendix 6.5: HMBC NMR spectrum of aloenin (**85**) at 600 MHz in DMSO-d₆.
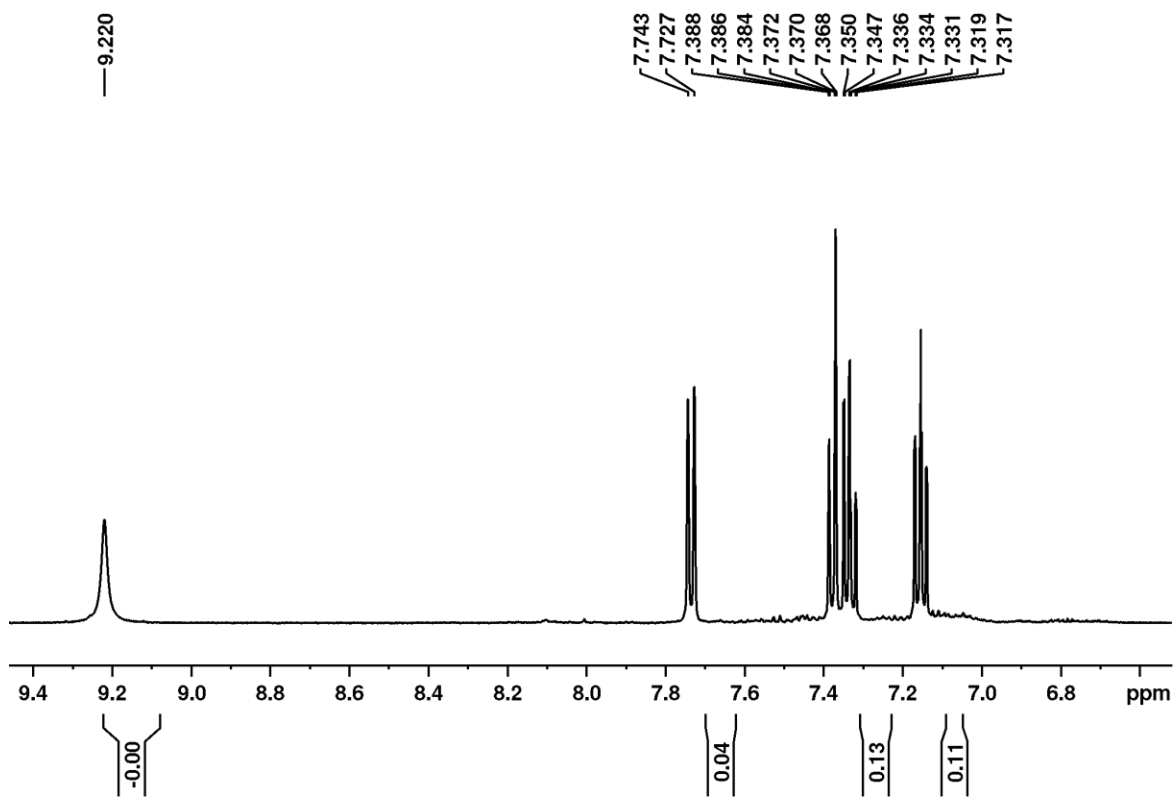
Figure 6.6: Expansion of ^{1}H NMR spectrum of aloenin (**85**) at 600 MHz in CD_2Cl_2.

Appendix 7: 1D and 2D NMR spectra of aloe-emodin (**86**) and laccaic acid-d-methyl ester (**87**).
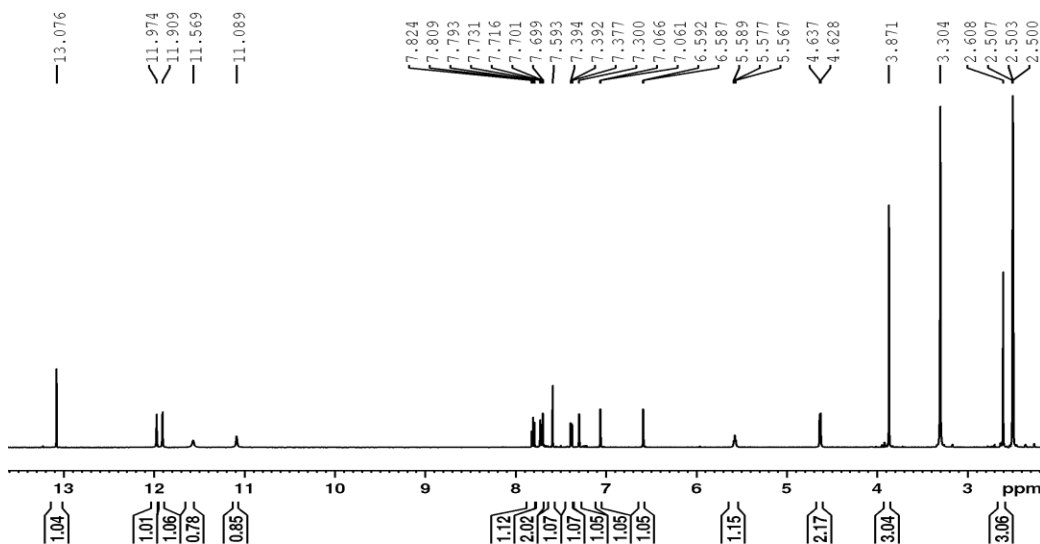
Appendix 7.1: ^{1}H NMR spectrum of a mixture of aloe-emodin (**86**) and laccaic acid ester (**87**) at 600 MHz in DMSO-d$_6$.
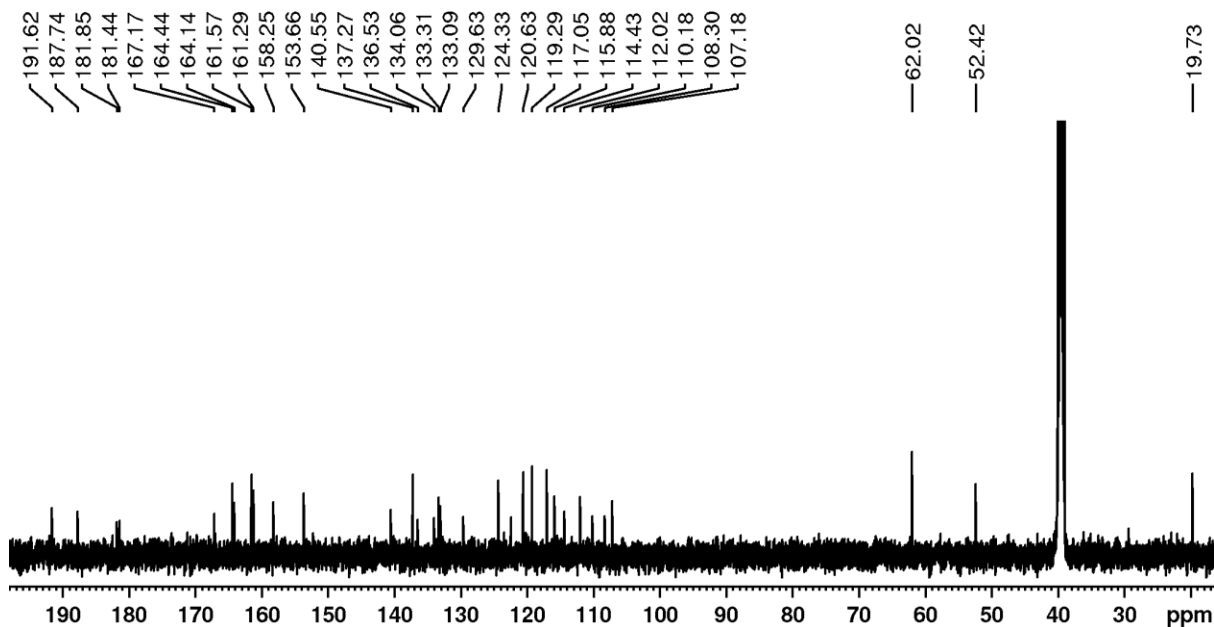
Appendix 7.2: ^{13}C NMR spectrum of a mixture of aloe-emodin (**86**) and laccaic acid ester (**87**) at 151 MHz in DMSO-d$_6$.
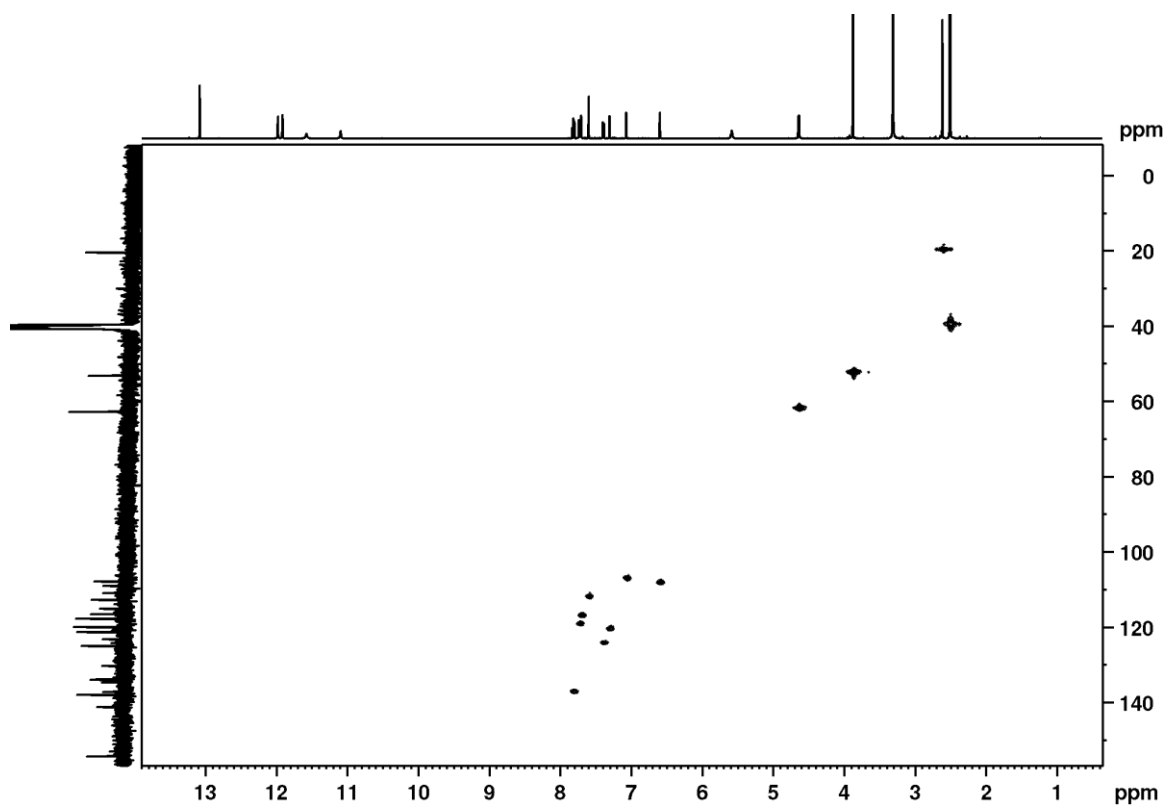
Appendix 7.3: HSQC spectrum of a mixture of aloe-emodin (**86**) and laccaic acid ester (**87**) at 600 MHz in DMSO-d$_6$.
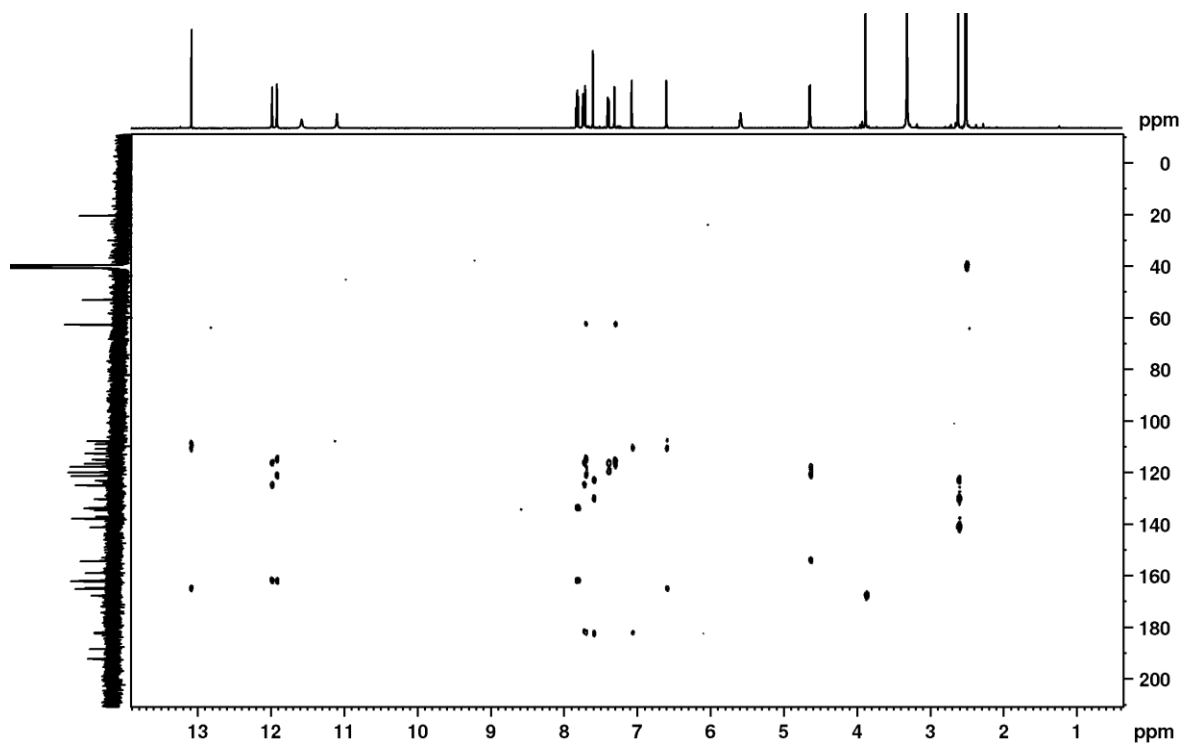
Appendix 7.4: HMBC spectrum of a mixture of aloe-emodin (**86**) and laccaic acid ester (**87**) at 600 MHz in DMSO-d$_6$.

Appendix 8: 1D and 2D NMR spectra of chrysophanol (**89**).
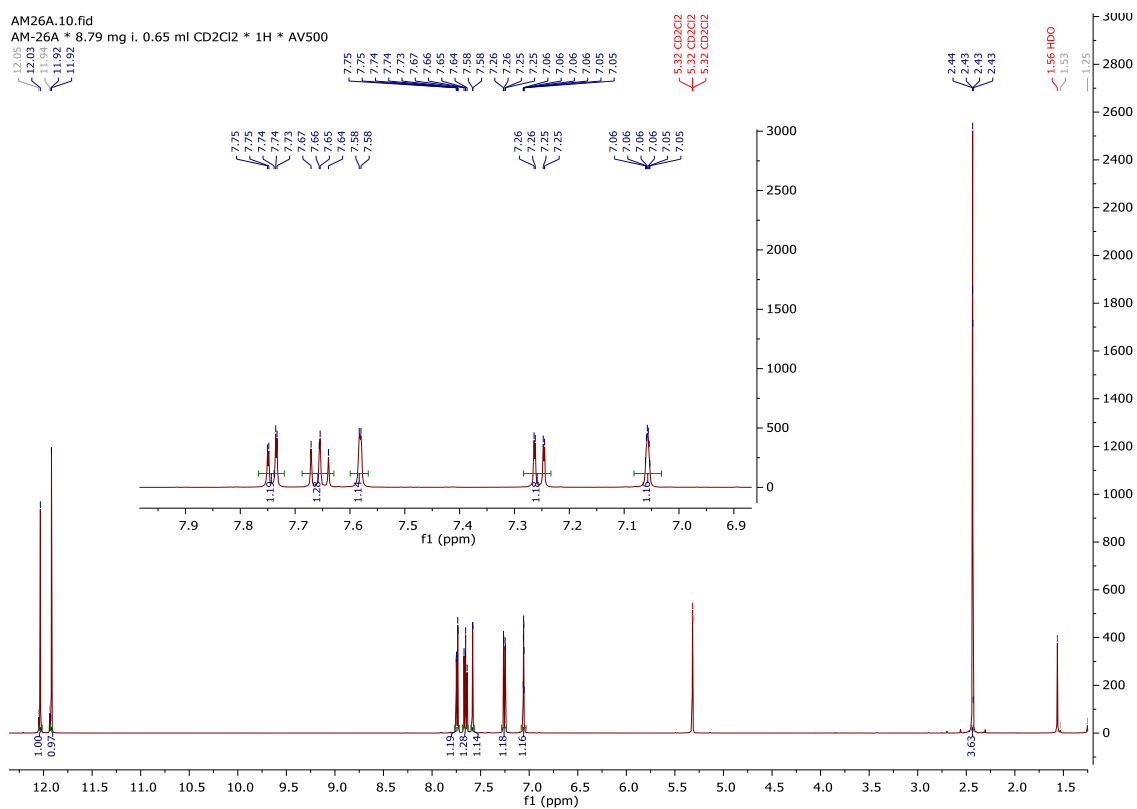
Appendix 8.1: ^{1}H NMR spectrum of a mixture of chrysophanol (**89**) at 151 MHz in DMSO-d[6].
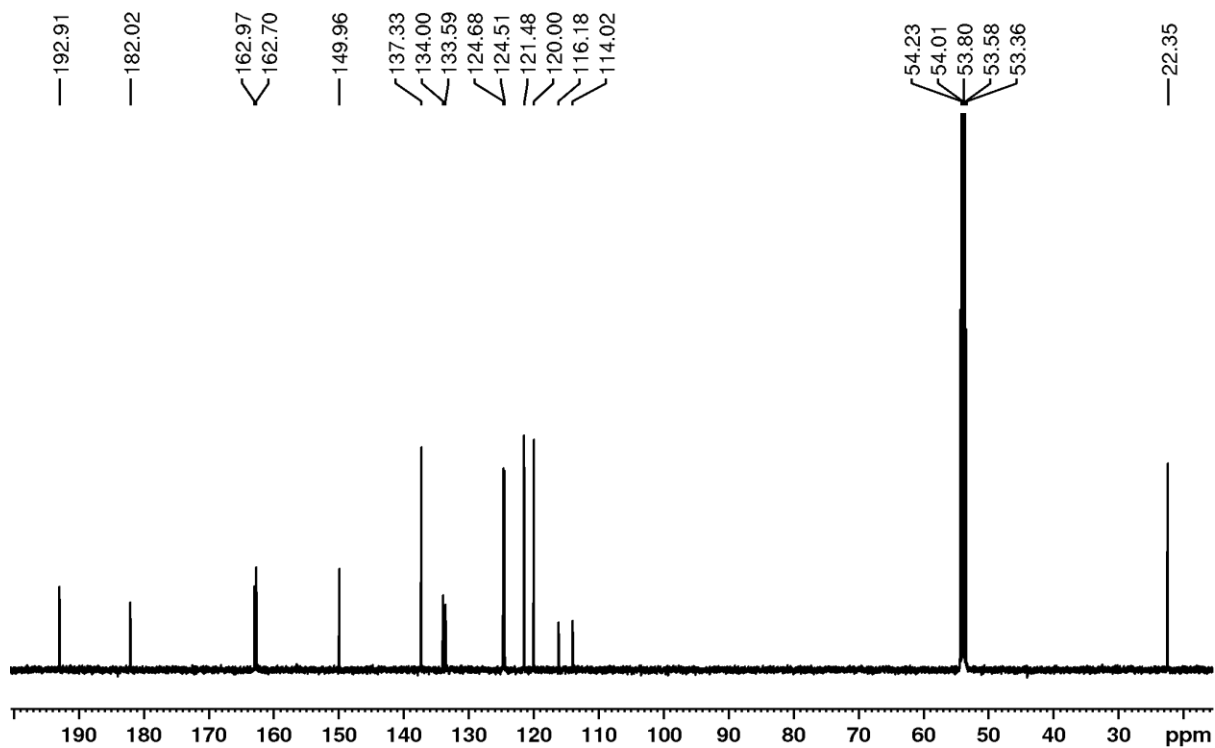
Appendix 8.2: ^{13}C NMR spectrum of a mixture of chrysophanol (**89**) at 151 MHz in DMSO-d$_6$.
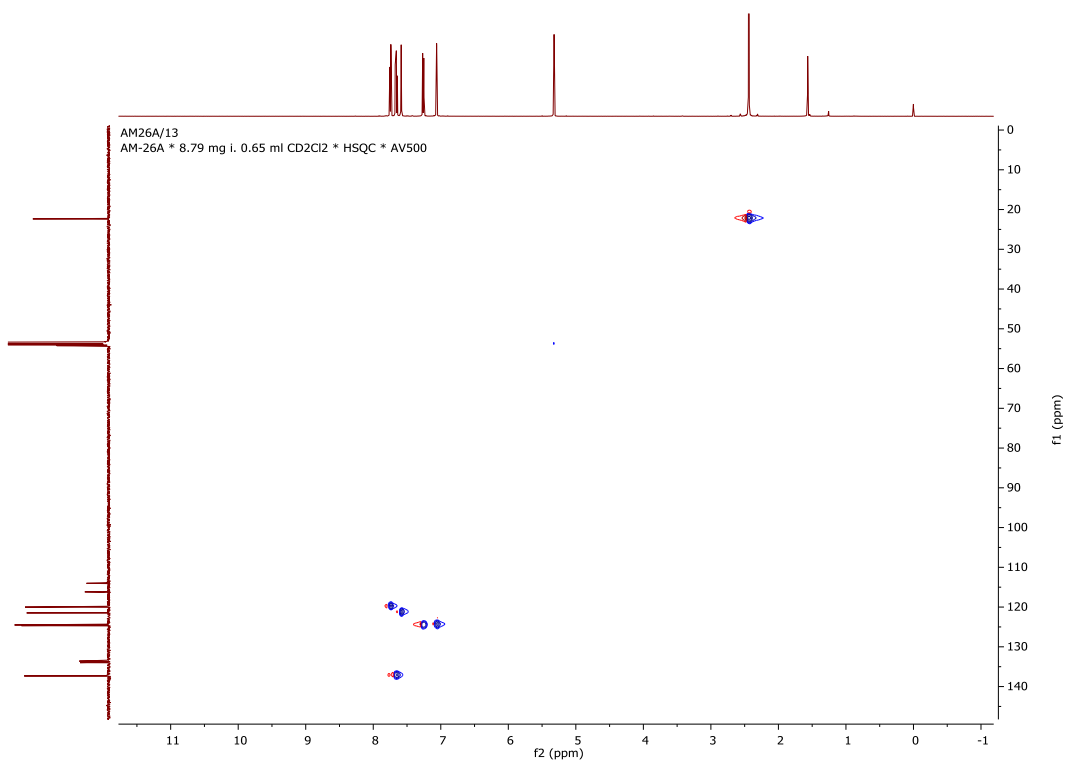
Appendix 8.3: HSQC spectrum of chrysophanol at 600 MHz in CD$_2$Cl$_2$.
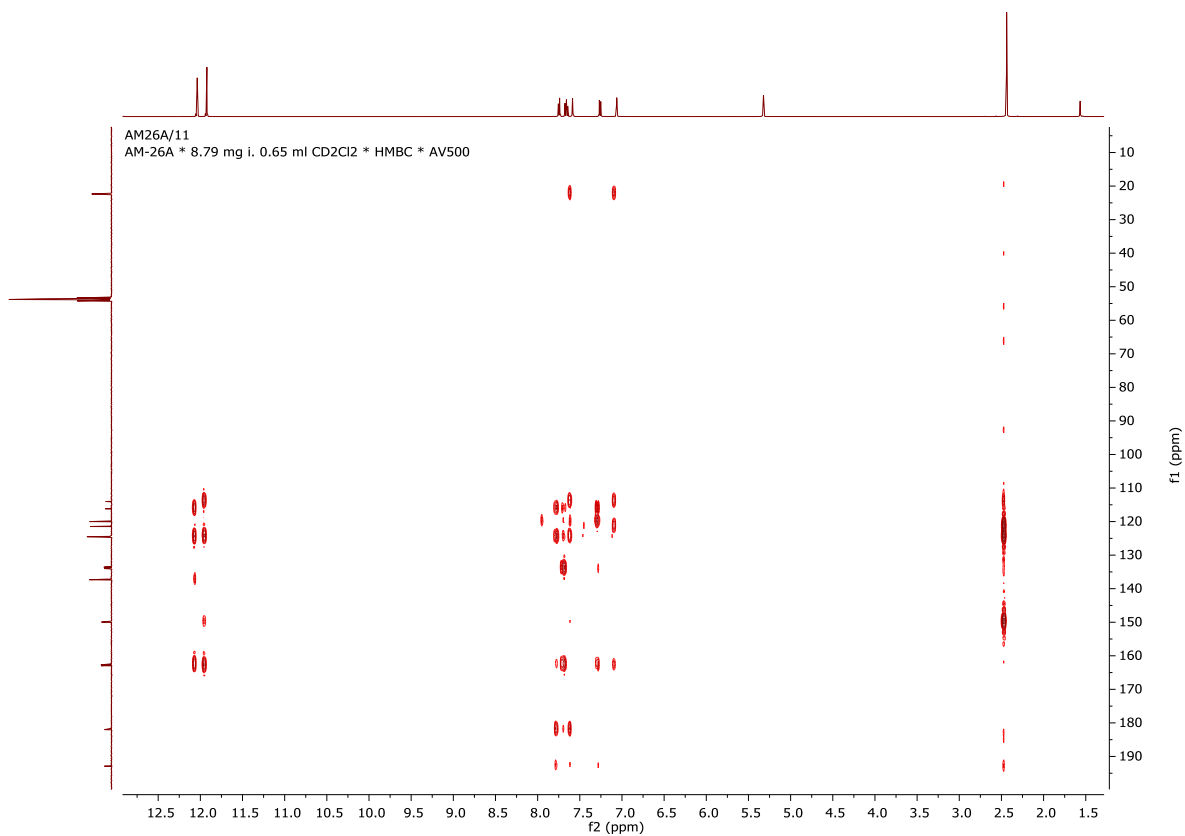
Appendix 8.4, HMBC spectrum of chrysophanol at 600 MHz in CD₂Cl₂.

Appendix 9: 1D and 2D NMR spectra of chrysalodin (**90**).
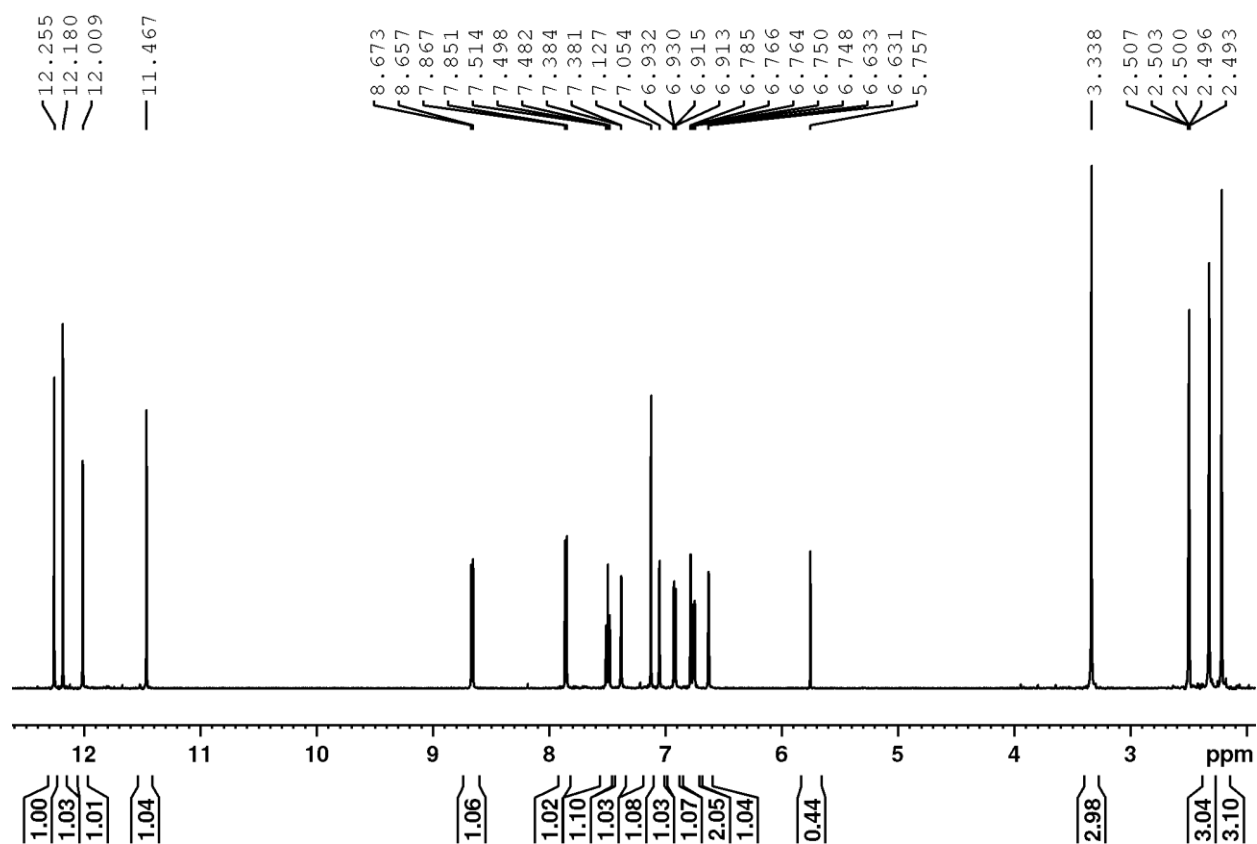
Appendix 9.1: ^{1}H NMR spectrum of chrysalodin (**90**) at 600 MHz in DMSO-d$_6$.
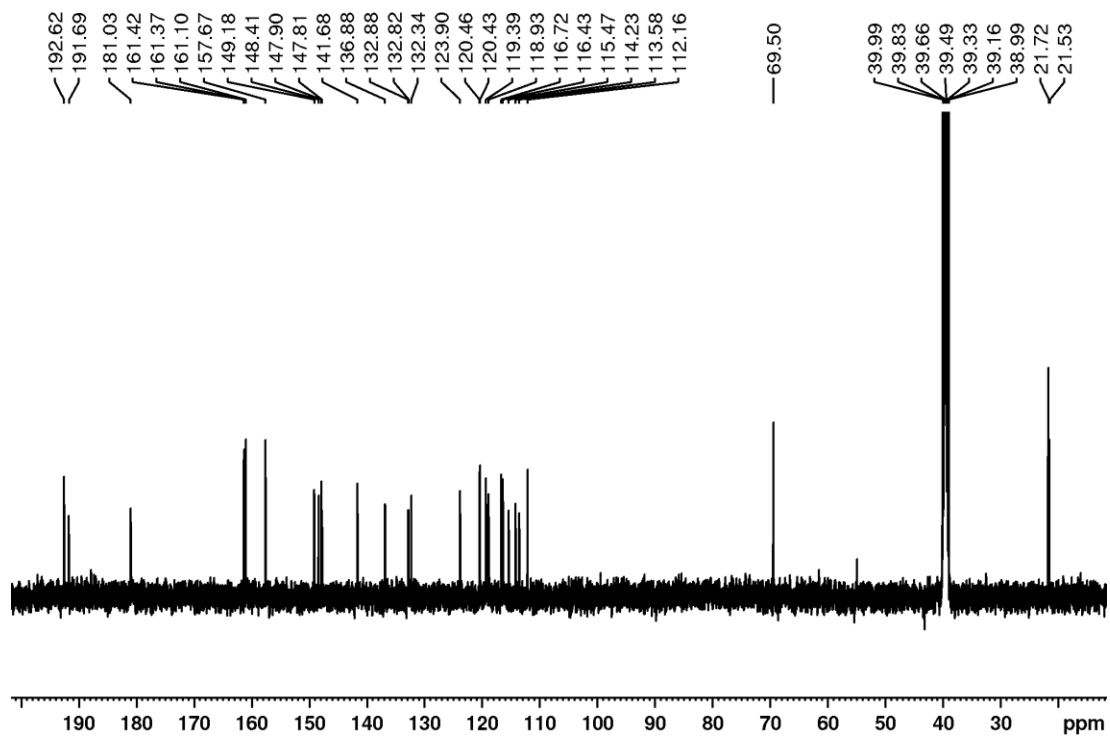
Appendix 9.2: ^{13}CNMR spectrum of chrysalodin (**90**) at 151 MHz in DMSO-d$_6$.
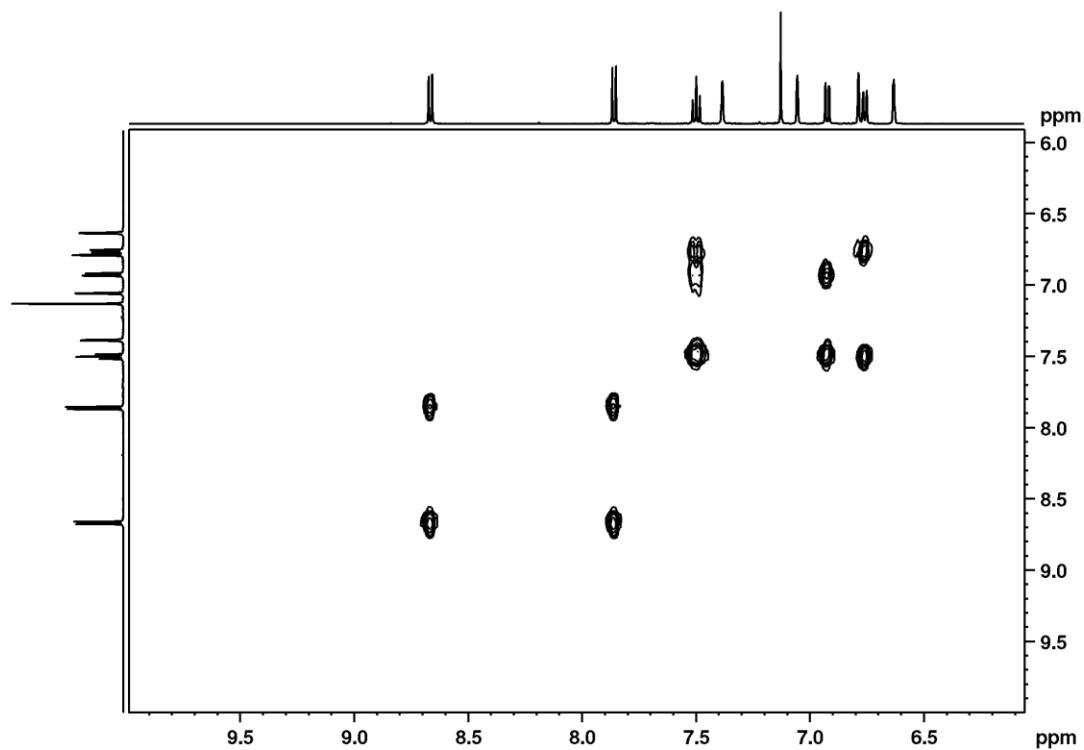
Appendix 9.3: Expansion of H-H COSY spectrum of chrysalodin (**90**) at 600 MHz in DMSO-d$_6$.
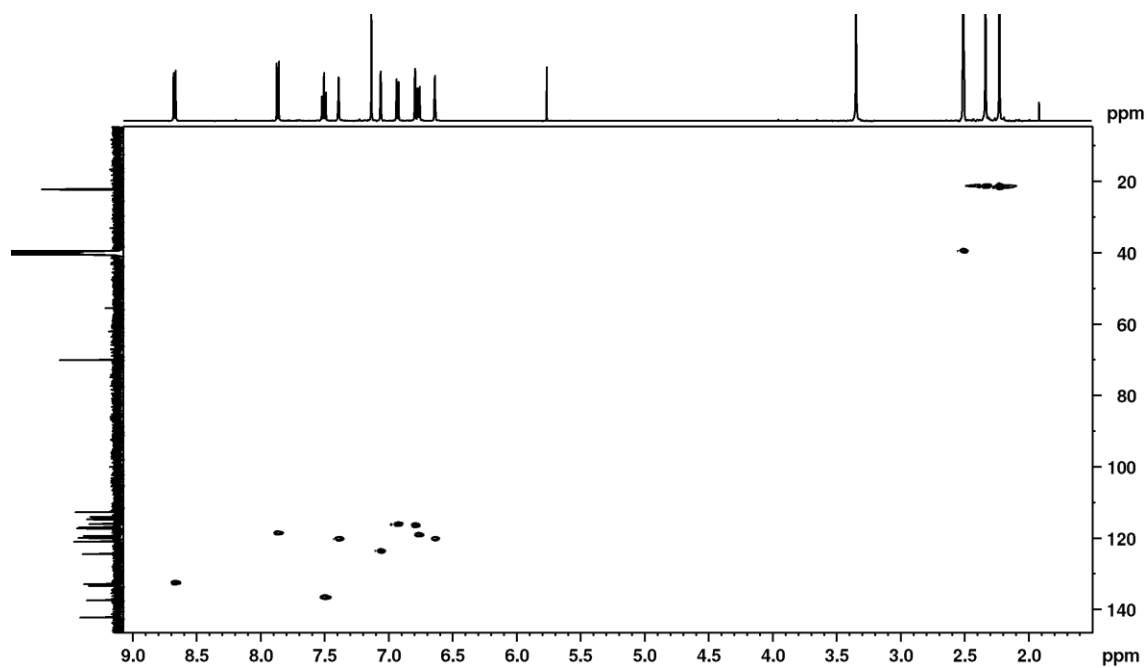
Appendix 9.4: HSQC spectrum of chrysalodin (**90**) at 600 MHz in DMSO-d$_6$.
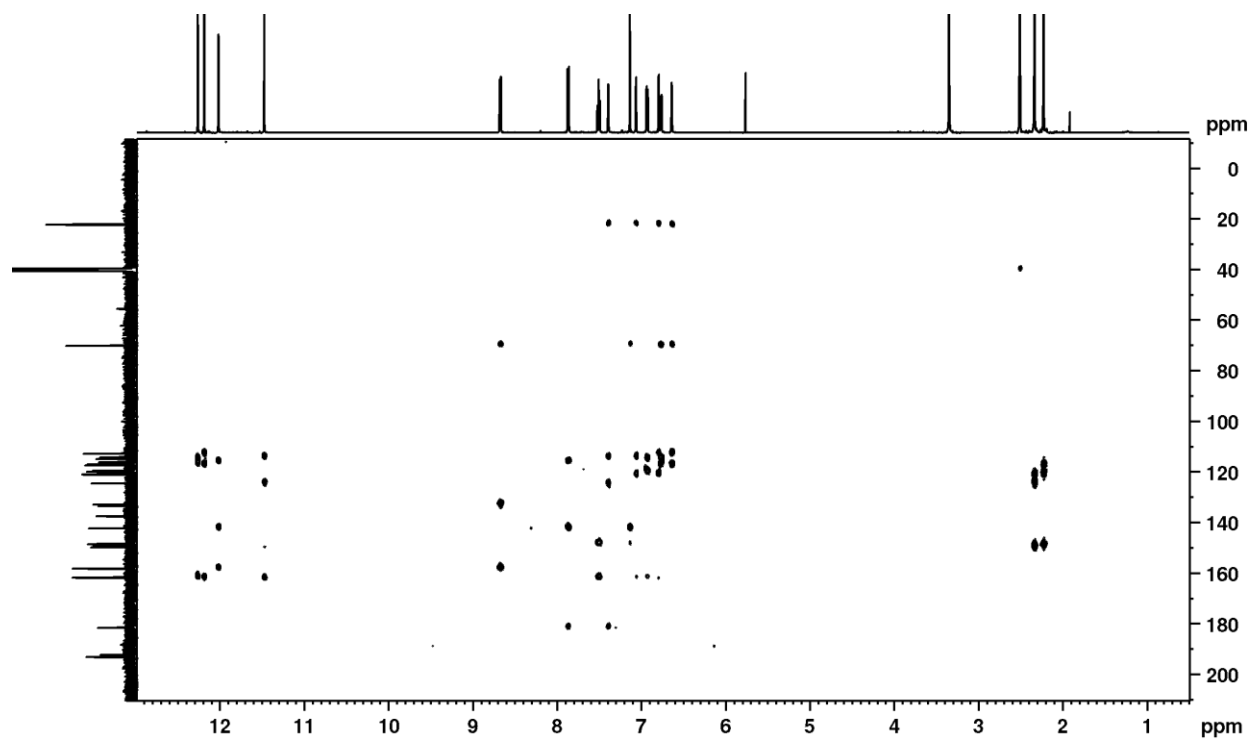
**Appendix 9.5**: HMBC spectrum of chrysalodin (**90**) at 600 MHz in DMSO-d$_6$.

Appendix 10: 1D and 2D NMR spectra of aloe saponarin I (**91**).
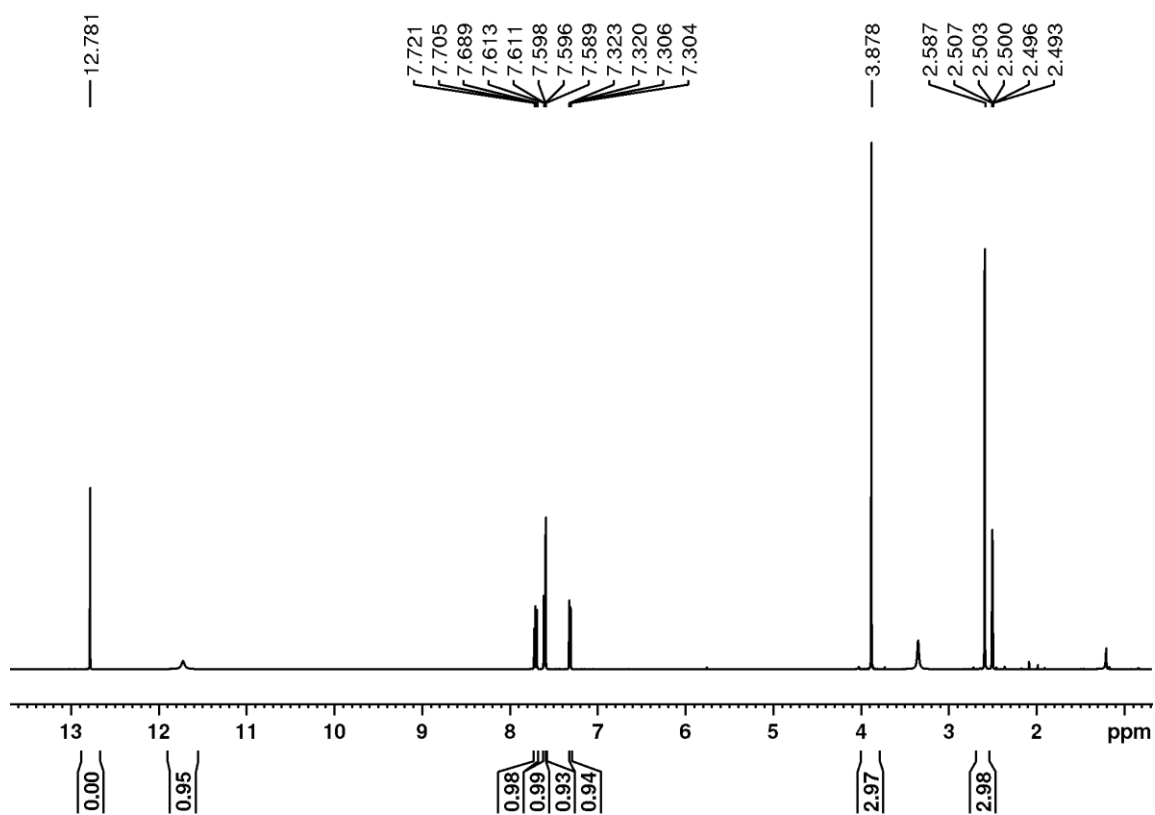
Appendix 10.1: ^{1}H NMR spectrum of aloesaponarin I (**91**) at 600 MHz in DMSO-d$_{6}$.
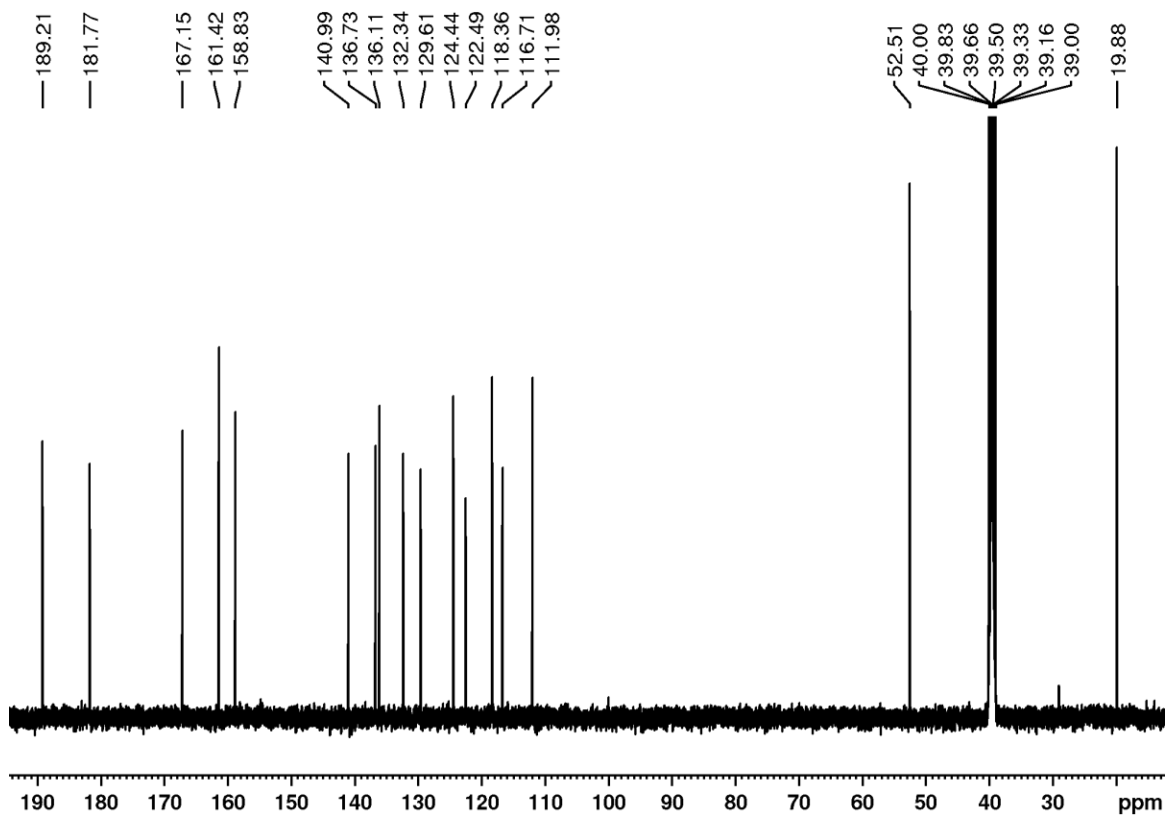
Appendix 10.2: ^{13}C NMR spectrum of aloesaponarin I (**91**) at 151 MHz in DMSO-d$_6$.
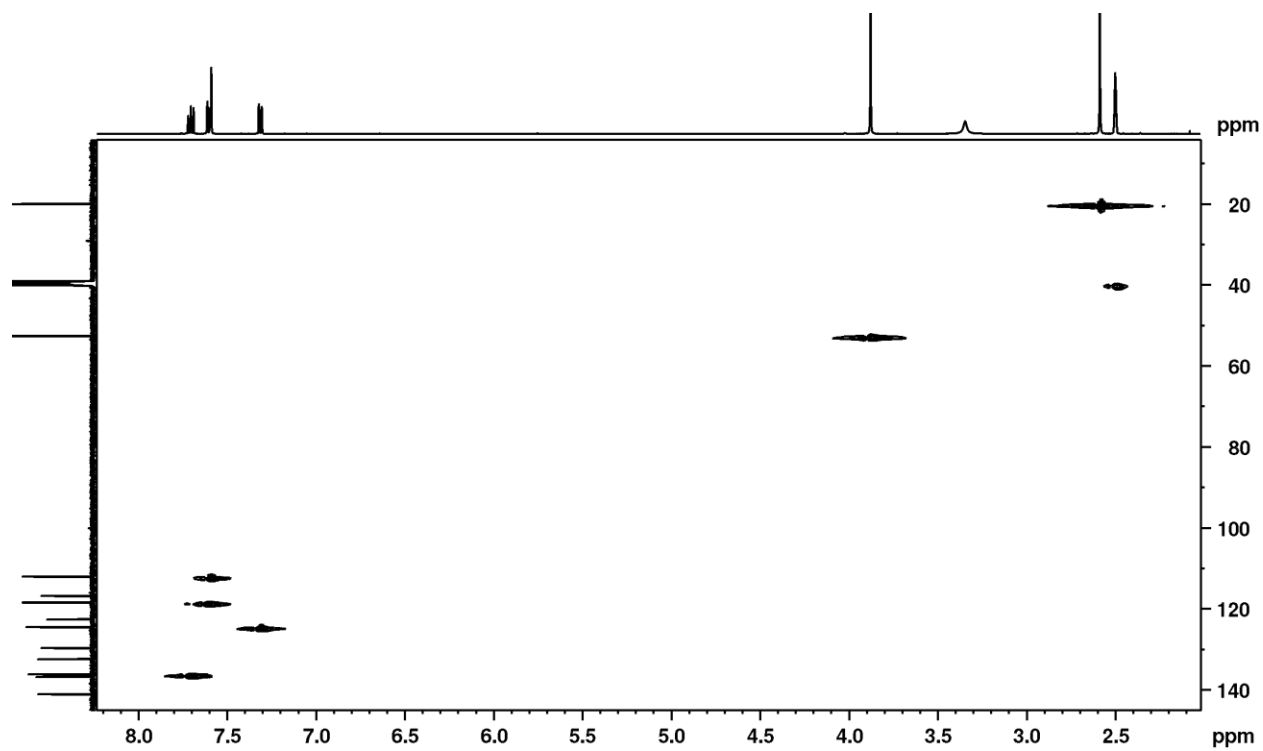
Appendix 10.3: HSQC spectrum of aloesaponarin I (**91**) at 600 MHz in DMSO-d$_6$.
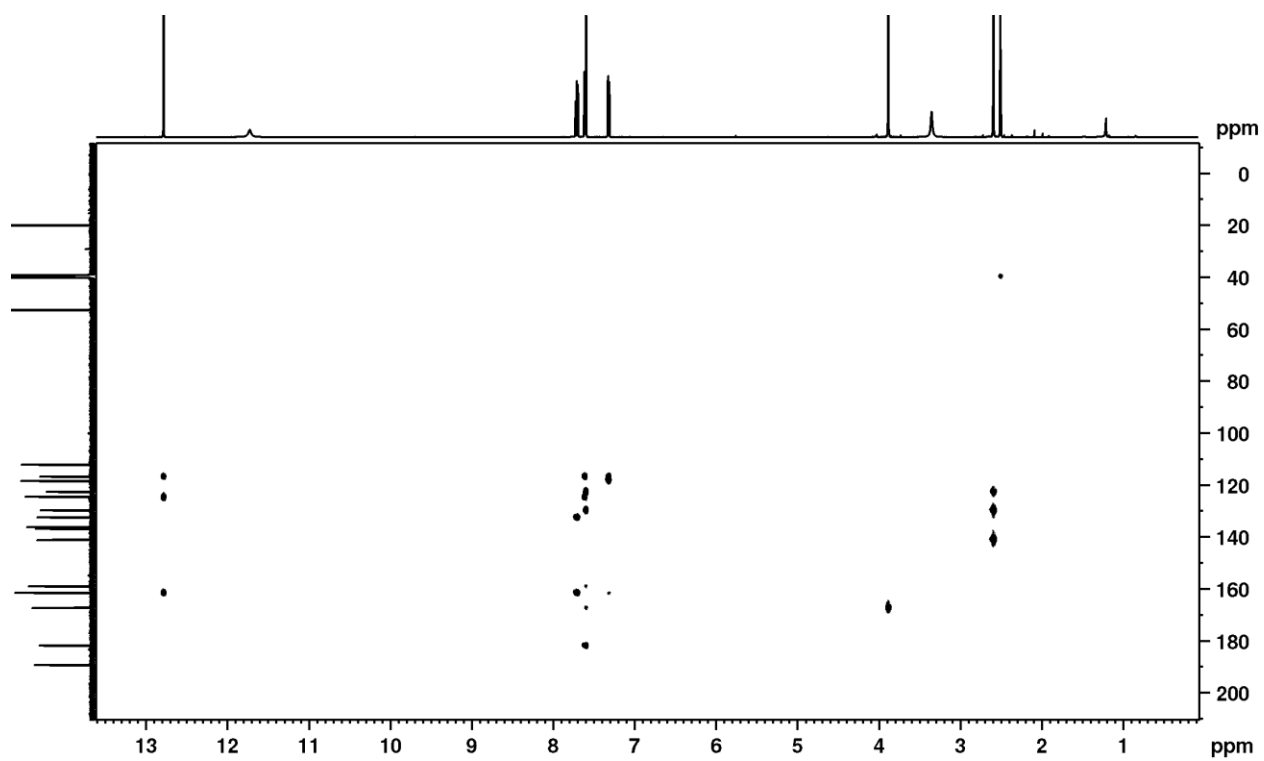
Appendix 10.4: HMBC spectrum of aloesaponarin I (**91**) at 600 MHz in DMSO-d$_6$.

Appendix 11: 1D and 2D NMR spectra of 5-allyl-3-methoxybenzene (**92**).
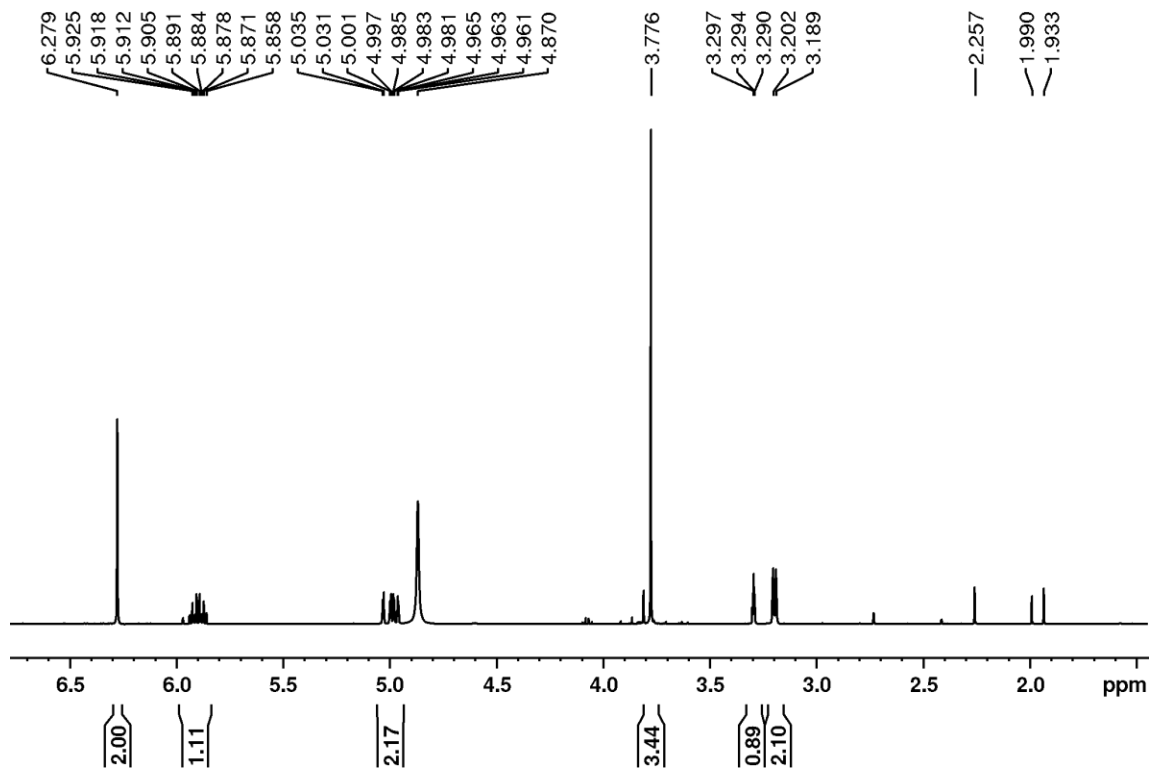
Appendix 11.1: ^{1}H NMR spectrum of 5-allyl-3-methoxybenzene (**92**) at 600 MHz in MeOD.
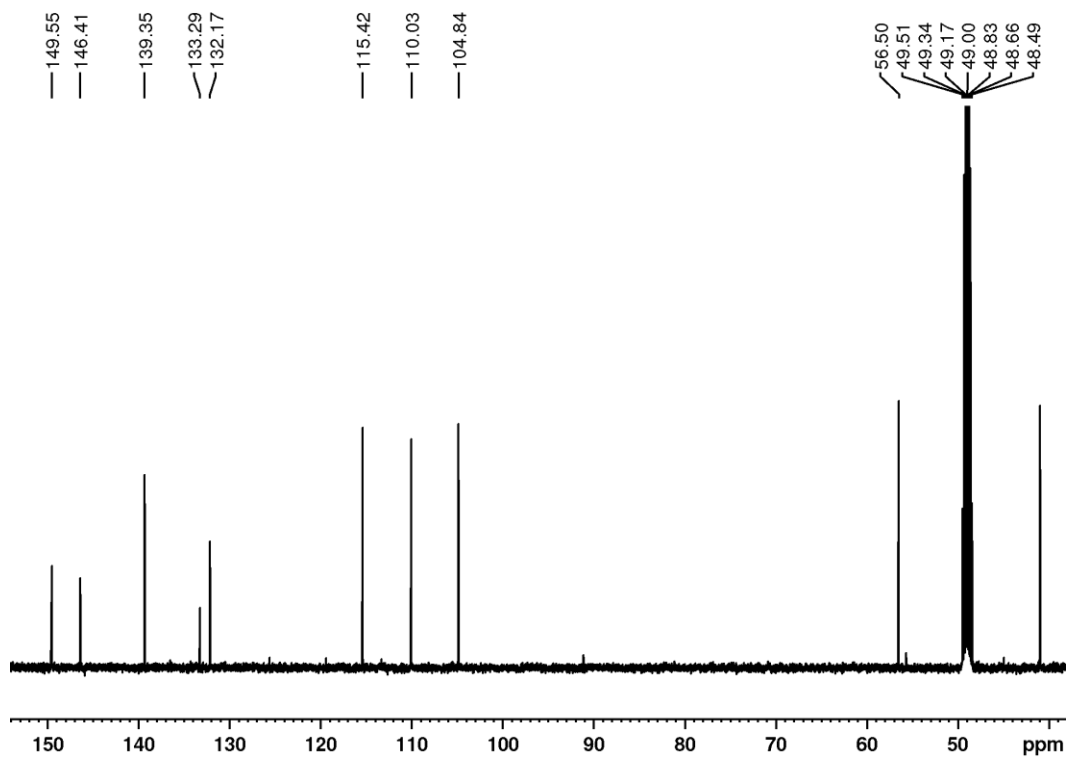
Appendix 11.2: ^{1}H NMR spectrum of 5-allyl-3-methoxybenzene (**92**) at 600 MHz in MeOD.
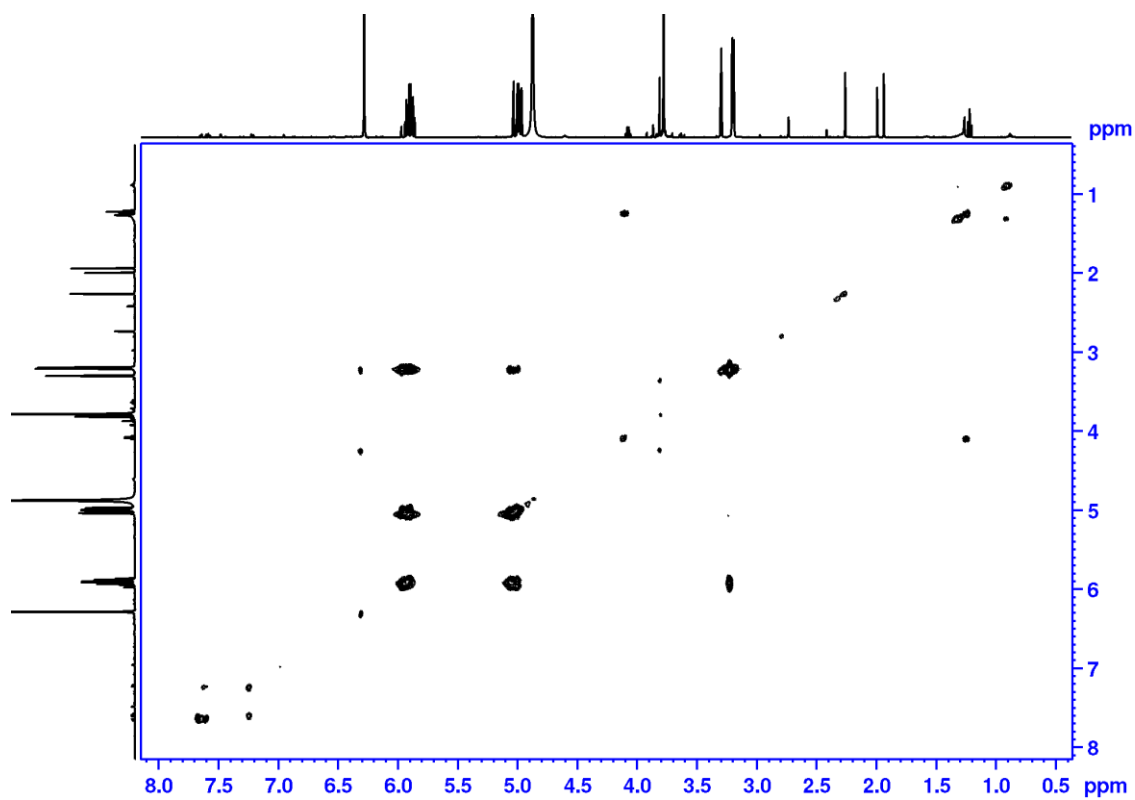
Appendix 11.3: H-H COSY spectrum of 5-allyl-3-methoxybenzene (**92**) at 600 MHz in MeOD.
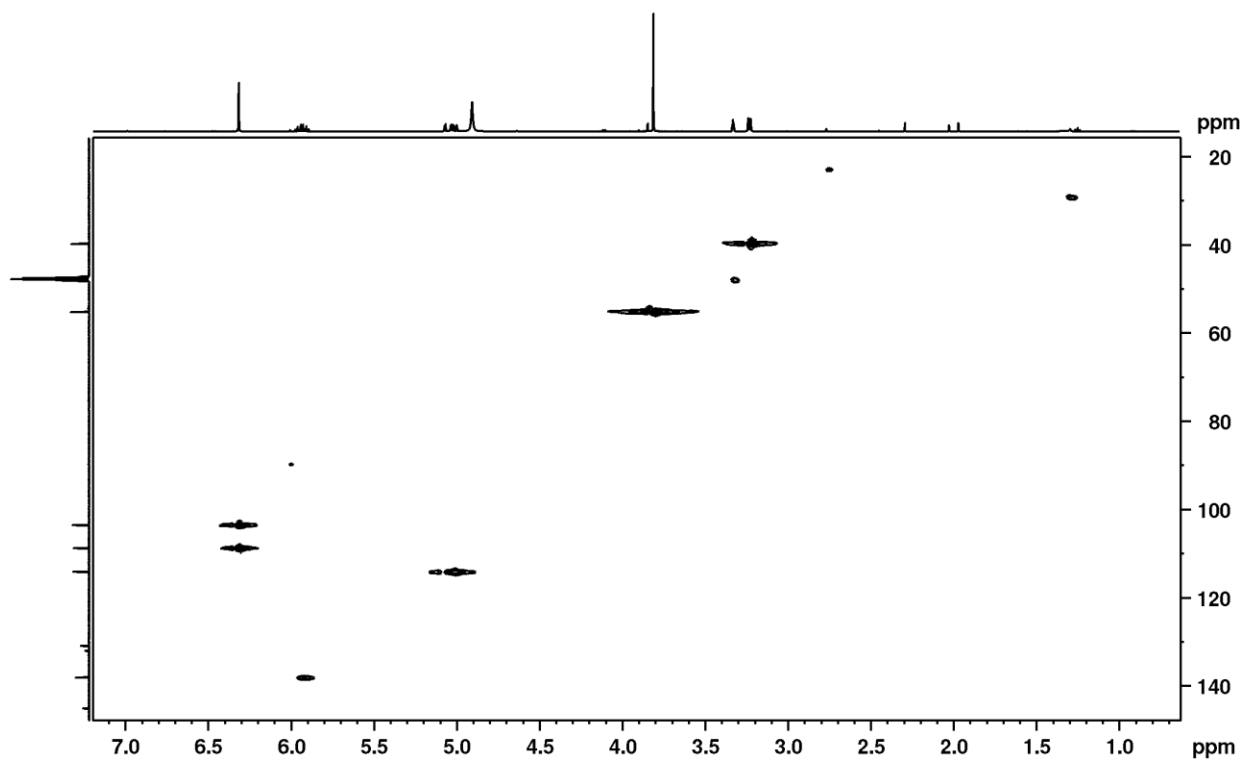
Appendix 11.4: HSQC spectrum of 5-allyl-3-methoxybenzene (**92**) at 600 MHz in MeOD.
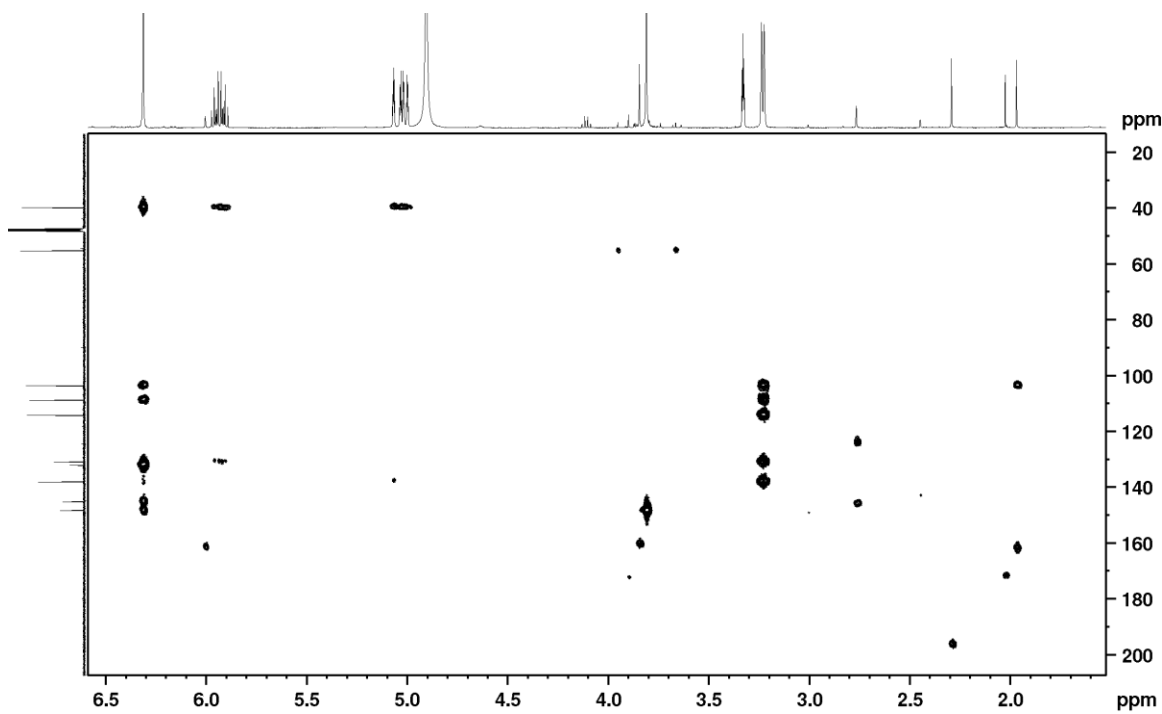
Appendix 11.5: HMBC spectrum of 5-allyl-3-methoxybenzene (**92**) at 600 MHz in MeOD.

Appendix 12: 1D and 2D NMR spectra of droserone (**93**).
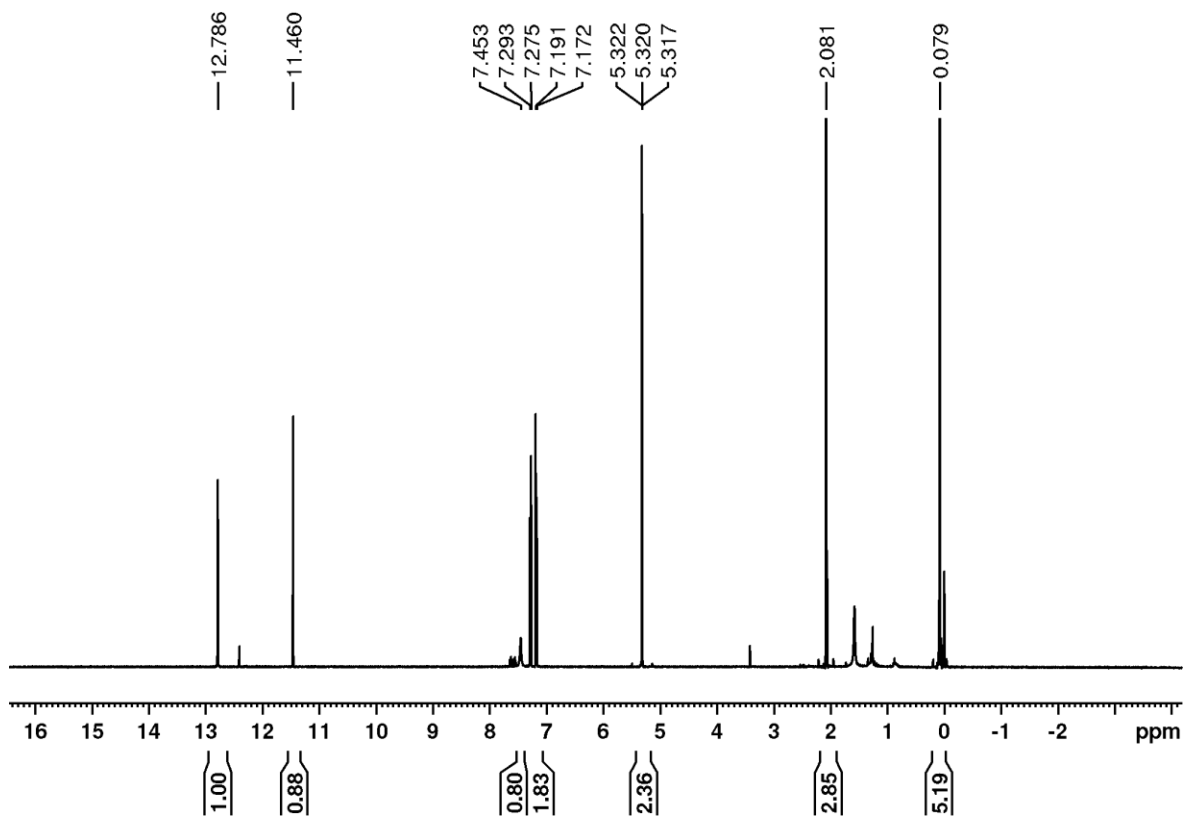
Appendix 12.1: ¹H NMR spectrum of droserone (**93**) at 600 MHz in CD₂Cl₂.
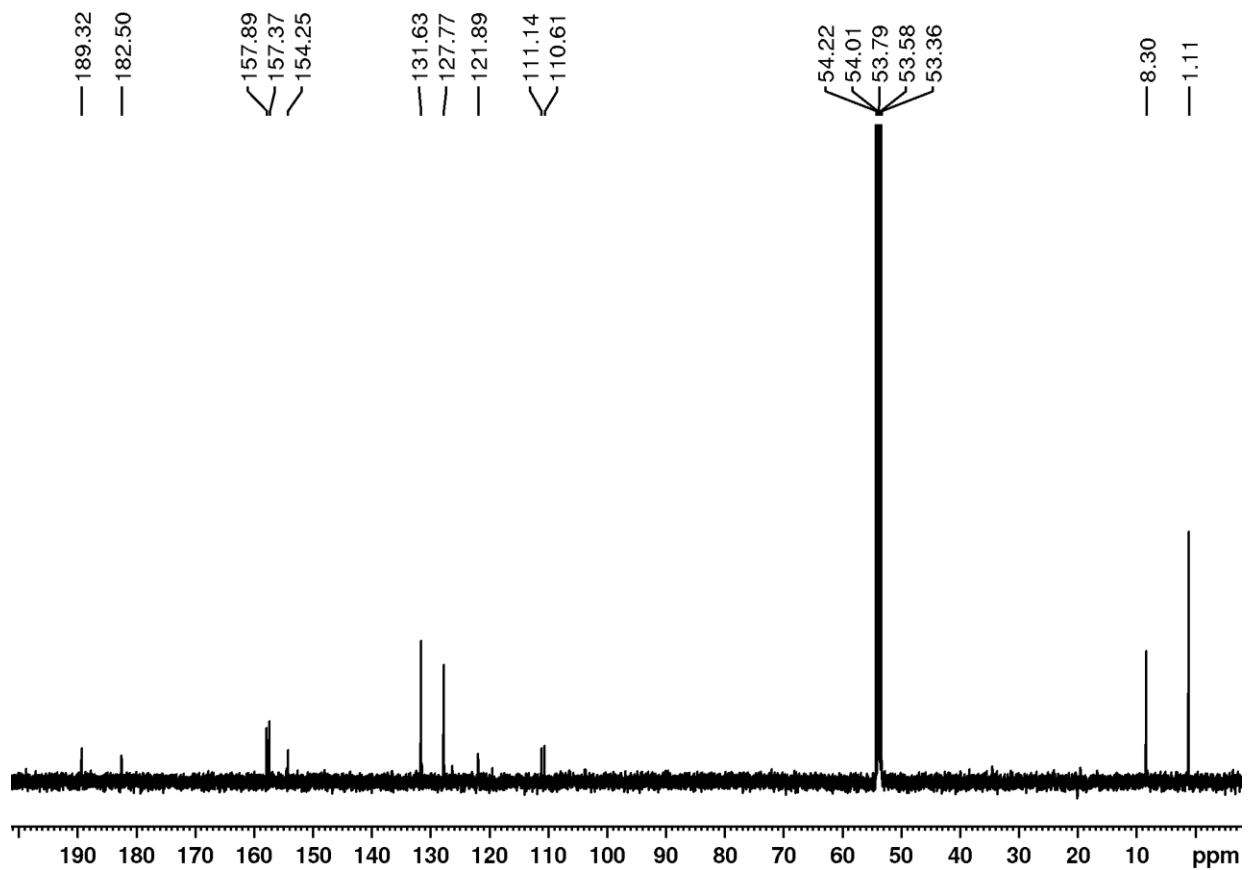
Appendix 12.2: ^{13}C NMR spectrum of droserone (**93**) at 151 MHz in CD_2Cl_2.
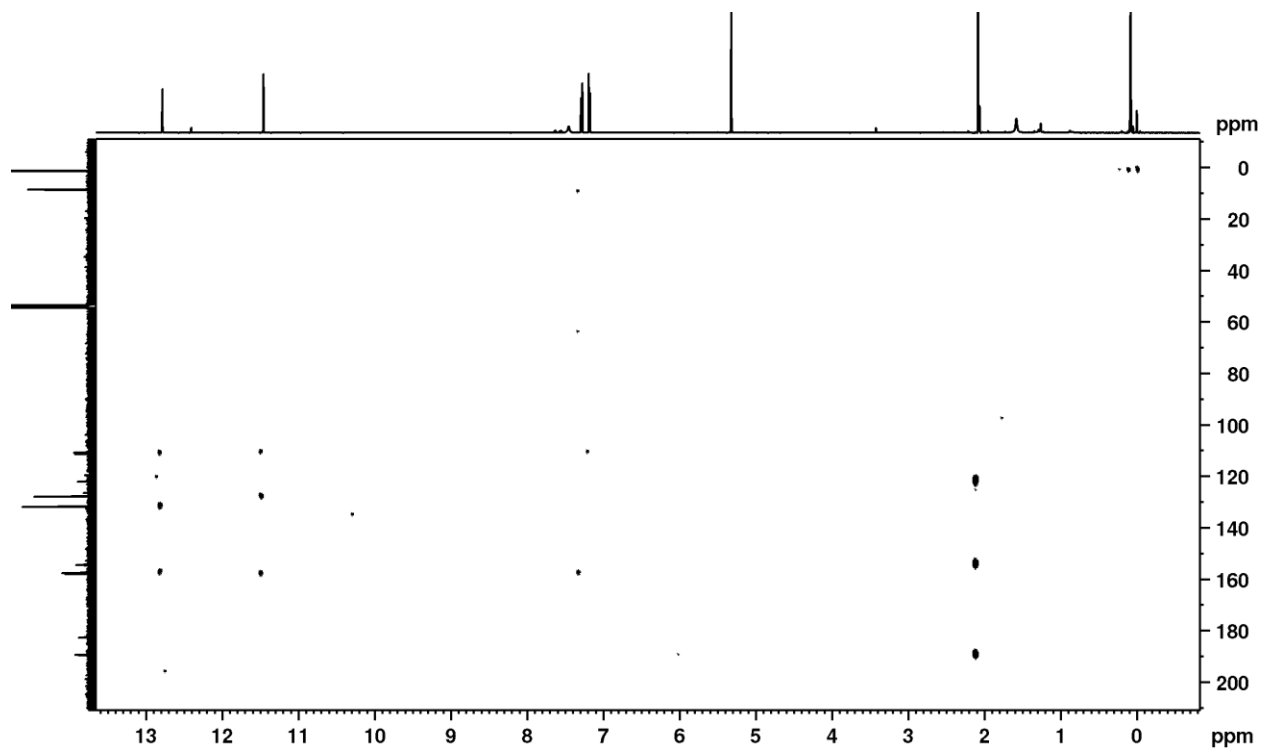
Appendix 12.3: HMBC spectrum of droserone (**93**) at 600 MHz in CD₂Cl₂.
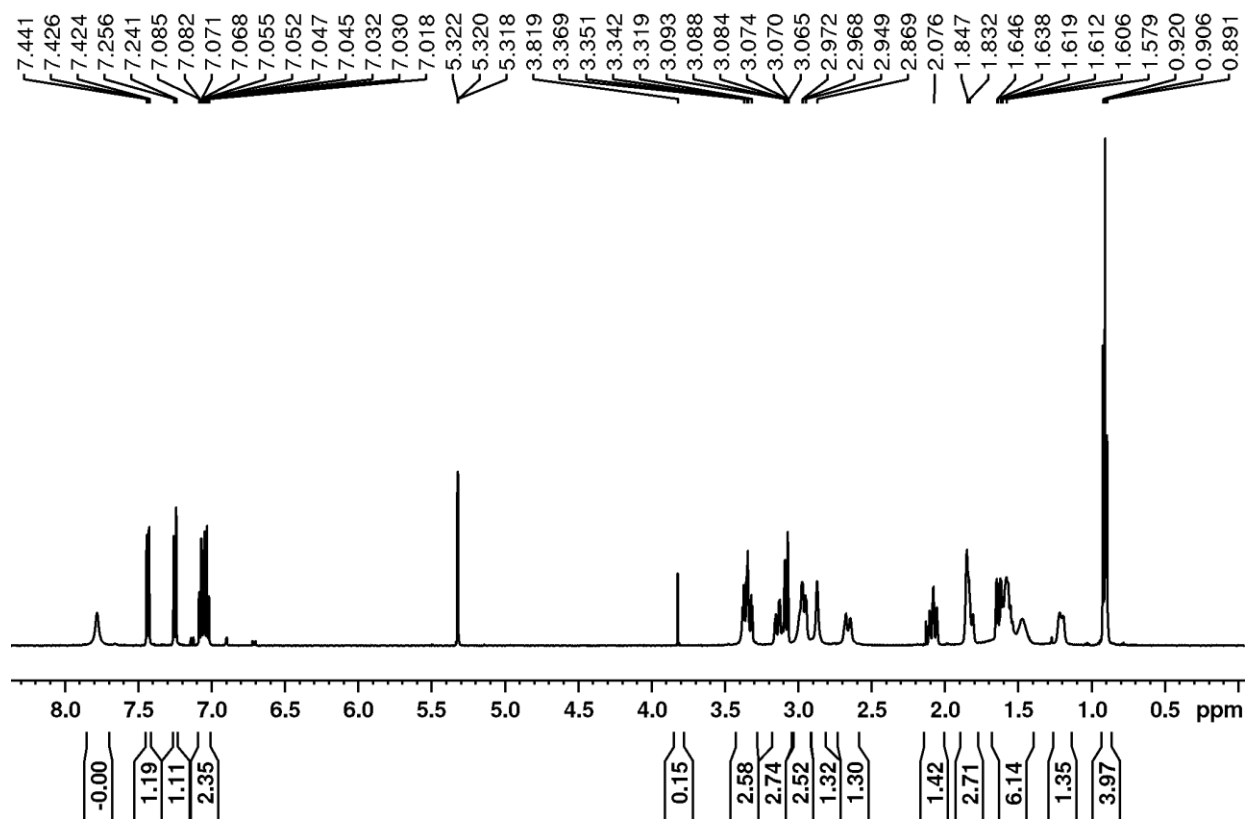
Appendix 13.1 ^{1}HNMR spectrum of ibogamine (**96**) at 600 MHz in CD_2Cl_2.
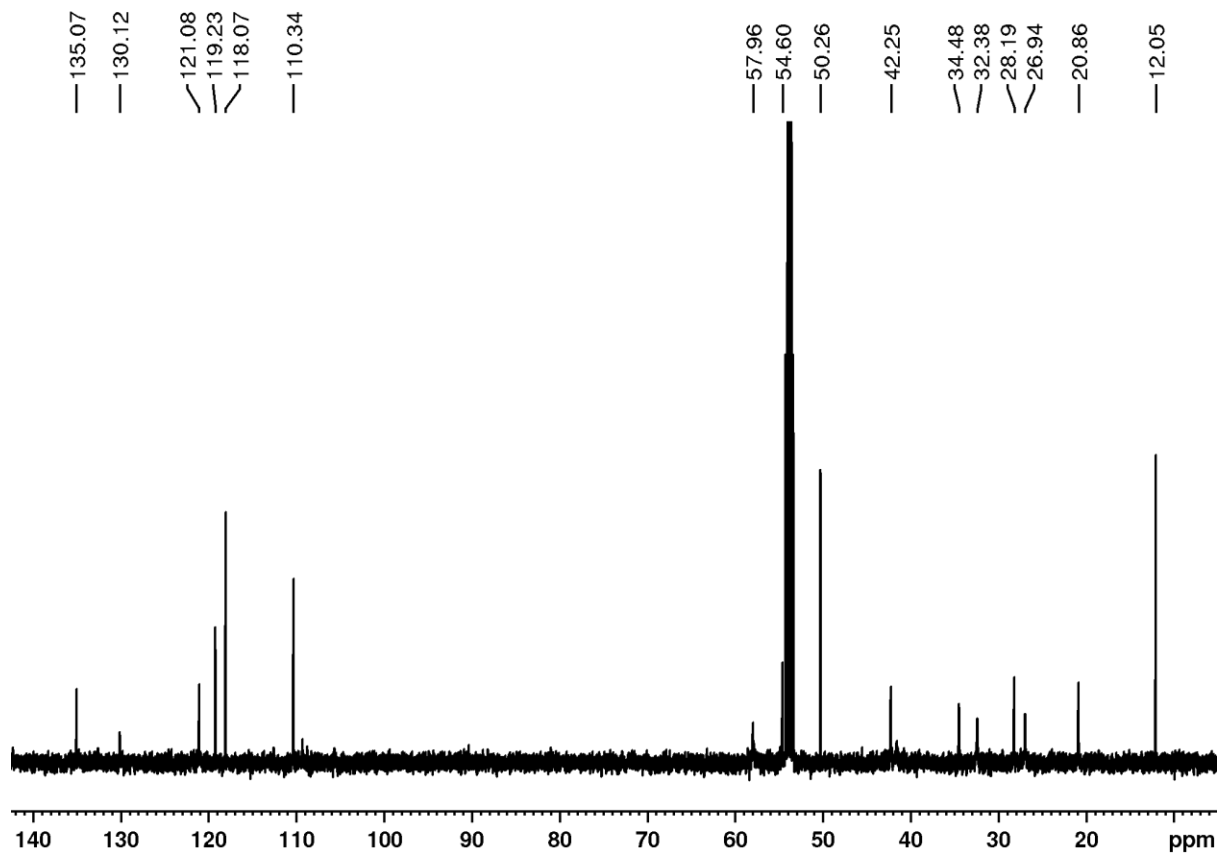
Appendix 13.2: ^{13}C NMR spectrum of ibogamine (**96**) at 151 MHz in CD$_2$Cl$_2$.
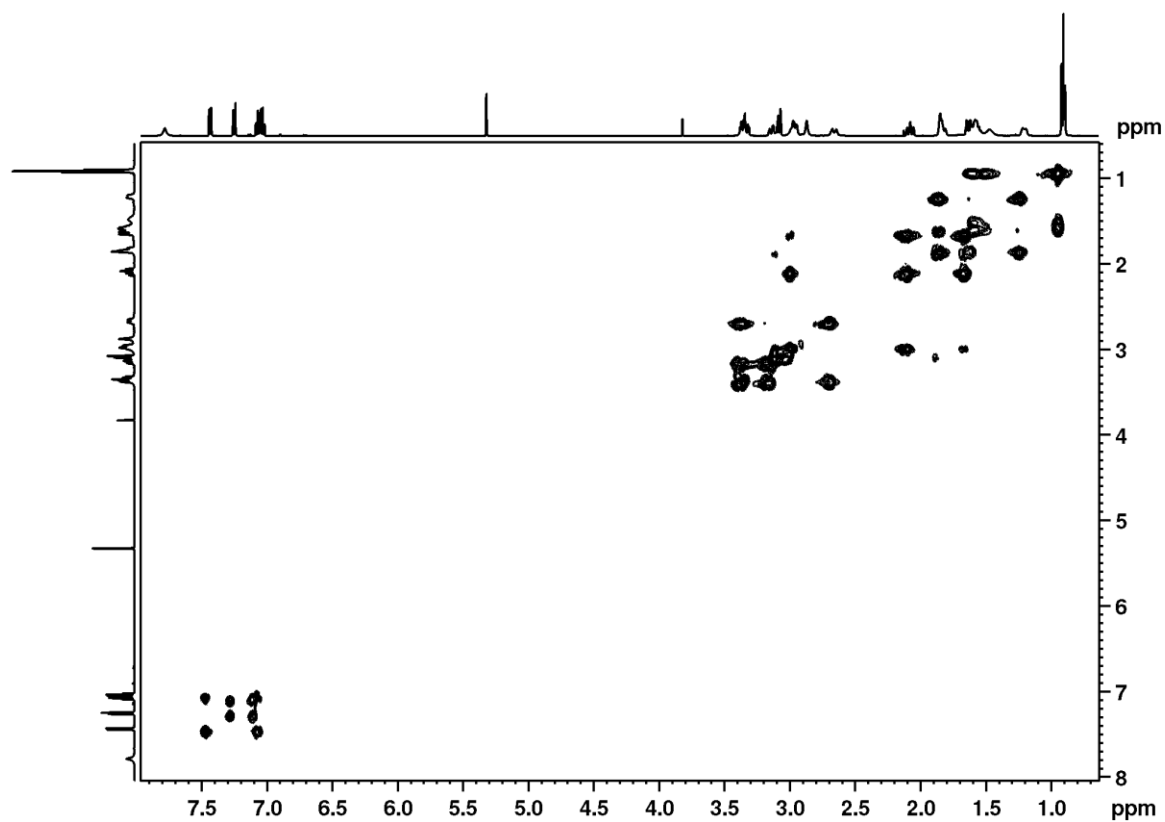
Appendix 13.3: H-H COSY NMR spectrum of ibogamine (**96**) at 600 MHz in CD$_2$Cl$_2$.
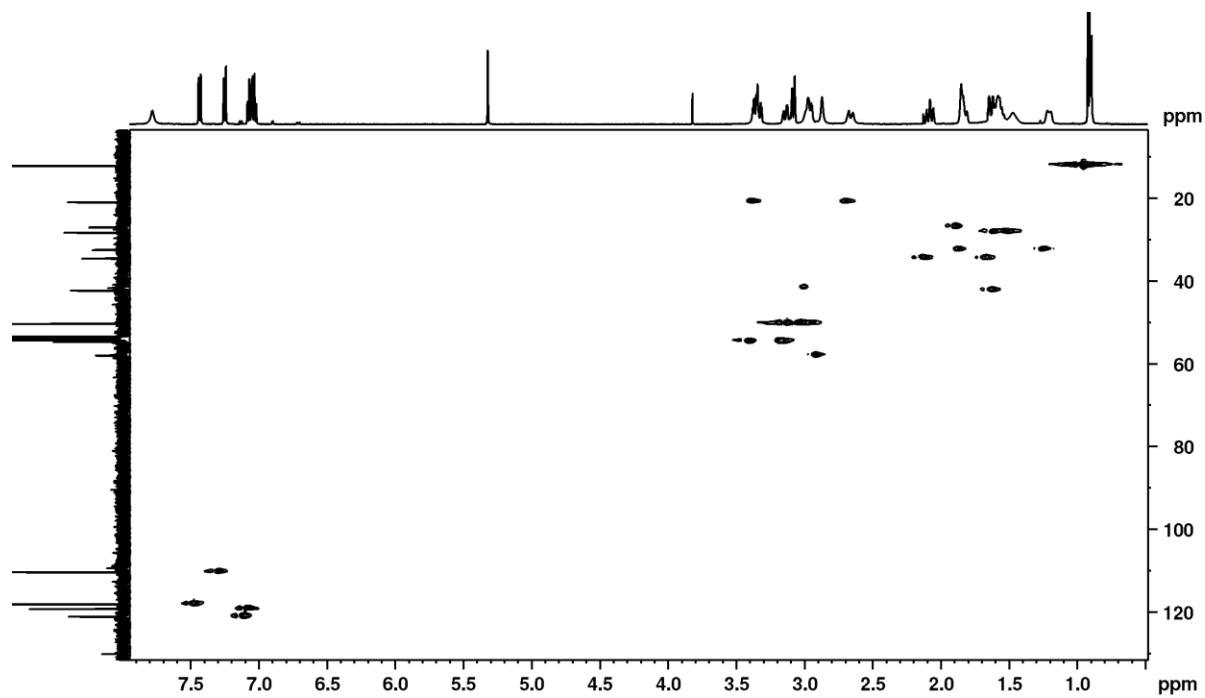
Appendix 13.4: HSQC spectrum of ibogamine (**96**) at 600 MHz in CD$_2$Cl$_2$.
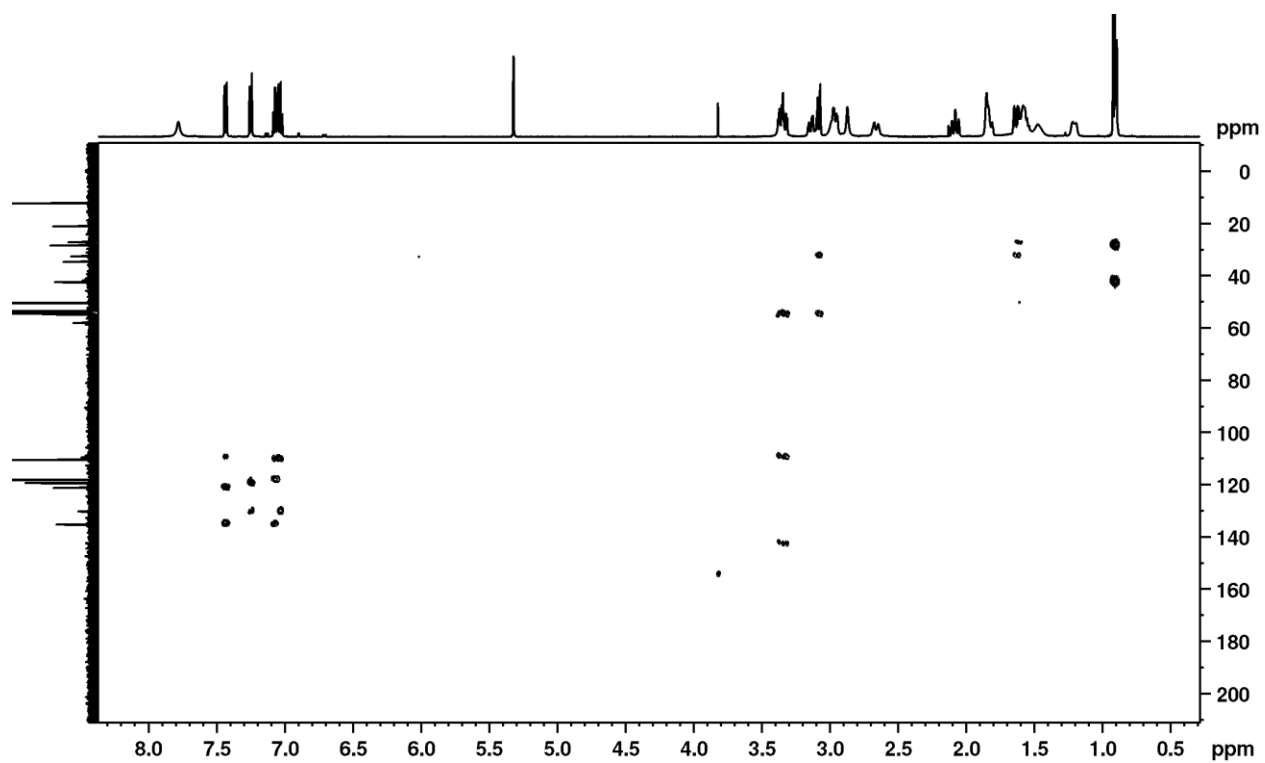
Appendix 13.5: HMBC spectrum of ibogamine (**96**) at 600 MHz in CD_2Cl_2.

Appendix 14.1 ^{1}HNMR spectrum of 10-hydroxyibogamine (**101**) at 600 MHz in MeOD.
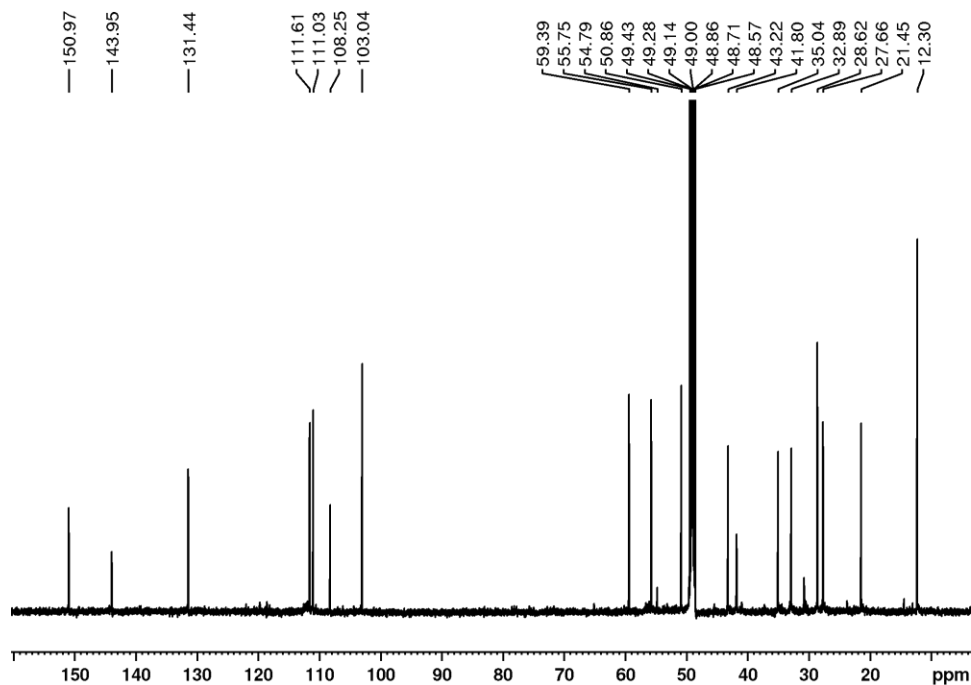
Appendix 14.2: ^{13}C NMR spectrum of 10-hydroxyibogamine (**101**) at 151 MHz in MeOD.
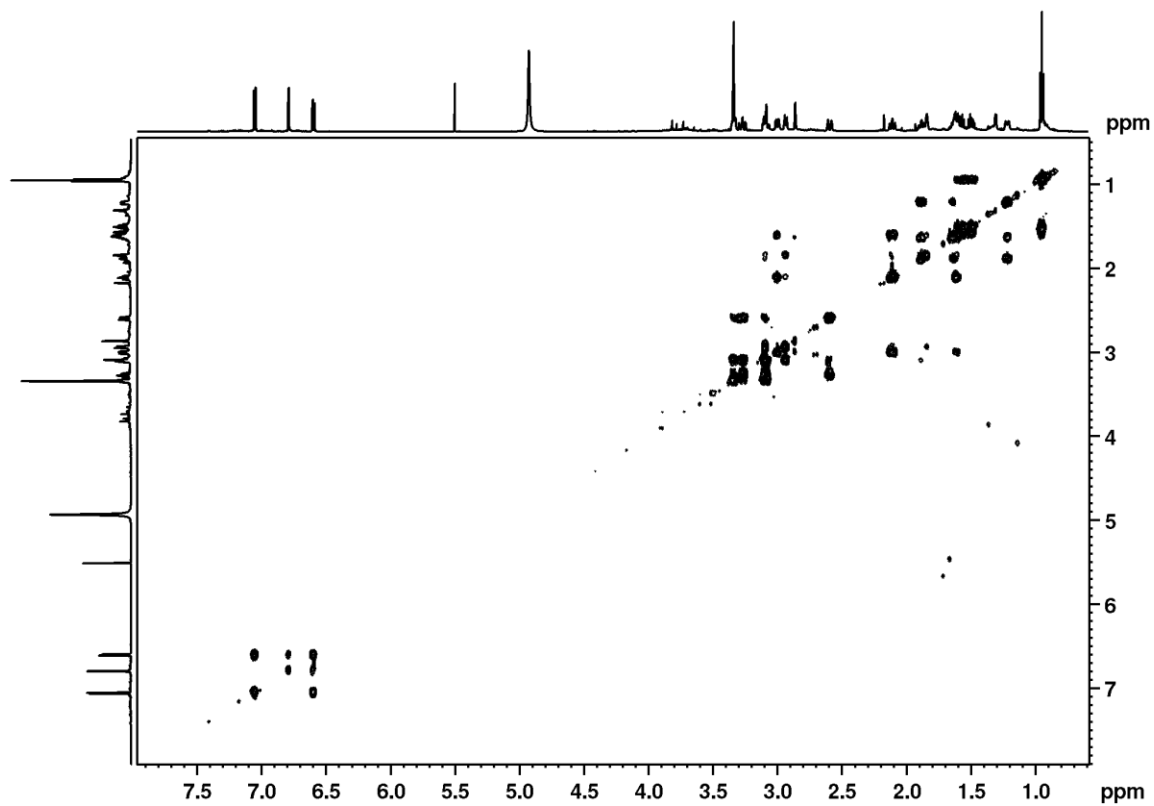
Appendix 14.3: H-H COSY spectrum of 10-hydroxyibogamine (**101**) at 600 MHz in MeOD.
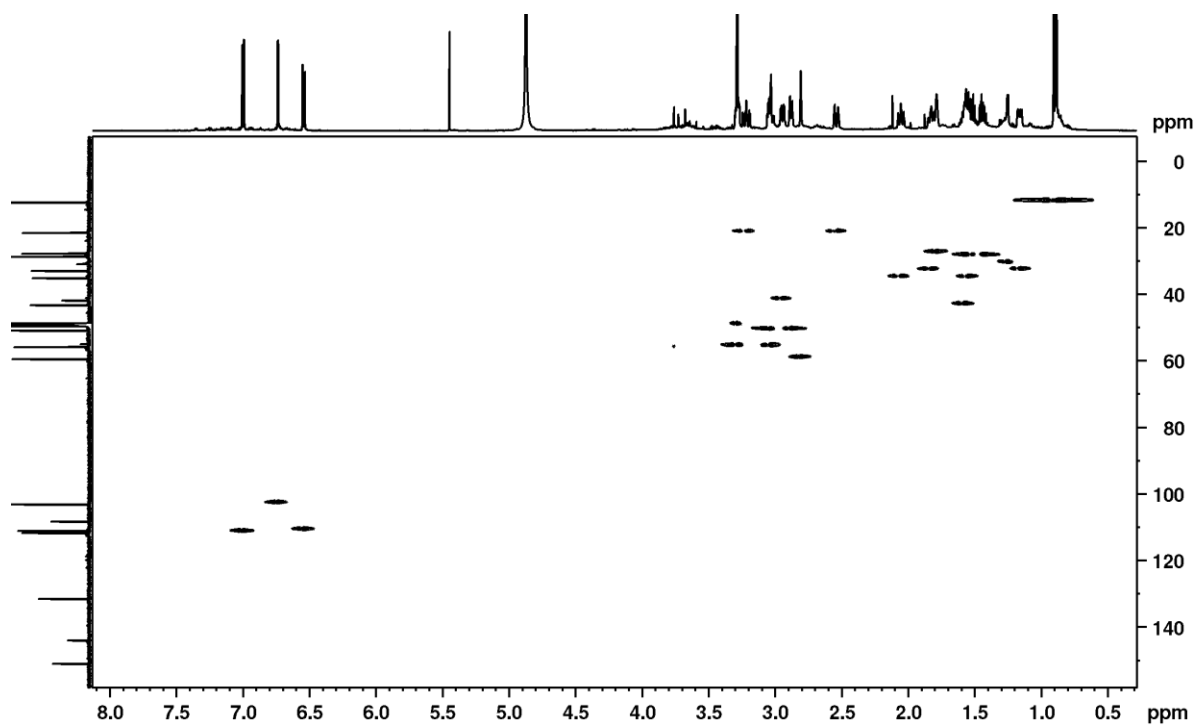
Appendix 14.4: HSQC spectrum of 10-hydroxyibogamine (**101**) at 600 MHz in MeOD.
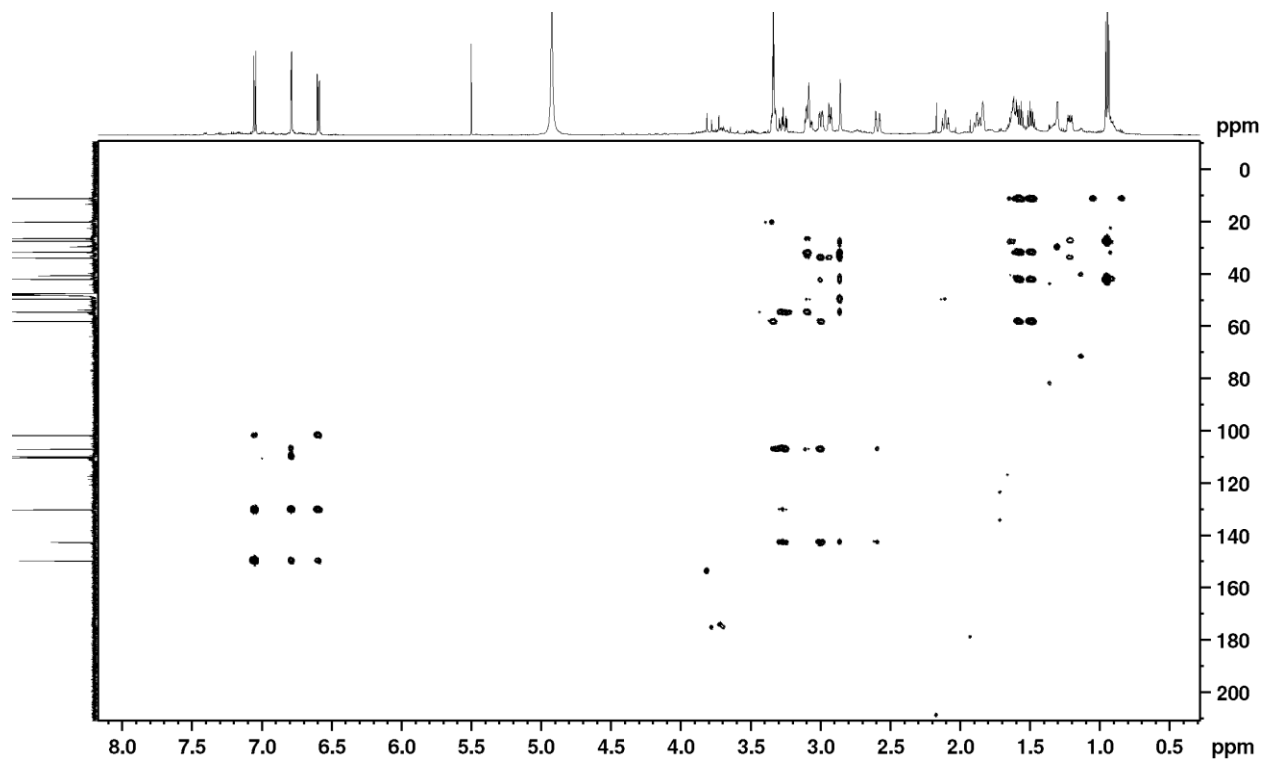
Appendix 14.5: HMBC spectrum of 10-hydroxyibogamine (**101**) at 600 MHz in MeOD.

Appendix 15: 1D and 2D spectra of 10-hydroxy coronaridin (**100**).
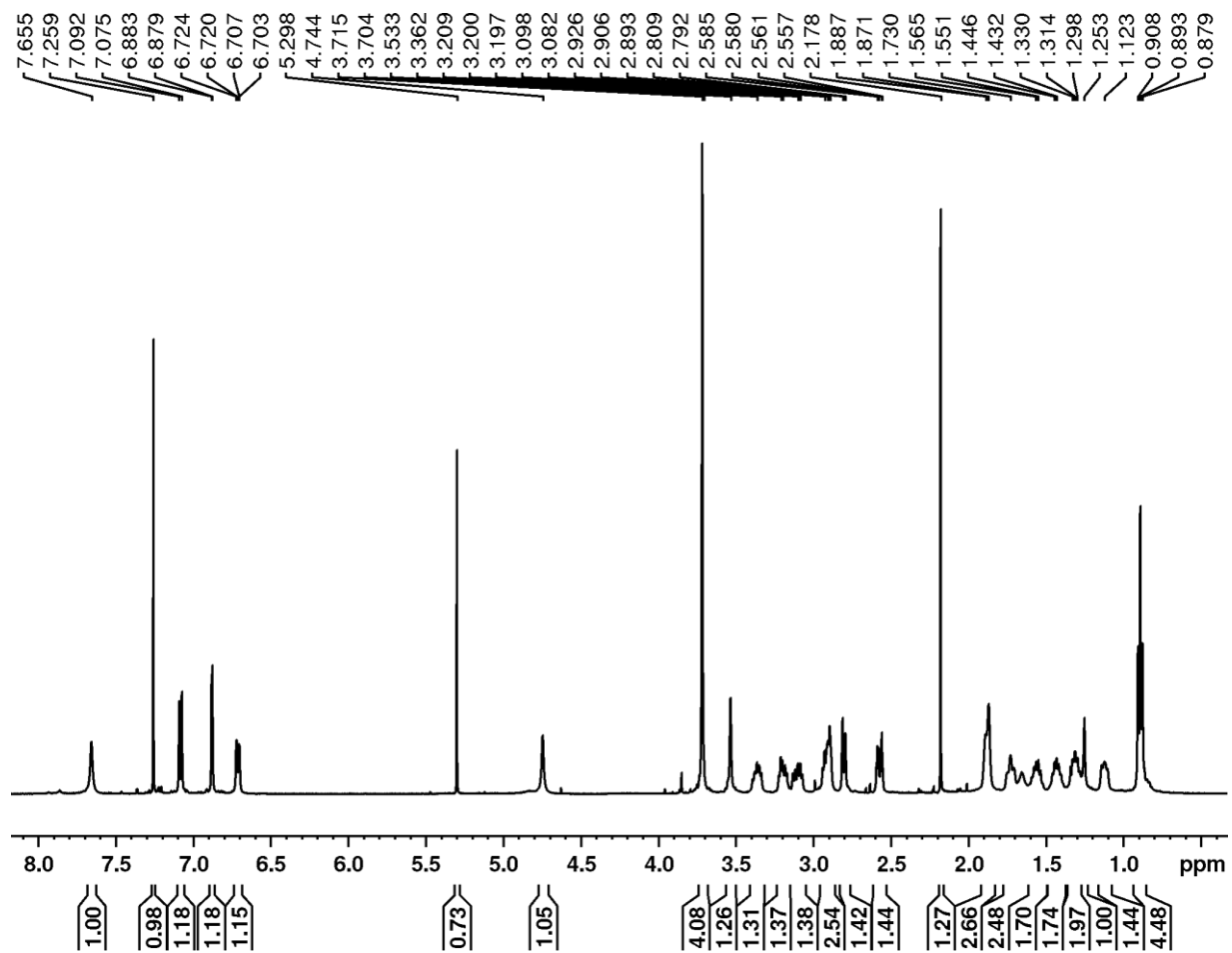
Appendix 15.1: ^{1}HNMR spectrum of 10-hydroxycoronaridin (**100** at 600 MHz in CDCl$_3$.
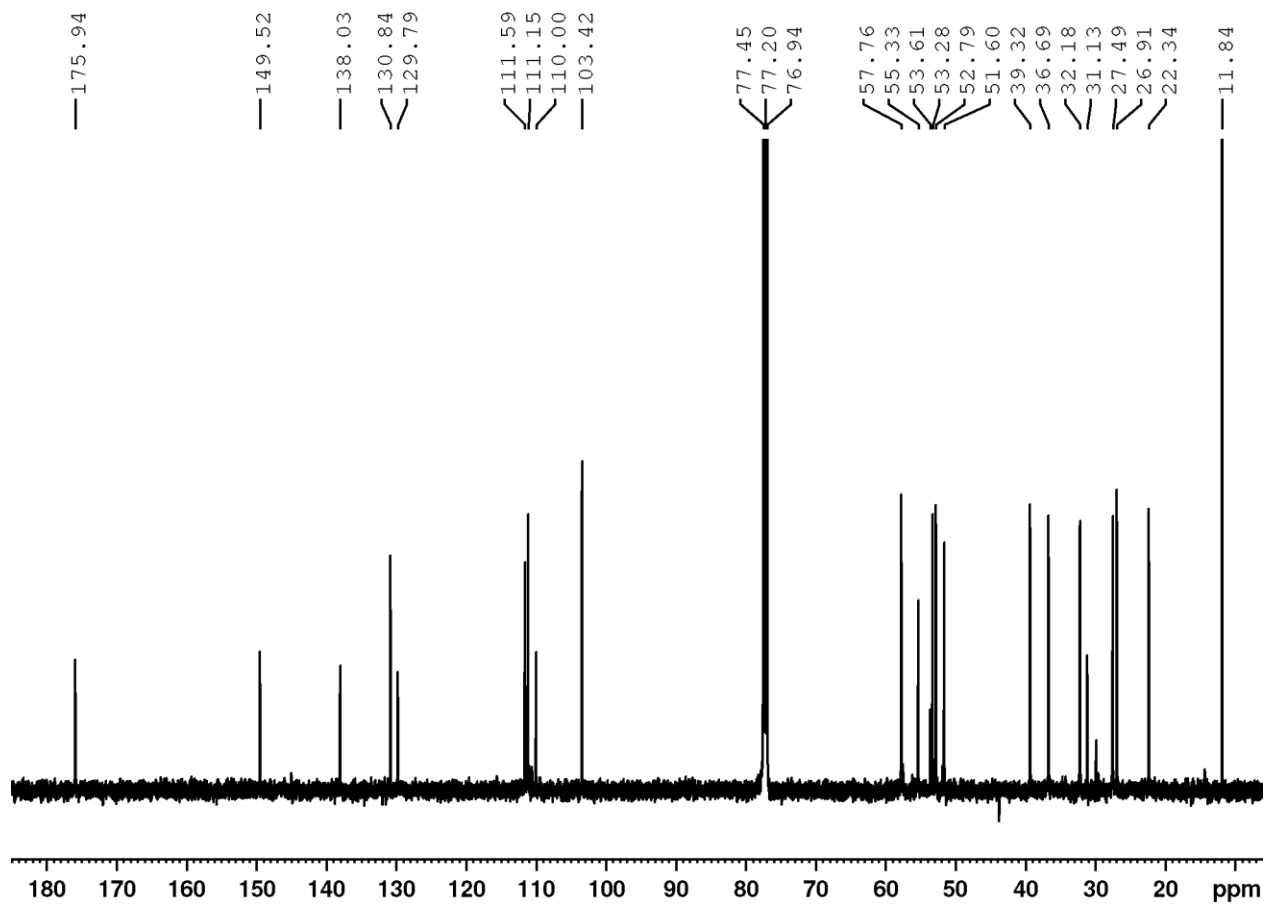
Appendix 15.2: ^{13}C NMR spectrum of 10-hydroxycoronaridin (**100**) at 151 MHz in CDCl$_3$.
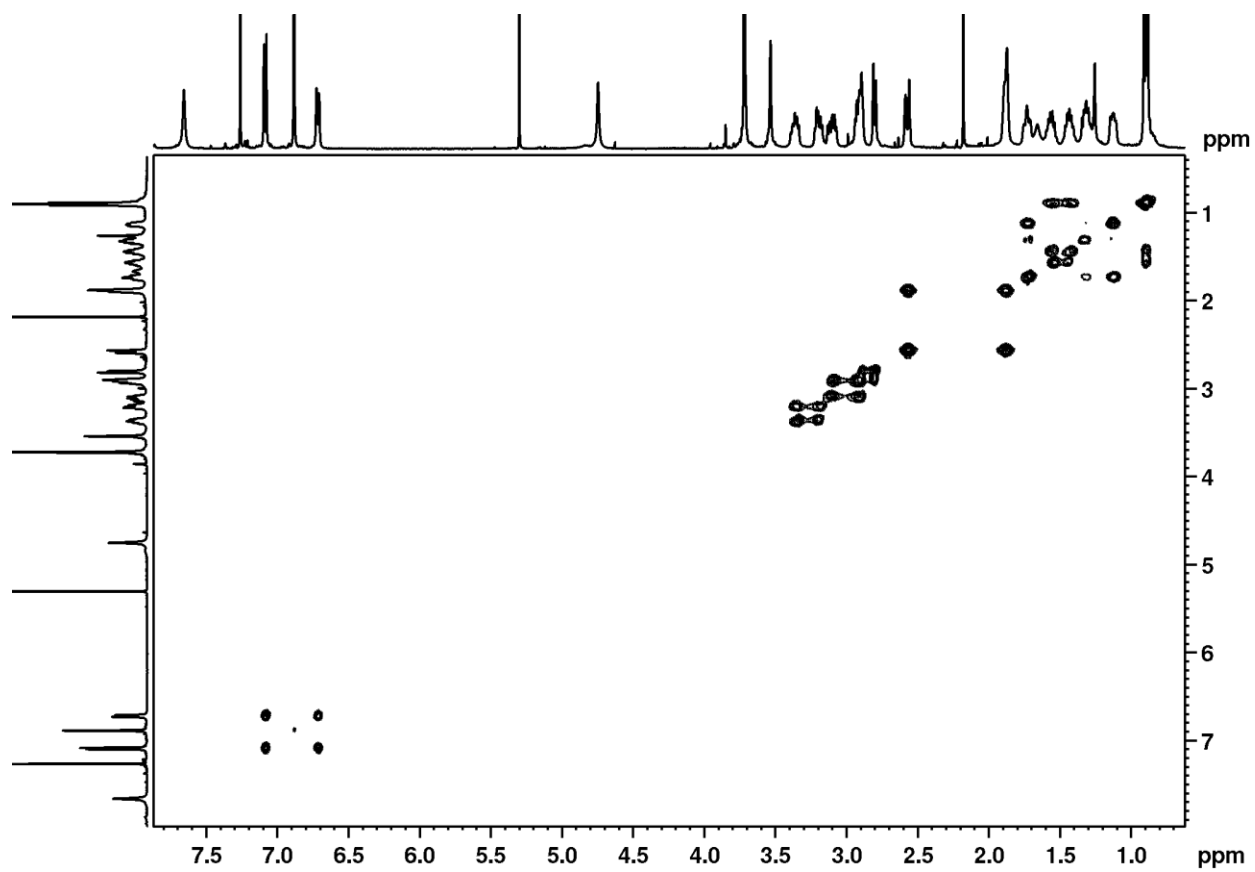
Appendix 15.3: H-H COSY spectrum of 10-hydroxycoronaridin (**100**) at 151 MHz in CDCl$_3$.
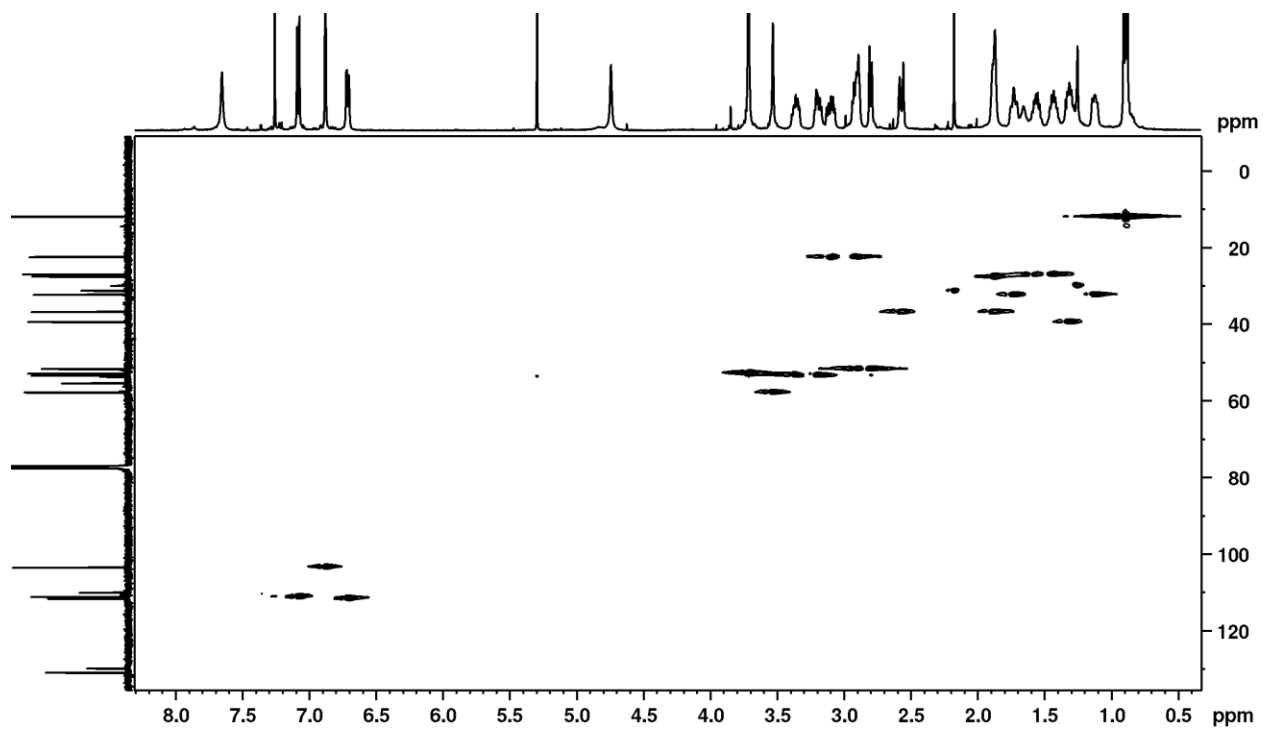
Appendix 15.4: HSQC spectrum of 10-hydroxycoronaridin (**100**) at 151 MHz in CDCl₃.
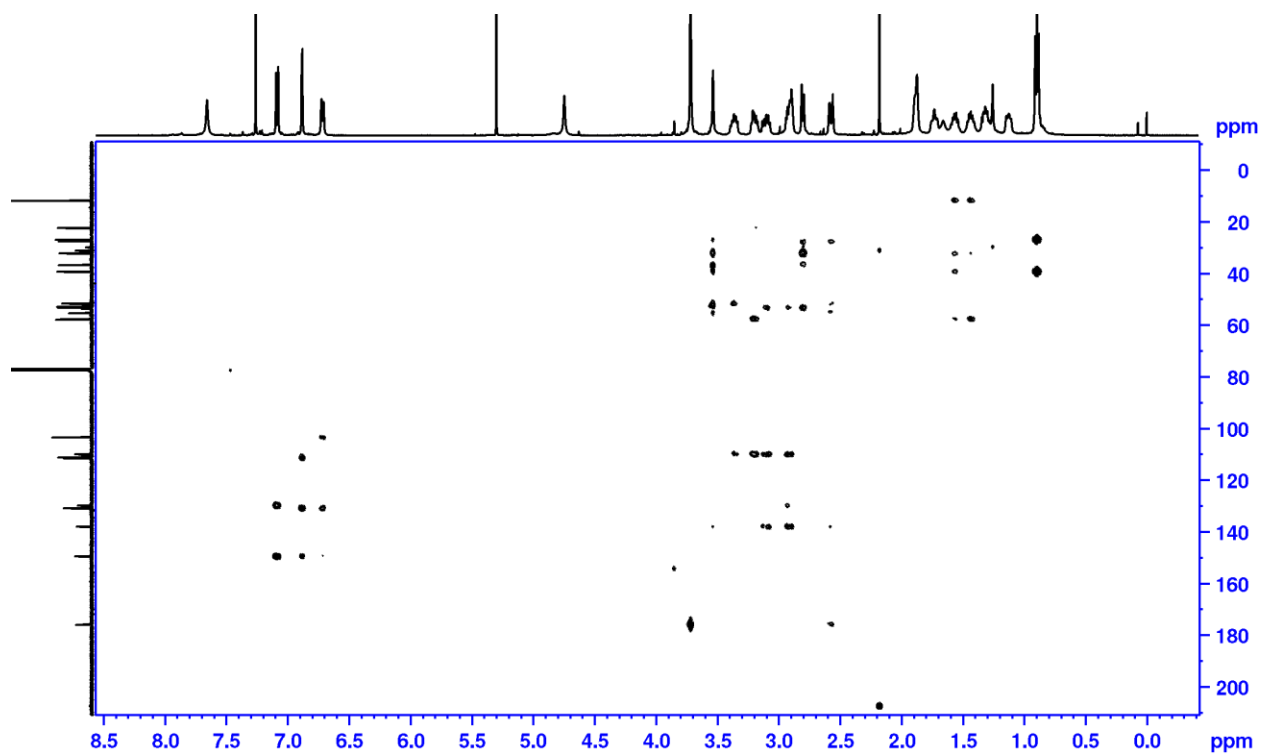
Appendix 15.5: HMBC spectrum of 10-hydroxycoronaridin (**100**) at 151 MHz in CDCl₃.

Appendix 16: 1D and 2D spectra of voacristine (**84**).
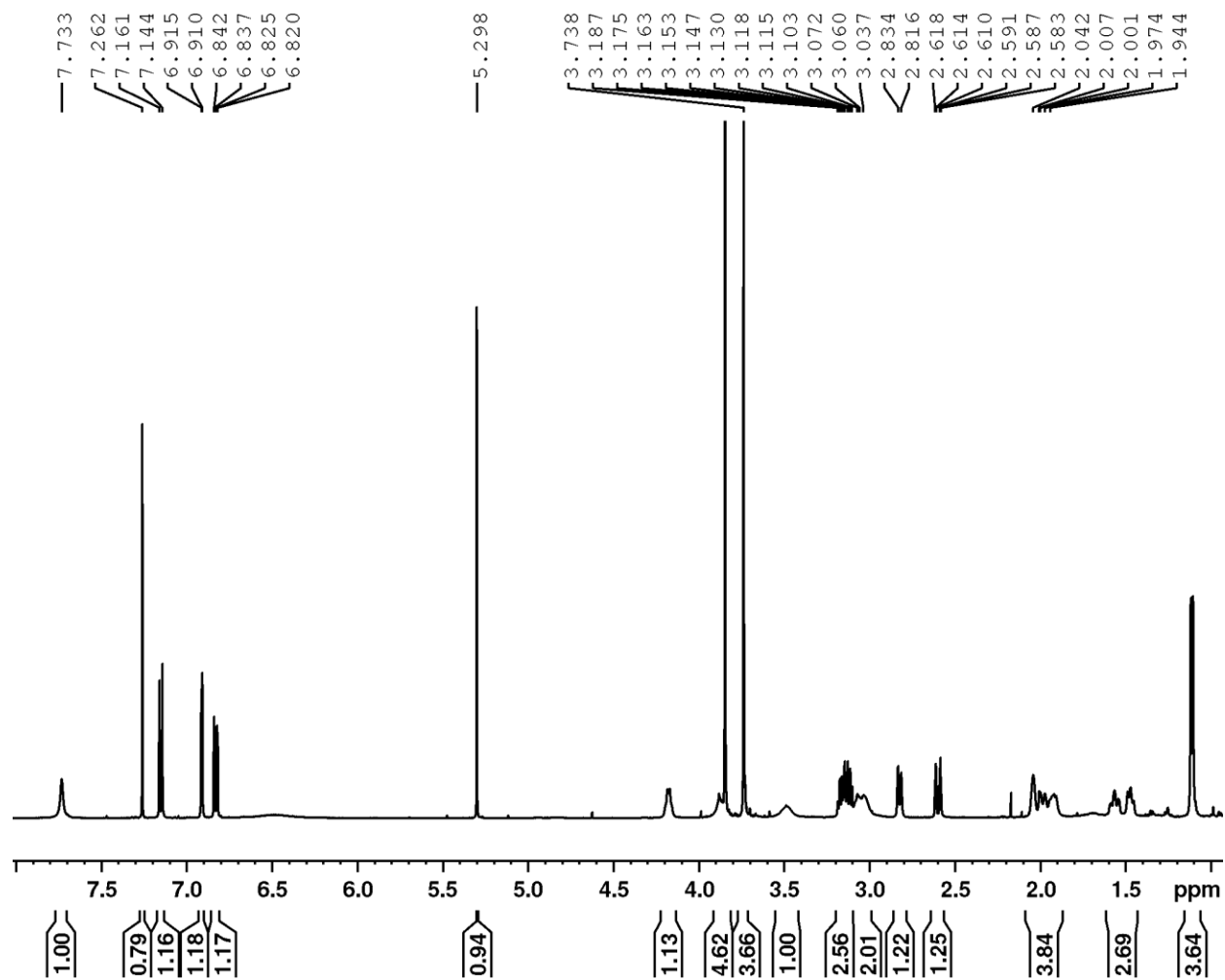
Appendix 16.1: ^{1}HNMR spectrum of voacristine (**98**) at 600 MHz in CDCl$_3$.
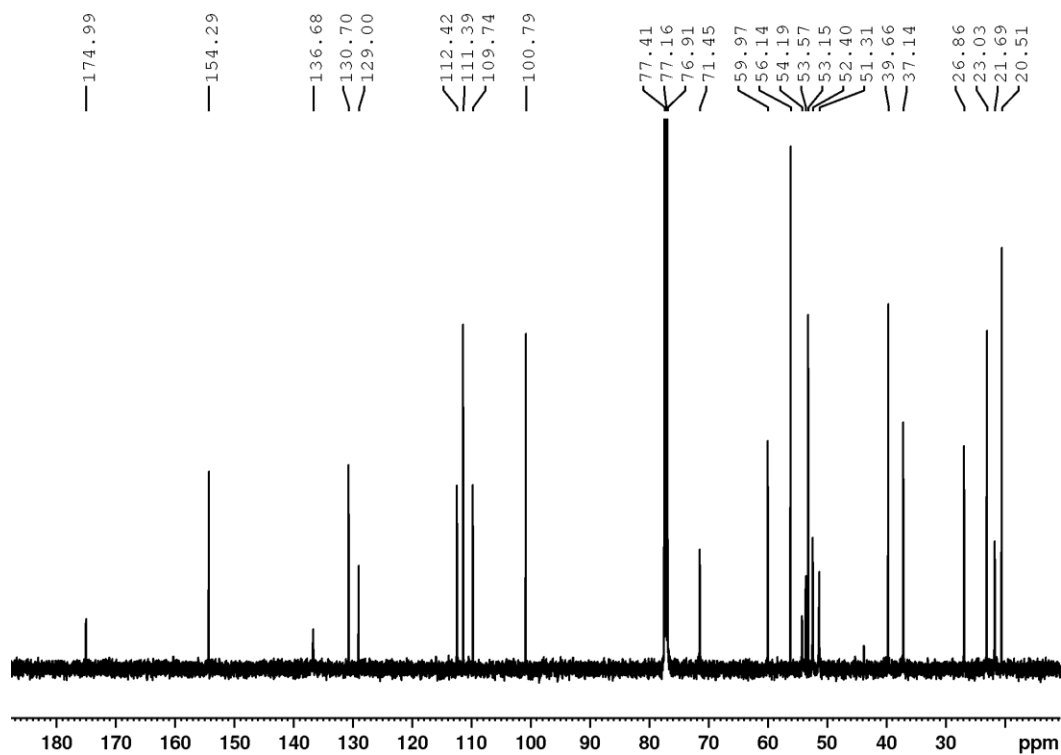
Appendix 16.2: ^{13}C NMR spectrum of voacristine (**98**) at 151 MHz in CDCl$_3$.
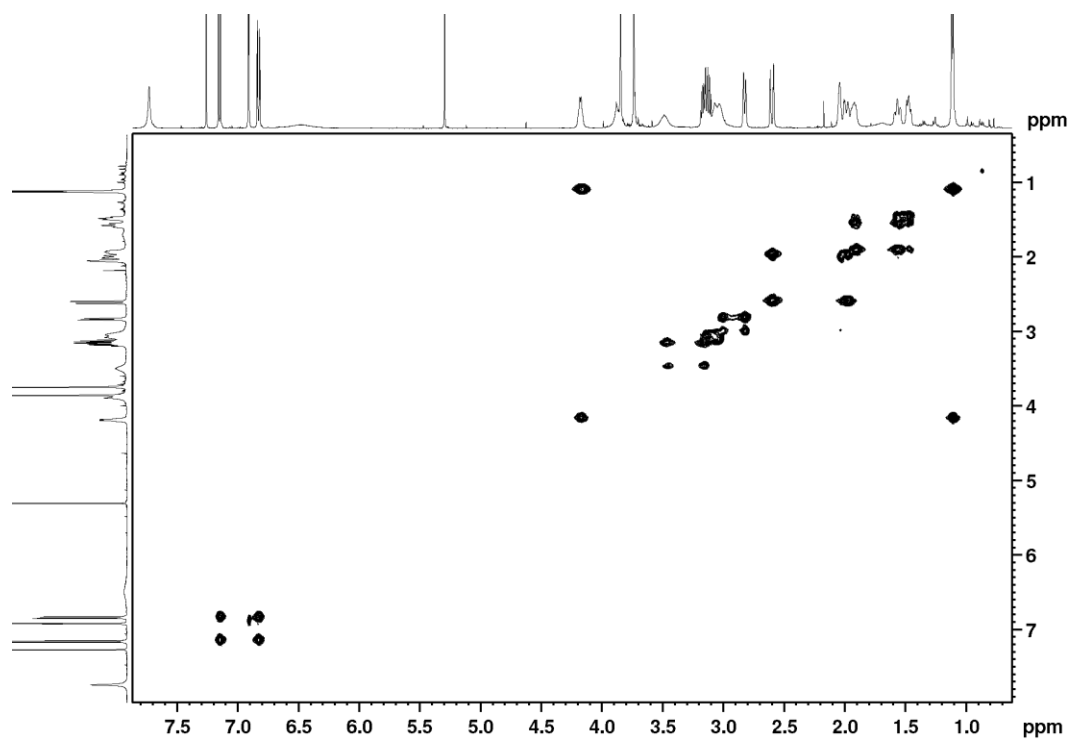
Appendix 16.3: H-H COSY spectrum of voacristine (**98**) at 600 MHz in CDCl$_3$.

226
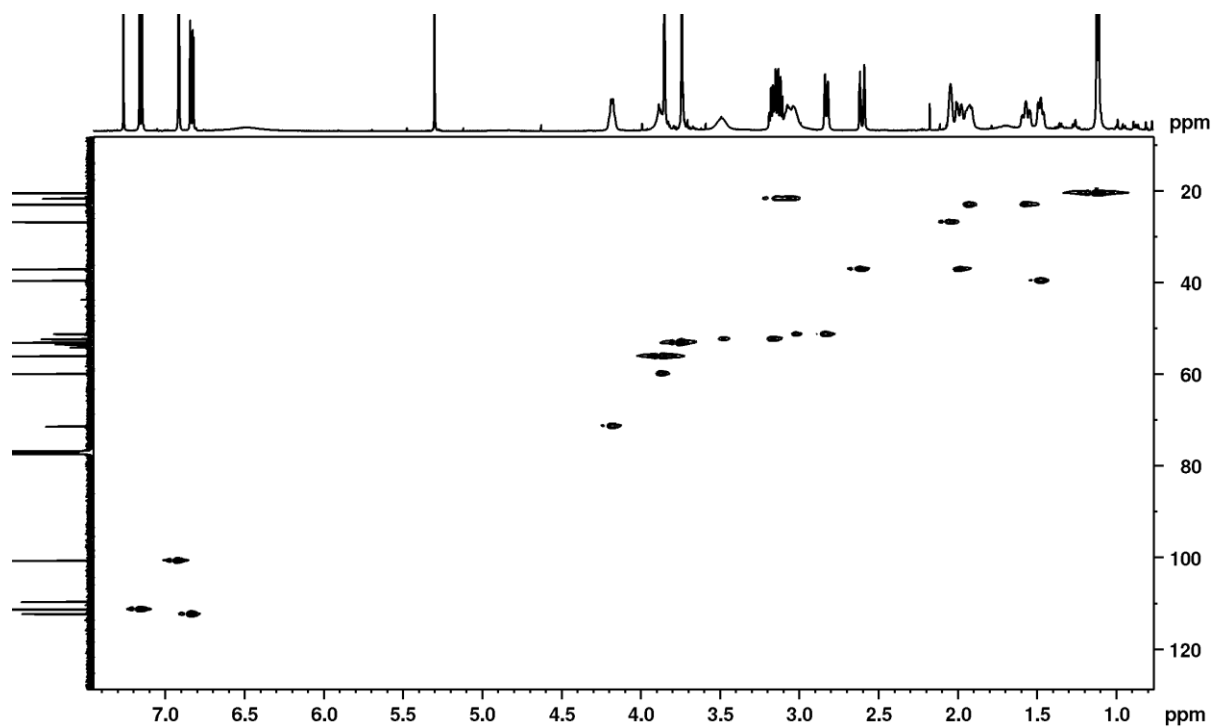
Appendix 16.4: HSQC spectrum of voacristine (**98**) at 600 MHz in CDCl₃.
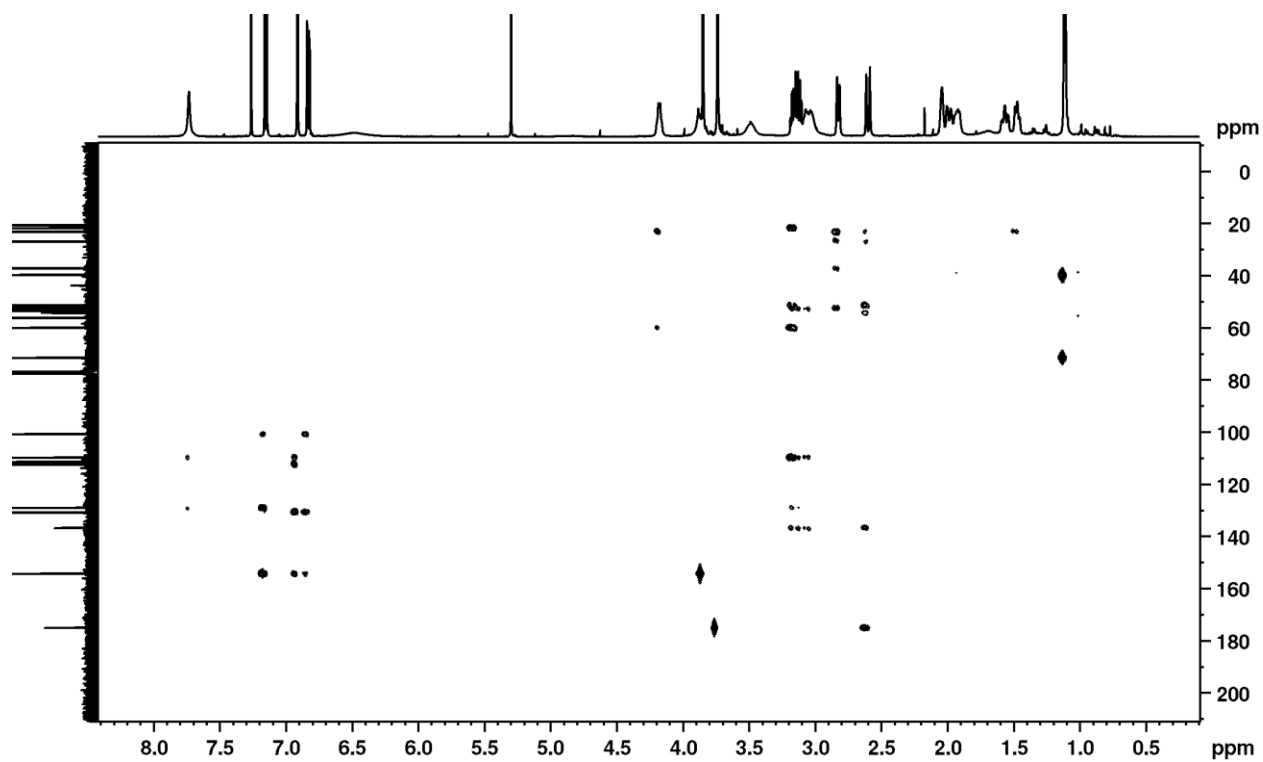
Appendix 16.4: HMBC spectrum of voacristine (**98**) at 600 MHz in CDCl₃.

227

Appendix 17: 1D and 2D spectra for 3-Ketopropylcoronaridine (**94**).
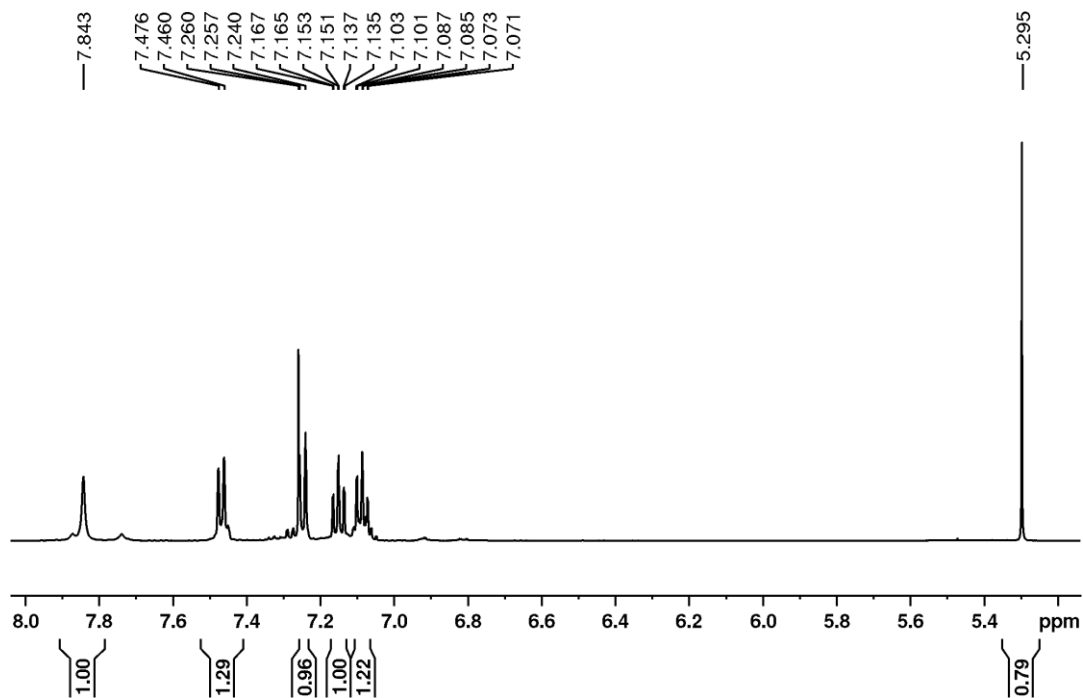
Appendix 17.1: Expansion of ^{1}H NMR spectrum of **94** at 600 MHz in CDCl$_3$.
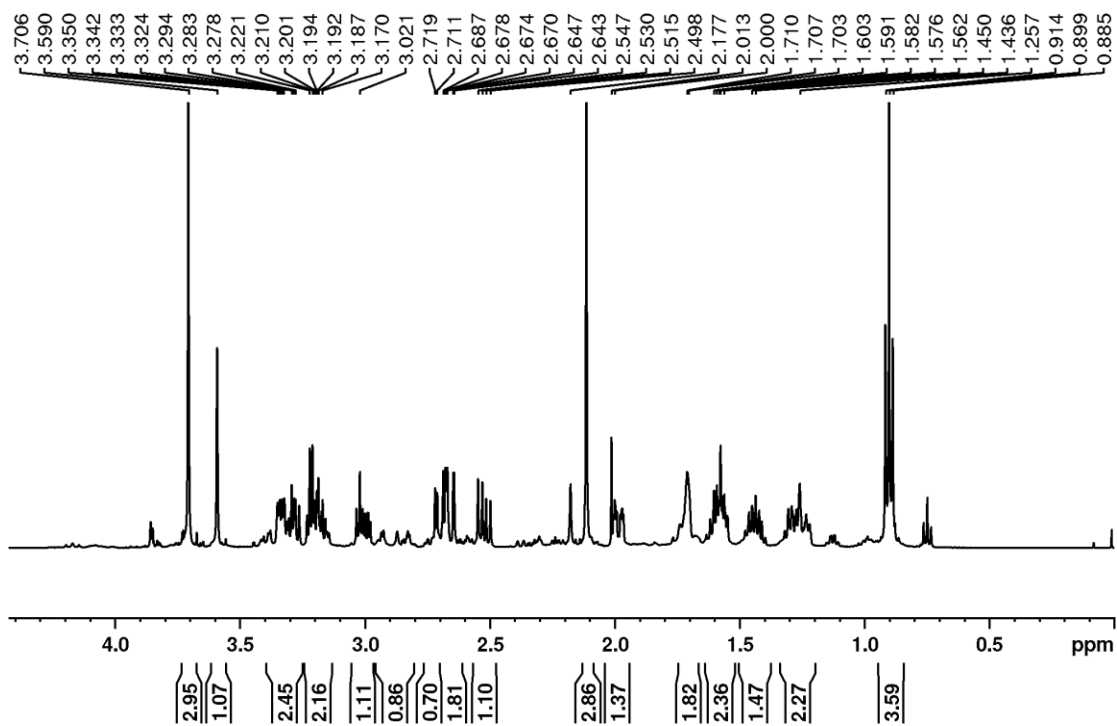
Appendix 17.2: Expansion of ^{1}H NMR spectrum of **94** at 600 MHz in CDCl$_3$.
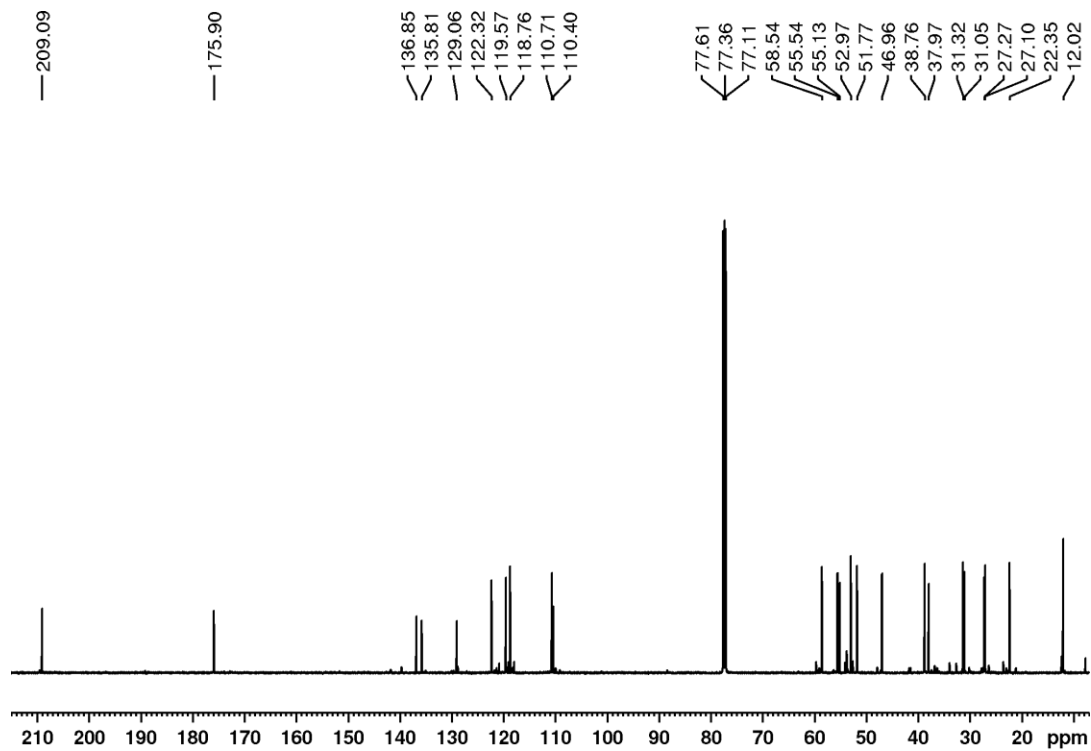
Appendix 17.3: ^{13}C NMR of **94** at 151 MHz in CDCl$_3$.
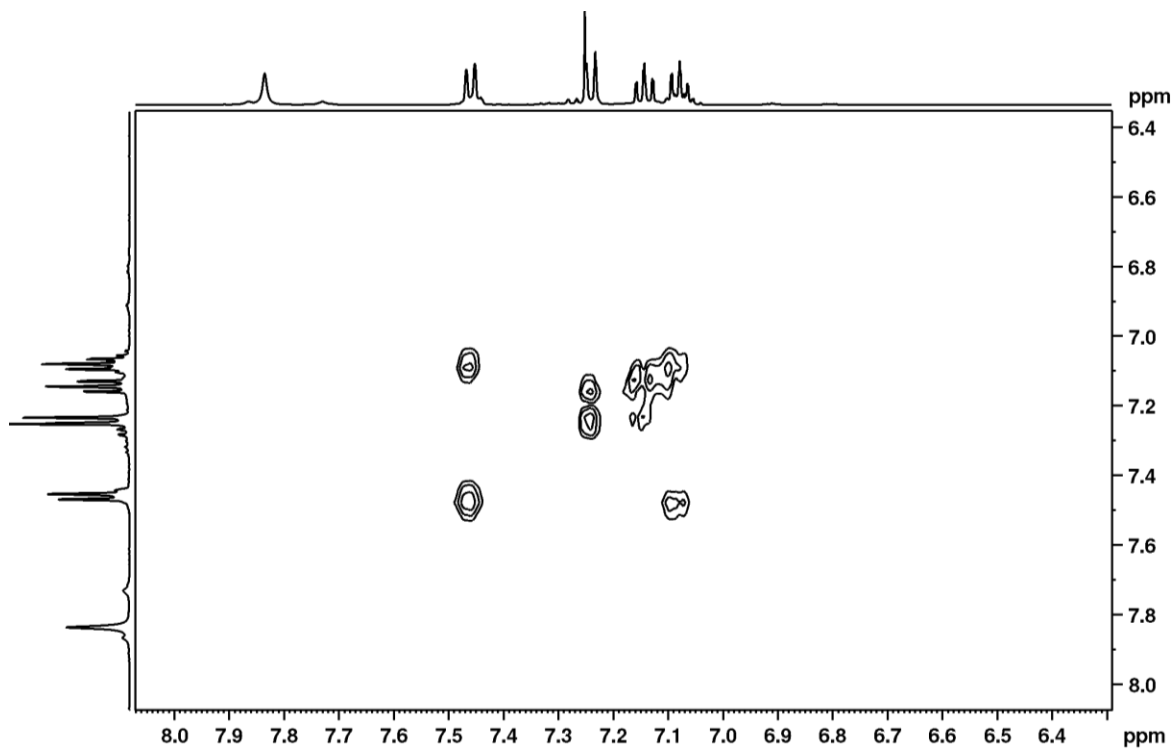
Appendix 17.4: Expansion1 of H-H COSY spectrum of **94 at** 600 MHz in CDCl$_3$.
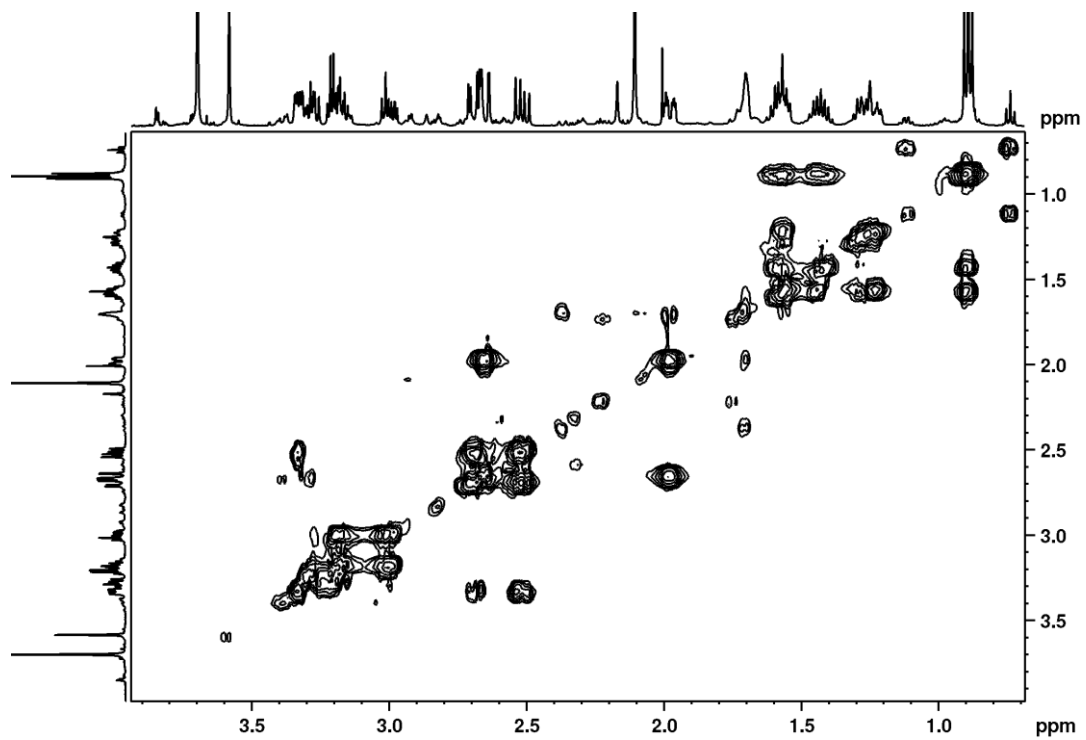
Appendix 17.5: Expansion 2 of H-H COSY spectrum of **94.**
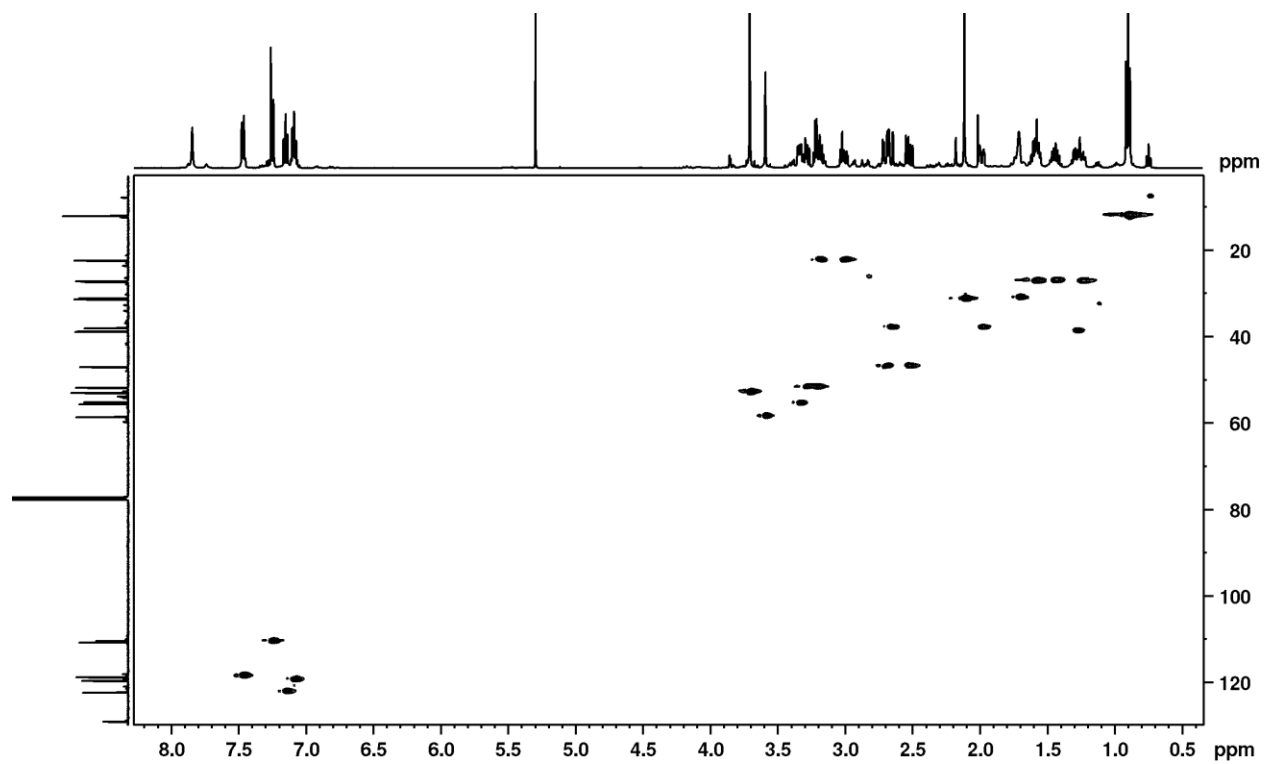
Appendix 17.6: HSQC Spectrum of **94** at 600 MHz in CDCl₃.
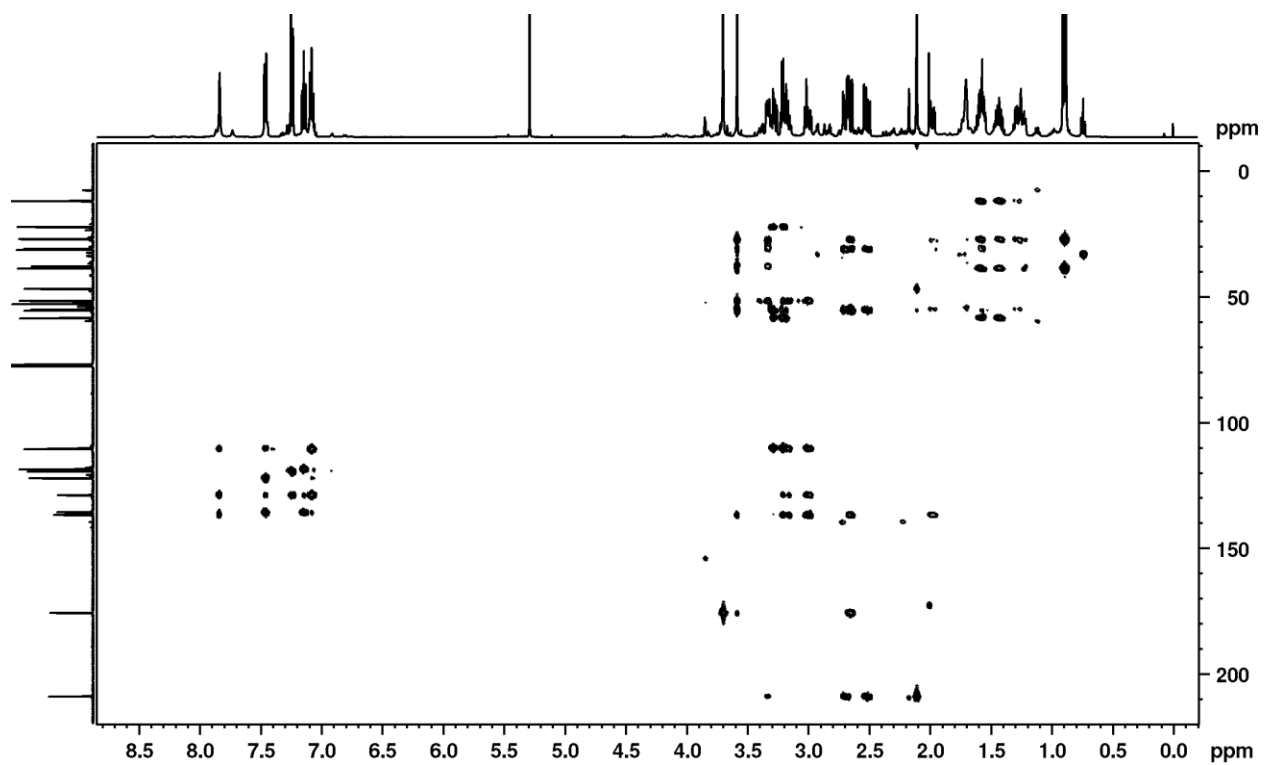
Appendix 17.7: HMBC spectrum of compound **94** at 600 MHz in CDCl$_3$.

Appendix 18: 1D, 2D and HRMSESI spectrum of vobasine (**95**).
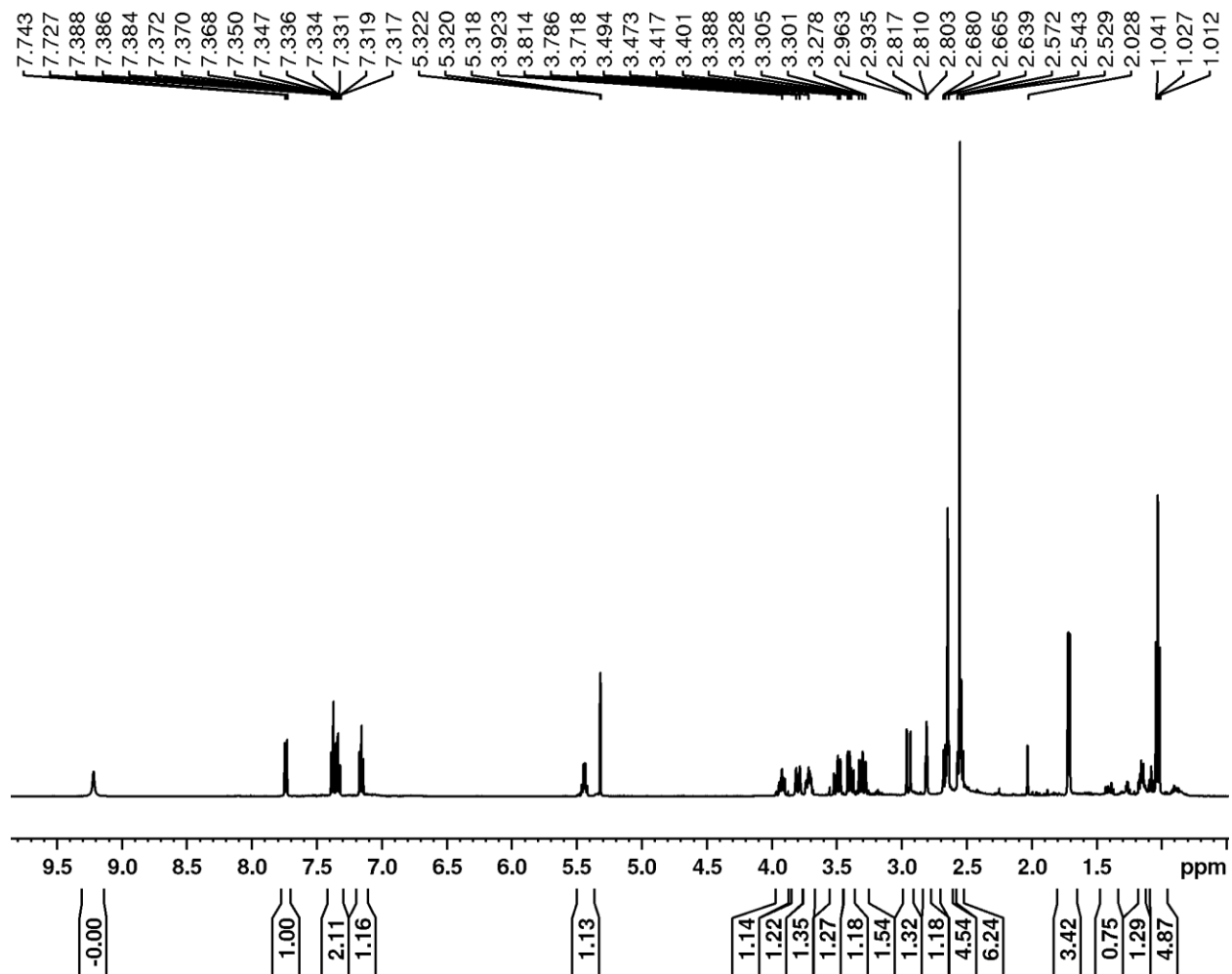
Appendix 18.1: ^{1}H NMR spectrum of vobasine (**95**) at 600 MHz in CD_2Cl_2.
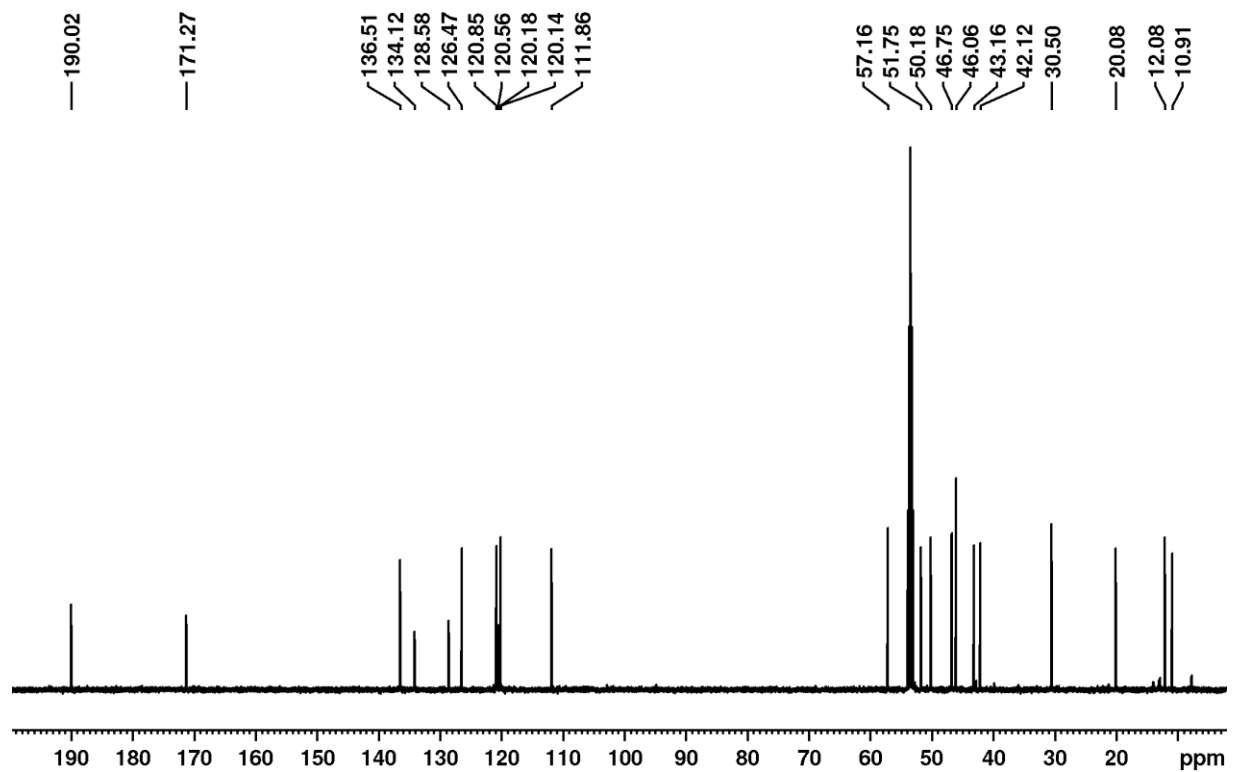
Appendix 18.2: ^{13}C NMR spectrum of vobasine (**95**) at 151 MHz in CD$_2$Cl$_2$.

233
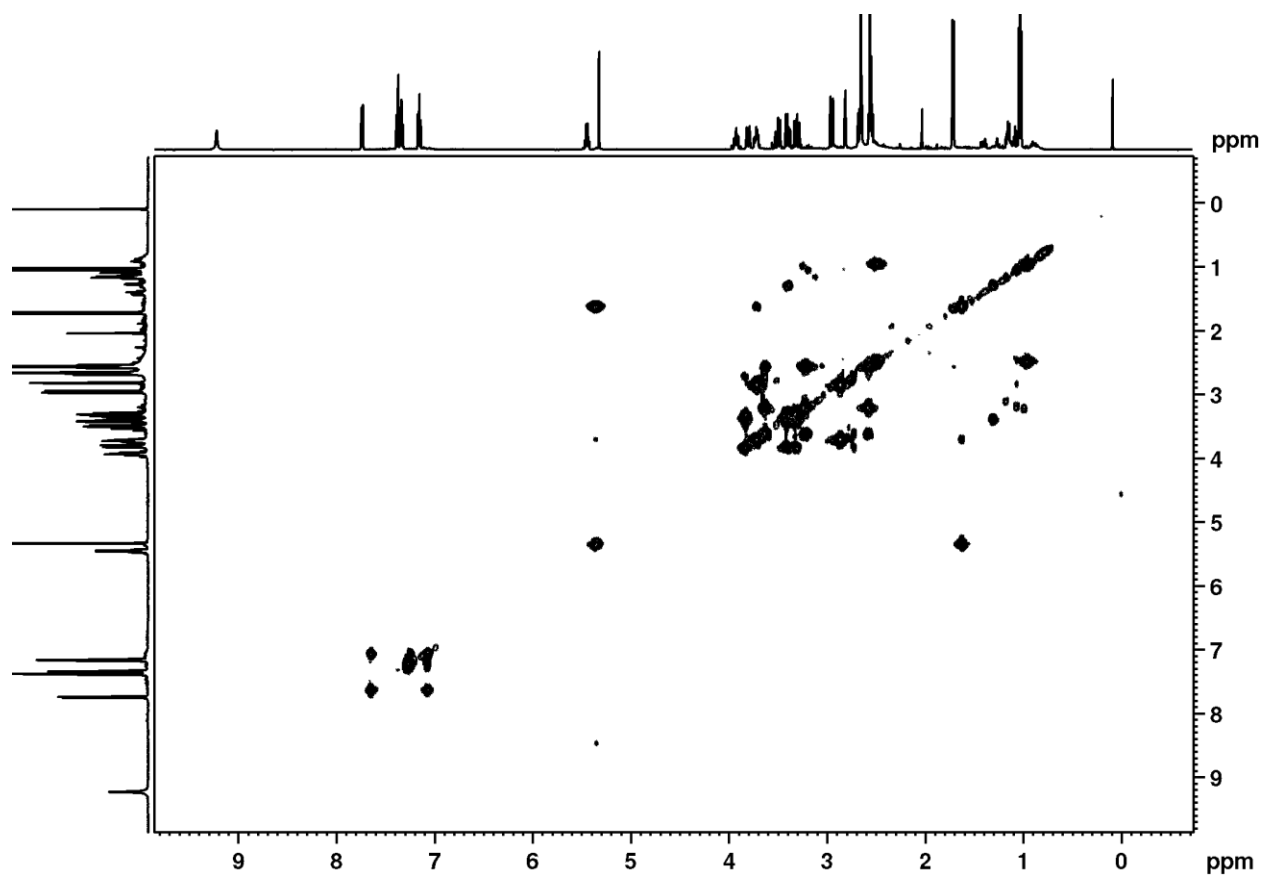
Appendix 18.3: H-H COSY spectrum of vobasine (**95**) at 600 MHz in CD_2Cl_2.
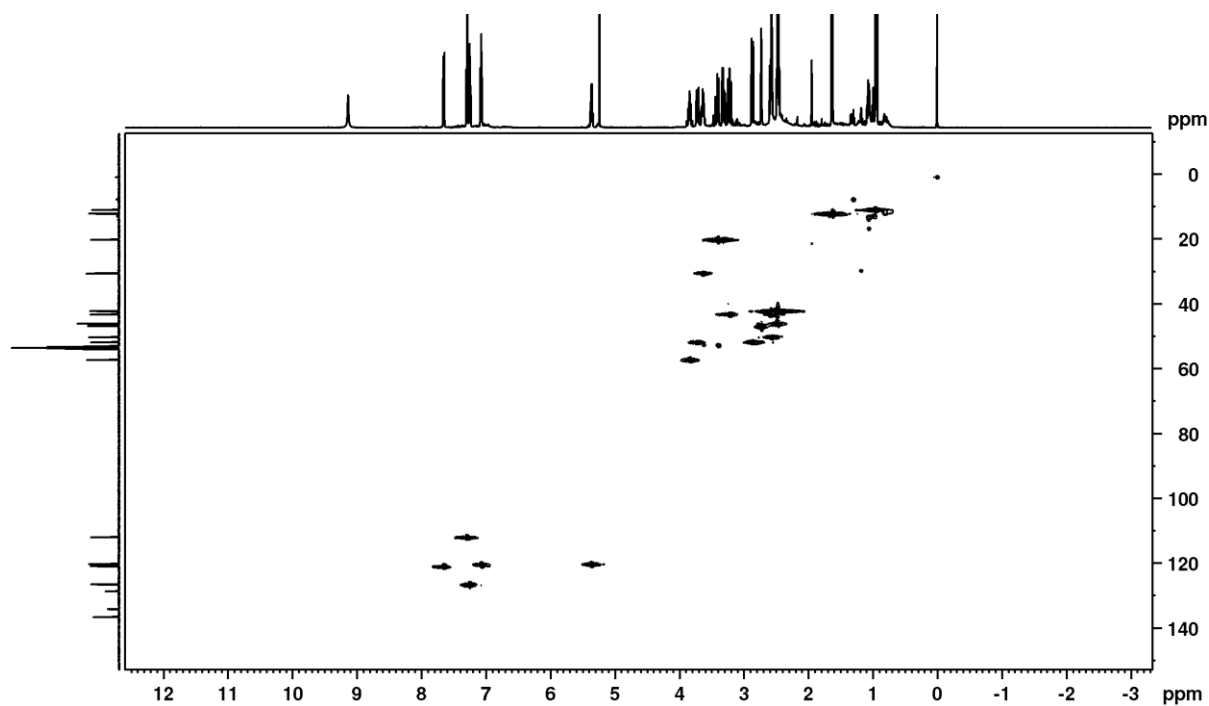
Appendix 18.4: HSQC spectrum of vobasine (**95**) at 600 MHz in CD_2Cl_2.
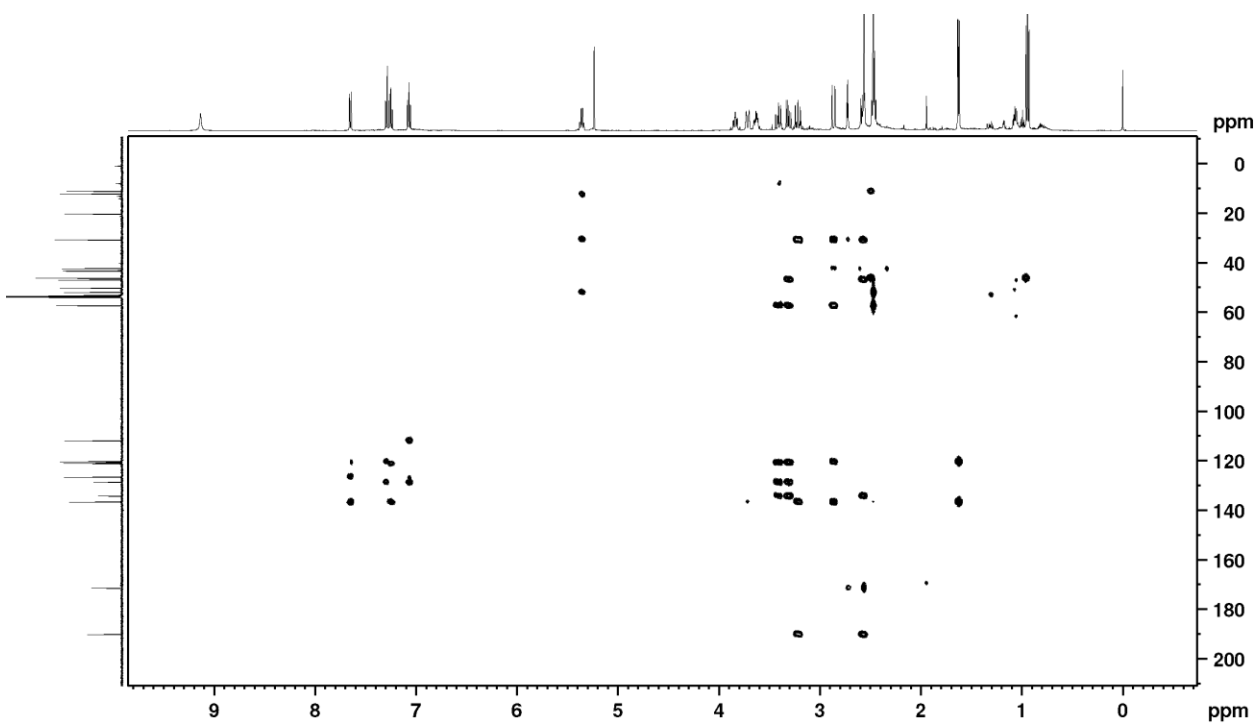
Appendix 18.5: HMBC spectrum of vobasine (**95**) at 600 MHz in CD_2Cl_2.
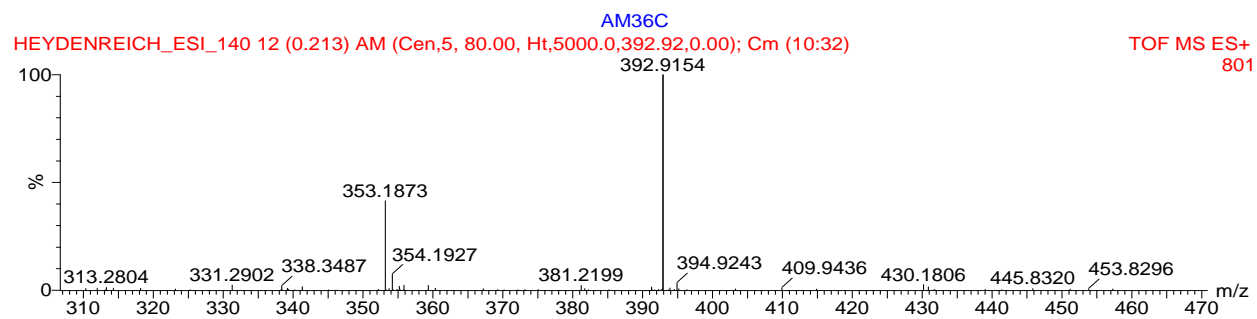
Appendix 18.6: HRMS spectrum of vobasine (**95**).

Appendix 19: 1D and 2D NMR spectra of ursolic acid (**99**).
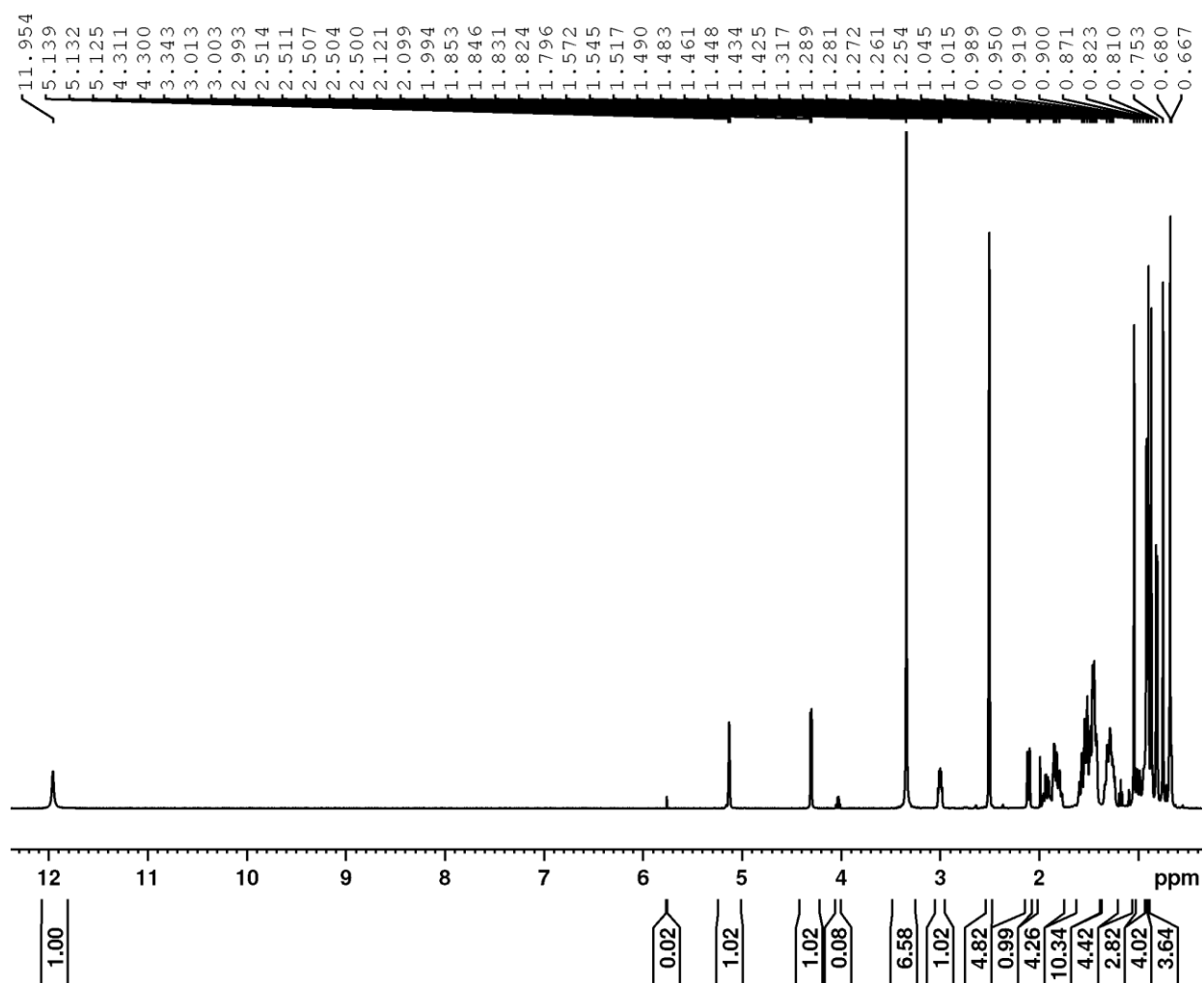
Appendix 19.1: ^{1}HNMR spectrum of ursolic acid (**99**) at 600 MHz in DMSO-d$_6$.
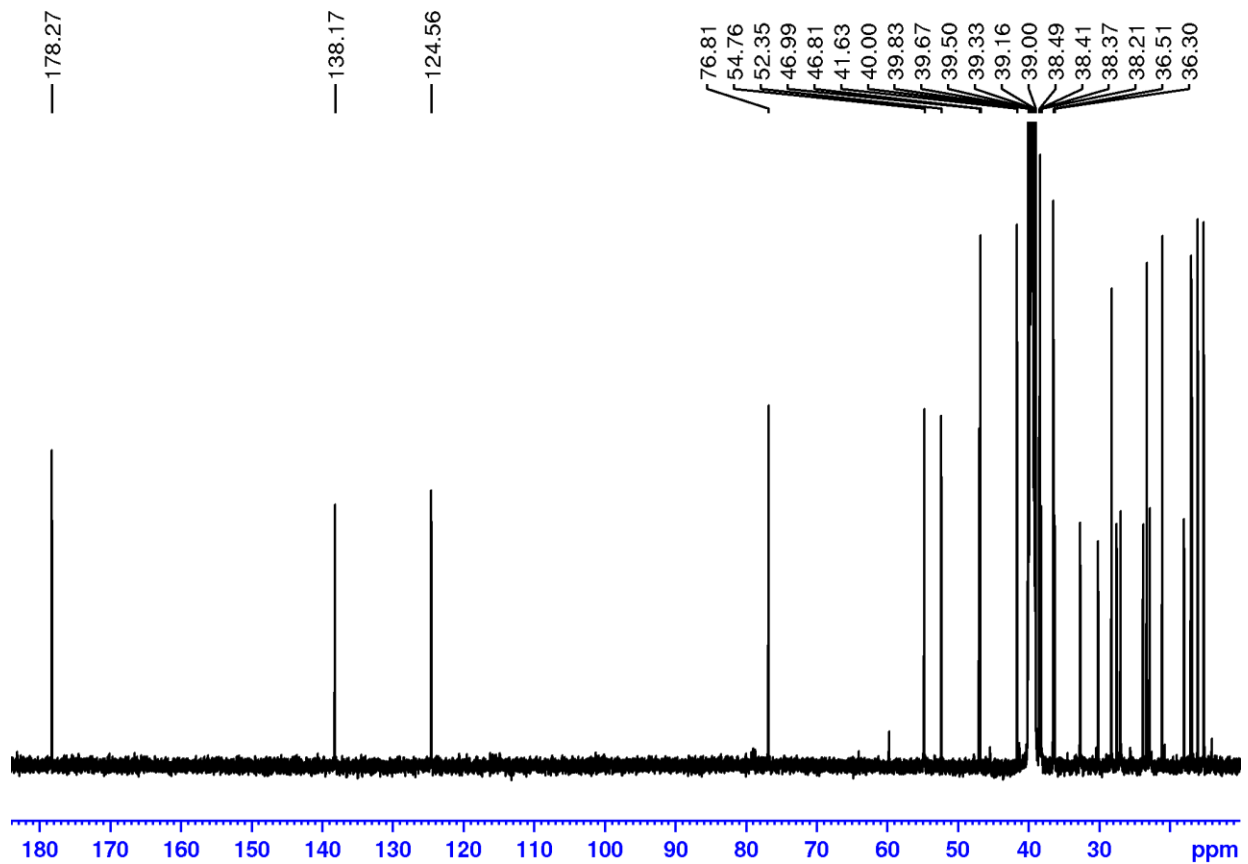
Appendix 19.2: ^{13}C NMR spectrum of ursolic acid (**99**) at 151 MHz in DMSO-d$_6$.
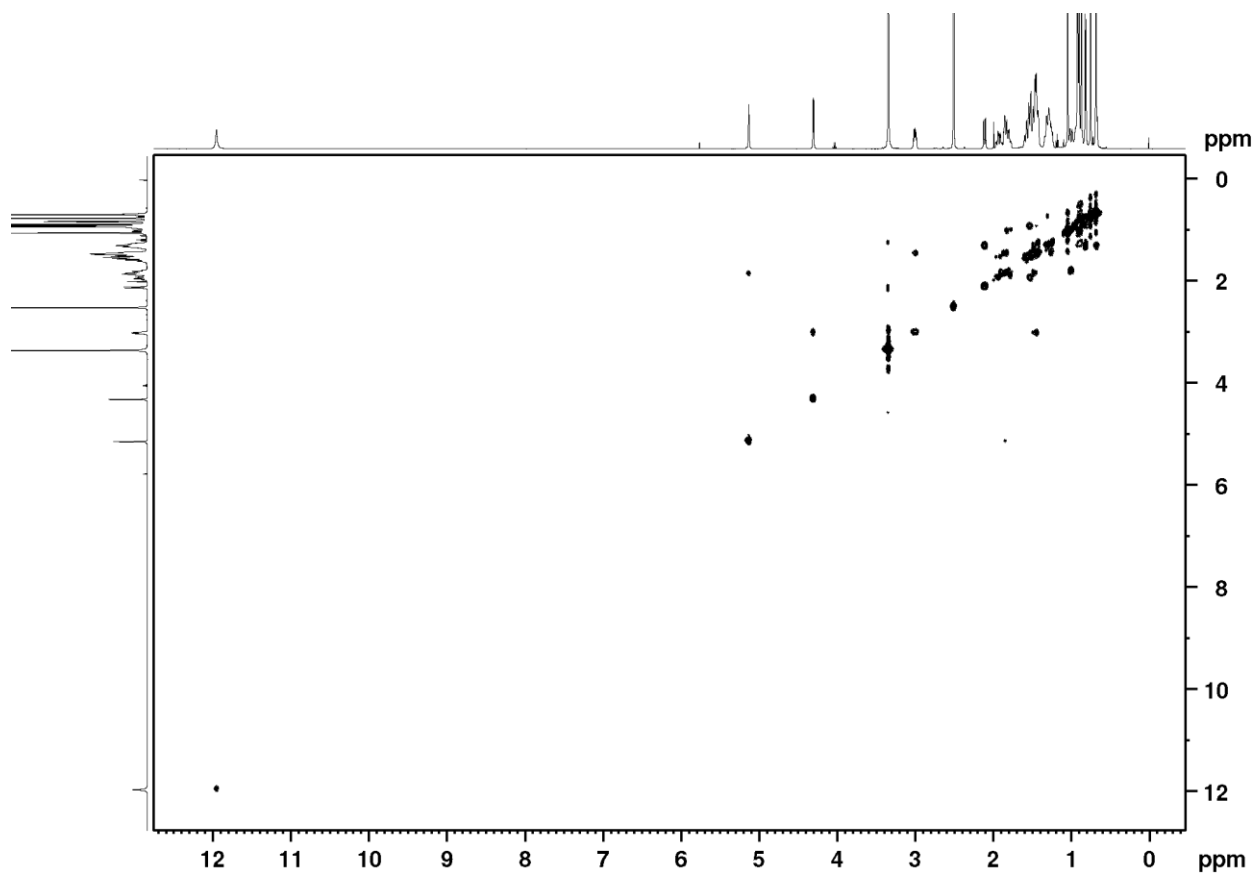
Appendix 19.3: H-H COSY spectrum of ursolic acid (**99**) at 600 MHz in DMSO-d$_6$.
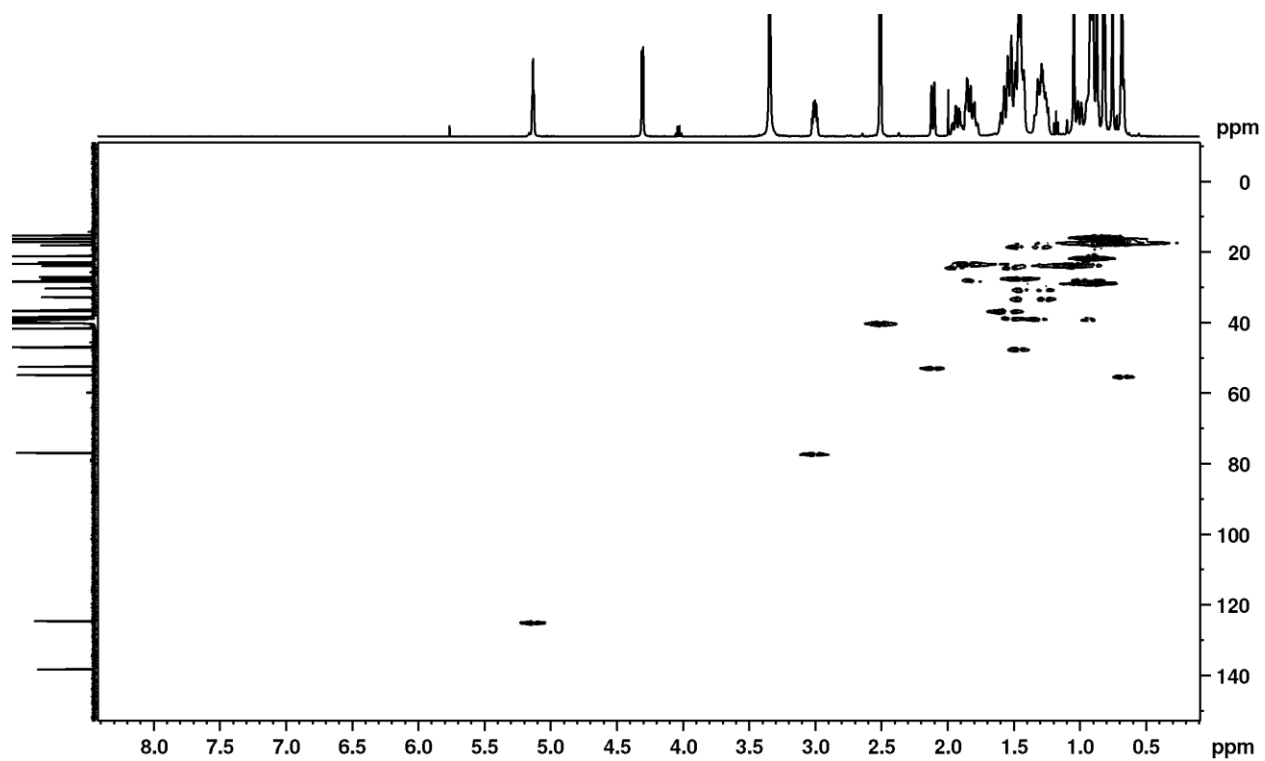
Appendix 19.4: HSQC spectrum of ursolic acid (**99**) at 600 MHz in DMSO-d6.
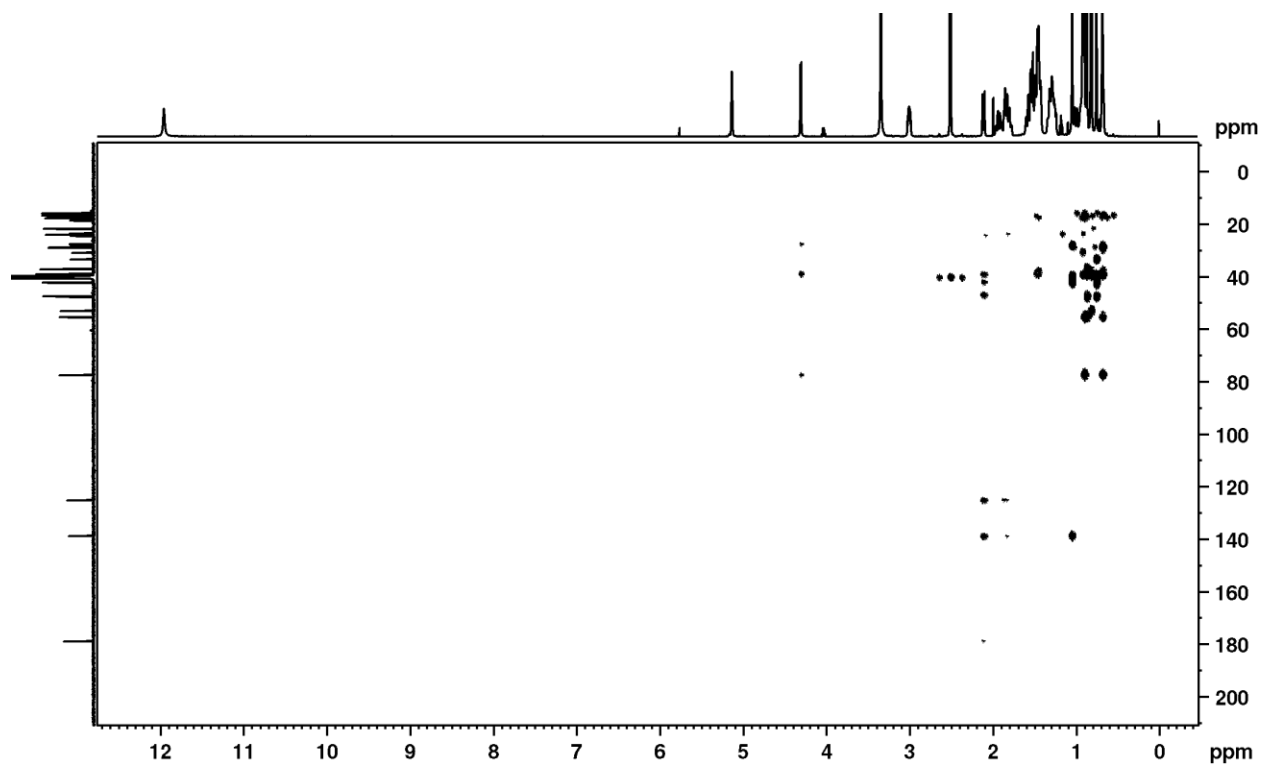
Appendix 19.5: HMBC spectrum of ursolic acid (**99**).

Appendix 20: 1D and 2D spectra of quebrachitol (**97**).
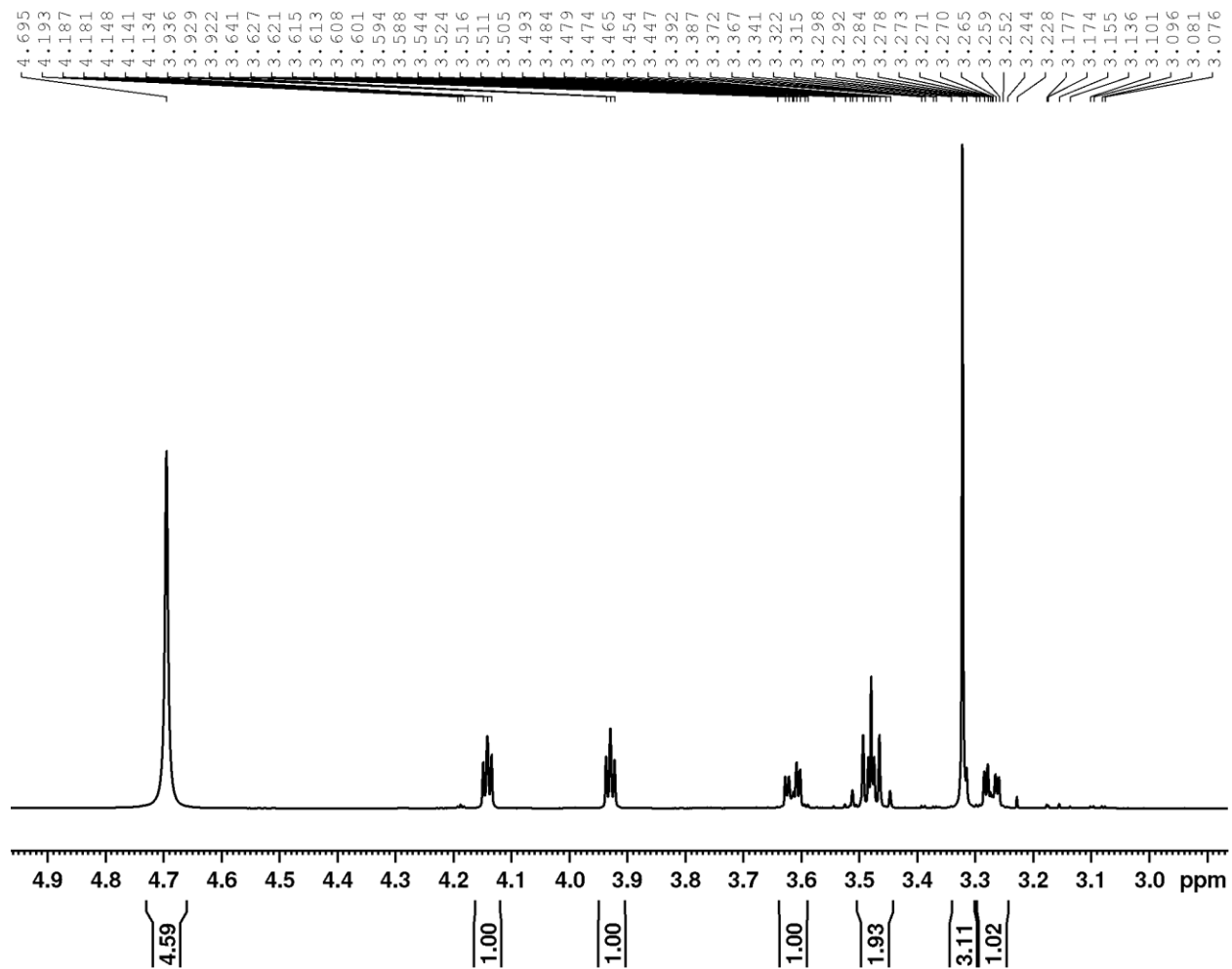
Appendix 20.1: ¹HNMR spectrum of quebrachitol (**97**) 600 at MHz in MeOD.
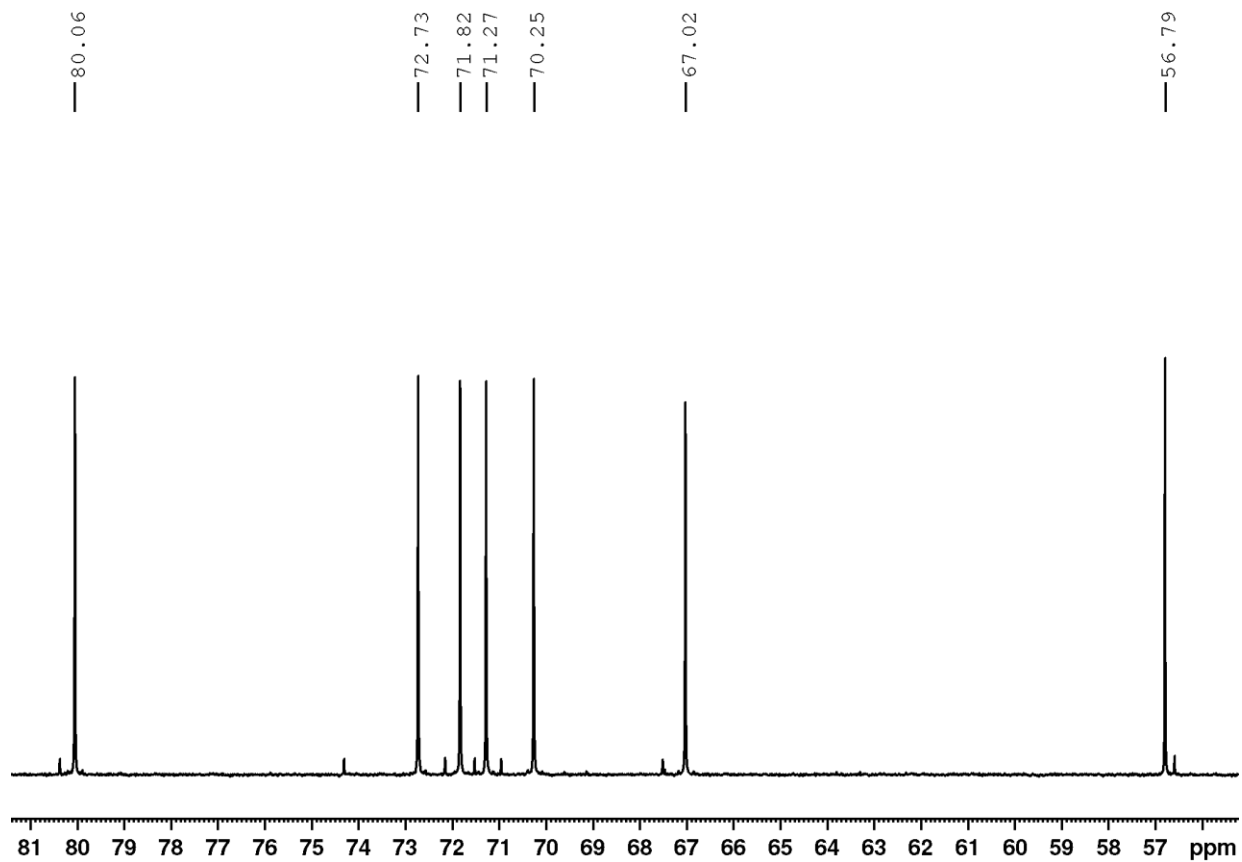
Appendix 20.2: ^{13}C NMR spectrum of quebrachitol (**97**) at 151 MHz in MeOD.
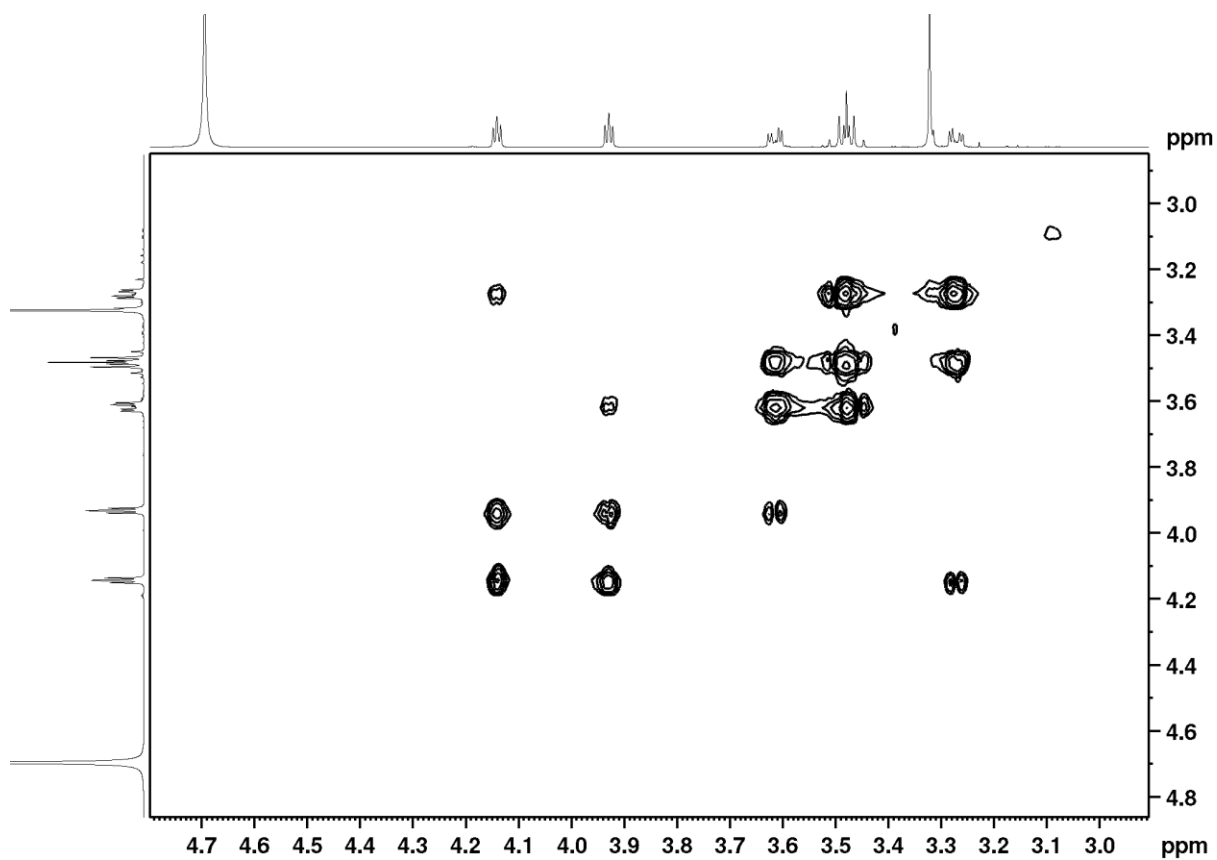
Appendix 20.3: H-H COSY spectrum of quebrachitol (**97**) at 600 MHz in MeOD.
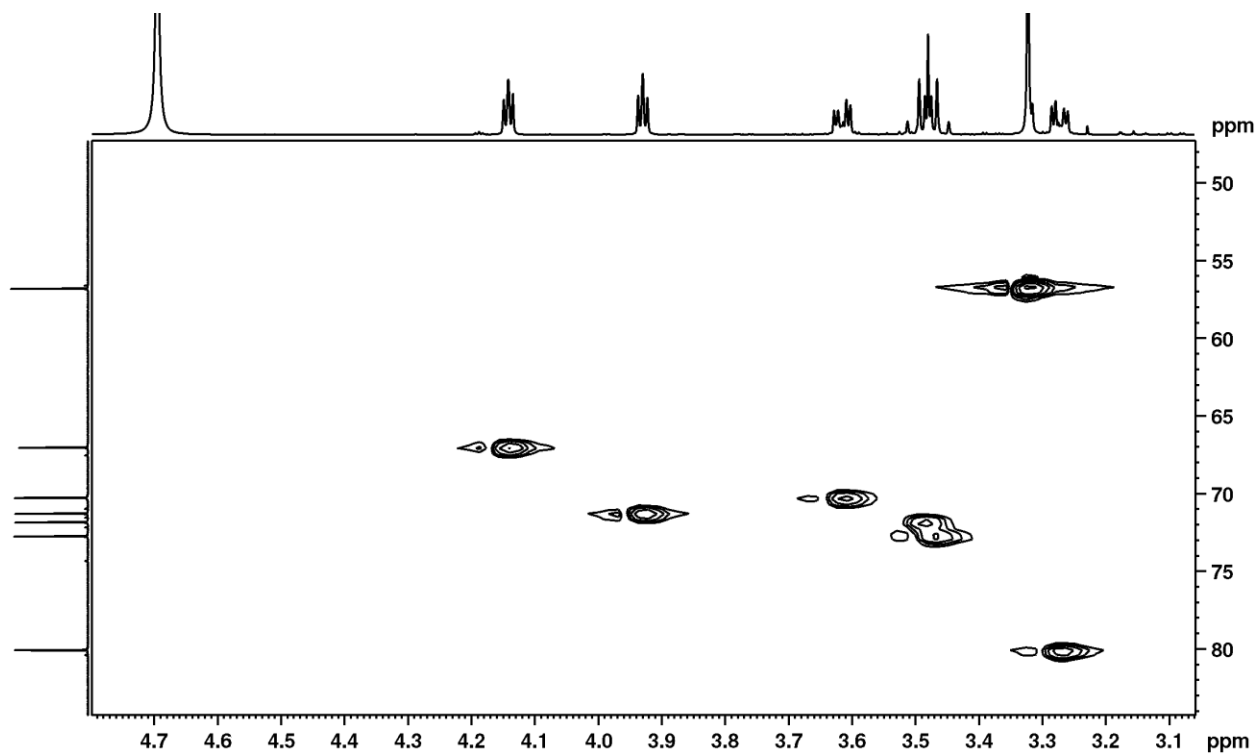
Appendix 20.4: HSQC spectrum of quebrachitol (**97**) at 600 MHz in MeOD.
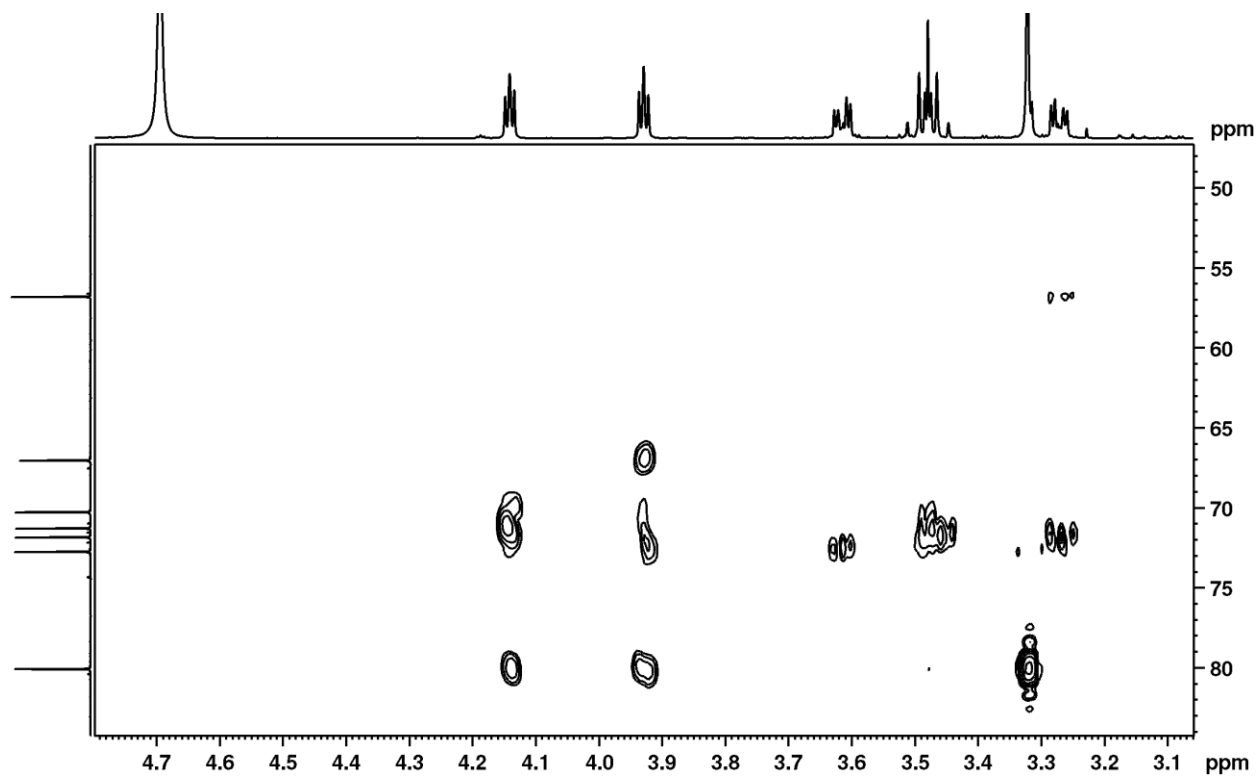
Appendix 20.5: HMBC spectrum of quebrachitol (**97**) at 600 MHz in MeOD.

Appendix 21: 1D and 2D spectra of β-sitosterol (4**5**).
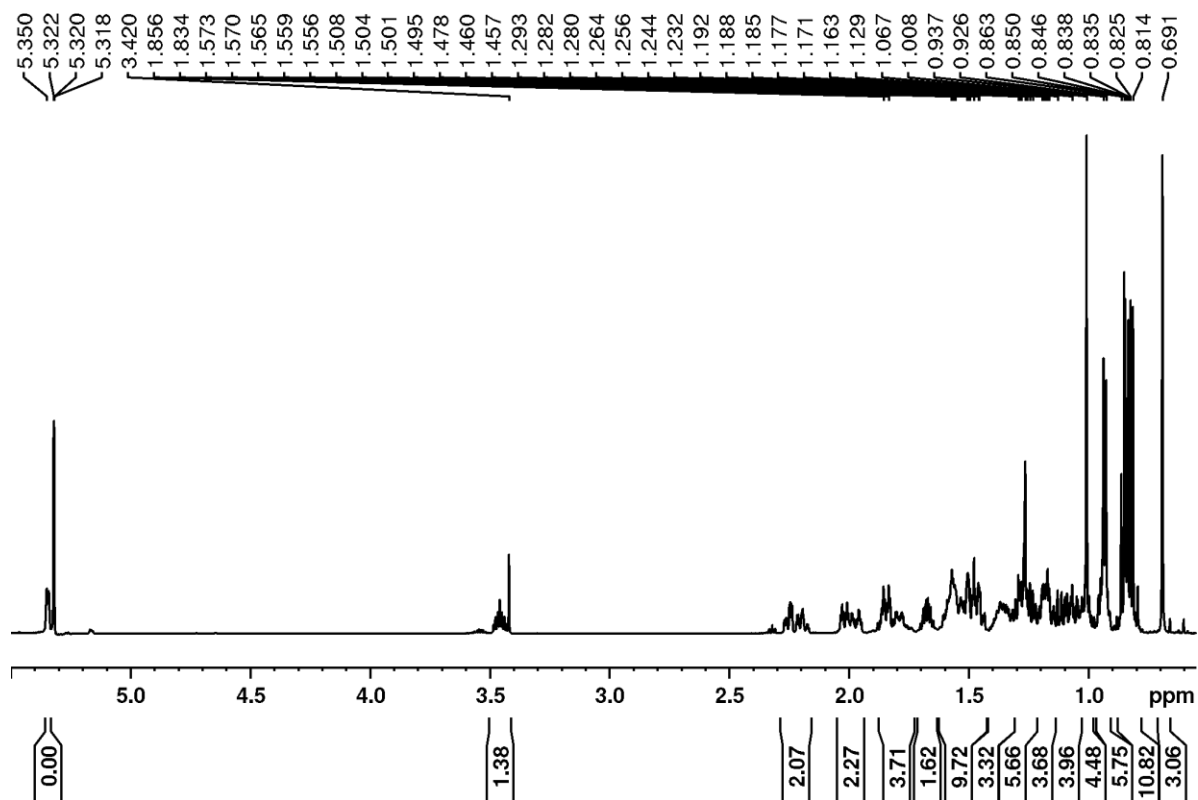
Appendix 21.1: ^{1}H NMR spectrum of β-sitosterol (4**5**) at 600 MHz in CD_2Cl_2.
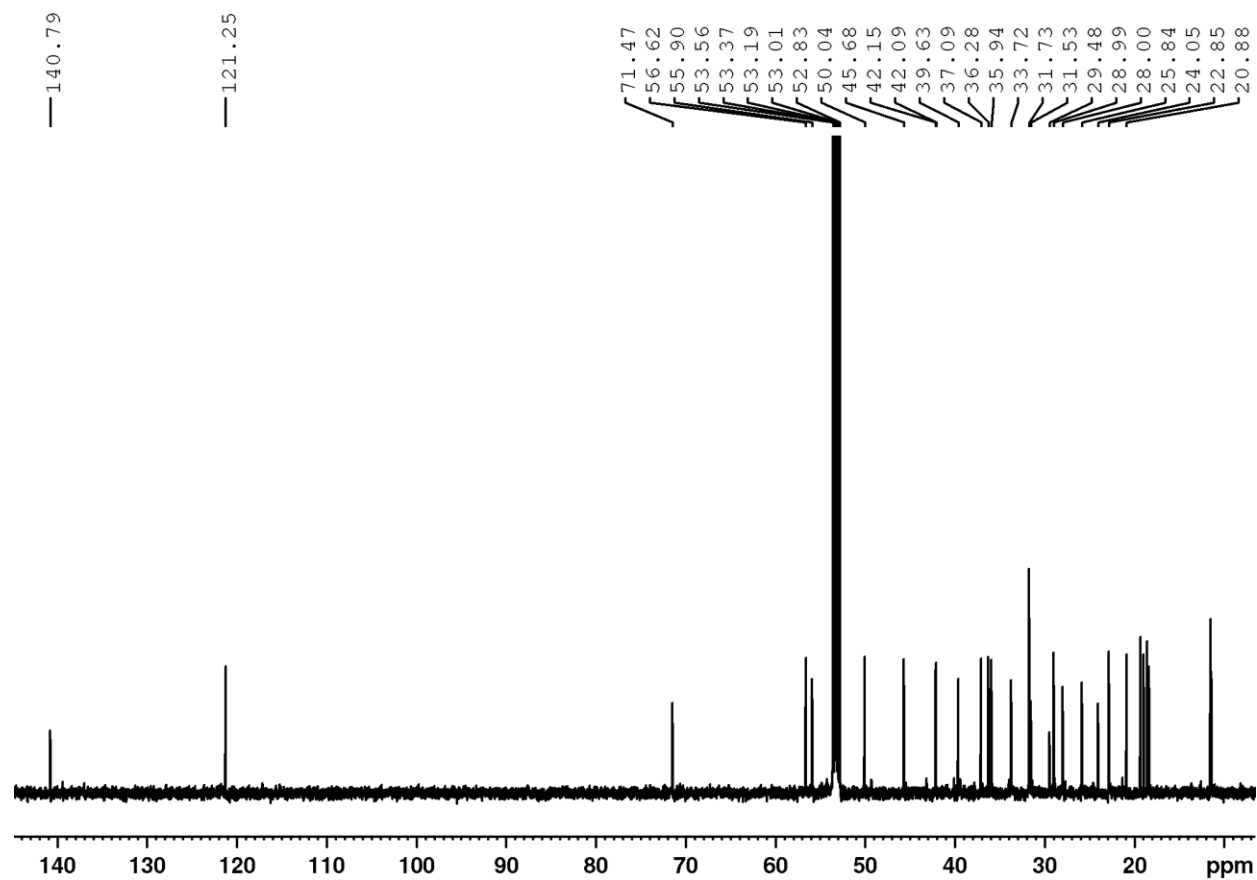
Appendix 21.2: ^{13}C NMR spectrum of β-sitosterol (4**5**) at 151 MHz in CD$_2$Cl$_2$.
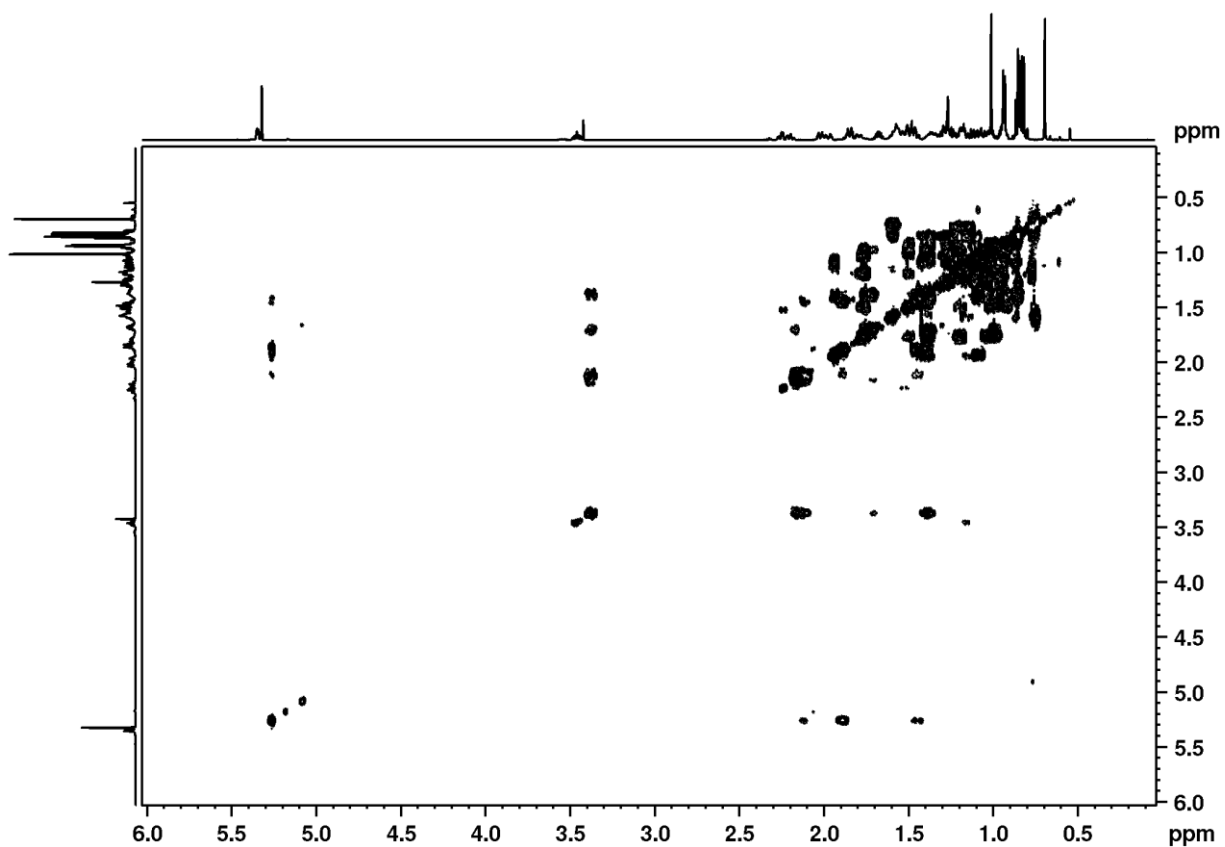
Appendix 21.3: H-H COSY spectrum of β-sitosterol (4**5**) at 600 MHz in CD₂Cl₂.
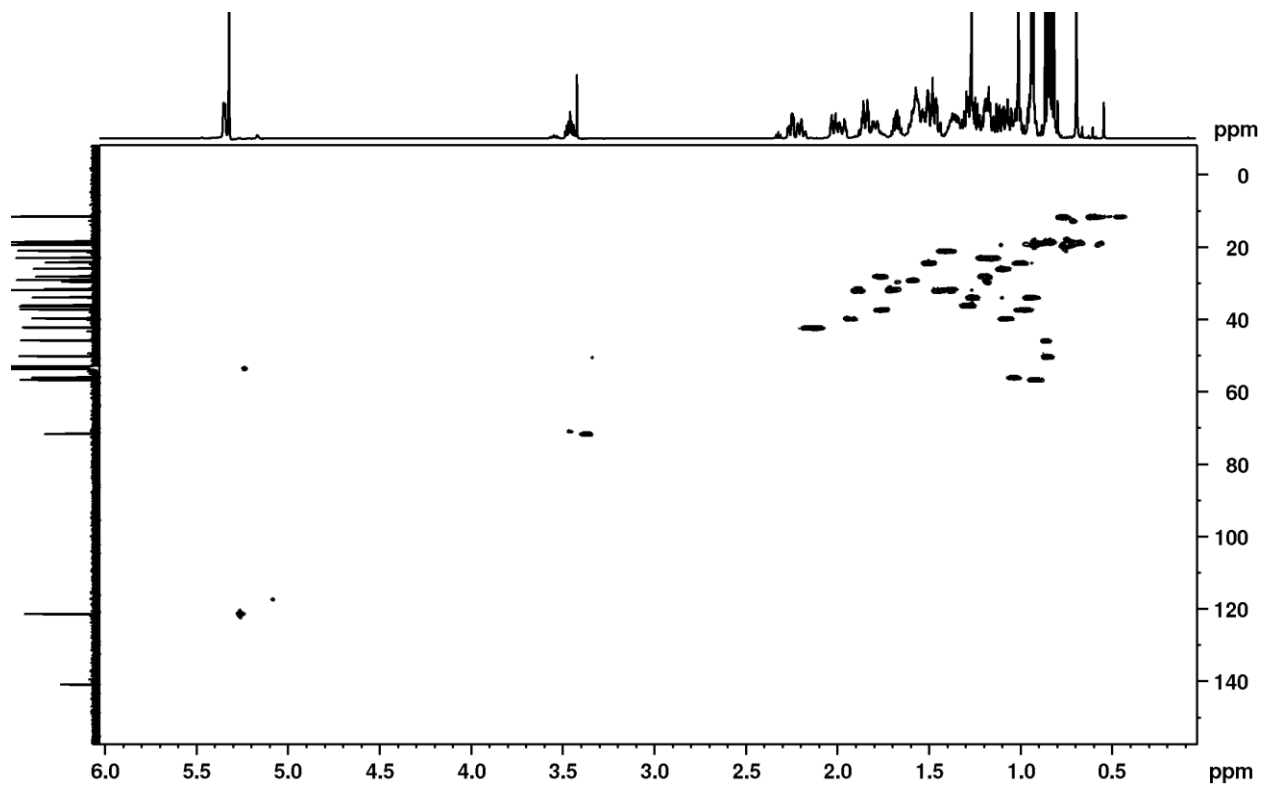
Appendix 21.4: HSQC spectrum of β-sitosterol (4**5**) at 600 MHz in CD$_2$Cl$_2$.
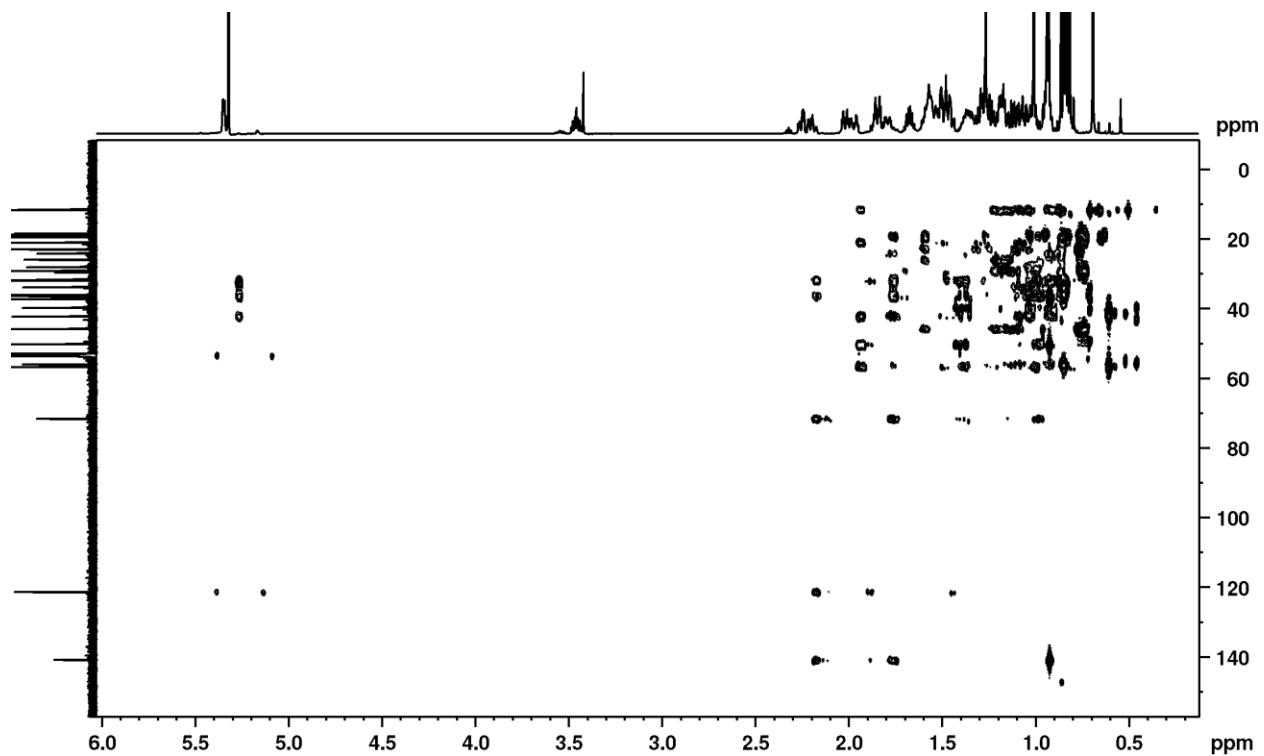
Appendix 21.5: HMBC spectrum of β-sitosterol (4**5**) at 600 MHz in CD$_2$Cl$_2$.

Appendix 22: 1D and 2D NMR spectra of stigmasterol (**47**).
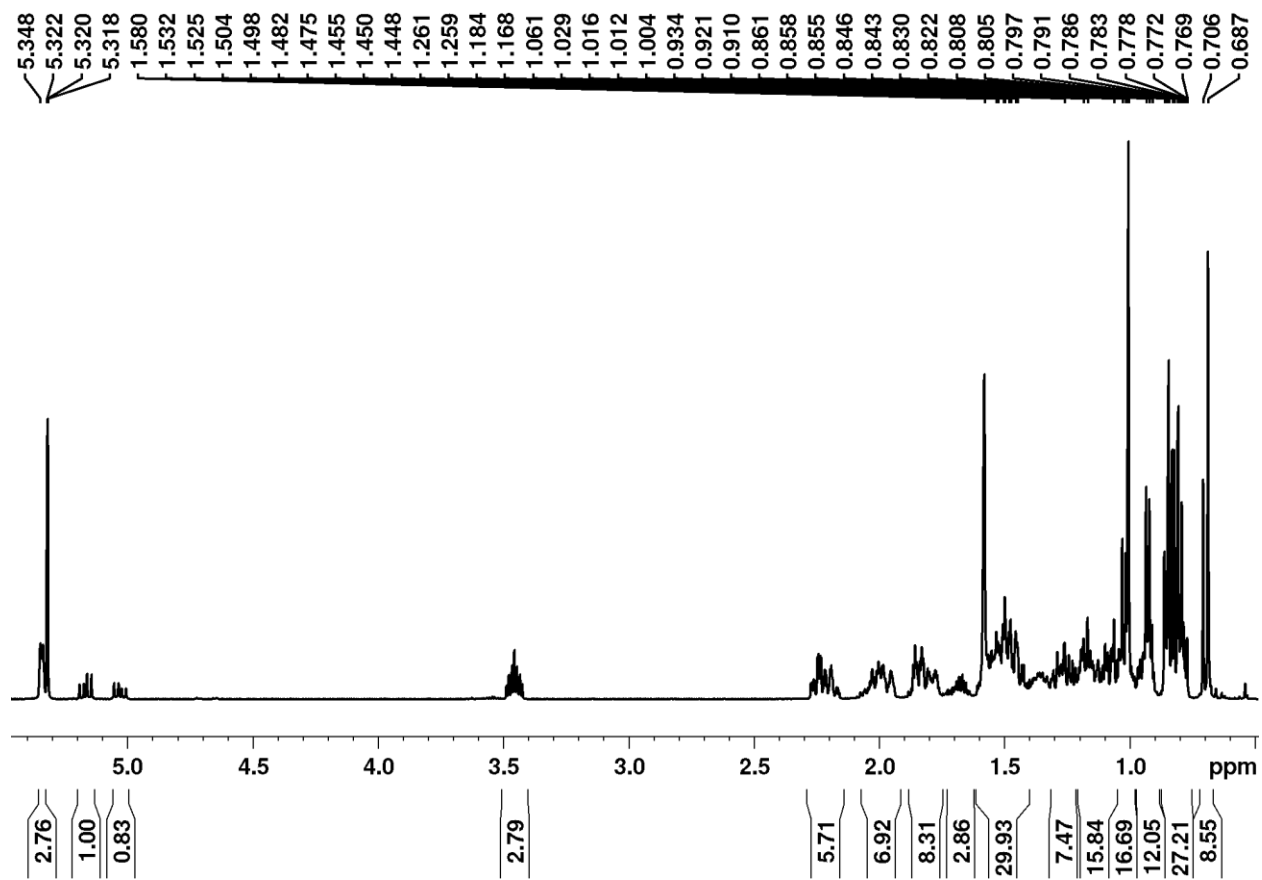
Appendix 22.1: ^{1}H NMR Spectrum of stigmasterol (**47**) at 600 MHz in CD$_2$Cl$_2$.
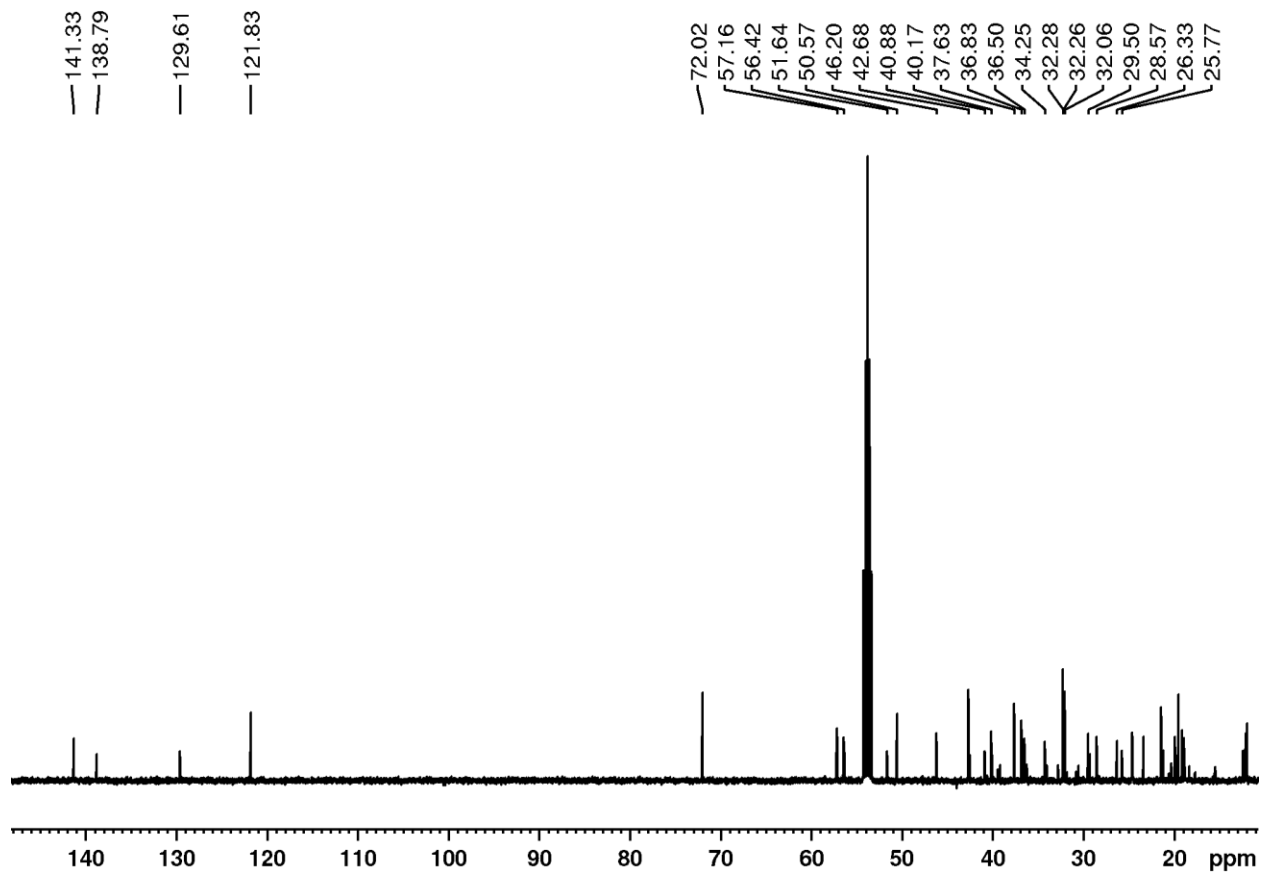
Appendix 22.2: ^{13}C NMR spectrum of stigmasterol (**47**) at 151 MHz in CD$_2$Cl$_2$.
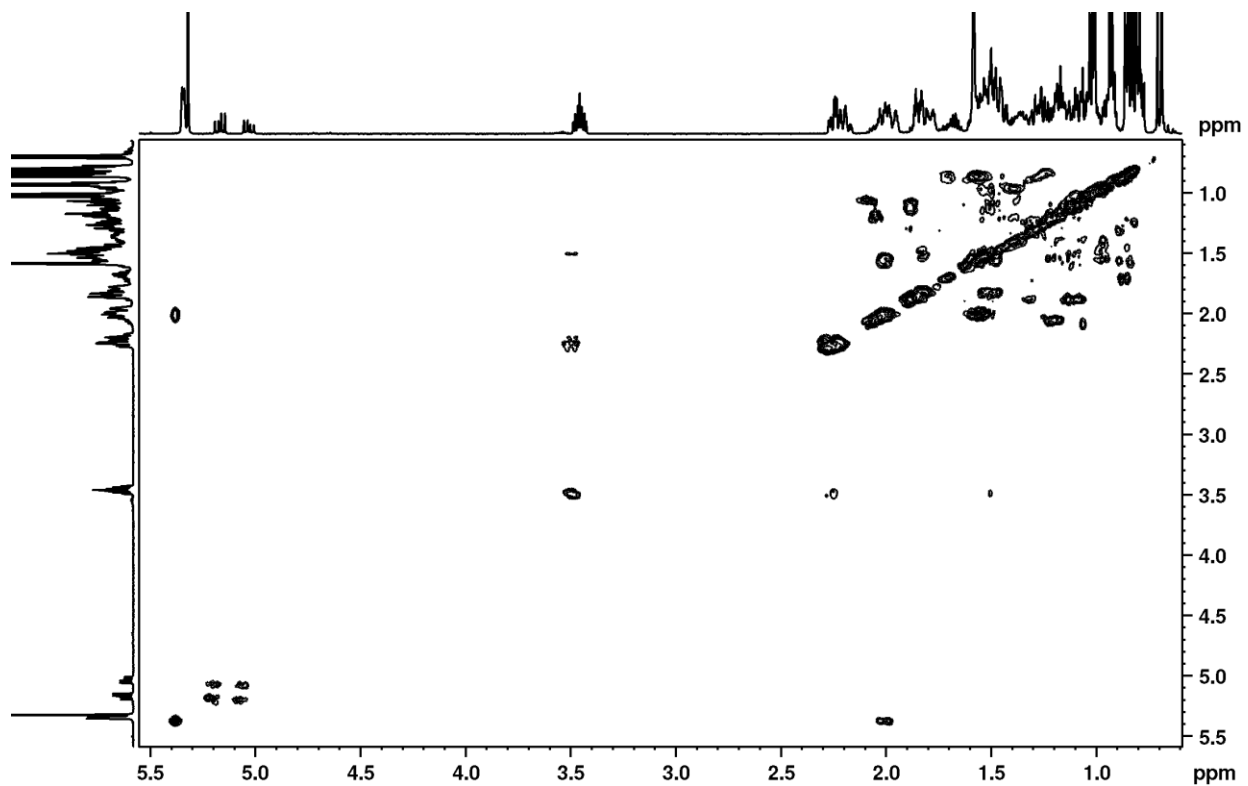
Appendix 22.3: H-H COSY spectrum of stigmasterol at 600 MHz in CD_2Cl_2.
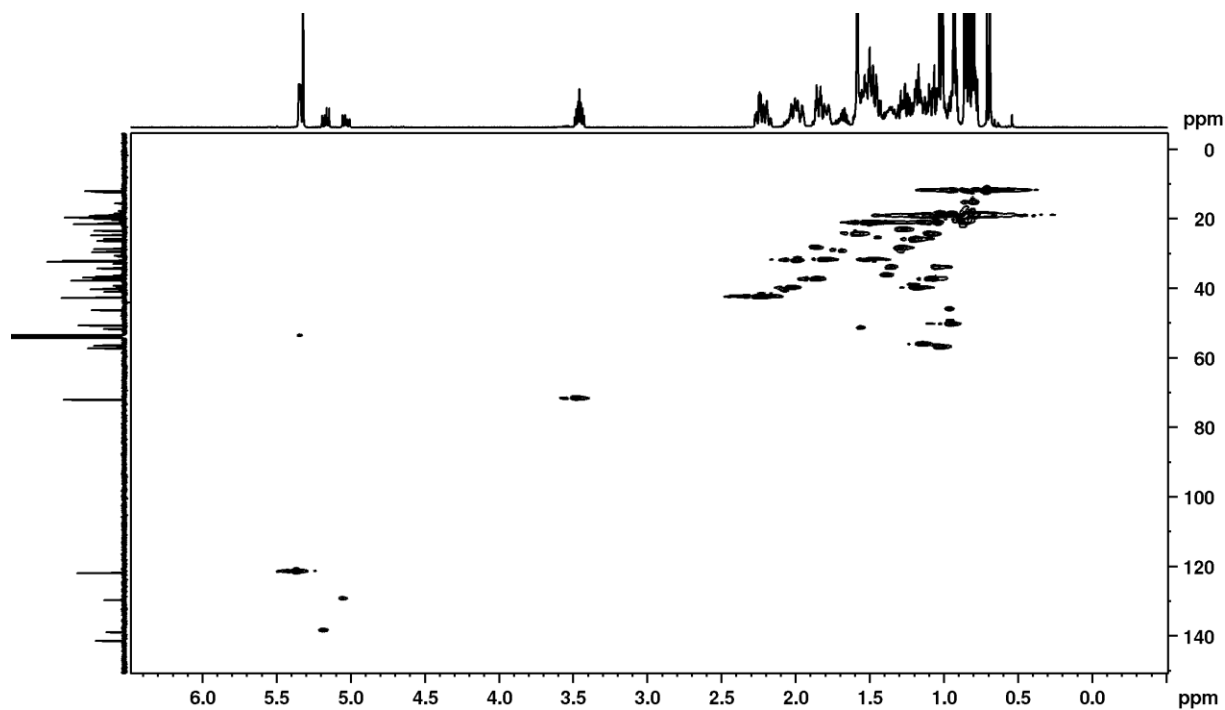
Appendix 22.4: HSQC spectrum of stigmasterol at 600 MHz in CD_2Cl_2.

253

Appendix 23: 1D and 2D NMR spectra of aloesaponarin II (**88**) in DMSO-d$_6$
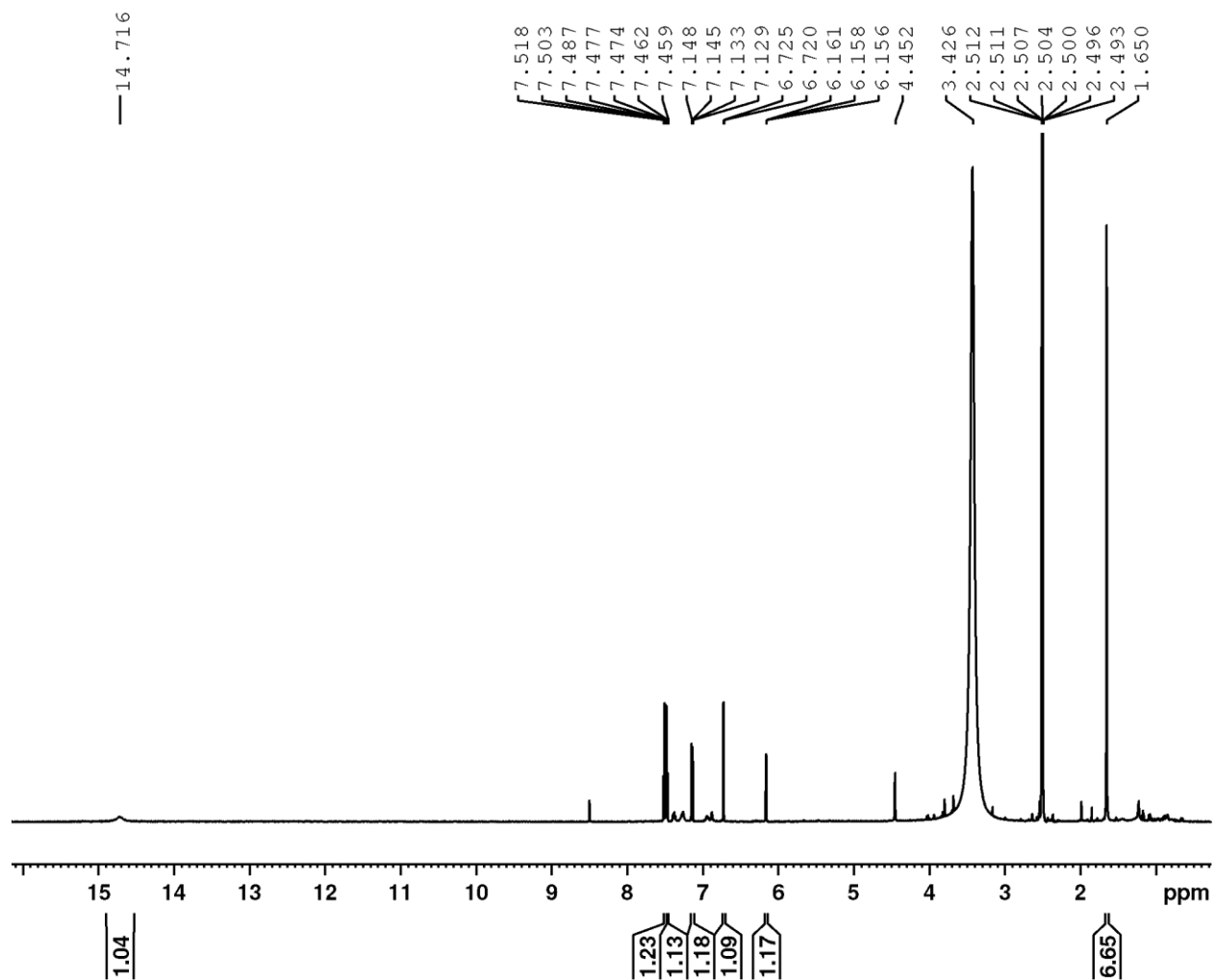
Appendix 23.1: ^{1}H NMR spectrum of aloesaponarin II (**88**) at 600 MHz in DMSO-d$_6$.
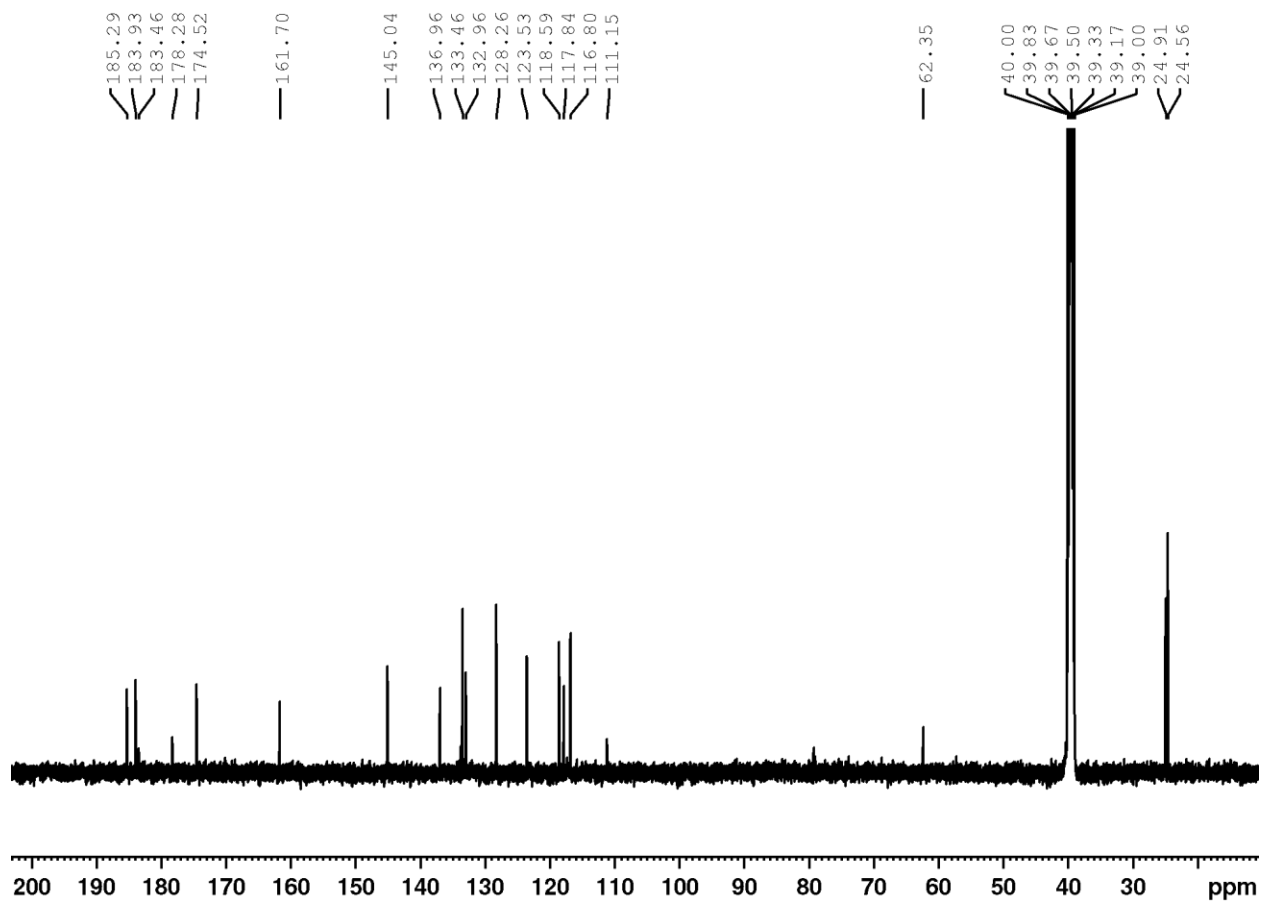
Appendix 23.2: ^{13}C NMR spectrum of aloesaponarin II (**88**) at 151 MHz in DMSO-d$_6$
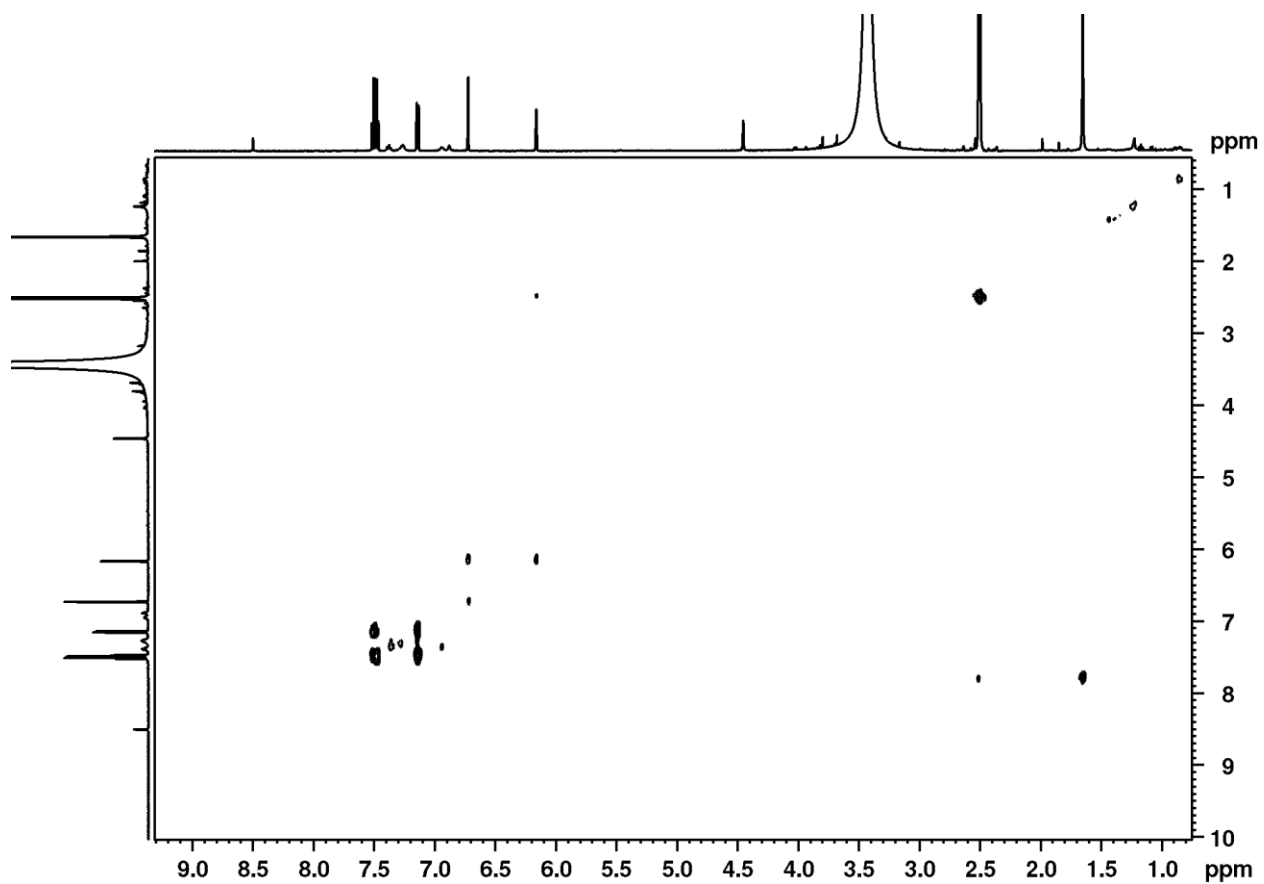
Appendix 23.3: H-H COSY spectrum of aloesaponarin II (**88**) at 600 MHz in DMSO-d$_6$
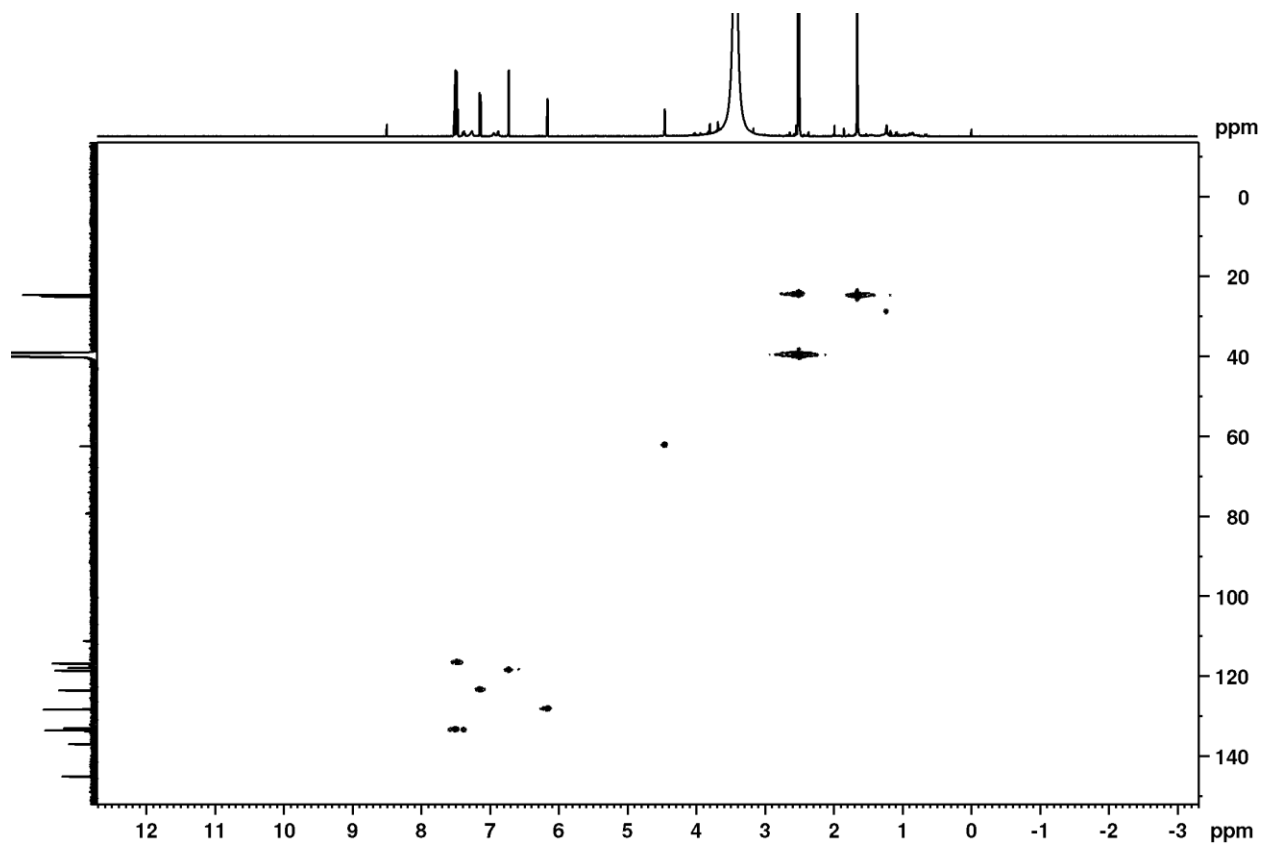
Appendix 23.4: HSQC spectrum of aloesaponarin II (**88**) at 600 MHz in DMSO-d$_6$
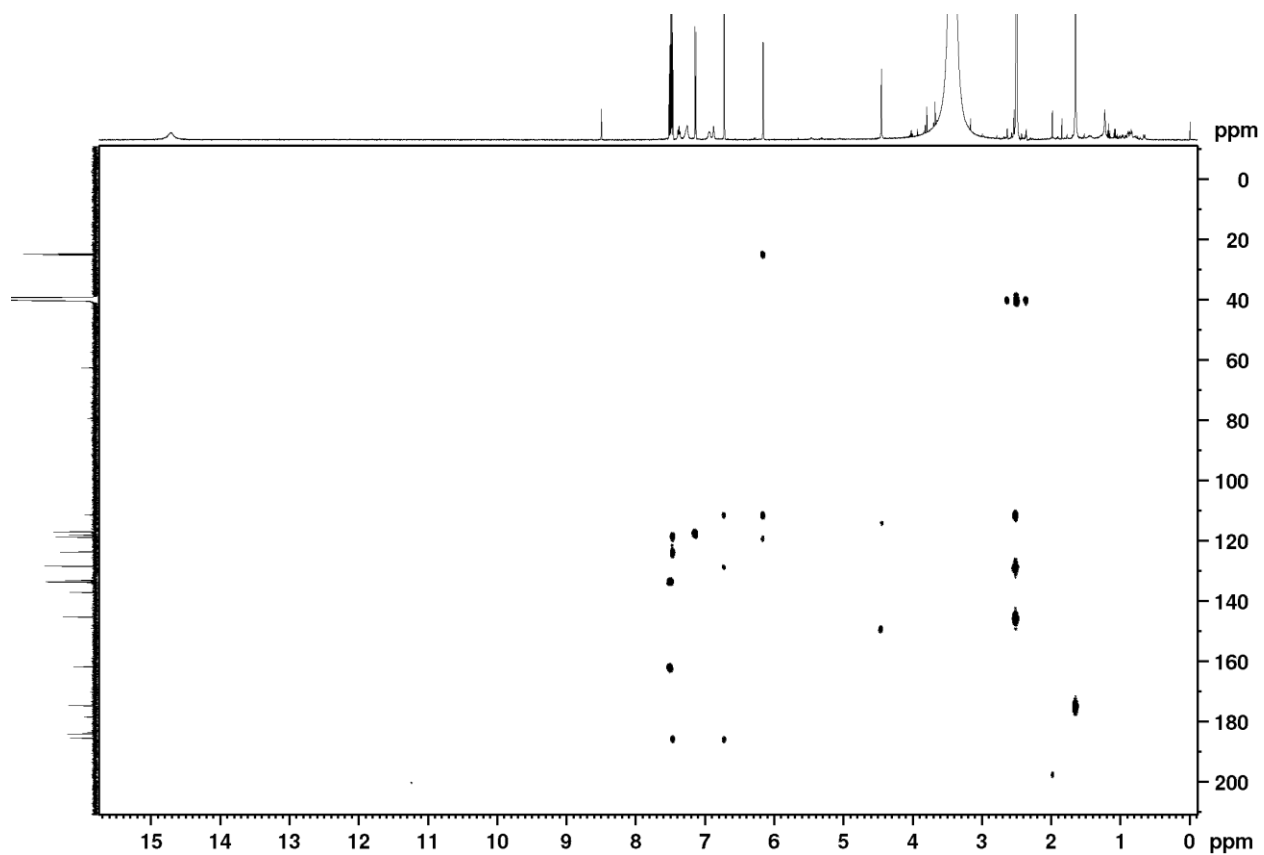
Appendix 23.5: HMBC spectrum of aloesaponarin II (**88**) at 600 MHz in DMSO-d$_6$

Appendix 24: Representative Graphs for *In Vitro* Bioassays.

The IC$_{50}$ values were determined by non-linear regression of the transformed data using Graphpad Prism Version 5.0. Cell viability is expressed as a percentage of the control group.
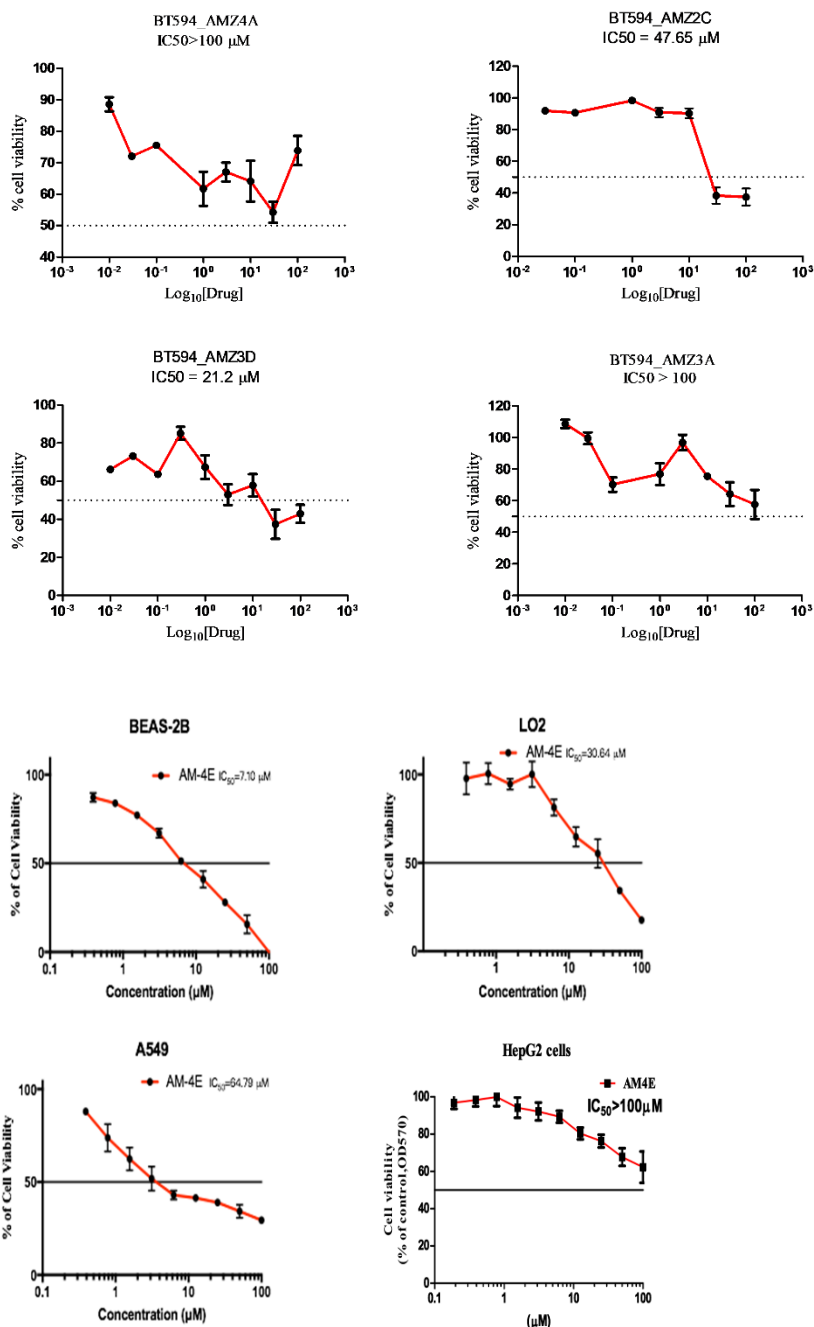
Appendix 24.1: Antiproliferative activity of compounds **80** (AMZ3A), **81** (AMZ3D), **82** (AMZ2C), **83** (AMZ4A) and **84** (AM4E). BEAS: Human bronchial epithelial cells, A549: Human alveolar basal epithelial cells, HePG2: liver cancer cells, LO2: normal liver cells, BT549: Breast cancer cells.
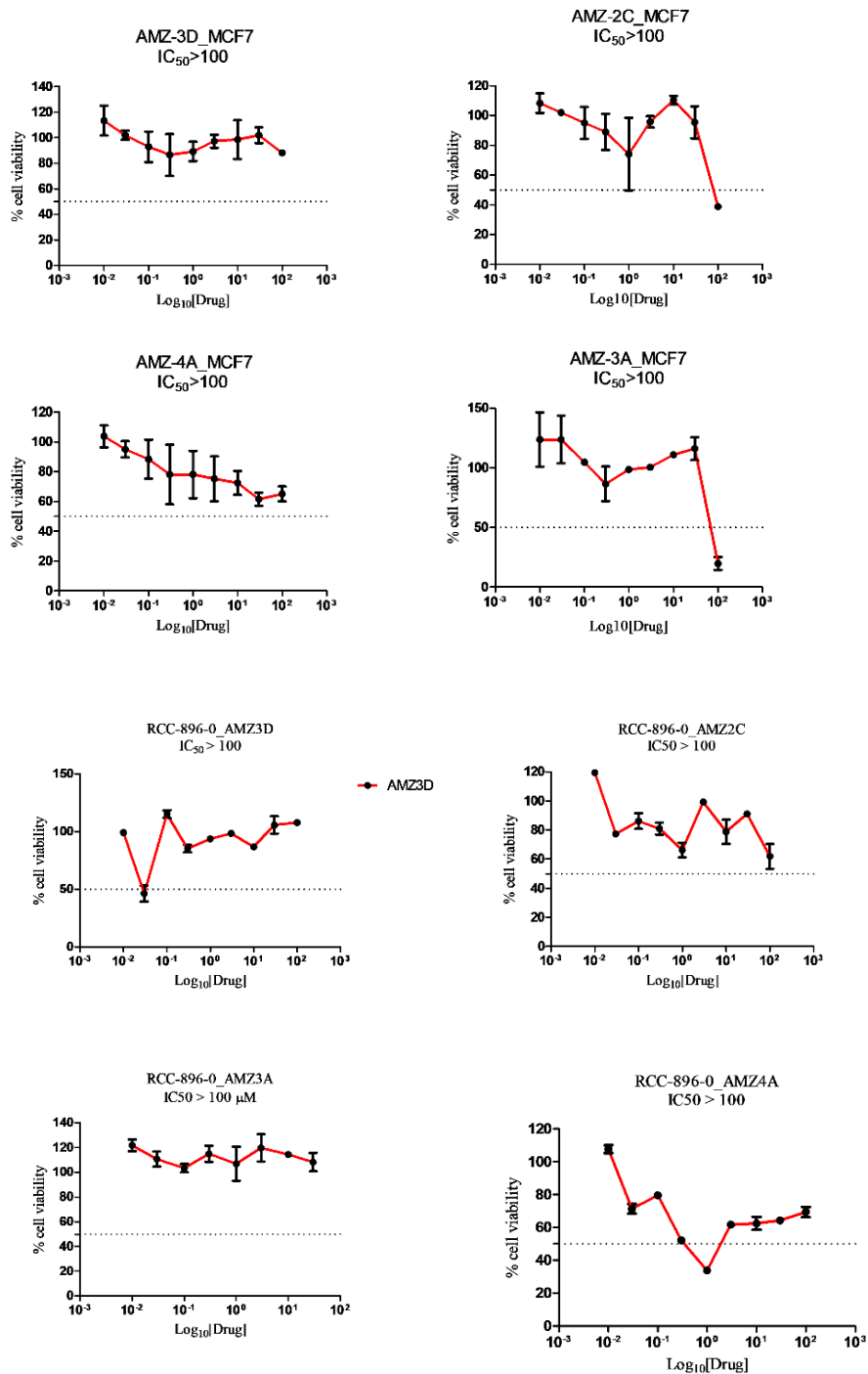
Appendix 24.2: Antiproliferative activity of compounds **80** (AMZ3A), **81** (AMZ3D), **82** (AMZ2C), and **83** (AMZ4A), against breast cancer cells (MCF-7) and renal cancer cells (RCC-896-0).
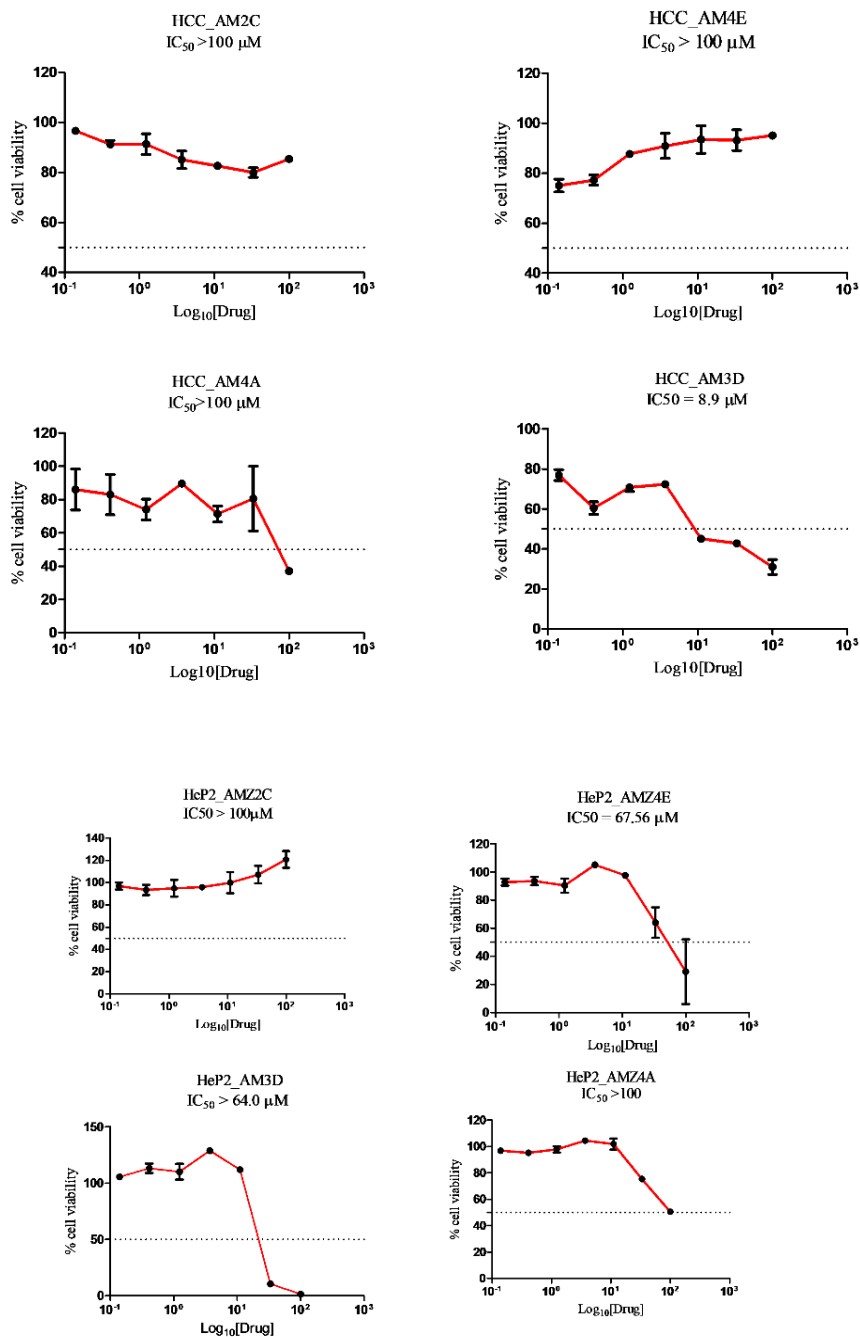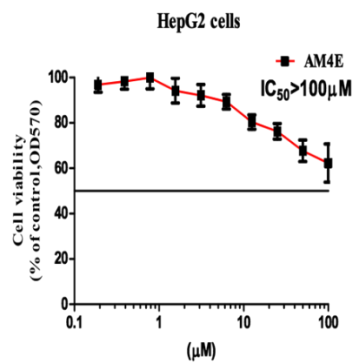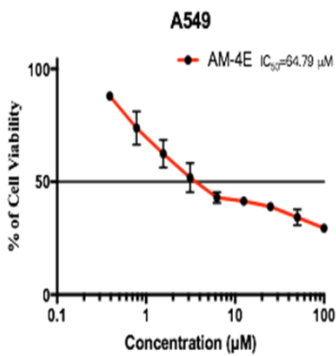
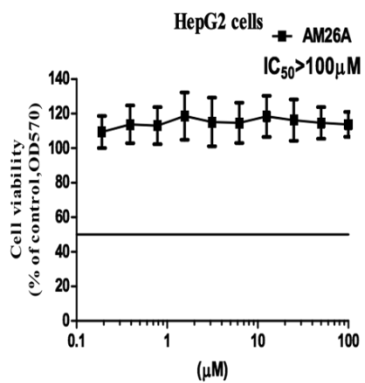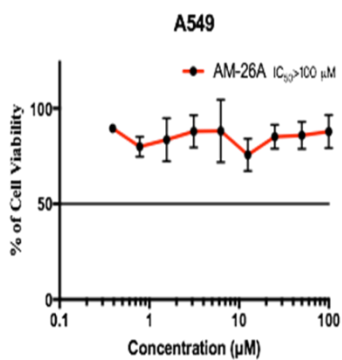**Appendix 24.3**: Antiproliferative activity of compounds **81** (AMZ3D), **82** (AMZ2C), and **83** (AMZ4A), against hepatocellular carcinoma (HCC) cells and lung cancer cells (HeP2).
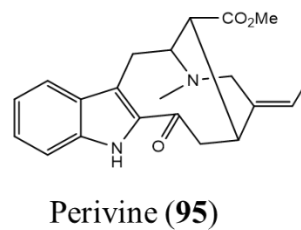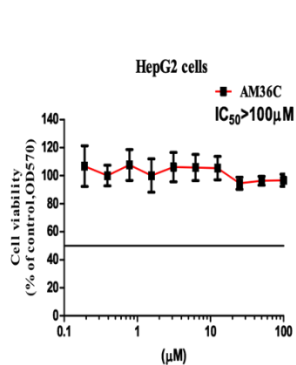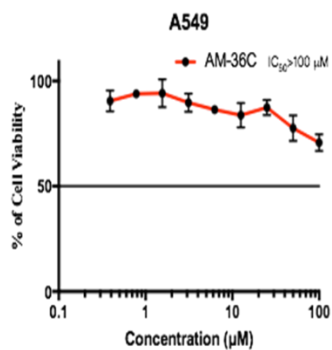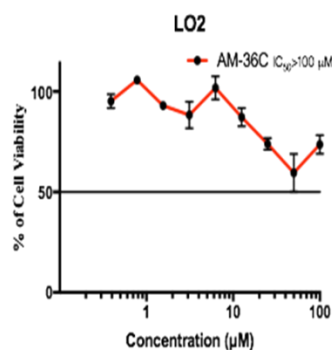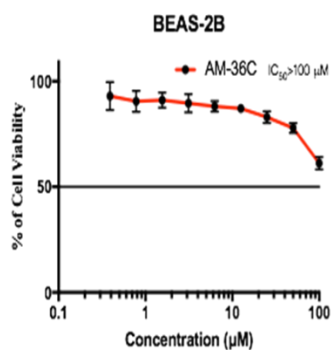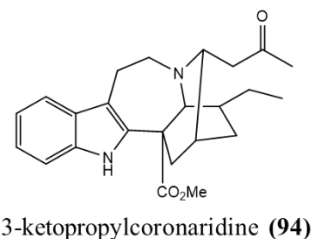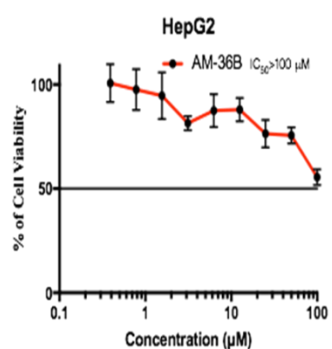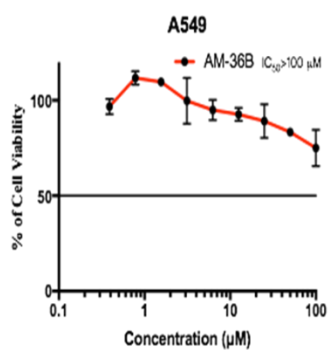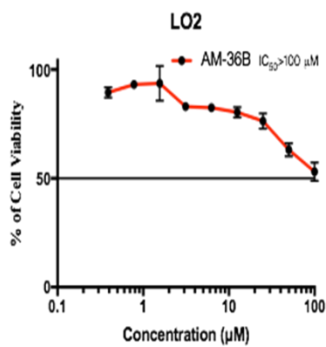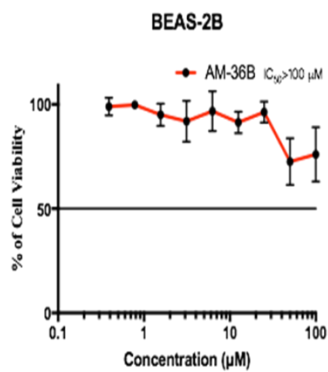
Appendix 24.4: Antiproliferative activities of compounds **94** and **95** against Human bronchial epithelial cells (BEAS), Human alveolar basal epithelial cells (A549). liver cancer cells (HePG2), and normal liver cells (LO2).

Ibogamine (**96**)
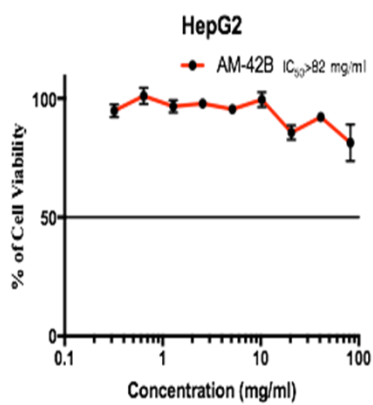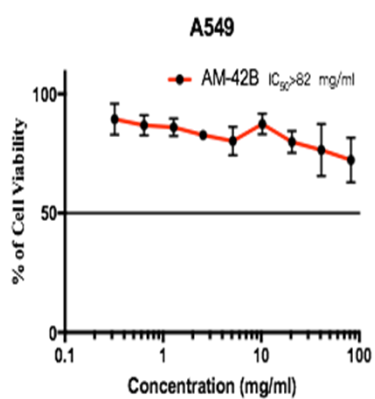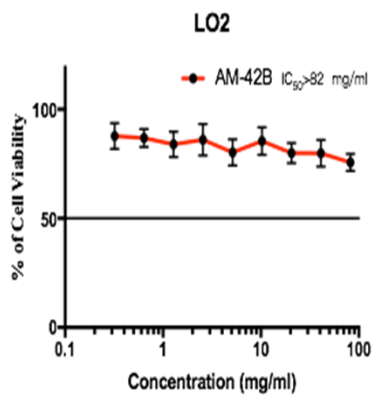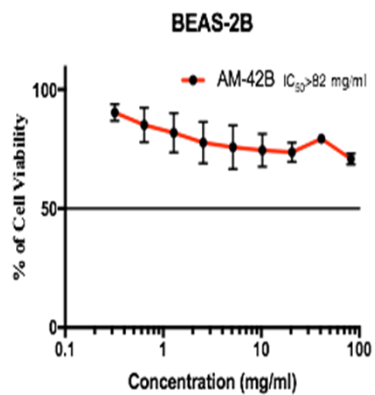
Appendix 24.5: Antiproliferative activity of ibogamine (**96**).

BEAS-2B — AM-40A $IC_{50} > 55\,mg/ml$

LO2 — AM-40A $IC_{50} > 55\,mg/ml$

Quebrachitol (97)

A549 — AM-40A $IC_{50} > 55\,mg/ml$

HepG2 — AM-40A $IC_{50} > 55\,mg/ml$

BEAS-2B — AM-44D $IC_{50} = 43.76\,mg/ml$

LO2 — AM-44D $IC_{50} = 67.54\,mg/ml$

A549 — AM-44D $IC_{50} = 55.31\,mg/ml$

HepG2 — AM-44D $IC_{50} = 8.84\,mg/ml$
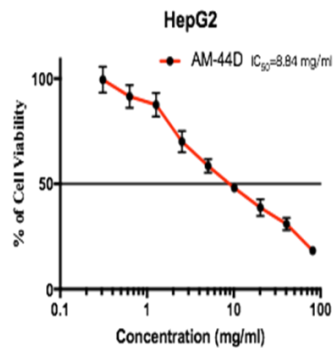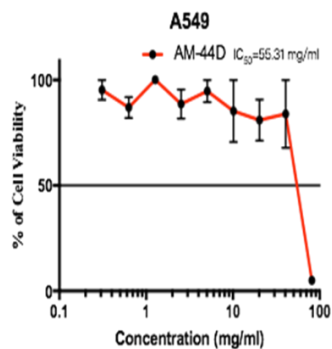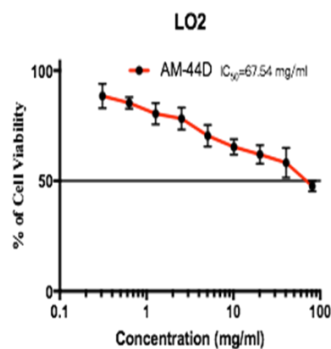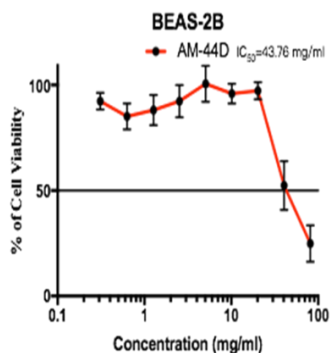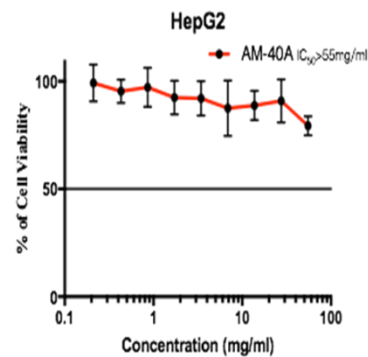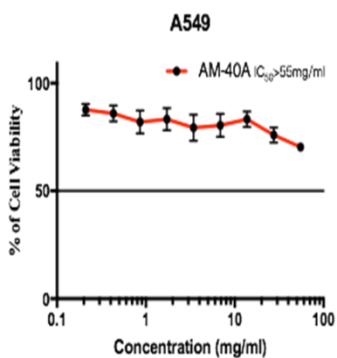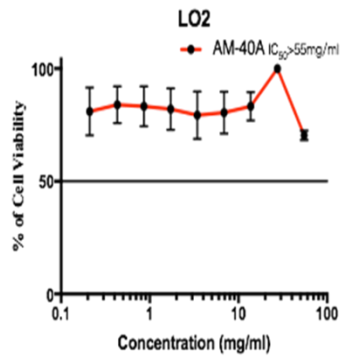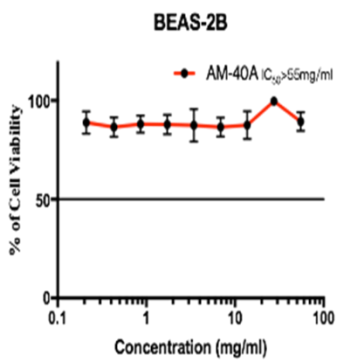
Voacristine (98)

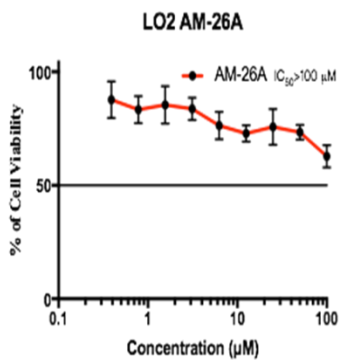**Appendix 24.6**: Antiproliferative activity of compounds **97** and **98**.
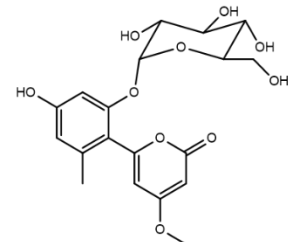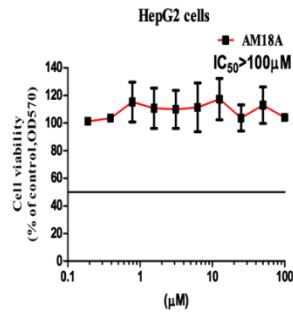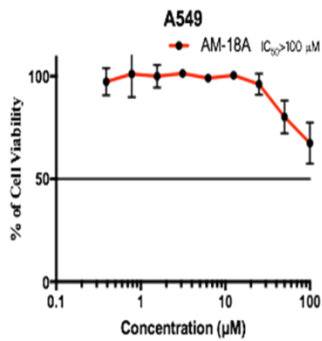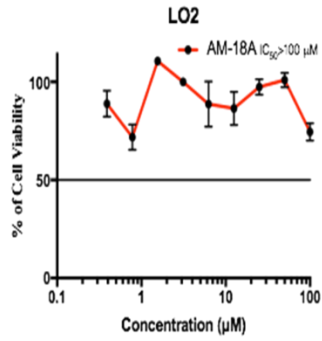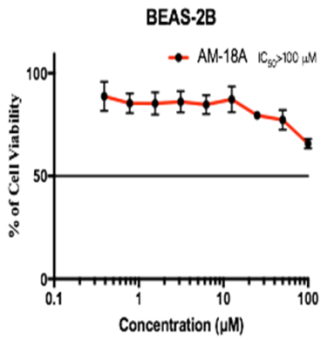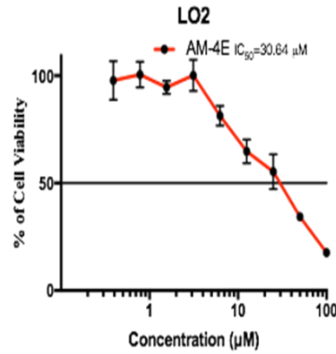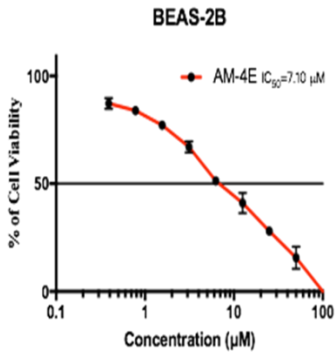
Appendix 24.7: Antiproliferative activity of compounds **84** and **85**.
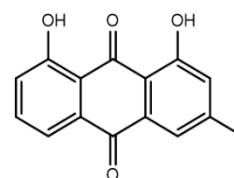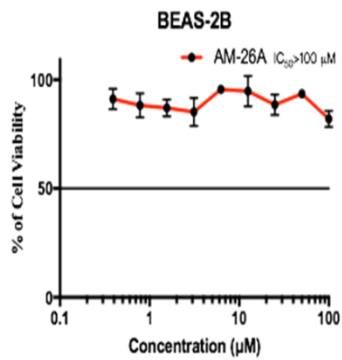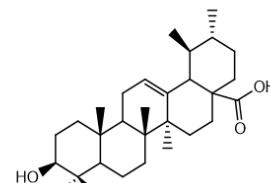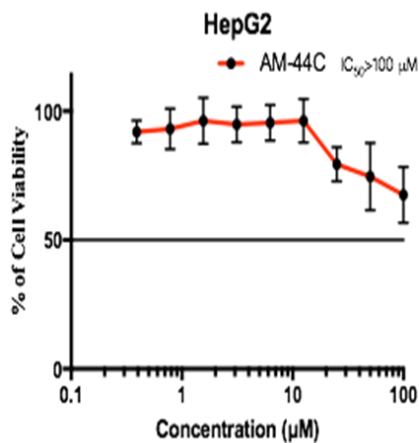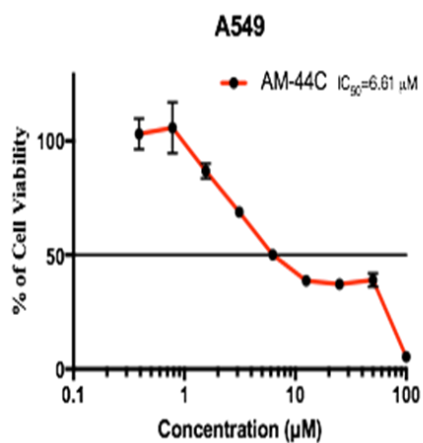
Appendix 24.8: Antiproliferative activity of compounds **89** and **99**

Appendix 25: Time-course for calorimetric reaction and standard curve for determination of β-sitosterol
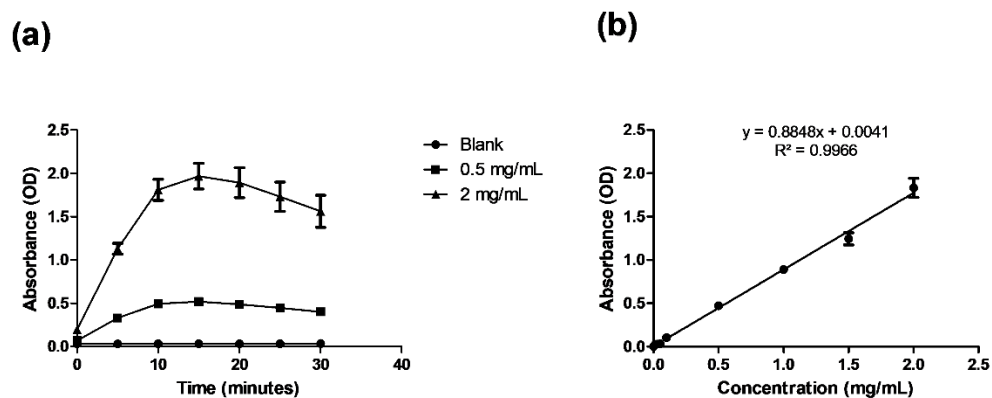
(a)

(b)

Figure 25.1: (a) Time course for calorimetric reaction of β-sitosterol with acetic anhydride and Conc. Sulphuric acid (Liebermann-Burchard reagent), (b) Standard curve for determination of β-sitosterol (n = 3)
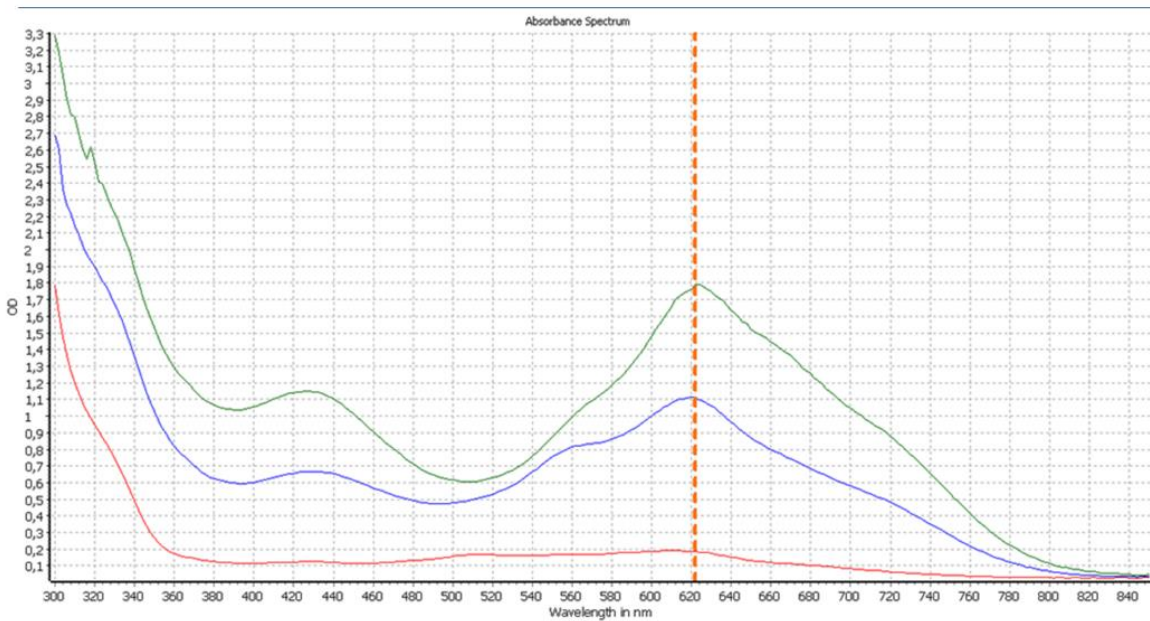

Figure 25.2: Sample UV-Vis absorption spectra for the calorimetric reaction of β-sitosterol at different concentrations with acetic anhydride and conc. sulphuric acid.

Appendix 26: Analytical Method validation

Appendix 26.1: Determination of intra and inter-assay precision of the method.

	Intra-Assay method Precision					Inter-Assay method Precision				
Concentration mg/mL	**1**	**0.25**	**0.1**	**0.5**	**0.05**	**1**	**0.25**	**0.1**	**0.05**	**0.0125**
Absorbance for three runs (OD)	1.016	0.329	0.136	0.475	0.081	1.025	0.313	0.148	0.081	0.04
	1.001	0.335	0.139	0.493	0.082	1.028	0.304	0.146	0.082	0.038
	0.994	0.333	0.131	0.469	0.083	0.987	0.306	0.143	0.083	0.039
Mean Abs at 622 nm	1.004	0.332	0.135	0.479	0.082	1.013	0.308	0.146	0.082	0.039
St.Dev	0.011	0.003	0.004	0.012	0.001	0.023	0.005	0.003	0.001	0.001
% RSD	1.120	0.919	2.986	2.608	1.220	2.255	1.536	1.728	1.220	2.564

Determination of intra-assay precision: standard solutions of β-Sitosterol at five different concentrations (see table) were assayed on the same day. All measurements were taken in triplicate.

Determination of inter-assay precision: standard solutions of β-Sitosterol at five different concentrations (see table) were assayed on three different days. In both cases, Precision was evaluated on the basis of the % root mean square deviation (RSD) with ± 2.00 % acceptance level.

Appendix 26.2: Spike recovery for determination of β-Sitosterol

Spiked amount (mg)	Recovered amount (mg)	Recovery (%)
0	0	0
0.4	0.3818	95.45
0.8	0.7767	97.0
1.5	1.554	103.60

Standard addition method was used to determine spike recovery (Shah M. U *et al.*, 2010). Briefly, to a stock solution of nanoparticles (0.5 mL) was added standard solution of β-sitosterol (1 mL) at three concentration levels (i.e. 0.4, 0.8 and 1.5 mg/mL) and mixed thoroughly on vortex. β-sitosterol was extracted from the spiked samples by shaking in DCM for 30 minutes. Absorbances of the recovered samples were measured at 622 nm after reacting with acetic anhydride and Conc. Sulphuric acid. The standard curve was used to calculate the amount of β-sitosterol recovered from the spiked samples. Equation 4 was used to calculate recovery with an acceptance level of ±5%

$$Recovery = \frac{[\beta-Sit \text{ in spiked sample}]-[\beta-Sit \text{ in unspiked sample}]}{[Spiked \text{ } sample]} \text{ } x \text{ } 100 \text{ } ....4$$

Appendix 27: Surface morphology of β-Sit-PLGA and PEG-PLA nanoparticles under physiological conditions
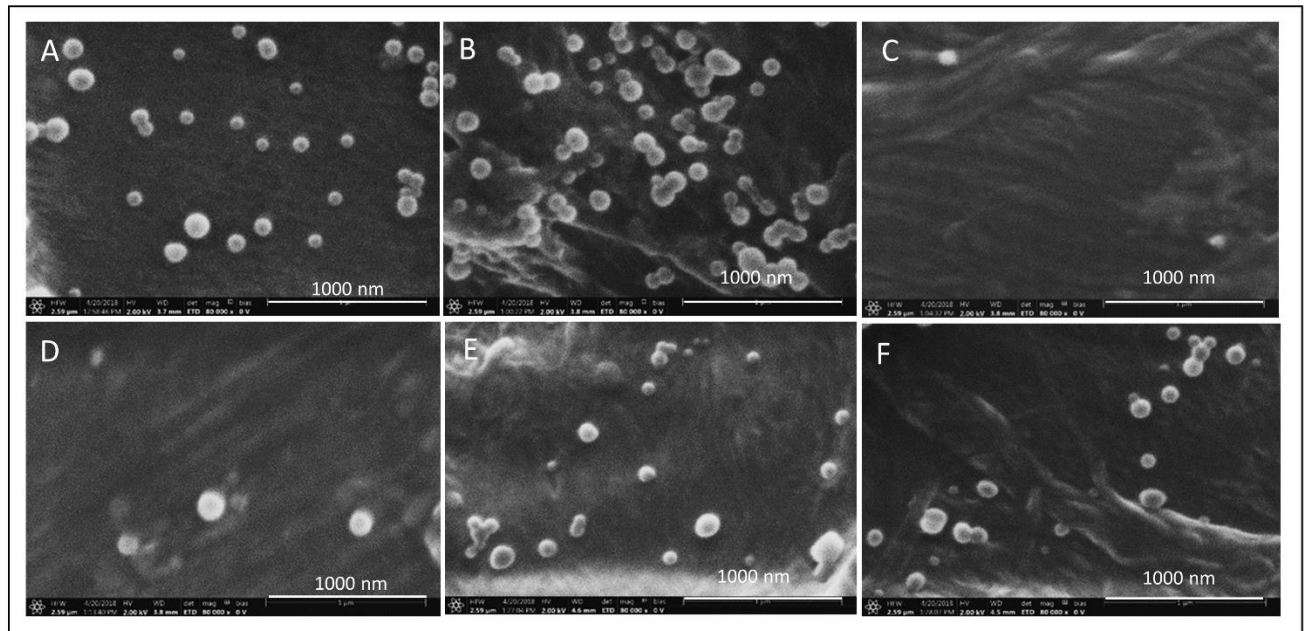
SEM images of nanoparticles after they were stored in PBS and PBS/FBS for 24 hours and on storage. (a) β-sit-PLGA in PBS/FBS, (b) β-sit-PLGA in PBS, (c) β-sit-PEG-PLA in PBS/FBS (d) Blank β-sit-PEG-PLA (e) Blank PLGA nanoparticles at room temperature and (f) Blank PLGA nanoparticles at 4 °C. Particles of PEG-PLA formulations were not visible in SEM, suggesting their instability.